



HAL
open science

In situ liquid phase transmission electron microscopy : from electrocatalysts to biomaterials

Nathaly Ortiz Peña

► **To cite this version:**

Nathaly Ortiz Peña. In situ liquid phase transmission electron microscopy : from electrocatalysts to biomaterials. Other [q-bio.OT]. Université de Strasbourg, 2019. English. NNT : 2019STRAE042 . tel-02498193

HAL Id: tel-02498193

<https://theses.hal.science/tel-02498193>

Submitted on 4 Mar 2020

HAL is a multi-disciplinary open access archive for the deposit and dissemination of scientific research documents, whether they are published or not. The documents may come from teaching and research institutions in France or abroad, or from public or private research centers.

L'archive ouverte pluridisciplinaire **HAL**, est destinée au dépôt et à la diffusion de documents scientifiques de niveau recherche, publiés ou non, émanant des établissements d'enseignement et de recherche français ou étrangers, des laboratoires publics ou privés.



**UNIVERSITÉ DE
STRASBOURG**



ÉCOLE DOCTORALE de Physique et Chimie Physique (ED182)
Institut de Physique et Chimie des Matériaux de Strasbourg
(UMR 7504 CNRS – Unistra)

THÈSE présentée par :
Nathaly ORTIZ PEÑA

soutenue le : 5 décembre 2019

pour obtenir le grade de : Docteur de l'université de Strasbourg
Discipline/ Spécialité : Physique et chimie

***In situ* liquid phase transmission electron
microscopy: from electrocatalysts to
biomaterials**

THÈSE dirigée par :

[Dr. ERSEN Ovidiu]

[Dr. SANCHEZ Clément]

[Dr. PORTEHAULT David]
Paris

Prof., Université de Strasbourg

Prof., Collège de France

D.R., Laboratoire de chimie de la matière condensée de

RAPPORTEURS :

[Dr. GONZALEZ-CALBET José]

[Dr. GACOIN Thierry]

Prof., Universidad Complutense de Madrid

D.R., Ecole Polytechnique Paris Saclay

EXAMINATEURES :

[Dr. SAVINOVA Elena]

[Dr. GERARDIN Corine]

Prof., Université de Strasbourg

D.R., Institut Charles Gerhardt Montpellier

“Lo esencial es invisible para los ojos”
« L'essentiel est invisible pour les yeux »

Antoine de Saint-Exupéry

Acknowledgements

First, I would like to thank my advisors Ovidiu, Clément and David for giving the opportunity to work not only in this project but also to explore multiple routes with the microscope. Their support and the scientific discussions were key to the completion of this work. The guidance from Christel, Sophie, Benedikt and Charles was also essential in this journey. Second, I deeply thank the patience and dedication of Dris, who taught me everything I may know about the microscope and the microscopist's art; he worked shoulder to shoulder by me in the long hours of in situ experiments, and gave me hope in times of despair. I am totally convinced that without him, this work would not have been possible. I also thank to every member of the group of microscopy, the ones who are still there and those who have left as well (I hope I don't forget anyone): Walid, Othmane, Yuvna, Kassioyé, Mounib, Corinne, Mariana, Gisele, Sorina, Sharmin, and maybe other names I'm forgetting, sorry!. I am very thankful as well to the group of LCPMC, Lionel, Simon, Audrey, Madeleine, Kim, Clément and so many others that welcomed me so warmly and with open arms. Thanks to the Protochips and Eden Instruments team for their openness and willingness to hear our needs concerning the holder: Stéphane, Mathias, Daniel, Madeleine, Rémy. Since I left Colombia, I have crossed pathways with many wonderful people that have enriched this experience and that, in one way or another, have contributed to get to this point in my career: Elisa, Nikhil, Bohdan, Ali, Mattia, Laurène, Juan David, Dominika, Professor San Miguel, Emmanuel, Kristof, Samer, Jagadeesh, Wenziz, Flo, Roxane, Charlenne, Laura and so many others that I would like to thank personally. Many thanks to Fernando for his love and support during these couple of years, for having my back in difficult times and for become my partner in life. Last, but not least, to all my friends in Colombia, Carlitos, Diana, Jessica, David, Sebas, Sarita, Ale, Dani, Juan, Juan Camilo, Christian, Vivian, Natalia, Paola, Andrea Melissa, Monica, Edward, Manuel, Elkin... and of course to my family to whom I owe everything I am and I have... Mamá, papá, gracias por el amor, el apoyo y el ejemplo, por permitirme ser quien yo quisiera y por enseñarme tanto, a mi hermana por ser también un ejemplo y porque a pesar de la distancia siempre sé que puedo contar con ella, a mis primas por ser como hermanitas y crecer a mi lado dándome tanto amor, a mi tía y mi tío por cuidar de mi como unos segundos papás, a mi abuelita por enseñarme tantas cosas de la vida y del mundo, gracias a cada uno por enseñarme y amarme tanto!!!

Table of content

Preface.....	8
Prologue	9
CHAPTER I: <i>In situ</i> and <i>operando</i> liquid phase TEM observations	16
1.1. A very brief introduction to <i>in situ</i> liquid (S)TEM	16
1.2. <i>In situ</i> liquid phase and electrochemical TEM set-up	22
1.3. Device cleaning, loading and reuse	26
1.3.1. Cleaning the microchips	26
1.3.2. Device loading and reuse	27
1.4. Imaging mode, resolution and electron dose.....	29
1.4.1. TEM or (S)TEM.....	29
1.4.2. Resolution.....	32
1.4.3. Electron dose	34
1.5. Electrochemical measurements <i>in situ</i> and <i>ex situ</i>	37
1.5.1. Sample preparation.....	38
1.5.2. Electrochemical reference and OER measurements	40
1.5.3. Beam effect and grounding	44
1.6. Additional considerations for data acquisition	45
1.6.1. Post-mortem analysis.....	45
1.7. Perspectives and future improvements	48
1.8. Concluding remarks	48
1.9. References.....	49
Chapter II. Spying on electrocatalysts	57
2.1. <i>In situ</i> and <i>operando</i> measurements for electrocatalysts.....	57
2.2. Cobalt oxide electrocatalysis: A “not so model” system	63
2.2.1. Morphological evolution monitored by <i>operando</i> STEM during cyclic voltammetry.....	65

2.2.2. Morphological evolution monitored by operando STEM during chronopotentiometry.....	69
2.2.3 Structural evolution: post mortem study	71
2.4. References.....	80
CHAPTER III: Monitoring nucleation and growth mechanisms <i>in situ</i>	90
3.1. Ending the guessing game	90
3.2 The case-study of iron oxide.....	92
3.2.1 Thermal decomposition.....	93
3.2.2 Triggering the thermal decomposition <i>in situ</i>	95
3.2.3 Electron dose impact in the nanoparticle growth	101
3.3. Conclusion	106
3.4. References.....	106
CHAPTER IV: Biomineralization processes <i>in situ</i>	112
4.1. Non-classical nucleation in biological systems	112
4.2. Calcium phosphate.....	114
4.2.1 <i>Ex situ</i> synthesis	115
4.2.2 Cryo-electron microscopy	116
4.2.3 <i>In situ</i> synthesis methodology	117
4.3. Calcite.....	122
4.3.1. CaCO ₃ <i>ex situ</i> synthesis	123
4.3.2. Synthesis in a copper grid: control	123
4.3.3. <i>In situ</i> synthesis methodology	124
4.4. Conclusions.....	130
4.5. References.....	132
CHAPTER V: New roads, ongoing work and perspectives	139
5.1 Electrodeposition of pyrocatechol.....	139
5.2. Magnetotactic bacteria.....	149
5.3. Concluding remarks and perspectives	152
5.4. References.....	153

Conclusion.....	158
Annexes.....	162
References.....	167
Annexed movies.....	169

Preface

Direct probing of dynamical processes at the nanoscale is key to move forward in the comprehension of formation, degradation and catalytic mechanisms of biological and synthetic materials. Furthermore, a deepened understanding of such processes in realistic synthesis or functioning conditions is crucial to improve their production and implementation methods in functional devices. Thereby, the development of *in situ* and *operando* characterization techniques arises as a logical step in the advancement of material sciences. *In situ* liquid phase transmission electron microscopy is part of the thriving characterization techniques allowing real time monitoring with nanometric resolution of processes taking place in liquid environments. Although, it is among the youngest techniques, its implementation comes with very high expectations given the extensive and prosperous use of conventional transmission electron microscopy for the comprehension of the atomic structure of a wide variety of materials. Therefore, the goal of this document is to illustrate how we have harnessed the opportunities provided by the *in situ* liquid phase transmission electron microscopy to study various materials, including electrocatalysts during operation, inorganic and biomimetic nanoparticles during crystallization and electroactive materials during formation.

Thus, first, in chapter 1, we will show the methodological approach that was developed to implement the *in situ* liquid phase TEM for the study of different types of materials. Then in chapter 2, the case of Co_3O_4 as a model for the study of electrocatalyzed oxygen evolution reaction similar to that in water electrolyzers, will be presented. In this chapter will be discussed the morphological and structural transformations observed *in operando* conditions. Later in chapter 3, nucleation and growth of nanoparticles *in situ* will be described. We will discuss the pre-nucleation stages observe in the synthesis of iron oxide by thermal decomposition. The impact of the electron dose in the growth of the nanoparticles will be also studied. In this way, we will arrive to chapter 4, where we will describe the *in situ* analysis of the mineralization process of calcium phosphate and calcium carbonate. Here, the crystallization pathways followed by both materials will be analyzed. Finally, in chapter 5, we will mention some new roads that will be pursue after completion of this PhD project which includes the electrodeposition of graphitic films from catechol using the electrochemical set-up and the biomineralization of magnetite within magnetotactic bacterias.

Prologue

L'analyse des matériaux synthétiques, biologiques, ou naturels à l'échelle nanométrique et dans des conditions dites « réelles » est un défi qu'ont en commun les Sciences des Matériaux, de la Terre et du Vivant. En effet, compte tenu de l'intime relation entre la structure de la matière condensée et ses propriétés physiques, chimiques ou biologiques, on ne peut prétendre comprendre ou exploiter un (nano)matériau si on ne connaît pas sa dynamique structurale dans son milieu naturel ou d'application. Pour surmonter ce défi, un mode dit environnemental a été implémenté en microscopie électronique en transmission (MET) permettant une analyse à l'échelle atomique de la matière avec différentes sélectivités, structurale, chimique ou de structure électronique. Cette nouvelle possibilité permet d'observer à l'échelle sub-nanométrique la dynamique de la matière dans un environnement liquide ou gazeux parfaitement contrôlé ouvrant des champs d'investigation immenses en synthèse des nanomatériaux, en électrochimie, en catalyse, mais aussi en géoscience, en biologie et en médecine.

Étudier les nanomatériaux dans leur milieu d'application ou de synthèse, qu'il soit liquide ou gaz, en utilisant les différentes modes de travail en microscopie électronique en transmission (imagerie à haute résolution, spectroscopie d'électrons ou de photons X, diffraction électronique etc.) est un véritable défi. En effet, l'émission et la propagation des électrons dans un microscope électronique nécessitent un milieu sous ultravide. En effet, à cause de la forte diffusion des électrons par les molécules du liquide ou du gaz, les résolutions spatiale et énergétique sont très vite dégradées. Pour conserver les performances « intrinsèques » d'un microscopie électronique traditionnel, il faut confiner l'environnement gazeux ou liquide dans la région des pièces polaires de la lentille objectif où se trouve l'échantillon. Il existe pour cela deux approches : l'utilisation des chambres environnementales ouvertes et des cellules fermées. C'est cette dernière que nous avons utilisée pour ces études. Cela consiste à confiner l'environnement liquide dans une zone restreinte autour de l'échantillon en utilisant une cellule environnementale fermée qui se compose de deux fenêtres en nitrure de silicium amorphe ; ces membranes doivent être suffisamment minces pour rester transparentes aux électrons et suffisamment résistantes pour contenir un liquide. La faible distance parcourue par les électrons dans l'environnement liquide (modulable de 50 nm à 5 μm) permet de limiter l'influence néfaste du processus de diffusion et d'observer, avec un rapport signal sur bruit

exploitable dans les images ou dans les spectres, la dynamique de nano-objets dans de nombreux solvants. Les paramètres de l'environnement sont finement contrôlables et ajustables *via* un système micro-fluidique qui permet d'injecter les liquides ou réactifs entre les deux fenêtres d'observation. Enfin, ces cellules micro-fabriquées peuvent intégrer des électrodes pour appliquer un potentiel électrique en milieu liquide et sonder les réactions électrochimiques, ou un système de chauffage constitué d'une céramique nanométrique qui permet de réaliser des montées en température très rapide et de la contrôler avec une très bonne précision.

Une fois ces développements technologiques réalisés et les équipements correspondants disponibles, un autre frein majeur à la généralisation des analyses en milieu liquide a été le fait que les interactions entre les électrons et les molécules du liquide entraînent la formation d'espèces secondaires telles que des molécules ioniques ou encore des radicaux. Ceci peut avoir pour effet de modifier considérablement l'environnement de l'échantillon et, par la suite, sa dynamique structurale et son évolution vers des états qui ne sont pas représentatives des processus à étudier. Malgré toutes ces inconvénients, le suivi en temps réel par microscopie électronique de la cinétique d'évolution et de la dynamique structurale d'un matériau, d'une cellule ou encore d'une enzyme, dans leur environnement natif ou dans un environnement proche de celui des applications visées (*in situ* et *opérando*), est possible en prenant certaines précautions, tel que le contrôle de la dose d'électrons ou encore en utilisant des modes spécifiques d'observation. De telles mesures permettent de fournir des informations dynamiques sur l'évolution de la structure électronique, sur les transformations morphologiques et les changements de compositions du milieu étudié ou de l'échantillon lui-même. Du point de vue phénoménologique, l'interprétation des données obtenues par microscopie électronique en milieu liquide nécessite une bonne compréhension des processus physico-chimiques qui se produisent lors des observations et la parfaite maîtrise des conditions expérimentales ; une fois les connaissances scientifiques et le savoir-faire expérimental acquises, ce type d'analyse in-situ offre des opportunités uniques pour l'exploration de différents phénomènes qui se produisent à l'échelle nanométrique dans les échantillons situés dans un milieu liquide et soumis éventuellement à une différence de potentiel électrique. .

Nous donnons ici un aperçu des expériences que nous avons développées dans le cadre de ma thèse en utilisant la cellule électrochimique Protochips insérée comme porte-objet dans un microscope électronique. Ce projet de thèse s'inscrit dans le cadre d'un projet

ANR intitulé « InSiChem: électrochimie *in situ* appliquée à la catalyse liée à l'énergie » qui a démarré en novembre 2016.

Dans un premier temps, le but de cette thèse a été de développer des approches méthodologiques permettant de débloquent différents verrous pour permettre l'étude *in situ* et *operando* de réactions d'électrocatalyse. Dans un deuxième temps, cette méthodologie a été appliquée aux nanoparticules de Co_3O_4 utilisées comme électrocatalyseurs pour la réaction d'oxydation de l'eau. Dans un troisième temps, les développements méthodologiques réalisés nous ont permis de suivre en temps réel les mécanismes de pré-nucléation, de nucléation et de croissance des nanoparticules d'oxyde de fer par le procédé de décomposition thermique. Puis, nous avons étudié, en temps réel et dans l'espace direct, les processus de cristallisation de biomatériaux tels que la calcite et l'hydroxyapatite. Enfin, nous avons obtenu des premiers résultats, très prometteurs, sur l'étude de l'électropolymérisation du pyrocatechol pour donner un film de type « graphène ». Toutes ces études sont présentées dans les différents chapitres du manuscrit ; pour finir, à la fin du manuscrit, nous proposerons également quelques pistes pour permettre d'améliorer la mise en œuvre globale des techniques de microscopie électronique *in situ*, en relation avec des expériences *ex situ* ou conventionnelles.

Résultats majeures

Le sujet de cette thèse a été axé sur l'étude *in situ* dans un milieu liquide par microscopie électronique à transmission d'électrocatalyseurs nanométriques de différente nature (spinelles d'oxyde, pérovskites) préparés à l'UPMC-Collège de France à Paris. Ainsi, nous avons tout d'abord déterminé les conditions d'acquisition les plus adaptées pour l'observation de ces catalyseurs pendant les mesures électrochimiques dans le microscope. Puisque ce travail a été le premier projet doctoral utilisant cette configuration d'analyse *in situ* dans notre équipe, une attention spéciale a été consacrée au développement de la méthodologie et à la détermination de protocoles spécifiques à utiliser pour des études futures. Des paramètres tels que la dose d'électrons, le temps d'exposition, le pH ou encore les techniques de dépôt de l'échantillon sur la membrane de la cellule ont été testés et optimisés pour simplement assurer une bonne reproductibilité des mesures ainsi qu'une bonne représentativité des différents phénomènes observés.

Le premier système étudié a été l'oxyde de cobalt, Co_3O_4 . Ce matériau a été largement étudié pour des applications électrocatalytiques, non seulement par les techniques de caractérisation conventionnelles, mais également par plusieurs autres méthodes *in situ* et *operando* telles que les spectroscopies de absorption de Rayons X, infrarouge ou encore Raman. Nous l'avons choisi comme système modèle pour comprendre les possibilités et les limites des études *in situ* par microscopie électronique en milieu liquide. Ceci nous a permis d'observer pour la première fois en temps réel, l'amorphisation de surface des spinelles d'oxyde de cobalt au cours de la réaction d'évolution de l'oxygène. Cette amorphisation atteint sa limite après quelques minutes dans les conditions d'observation et ceci quel que soit l'électrolyte utilisé (tampon KOH basique ou phosphate neutre). Cette restructuration apparaît bénéfique pour l'activité électrocatalytique de l'oxydation de l'eau et démontre que la phase amorphe formée au cours de la réaction est l'espèce active pour l'évolution électrocatalytique d'oxygène sur des matériaux à base de nanoparticules de Co_3O_4 . Cependant, contrairement à d'autres résultats dans la littérature, nos observations montrent sans ambiguïté que l'amorphisation du matériau n'est pas réversible dans les conditions électrochimiques utilisées, en particulier à courant constant, ce qui correspond aux conditions opérationnelles de la plupart des cellules électrochimiques pour la production d'hydrogène. Les électrodes étudiées électrochimiquement *in situ* et *ex situ* ont été ensuite analysées par imagerie à haute résolution, la diffraction d'électrons (SAED) et spectroscopies de perte d'énergie des électrons et de dispersion d'énergie de photons X (EELS et EDS, respectivement), fournissant ainsi une image plus globale de la composition des électrocatalyseurs à différents stades, des transformations microstructurales et de la présence de nouvelles phases induites par le processus électrocatalytique.

Ensuite nous avons exploité les possibilités uniques offertes par la microscopie électronique en milieu liquide pour étudier d'autres types de processus ou de mécanismes physico-chimiques. Nous avons commencé par étudier le processus de nucléation dans un mélange réactionnel pour la synthèse d'oxyde de fer par le procédé de décomposition thermique. Dans ce cas, le faisceau d'électrons a joué le rôle de source d'énergie, en remplaçant de l'énergie thermique utilisée dans le processus de synthèse classique. Grâce à la haute résolution spatiale de la microscopie électronique, il a été possible d'observer les étapes intermédiaires de la nucléation à partir de la formation et de l'organisation interne des monomères. Au-delà de la théorie de La Mer, nos observations montrent que les noyaux s'assemblent dans des structures globulaires, similaires aux vésicules et aux micelles, avant de commencer à former un cristal. Dans le

même contexte, en utilisant la même approche expérimentale, l'impact de la quantité d'énergie apportée sur la morphologie finale des nanoparticules d'oxyde de fer a pu être mis en évidence.

Dans un troisième temps, l'utilisation de cette approche a permis l'observation de la croissance cristalline de biominéraux de calcium dans des environnements biomimétiques. En effet, la cristallisation de CaCO_3 peut être impactée par la présence de différents acides aminés qui peuvent influencer la cinétique de croissance. A ce sujet, en présence d'acide aspartique nous avons observé la formation d'une vésicule « capturant » le calcium du milieu pour former le complexe Ca/Asp/CO_3 suivie par une précipitation cristalline. En revanche, lorsqu'on rajoute de la glycine dans le milieu réactionnel, une coexistence des deux phases, la calcite et la vaterite, a été observée. A titre de comparaison, nous avons réalisé une deuxième étude de biominéralisation en utilisant toujours la microscopie en milieu liquide. Il s'agissait cette fois-ci du suivi à l'échelle nanométrique de la formation et de la stabilité dans le temps des différentes phases intermédiaires qui apparaissent lors de la transformation de l'hydroxyde de calcium (Ca(OH)_2), en présence de l'acide phosphorique (H_3PO_4), en phosphate de calcium amorphe (CaP) pour donner finalement une structure d'hydroxyapatite cristalline. Ceci nous a permis d'observer en première la présence des globules de séparation de phase liquide-liquide dans le mélange réactionnel lors de l'initiation du processus de cristallisation de l'hydroxyapatite.

Enfin, nous avons utilisé cette même méthodologie d'analyse *in situ* pour étudier en temps réel la croissance électrochimique des films de carbone graphitisé à partir d'une molécule organique simple comme le pyrocatechol. Les premiers résultats sont encourageants car ils démontrent la formation des régions cristallines après l'exposition du milieu réactionnel à quelques cycles voltamétriques. Malgré le fait qu'il n'a pas été possible d'observer ce processus de cristallisation en direct dans l'électrolyte, nous avons mis en place un protocole permettant d'identifier des fractions graphitiques autour des électrodes et de suivre leur évolution à travers des clichés « instantanés » enregistrés au même endroit après chaque cycle. Cette stratégie, bien qu'encore perfectible, sera très utile pour suivre les processus de formation d'autres types de matériaux à des échelles sub-nanométriques, surtout si ces matériaux sont difficiles à suivre directement par *in situ* liquide ou si les analyses post-mortem conventionnelles ne permettent pas d'obtenir des informations sur la cinétique du processus ou sur ses étapes intermédiaires.

Conclusions

Cette thèse a permis de développer une nouvelle approche d'analyse à l'échelle nanométrique, dans l'espace direct et en temps réel, des processus dynamiques dans les matériaux situés dans un environnement liquide, à travers l'utilisation de différents modes de travail dans un microscope électronique en transmission. Les conditions d'observation, difficiles à appréhender, doivent en plus être adaptées aux différents types d'échantillons et à la problématique d'intérêt. Pour ce faire, nous avons dû réaliser des investigations approfondies sur les aspects techniques limitant les expériences telles que l'interaction des électrons avec le milieu, l'effet de la dose d'électrons sur les mesures électrochimiques, la méthode de dépôt d'échantillon sur le support et le mode d'imagerie. De plus, les paramètres d'observation ont été optimisés pour permettre le suivi de l'évolution des phénomènes étudiés dans les conditions réelles de leur utilisation.

Nous avons d'abord étudié les transformations structurelles et morphologiques des nanoparticules d'oxyde de cobalt dans des conditions de fonctionnement similaires aux dispositifs pour électrolyser de l'eau. Des changements dans la morphologie des nanoparticules de façon quasi-réversible ont été observés en direct pour la première fois. Cette étude a permis de mettre en évidence le grand bénéfice des méthodologies *in situ* et *operando* pour la compréhension des phénomènes electrocatalytiques. Dans un autre contexte, les travaux réalisés durant cette thèse démontrent également la puissance des techniques de microscopie électronique en transmission *in situ* pour l'élucidation de processus dynamiques qui sont activés dans les premières étapes de formation des structures biomimétiques, inorganiques et même hybrides. De manière générale, ces développements méthodologiques et techniques ouvrent la voie à une meilleure compréhension des mécanismes de synthèse et par conséquent permettent d'envisager un meilleur contrôle et optimisation des propriétés des nanomatériaux pour des applications spécifiques. Finalement, nous avons pu compléter nos travaux par des études *in-situ* des mécanismes de croissance des nanoparticules qui impliquent multiples phénomènes physiques ou chimiques tels que la dissociation, la diffusion et l'arrangement de molécules, ainsi que les étapes ultérieures de mûrissement ou de coalescence.

Chapter I

CHAPTER I: *In situ* and *operando* liquid phase TEM observations

- 1.1. A very brief introduction to *in situ* liquid (S)TEM
- 1.2. The *in situ* electrochemical set-up
- 1.3. Device loading, cleaning and reuse
 - 1.3.1. Cleaning the microchips
 - 1.3.2. Device loading and reuse
 - 1.3.2.1. Electrocatalysts deposition
 - 1.3.2.2. Reaction mixtures deposition
- 1.4. Imaging parameters, resolution and electron dose
 - 1.4.1. TEM or STEM
 - 1.4.2. Resolution
 - 1.4.3. Electron dose
- 1.5. Electrochemical measurements *in situ* and *ex situ*
 - 1.5.1. Sample preparation
 - 1.5.2. Electrochemical reference and OER measurements
 - 1.5.3. Beam effect and grounding
- 1.6. Additional considerations for data acquiring
 - 1.6.1. Post-mortem analysis
- 1.7. Concluding remarks
- 1.8. References

1.1. A very brief introduction to *in situ* liquid (S)TEM

The invention of electron microscopy pushed the boundaries in the exploration of the fundamental structure of matter. Resolved imaging at the nanoscale opened new paths

towards the comprehension of the impact of the atomic order in the macroscopic properties of materials. Thanks to de Broglie's equation, it was possible to understand that the double behavior of the light could also be applied to electrons and so, back in 1933, Ruska and Knoll achieved to form images using electrons as illumination source.¹

The electron-matter interaction can produce different signals as represented in figure 1.1. In the case of thin samples (<100-150 nm), the transmitted primary electrons allow to form highly resolved images of the sample. Additional information can be withdrawn simultaneously from the other signals, making the EM a powerful spectroscopic technique.

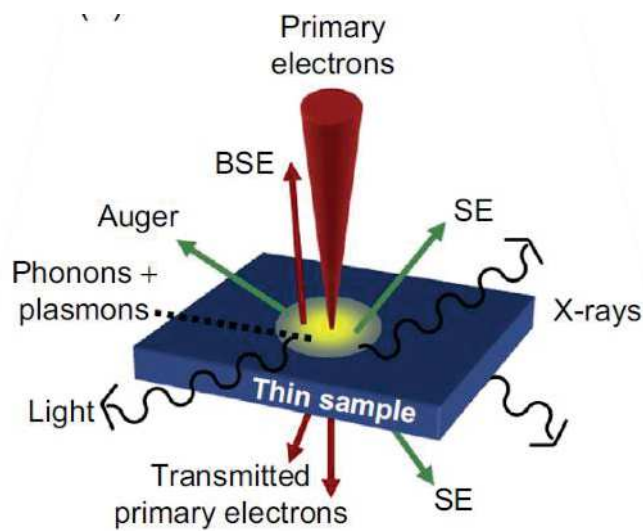


Figure 1.1. Useful signals generated by electron-matter interactions in a thin sample. Adapted from Ref. ²

The principle of Transmission Electron Microscopy (TEM) resides in irradiating a sample with an electron beam acting as an illumination source to create a magnified image. Given that the non-relativistic description of the wavelength of accelerated electrons in a beam is:

$$\lambda = 1.22/E^{1/2} \quad (1)$$

Being E the accelerating voltage, the theoretical resolution gets rapidly at the subnanometric scale. Nowadays typical TEM accelerating voltages span the range 100 to 300 kV meaning that wavelengths between $3.7 \cdot 10^{-3}$ nm and $1.97 \cdot 10^{-3}$ nm can be attained. Nonetheless, the mean free path of electrons is very small, due to the very strong interaction with matter.³ Indeed, even gaseous environments deviate electrons in their path from the source through the sample to imaging system.⁴ Consequently, to warrant

well-functioning electron sources and a sufficient amount of electrons with the desired wavelength reaching the sample, it is necessary to ensure their propagation in ultra-high vacuum (UHV) conditions within the column of the microscope. This requirement is trivial but one of the most challenging parts when envisioning *in situ* liquid observations. Certainly, most liquids evaporate in UHV. This can be sorted out by enclosing the liquids to isolate them from the vacuum conditions in the column. However, even in this case, the electron beam crosses a finite thickness of liquid, which largely diffuses the beam compared to a dry sample under vacuum. Hence, the spatial resolution and the signal to noise ratio (SNR) are strongly degraded. Furthermore, additional interactions may occur between electrons and ions or molecules in the liquid, such as the creation of ionic, radical and solvated electron species. Those are generated locally in the illuminated area and alter the chemistry of the media.⁴

Despite all the difficulties, observations within liquids have been a primary goal from the very creation of EM, since most biological and chemical processes take place in liquid media. Cellular division, protein production, enzymatic structure/function; crystallization, corrosion and degradation processes of materials take place most of the time in aqueous and/or organic solvents. Moreover, all these processes involve numerous dynamic solid/liquid or solid/solid interaction interfaces, making them complex and probably multistep.

Probing specimens, whether it is a material, a cell or an enzyme, in their native or functioning environment is the aim of *in situ* liquid measurements. In addition to providing information about the electronic structure, the morphological and compositional characteristics of the sample in realistic conditions, these approaches can give direct access to the dynamics of the processes, provided their time-scale is suitable with the acquisition time of the measurement. Moreover, if the subject of the study is probed while performing the function it is intended to, then it is an *operando* experiment.⁵ This type of measurements can help to determine, for instance, the impact of an electrolyte on the morphology of an electrode material, the solvation and pH effects on the folding of an enzyme or the movement of cellular organelles in a biological medium. Furthermore, in the case of *operando* studies, it allows to establish the actual active species on a catalytic material or an active enzymatic site.

Thus, the idea of observing objects in liquid environments was born simultaneously with the invention of the electron microscopes⁶⁻⁸, even if the feasibility of such observations had to wait some decades. In the meantime, EM observations of biological or hydrated

samples was achieved by drying or freezing the sample. Before the invention of cryo-electron microscopy, EM brought a deepened comprehension of biological systems as can be evidenced throughout Ruska's Nobel lecture⁹. He narrates with humble pragmatism all the barriers, not only scientific but also social, economic and technical, that had to be overcome in order to get the first electron micrograph but specially the subsequent challenges to continue the research. There, it is possible to find the exciting story of the first image of a bacteriophage¹⁰, the close-up on the wing of a fly as well as bacteria fixed with formalin and embedded in a supporting film stained with a heavy metal salt¹¹, all of which changed the understanding of biological structures. Later, cryo-electron microscopy was key to unveil the role of water molecules in the active structure of proteins, as well as viruses and even inorganic/organic materials.¹²⁻¹⁵ However, cryo-EM gives us only snapshots in a probably long sequence of processes, thus this strategy is limited in the exploration of realistic and dynamical processes.

Throughout the years, there have been some examples of “wet-samples” in electron microscopy. There are two main approaches to observe wet specimens: use an open chamber or a closed cell already mentioned above. In figure 2, Parsons¹⁶ describes the configuration of the chambers in both, open and closed approaches. First, the open chamber configuration (Figure 1.2a) relies on differential pumping to reach pressures up to 0.3 mbar, which allows the condensation of some liquid droplets within the specimen chamber. The open chamber configuration does not allow controlling the thickness or amount of the droplets. This approach is still used for studies in gas environments not only in TEM but in scanning electron microscopy¹⁷ as well. The open chamber approach will not be discussed further in this manuscript. The second approach consists in using a closed chamber (Figure 1.2b) with thin electron transparent windows. It is interesting to note that already back in 1944, one can find examples of closed cells designed to observe colloidal solutions¹⁸. Back then, there was full awareness of the main challenges to overcome: “The essential requirements for windows in the cell are: (a) ready permeability to electrons, so that scattering is insufficient to obscure the image; (b) mechanical strength to withstand a vacuum; and an imperviousness to vapor of water or other solvent medium”. Throughout the years, different materials have been tested to act as isolating membranes. Early examples included cellulose films, aluminum foils, carbon and polymeric membranes. However, the first attempts encountered difficulties with the liquid and membrane thickness along with the control of the distance between the walls of the closed cell.

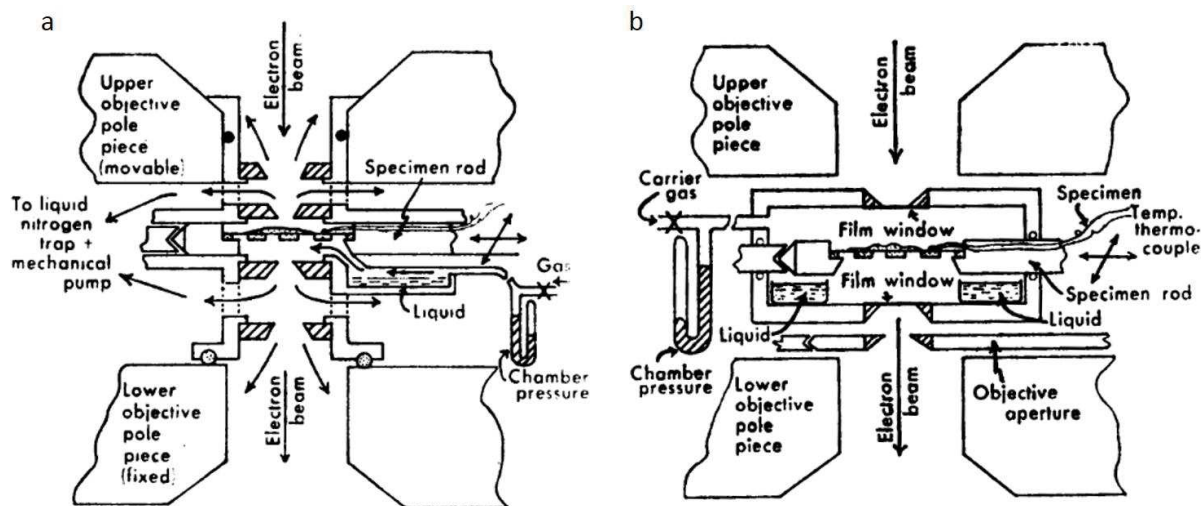


Figure 1.2. a) Generalized diagram of a differentially pumped environmental chamber with inner (100-mm) and outer (300-mm) apertures. Most of the gas escaping from the inner pair of apertures passes into the pole piece gap and is pumped off by a liquid nitrogen trap and mechanical pump. Gas escaping from the outer apertures is removed by the microscope vacuum system with or without the aid of a small booster diffusion pump. The aperture assembly is aligned on the beam by a slight displacement of the upper pole piece. For clarity the objective aperture assembly and the arrangements for temperature control of the chamber are not shown. b). Generalized diagram of an electron microscope environmental chamber closed by thin film windows. The temperature of the specimen and the pressure of the chamber are monitored by a thermocouple and by an external manometer, respectively. The liquid vapor pressure can be supplemented by the addition of other gases. The specimen grid can be completely scanned between the windows in the normal specimen plane in the objective pole piece gap. The objective aperture functions normally. The electron beam penetrates the upper window, the chamber vapor and gas space, the wet specimen, and the lower window in that order. Taken from ref ¹⁶

Therefore, only the advancement in microfabrication techniques permitted the construction of modern observation set-ups for the *in situ* liquid TEM studies. More precisely, the production of thin electron-transparent membranes able to enclose liquids, strong enough to isolate the liquid from the vacuum, with controllable thickness, light contrasting elements and sufficiently chemically inert was critical for the feasibility of *in situ* liquid measurements. Today most of the liquid cells used for *in situ* devices possesses SiN windows that can be fabricated with thickness <50 nm keeping good mechanical resistance and reproducibility.¹⁹ Another very popular membrane material is graphene. Thanks to its great mechanical properties with extremely thin thickness, it is

very appreciated for the highly resolved images that can be achieved. Yet, the use of graphene suffers from a lack of deposition reproducibility and a poor control of the liquid thickness.²⁰

Additional progress in microfluidic channeling as well as microelectromechanical systems have permitted also the miniaturization of electronic circuits allowing direct application and measurements of stimuli over the materials deposited in the observation windows. Thus, some of the first examples using modern holders were provided by Ross and collaborators to study electrochemical processes²¹, as the electrodeposition of metallic nanoparticles or oxide layers.

In situ liquid TEM studies have greatly benefited from these latter developments, which is evidenced in the increasing number of publications using modern holders²². Nucleation and growth of metal and metal oxides nanoparticles have been assessed in depth at the nanoscale, permitting to understand nucleation mechanisms, growth kinetics, and coalescence within a reaction mixture^{23–25}. In these observations, the trigger for the solid formation is mostly the electron beam, which clearly differs from the events occurring in a reaction vessels²⁶. Nevertheless, the information retrieved is still significant for the comprehension of the processes²⁶. Most recent holder designs also include nanopatterned inductors allowing heating the liquid up to 100 °C. Hence, hydro- and solvo-thermal precipitation²⁷ as well as nucleation-growth processes in ionic liquids²⁸ can be observed during heating and cooling.

Furthermore, *in situ* liquid TEM has more recently become an important tool to characterize deactivation and degradation processes in Li-ion battery electrodes and at the electrolyte-electrode interface, including the evolution of the solid electrolyte interphase (SEI) layer, composed of inorganic and organic electrolyte byproducts.²⁹ The field has recently evolved towards the analysis of electrocatalysis events, although it has been mostly confined to the analysis of highly contrasted objects based on precious metals, as will be detailed in chapter 2.

Of course, just like since the very beginning, the study of structures and processes of biological interest keep being of great importance for the microscopy field. As mentioned before, the progress of *in situ* liquid techniques allows to access the dynamical aspects of such processes, that are key for the comprehension of biological systems. Thereby, there are different examples of biomineralization investigated using *in situ* liquid phase TEM. Thanks to this approach, it has been possible to unveil new aspects of the interaction between a biomimetic matrix and a crystallizing substrate. For instance, Smeets *et al.*³⁰

have used a two inlets holder to inject simultaneously a mixture of polystyrene sulphonate (PSS) and of CaCl_2 on one side, and $(\text{NH}_4)_2\text{CO}_3$ on the other inlet. These authors showed that the binding of calcium ions to form Ca–PSS globules is a key step in the formation of metastable amorphous calcium carbonate (ACC), an important precursor in many biomineralization systems.³⁰ Other examples include the observation of the formation of magnetite using selected enzymes from magnetotactic bacteria, or even direct observation of the mineralization in the bacteria by combining confocal fluorescent microscopy to *in situ* liquid TEM.^{31,32}

Even though *in situ* liquid TEM is a flourishing field that has moved a long way during the last years, it is still not a standardized analysis method. A lot of uncertainty comes from the interaction of the electrons with the liquid, the confinement of the liquid layer, the formation of bubbles, among other differences with conventional lab-bench experiments. Thus, in this work, a lot of time has been invested in order to develop a protocol not only for the sample deposition but also for the observation and data recording, to ensure that the *in situ* observations mimic as well as possible the lab-scale experiments. Different aspects that could affect the fidelity of the data compared with the *ex situ* experiments have been evaluated. Thereby, below the reader will find a detailed discussion of the critical parameters that were taken into account to make *in situ* experiments reliable.

1.2. *In situ* liquid phase and electrochemical TEM set-up

As mentioned above, from the very beginning of EM implementation, there have been several designs to attempt *in situ* liquid observations.²² Early designs of *in situ* setups were “home-made”. Some of the first modern liquid TEM cells included glued Si microchips as can be seen in figure 1.3. This configuration implemented by Ross *et al.*²¹ to study the electrodeposition of copper consisted in two lithographed silicon wafers that possessed a Si_3N_4 observation window and a gold working electrode placed on the window. The electrolyte was deposited between the chips and the cell was sealed with glue to ensure the tightness of the cell. Although this device allowed for the observation of Cu electrodeposition, it was limited to a static volume of liquid that was enclosed from the beginning of the experiment, thus impeding the renovation of the electrolyte. Nowadays one can not only enclose a layer of liquid statically but also pass a flowing stream thanks to microfluidic channels going throughout the holder and passing through

the observation window. We will see in the next chapters how this operation mode is important to limit beam damage.

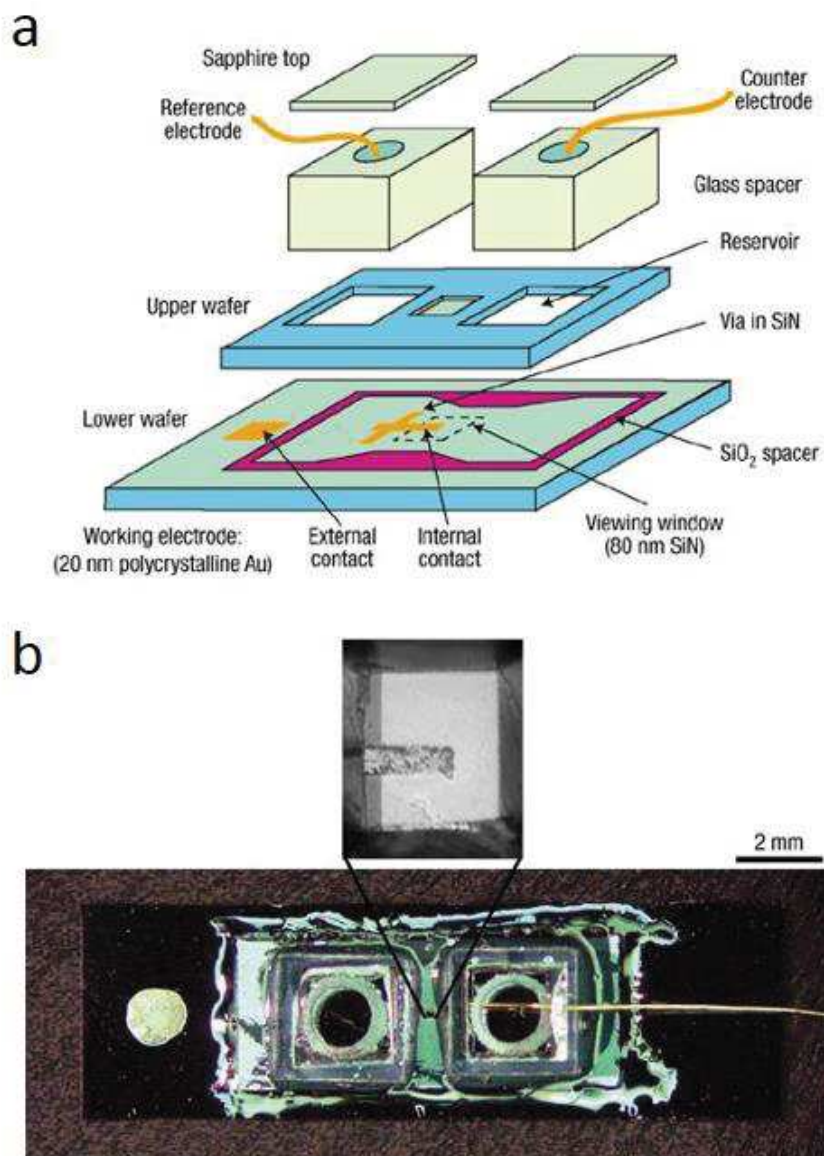


Figure 1.3. One of the first liquid electrochemical TEM cells. a) Components of the cell. The viewing window is enlarged for clarity. b) Photograph of a two-electrodes cell with an optical micrograph of the viewing window. Adapted from ref ²¹

General depiction of the microfluidic channels in modern holders can be seen in figure 1.4. The liquid ports in the tip are connected to tubing made of materials such as flexible and highly chemically resistant polyetheretherketone (PEEK), of an outer diameter of 0.360 mm and an inner diameter of 0.100 mm. Since the tubing can easily become contaminated with sample material, it is disposable and easily replaced. Ideally, the tip fits in the shaft of the holder and can be replaced as well. The material of the tip and of

the lid is a hard metal, biologically inert and nonmagnetic, such as titanium. The chips fit tightly into a precision-made slot that the windows overlap.³³

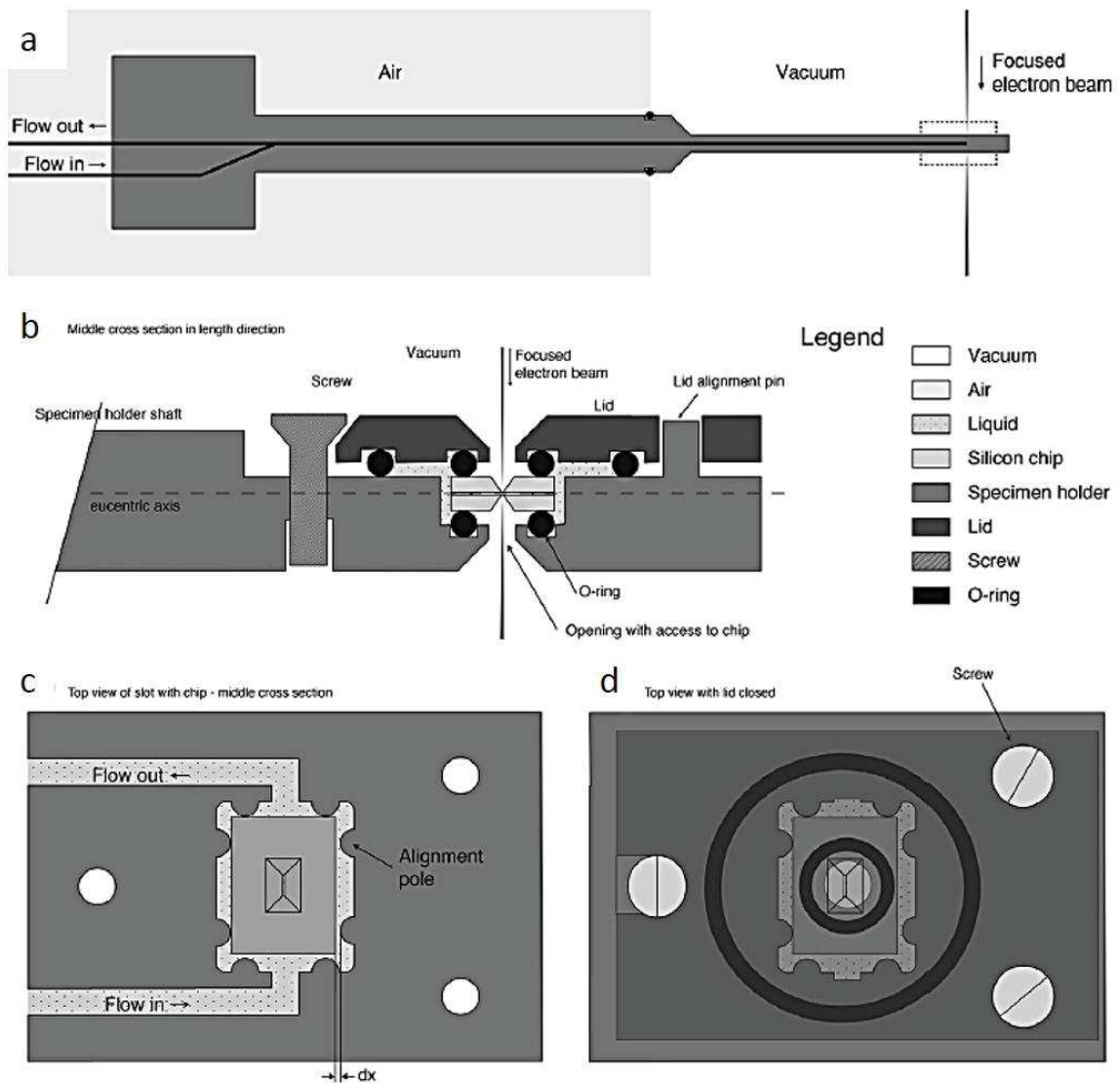


Figure 1.4. Schematic drawings of the tip of a liquid-flow TEM specimen holder. The dimensions are not to scale. a) The shank of the holder is placed in the vacuum of the electron microscope so that the electron beam passes through the tip. b) Side view cross section through the tip showing the positioning of the microchips with respect to the electron beam. c) Top view of the tip with the lid opened so that the liquid paths around the microchips. d) Top view with the lid closed, the color of the lid is transparent so that the positioning of the O-rings can be seen. Adapted from ref ³³

Nowadays, multiple companies provide environmental holders for performing *in situ* liquid measurements. The Poseidon electrochemical set-up of the Protochips company was implemented to develop this work. A depiction of the holder can be seen in figure 1.5. This customized holder is composed of a microfluidic circuit allowing the circulation of a liquid into an observation chamber formed by two silicon chips with an electron

transparent SiN window similar to the one in figure 1.4. Different microchips configurations are available that can be chosen for the observation. The space between the top and bottom chips can be selected in a range from zero to 1 μm , including 50, 150 and 500 nm. This distance is determined by pillars on the bottom chip (see annex 1). Depending on the experiment needs, different window features can be chosen: microwell, heating, electrochemical setting. The device is completed by a rubber o-ring that ensures the tightness of the system. A Gamry Reference 600 potentiostat was used to perform the electrochemical measurements. Even though the set-up here described is specially designed to perform simultaneous electrochemical measurements, it allows as well *in situ* observations in liquids that do not require electrochemical stimuli, such as nucleation and growth processes.

In the specific case of the electrochemical set-up, as can be seen in figure 1.5 in the transversal view of the chamber, the top chip possesses a three electrode printed design: an electron transparent glassy carbon working electrode placed over the SiN observation window and contacted to the rest of the chip with a platinum end. Out of the observation window are a reference and counter electrodes, both made of platinum. Right from the beginning it was noted that the closeness between the electrodes³⁴ in the cell makes the deposition of the sample challenging, since it is not desirable to have the sample all over the surface of the chip, which may cause short circuits. Thus, in the following sections, the sample deposition will be presented. Depending of the type of sample, different approaches were used.

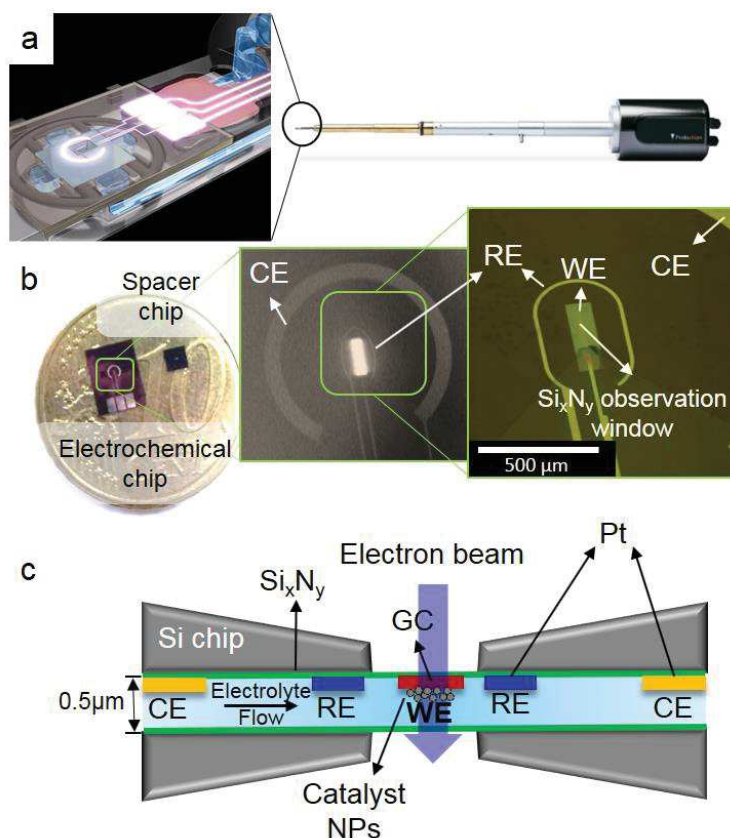


Figure 1.5. a) *In situ* liquid electrochemical Poseidon© TEM holder from Protochips© (the inset shows the tip of the holder where the miniaturized electrochemical cell is integrated. Taken from ref. ³⁵. b) *In situ* disposable chip positioned at the tip of the sample holder, and zoom-in on the working and reference electrode central area of the chip. The working electrode is made of glassy carbon and the reference electrode is actually a pseudo-reference of Pt. The counter electrode is also made of Pt. c) Transversal schematic view of the assembled cell. WE, CE and RE are the working, counter and pseudo-reference electrodes, respectively. GC is the glassy carbon current collector in the WE. The radial distances between WE and RE and between RE and CE are $\sim 90 \mu\text{m}$ and $\sim 500 \mu\text{m}$, respectively.

1.3. Device cleaning, loading and reuse

1.3.1. Cleaning the microchips

The chips are protected by a photoresist coating to avoid contamination and/or breaking from the moment of fabrication, during transportation and until their use. Hence, the first step before use is to remove the coating by plunging them in HPLC-grade acetone during 2 min. Immediately after, without letting the acetone dry, the chips are submerged into methanol during 2 min and finally rinsed with ethanol and dried with compressed air. The drying airflow must be delicate enough to avoid cracking the window but strong enough to not allow solvent traces in the surface of the chips. As suggested by de Jonge *et al.* ¹⁹ the microchips should always be checked under a

binocular microscope to ensure that the windows are entirely clean. In some cases, this cleaning procedure needs additional Ar or O₂ plasma cleaning during 10 s.

1.3.2. Device loading and reuse

Sample deposition can be done on the top, the bottom chip or through the liquid flow. The choice will depend on the type of observation desired. In this work, we can find two main cases: electrocatalytic processes and nucleation/growth of nanostructured materials. Hence, one can think of two scenarios, one in which the material of study is present from the beginning, like in electrocatalysis. Second case, there is no solids in suspension and its apparition occurs during the observation. The deposition procedures are detailed below.

1.3.2.1. Electrocatalysts deposition

In the case of the electrocatalytic processes, the catalyst needs to be in contact with the glassy-carbon working electrode and hence the sample is drop-casted over the top window where the electrodes are printed. However, before depositing the nanoparticles, a thin carbon layer is deposited by evaporation over the window. From our observations, this layer helps to avoid the migration of the nanoparticles from the surface. Moreover, it improves the evacuation of the beam-induced surface charges.³⁶ The carbon layer of around 2 to 5 nm was deposited with a MED 010 Balzers Union Carbon Coater. A mask was employed to delimitate the carbon layer and the sample avoiding spreading out of the observation window. A support was adapted to properly align the mask aperture and the window. The Teflon support is shown in figure 1.6a, where a slot of the chip and mask dimensions was constructed. As can be seen in figure 1.6b, without the presence of the mask the sample spreads beyond the desire area.

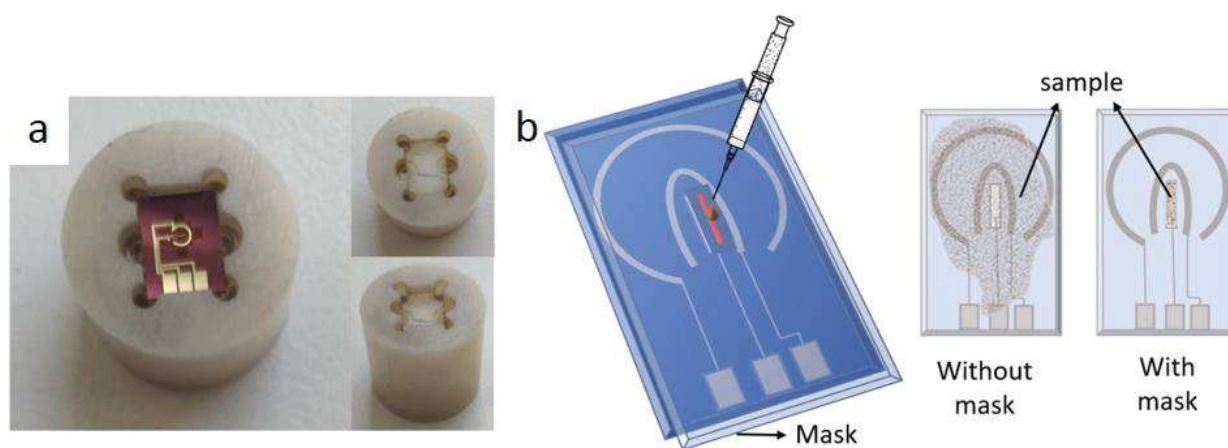


Figure 1.6. a) Teflon support designed to align the mask and the chip. The support has a slot with the dimensions of the chip to facilitate the alignment. b) Schematic representation of the sample deposition and its distribution over the chip with and without the mask.

After drop-casting the catalyst ink, it was dried under air during 1h. Next, the system was closed and the electrolyte solution could be flushed through the holder.

1.3.2.2. Reaction mixtures deposition

In the case of nanostructured material nucleation and growth, a drop of precursor solution was deposited on the bottom chip and the cell was immediately closed with the top chip as shown in figure 1.7, thus avoiding drying of the sample. This method was particularly used in static mode observation, where no additional liquid was introduced once the cell was loaded. On the other hand, if the liquid layer needs to be renewed one can load the mixture through the microfluidic system. It is worth mentioning that the device used to develop this work possesses only one inlet. As will be explained in chapter 4, if nucleation is expected to be a fast process with time-scale much shorter than the renewal of the solution in the cell, the ideal configuration is to mix the reagents only at the tip in the observation window, not before. To accomplish this, a drop of one of the reagents can be loaded in the holder and the other reagent delivered with the microfluidic system. Frequently, different loading procedures were tested for the same set of samples.

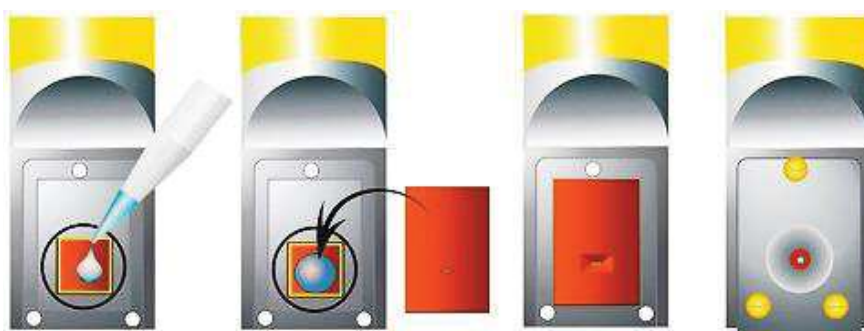


Figure 1.7. Sample deposition over the bottom chip. This procedure was most often used in static mode or when one needed a reagent to be present before starting of the solution flow. In the latter case, a droplet of the reaction mixture was deposited and the top chip was quickly placed to avoid drying of the mixture.

In general, reuse of the chips is only feasible in the case of the bottom chip from the electrochemical set-up, after careful check that no deposits have appeared on the chip. In the other cases, the chips can be used only once.

1.4. Imaging mode, resolution and electron dose

TEM experiments were conducted in a JEOL 2100F probe corrected field emission analytical microscope operated at an acceleration voltage of 200 kV. Generally, once the sample is ready to be analyzed by conventional TEM, the first thing to do is the alignment of the microscope. In the case of liquid phase TEM, this step must be done before introducing the liquid cell, commonly by using a regular copper grid for a variety of reasons. First, the liquid induces a very large diffusion of the beam making the alignment difficult. Second, concentrating too much the beam can exacerbate the creation of bubbles or reactive species resulting from the interaction between the beam and the liquid. Third, try to minimize the non-monitored exposure when trying to observe the nucleation and growth of nanoparticles triggered by the beam. Once the microscope is well aligned, the *in situ* holder can be introduced.

1.4.1. TEM or (S)TEM

The beam can irradiate the sample in two principal modes as can be seen in figure 1.8. On the one hand, TEM mode where the electron beam is parallel and incident onto a defined area of the specimen. Electrons transmitted through the specimen are focused by lenses and collected by a parallel detector to form an image. On the other hand, the scanning mode uses an electron beam focused to a spot and is scanned sequentially across the specimen.³⁷

Furthermore, two different detectors can be used to form the image. To start, a bright field detector where the unscattered (transmitted) electron beam is selected with the aperture, and the scattered electrons are blocked. Since the unscattered beam is selected, areas with crystalline or high mass materials will appear dark. Contrarily, in a dark field detector the unscattered electron beam is excluded from the aperture, and the scattered electrons are selected instead. Hence, the areas where there is no electron scattering and (*e.g.*, the areas around the sample) will be black, while the areas with materials will appear bright. This technique can be used to enhance contrast when the bright field image is not clear enough, especially when imaging crystalline features that are too small or are drowned out of view. It can also be used to study the crystal lattice, crystal defects, stacking faults, dislocations and particle/grain size. Heavier atoms scatter electrons more intensively than lighter atoms. The simultaneous acquisition with both detectors allows obtaining complementary information about crystal orientation,

electron/mass density, staking, and so on. This is particularly convenient for *in situ* observations where dynamic processes of multiple nature are occurring at the same time.

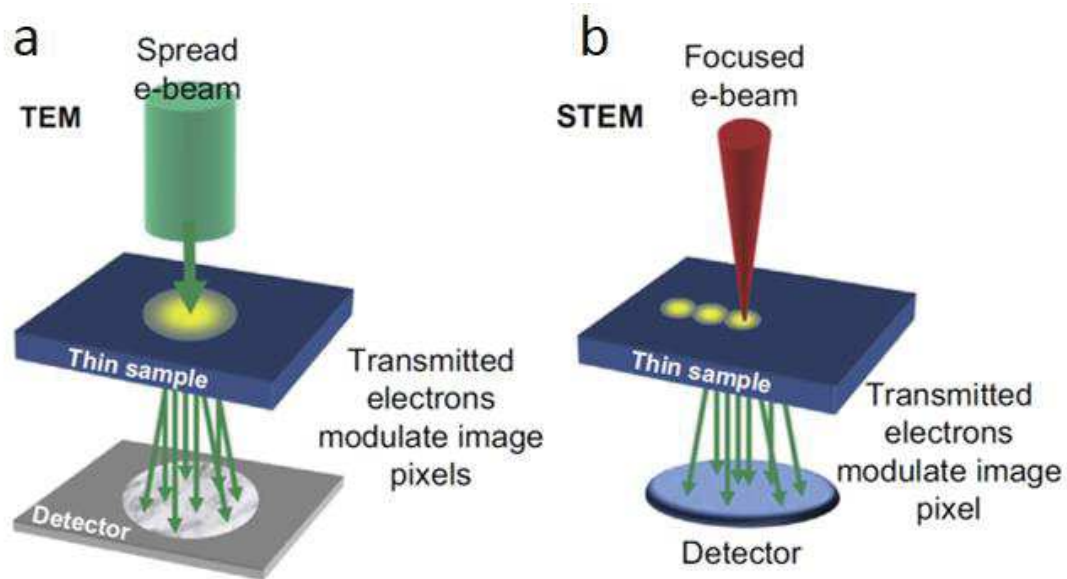


Figure 1.8. a) Parallel image acquisition in TEM. b) Serial collection of transmitted electrons in STEM.

The choice between the TEM parallel beam and the STEM convergent probe will be linked to the position of the sample within the cell and to the control of the electron dose during the experiment. As mentioned before, the sample can be deposited over the top chip, the bottom one or grown during the experiment. de Jonge, Ross and collaborators³⁸⁻⁴³ have largely discussed the use of either configuration as a function of the experiment needs. In figure 1.9, one can find a schematic representation of the path of the beam in each configuration.

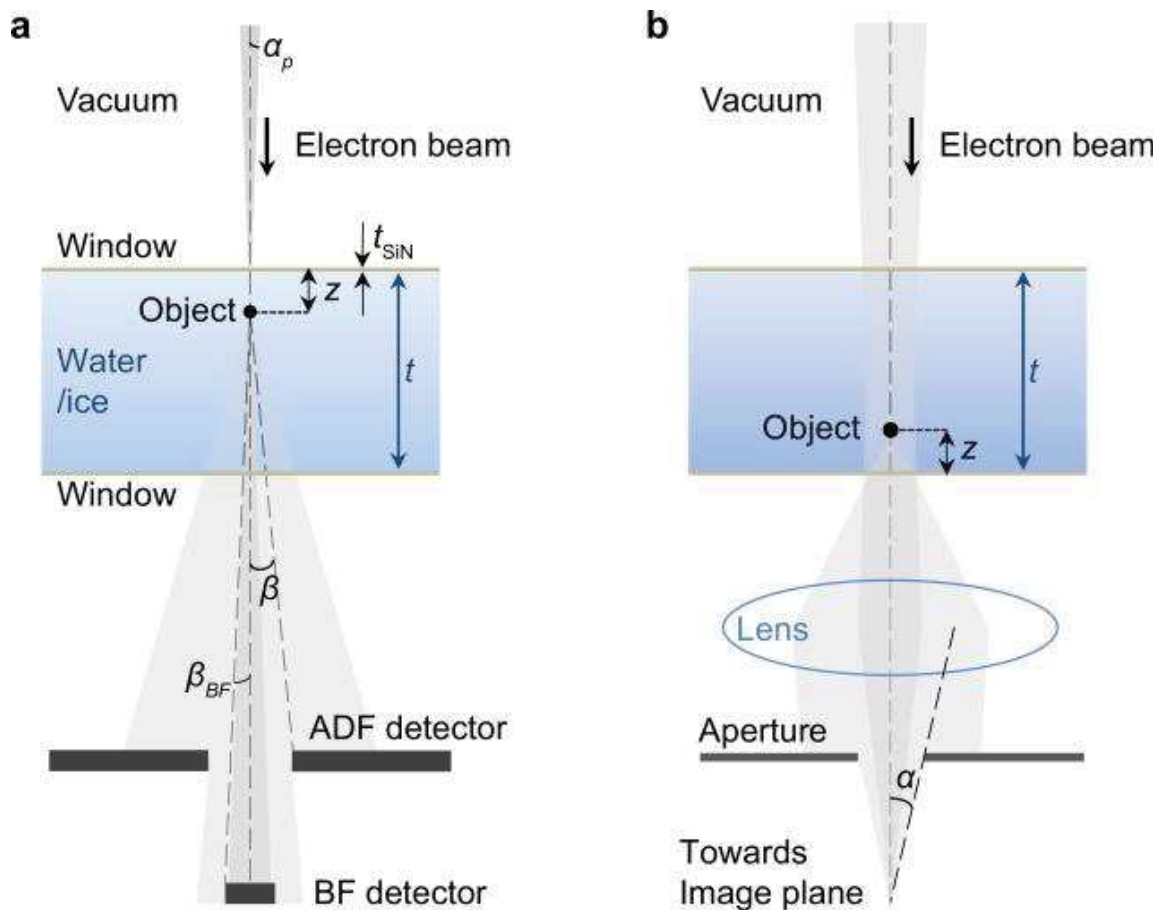


Figure 1.9. Configurations for scanning transmission electron microscopy (STEM) or TEM of nanoscale objects (e.g., nanoparticles, proteins) in a liquid water layer enclosed by two thin silicon nitride (SiN) membrane windows. The sample configuration also applies for a thin sample of amorphous ice but then the thin membrane windows are not present. Sketch not to scale. a) Configuration for STEM mode where the best resolution is obtained for an object close to the beam entrance window at vertical distance z . The thickness of the water is t and the thickness of a SiN window t_{SiN} . The electron probe semi-angle is denoted as α_p . Detection is via the annular dark field (ADF) detector with opening semi-angle β , or via the bright field (BF) detector with opening semi-angle β_{BF} . b) TEM of an object positioned just above the exit window in the liquid for the highest possible spatial resolution. The opening semi-angle towards the camera α is adjusted by the objective aperture. The specimen is imaged with a slight defocusing of the electron beam for optimal contrast. Either bright field scatter contrast or phase contrast is obtained. Taken from reference ³⁸.

For samples at the bottom of the liquid layer or far from the beam entrance, the best spatial resolution will be provided by the TEM mode. This configuration was particularly useful in the observation of the nucleation and growth of iron oxide nanoparticles within an organic solvent at high electron doses and of the growth of calcite and the transformation of hydroxyapatite, which will be discussed in chapters 3. In these cases, nucleation is more likely to take place within the liquid layer far from the beam entrance. Although, there were cases where some nuclei were observed on the windows surface, both the top and bottom ones.

On the other hand, as mentioned in the loading section, for the study of electrocatalysts, the nanoparticles should be in contact with the working electrode, meaning that they will be always placed at the top of the liquid layer and hence the best spatial resolution will be provided by the STEM mode. Moreover, the STEM does not interfere with the electrochemical measurements as will be described latter on in section 1.5.

1.4.2. Resolution

The interest of using the electron microscope is accessing the nanometric, or even atom-scale, structure of materials. Introducing a liquid in the medium will be directly in conflict with the resolution that can be attained in comparison with vacuum observations. Conventional (S)TEM in our microscope shows a resolution of around 0.24 nm at 200 kV. However, both spatial and temporal resolution within the liquid will be limited by the thickness, the stability of the material and the electron dose. Typical experiments in this work were carried out within liquid layers with thicknesses ranging from 10 to 1000 nm. Calculations of the minimum resolution that can be achieved as a function of the liquid layer thickness in STEM and TEM can be seen in figure 1.10.^{38,41} For high contrasting elements like Au within a 50 nm layer, a minimum resolution of around 1-2 nm is expected whereas for lighter elements like carbon this limit goes up to 7-8 nm.

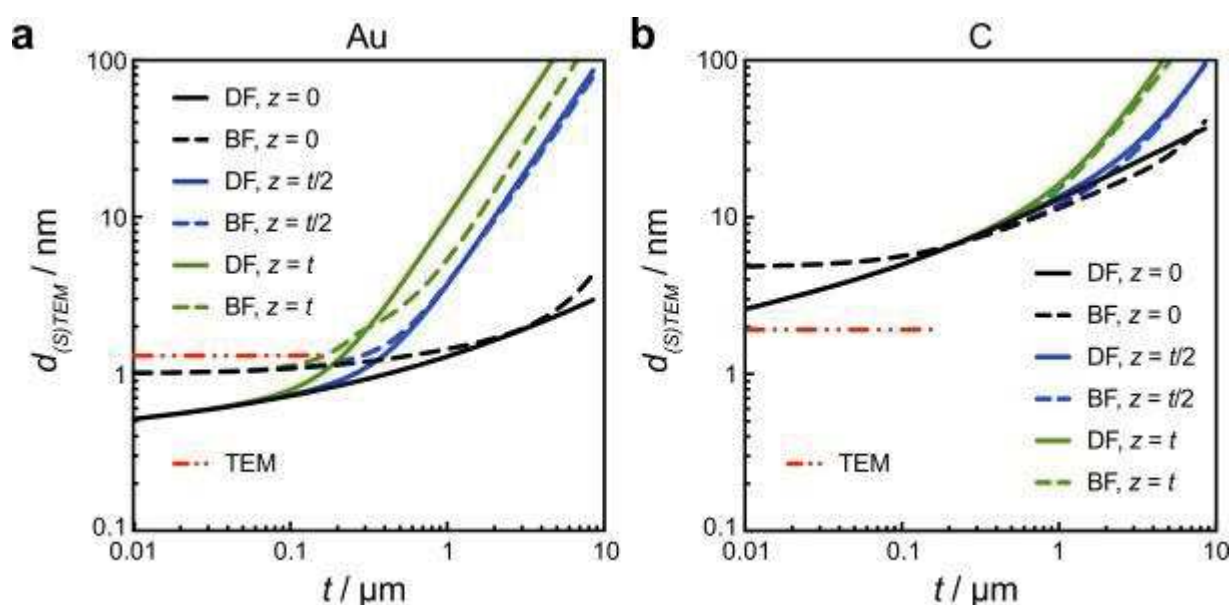


Figure 1.10. Calculations of the spatial resolution d_{STEM} and d_{TEM} as a function of the thickness t of a liquid water or amorphous ice layer for STEM and phase contrast TEM, respectively, at the optimal choice of the detector-opening angle. Taken from ref ³⁸.

Considering the importance of the liquid thickness in the final resolution, it is again good to know that the pressure difference between the fluid in the liquid cell and the exterior vacuum generates bulging of the SiN (figure 1.11). This increases the imaged fluid volume, particularly the liquid film thickness, which decreases the signal-to-noise ratio (SNR), limiting the achievable spatial resolution and contrast. Note that determining the actual thickness can be done by using electron energy loss spectroscopy.⁴²

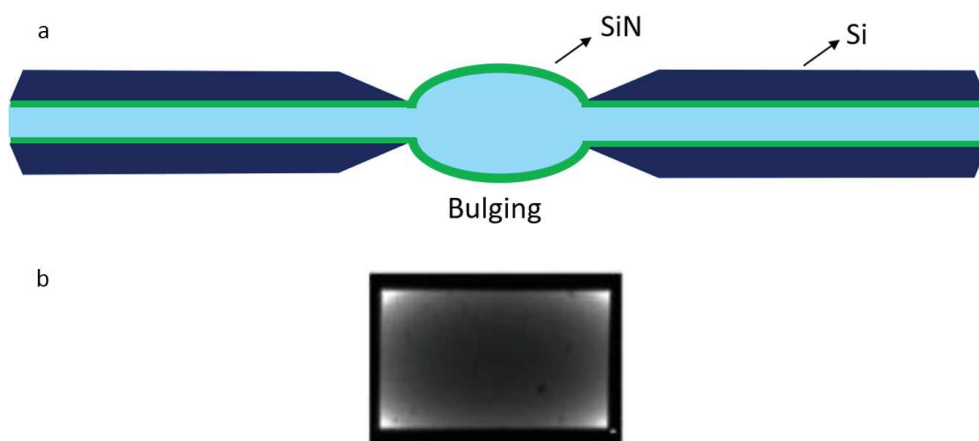


Figure 1.11. a) The top figure illustrates the bowing effect. When two windows are placed back to back the pressure difference between the inner and outer parts causes the thin windows to bow or bulge out. b) The bottom figure shows a TEM image of a window. The light and dark contrast is a direct result of bowing. The thinnest regions are on the corners, resulting in bright contrast. Adapted from ref ⁴⁴

In view of the calculations described above, the resolution that can be achieved ranges from 1 to 8 nm in the materials studied in this work. Such resolution was sufficient to observe the electrocatalytic transformation of Co_3O_4 during water splitting, but might be limiting in the study of subnanometric processes. Nonetheless, these conditions were sufficient to observe very early stages of the nucleation processes, both in aqueous and organic solvents, as will be discussed in chapter 3 and 4.

Another factor influencing the resolution is the formation of bubbles within the observation chamber. The formation of bubbles may arise from the interaction between the electron beam and the liquid that results in H_2 or O_2 .⁴⁵ These bubbles may have a beneficial effect on the resolution given that only a thin layer of liquid remains adhered

to the windows, thus permitting to increase the SNR during the observation. We must however keep note that very thin liquid layers can affect the behavior of the observed systems when compared with conventional experiments.⁴⁶

Regarding the temporal resolution, main limiting factors arise from the image acquisition speed/exposure time. Again, it is necessary to find the best compromise between the signal to noise ratio and the beam exposure. As will be discussed in the next section, the interaction between the beam and the liquid can create reactive species as well as surface charges in the entrance of the beam, thus causing the detachment of the deposited sample. Therefore, one needs to limit the duration of the observation on the same area. Particularly for dynamical processes (*i.e.* electrocatalytic processes) studied by STEM, the signal requires significant fly-back time of hundreds of milliseconds⁴¹, so to minimize the acquisition time, the videos are directly recorded from the microscope handler software with a minimized pixel dwell time of around 40 μ s.

1.4.3. Electron dose

In addition to the challenges related with the liquid thickness, the interaction between the beam and the liquid results in the formation of reactive species that can ultimately change the chemistry of the medium, among other effects. Thus, like in the case of fragile materials, the observation of specimens in liquids requires finding the best compromise between the electron dose to optimize the signal to noise ratio and the beam influence on the *in situ* observations in terms of beam damage and charge accumulation. The electron dose d provides a measure of the amount of electrons per area unit and time.

$$d = i_e/eA \text{ (e}^-/\text{nm}^2\text{s)}$$

i_e = electron beam current (pA)

e = elemental charge of an electron ($1.602 \cdot 10^{-19}$ As/e⁻)

A = irradiated area (nm²)

In the case of TEM, A corresponds to the whole observation window. In the case of STEM, A will depend on the image size typically given in pixel*pixel and dwell time.

In the case of aqueous electrolytes, the species formed upon irradiation are summarized in eq. (2)



Over time, the concentration of such species varies as shown in figure 1.12. After a few initial ms the concentration of all the species reaches a concentration plateau. The apparition and persistence of these species can lead to changes in the local pH or of the chemical environment in general. These species may also yield etching and/or other forms of degradation of the sample^{4,47,48}. This effect is generally more severe when irradiation is continuous, like in the TEM illumination mode. On the other hand, the scanning probe of STEM permits diffusion of the species formed on a specific position before the probe scans again this position. Hence, a better control over the electron dose is achieved, although the reactive species are still formed.

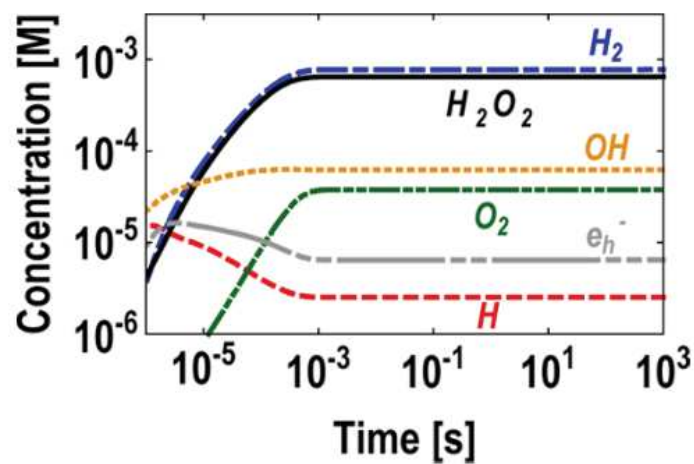


Figure 1.12. Concentrations of e_h^- , H^\bullet , H_2 , H_2O_2 , OH^\bullet , and O_2 as a function of time of irradiation in water, when the sample is irradiated continuously at a dose rate of 7.5×10^7 (Gy/s) into degassed water. Taken from ref ⁴⁹.

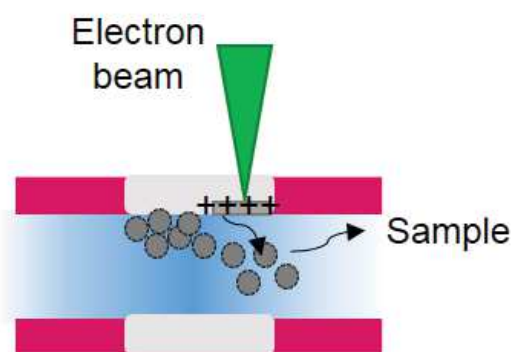


Figure 1.13. Nanoparticles detachment induced by surface charges.

Another important consequence of the beam irradiation is the accumulation of charges. Although these charges can diffuse easily into the liquid, they may also accumulate on the surface of the amorphous isolating SiN windows.⁵⁰ The charge can then induce the detachment of the nanoparticles from the window as schematized in figure 1.13.⁴⁶ The detached sample can then migrate far from the window surface, degrading the spatial

resolution up to the total loss of visibility, particularly in STEM. Thus, limiting the applied beam current is important not only to reduce the amount of radiolysis byproducts but also to avoid accumulation of charges.

Overall, optimizing the illumination conditions means reaching the best compromise between spatial and temporal resolution, signal-to-noise ratio on one side, and radiolysis species production, charge accumulation and particles detachment on the other side. In the case of Co_3O_4 nanoparticles discussed in chapter 2, figure 1.14 shows that at low beam currents, the nanoparticles remain on the observation window for longer periods of time yet with a rather low SNR. However, at high beam currents, the particles do leave the region of interest (ROI) in less than 1 min, hence limiting the observation time because of the accumulation of charges on the surface⁵⁰. It is noticeable that, even after a long exposure time, the nanoparticles did not present the morphological transformations as observed when the electrocatalytic conditions are imposed. This observation demonstrated that the structural evolution, especially the amorphization process observed in OER conditions, is not induced by the electron beam. More details about these results are given in chapter 2. The STEM observations reaching the best compromised mentioned above correspond to a beam current of 35.1 pA. This was the beam current employed for most of the *in situ* measurements, unless said otherwise. The beam current was varied only to evaluate the effect of the electron dose in the nucleation and growth process, as will be described in chapter 3.

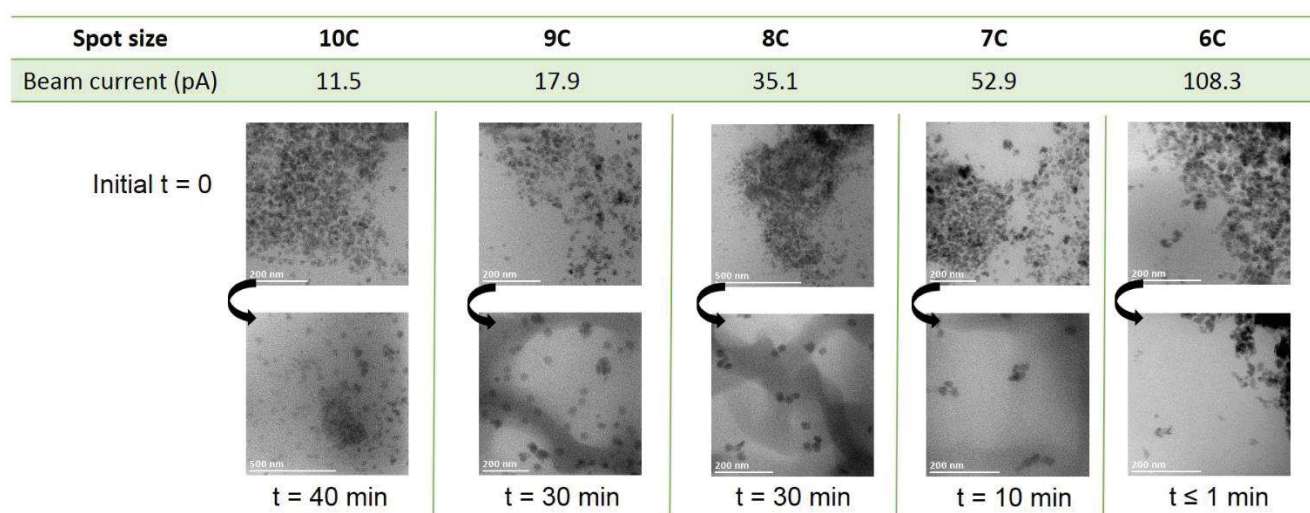


Figure 1.14. Impact of the STEM beam current on the surface detachment of Co_3O_4 nanoparticles due to charge accumulation on the window surface.

1.5. Electrochemical measurements *in situ* and *ex situ*

One of the main interests in this work was the study of electrocatalysts *in situ* and *operando*, i.e. during the electrocatalysis process. As emphasized since the beginning of this chapter, *operando* electrochemical measurements need to be reliable when compared to those yielded at the end of the classical *ex situ* measurements ensuring that any morphological or structural change can be traced back to the electrocatalytic activity.

In figure 1.15 are summed-up three key aspects when considering the implementation of the *in situ* electrochemical set-up: the quality of the images and videos acquired, the accuracy of the electrochemical data and the reliability compared to the phenomena observed *ex situ*. These three elements are highly connected and need special attention to be optimized. In the previous sections the main aspects concerning the acquisition of images were addressed. In this section we will discuss the practical aspects to achieve reliable electrochemical data and how that can affect the other aspects.

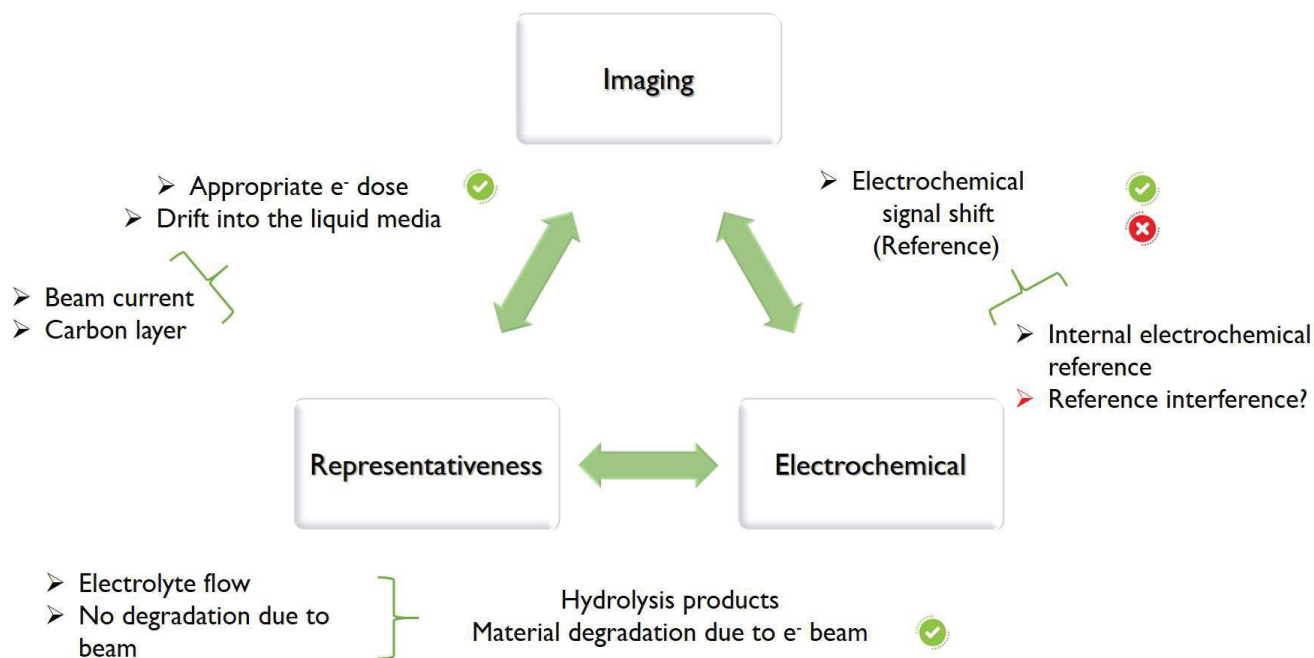


Figure 1.15. Schematic representation of the different aspects involved when performing *in situ/operando* liquid phase electrochemical (S)TEM

Whether it is the oxygen evolution reaction, the hydrogen evolution reaction or the oxygen reduction reaction, the goal of electrocatalysis is to minimize the overpotential (η) required to perform the reaction. The overpotential is the difference between the applied potential (E) and the equilibrium Nernst potential. Therefore, η corresponds to the

energy needed to overcome kinetic limitations. The lower η , the closer to the equilibrium potential the reaction occurs, so the more active is the electrocatalyst. η depends on the specified current density, so that comparison of electrocatalysts must be done at the same current density⁵¹.

Lab-bench evaluation of electrocatalytic properties relies on the preparation of the working electrode. Typically, a suspension called ‘ink’, composed of the catalyst nanoparticles, an electron-conducting matrix (e.g. black carbon, Vulcan, etc) and a fixing but ionic conductor polymeric agent such as Nafion is prepared. The ink is deposited over the current collector (or substrate) of the working electrode, forming a uniform layer on the surface that acts as the working electrode. The simplest technique to assess electrocatalytic properties of an electrode material is cyclic voltammetry, where the applied voltage is varied and the current measured in a three-electrode setup. At the voltage corresponding to the onset of the reaction, the current increases in absolute value, showing the exchange of charges between the working and the counter electrode, which should correspond to the occurrence of the electrocatalytic reaction, as seen in figure 1.16.

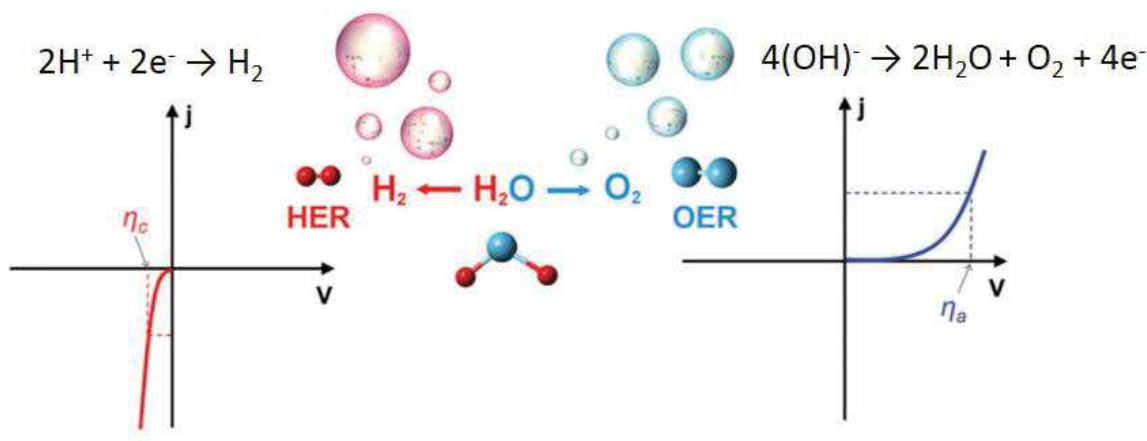


Figure 1.16. Polarization curves for hydrogen evolution reaction (HER) and oxygen evolution reaction (OER). The η_c and η_a are the overpotentials for the cathode and the anode at the same current (j), respectively. Taken from ref ⁵¹

1.5.1. Sample preparation

Thus, a first consideration is related to the sample preparation. Although ink preparation described above is extensively implemented on the lab-bench, polymeric

agents, as Nafion, can easily degrade under the electron beam. Moreover, the electron-conducting matrix, such as black carbon, can deteriorate the contrast and hinder the interpretation of the images. Therefore, inks evaluated *in situ* were composed only of the catalyst nanoparticles dispersed in ethanol. As the polymer exhibits acid-base properties, its presence or absence may change the electrochemical response of the material. To insure that the behavior of the catalyst would not be affected by the ink's composition, the 'only catalyst' inks, made of solely the electrocatalysts nanoparticles dispersed in ethanol, were tested in a classical *ex situ* set up. Co_3O_4 nanoparticles ink and $\text{La}_{0.7}\text{Sr}_{0.3}\text{MnO}_3$ (LSMO) were used to test OER and ORR potential ranges, respectively. In figure 1.17 shows that even upon several CVs there are no significant losses in the current over 100 cycles for Co_3O_4 and 20 cycles for LSMO. Hence, although there is no fixing agent, the particles remain on the surface of the electrode. Moreover, the contact between the electrode and the electrocatalytic material is apparently not limiting charge percolation, so that an electron-conducting matrix such as black carbon is not needed for the materials studied herein (figure 1.17c).

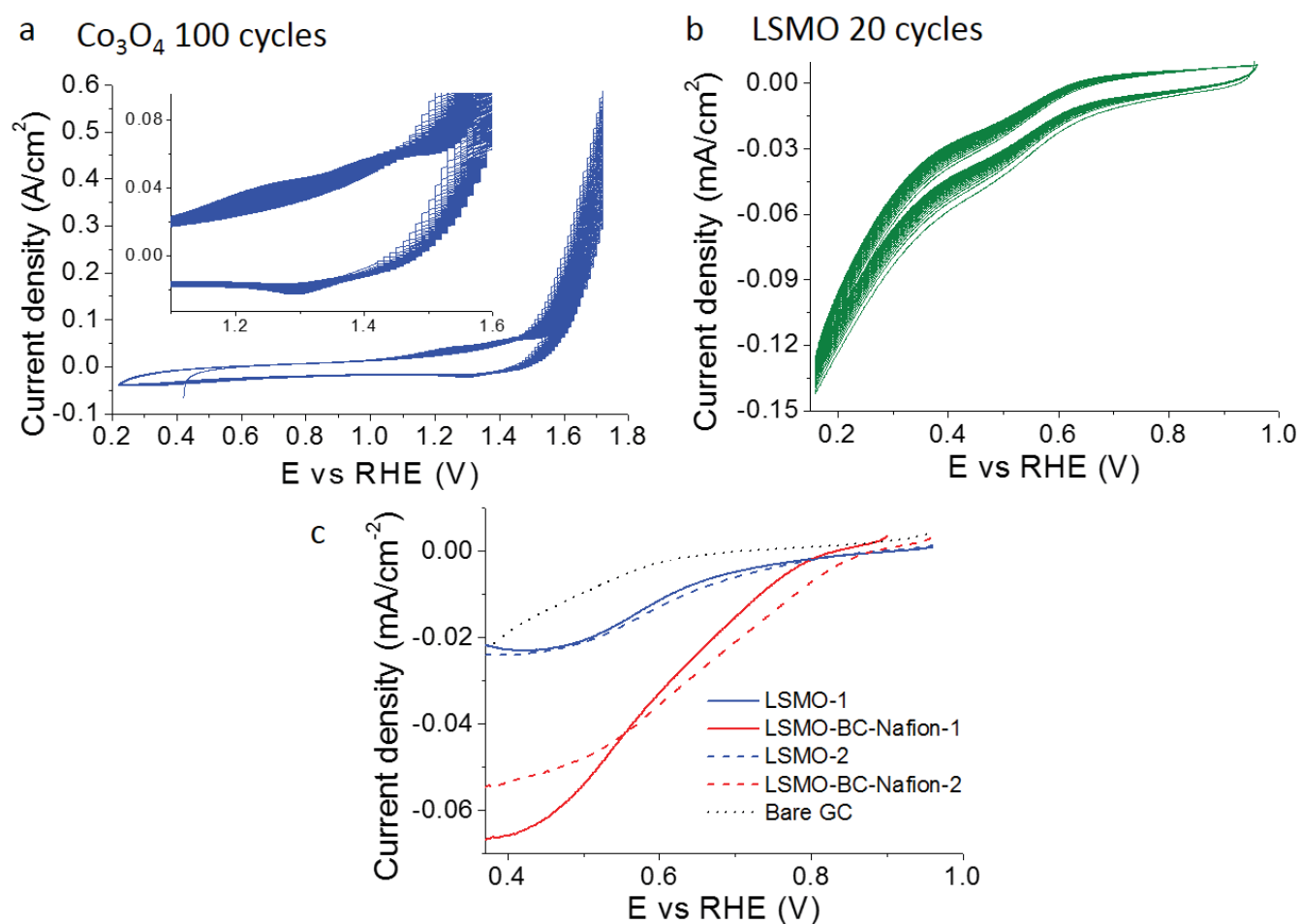


Figure 1.17. Cyclic voltammetry measurements at 100 mV/s of a) Co_3O_4 during 100 cycles and b) $\text{La}_{0.7}\text{Sr}_{0.3}\text{MnO}$ during 20 cycles ‘only catalyst’ ink tested for OER and ORR potential ranges, respectively. c) Comparison between LSMO conventional ‘ink’ with nafion and black carbon and ‘only catalyst’ ink. Electrochemical measurements were performed in a three electrodes cell with a rotating glassy carbon disc as a working electrode at 1600 rpm.

1.5.2. Electrochemical reference and OER measurements

As it has been mentioned above, the miniaturized electrochemical cell possesses a Pt contact acting as a pseudo-reference electrode. However, platinum is not strictly speaking a reference. Indeed, Pt is considered as a pseudo-reference, because it is not ideally nonpolarizable electrode. That is to say that depending on the current density applied there is a shift of its potential during the measurements. Furthermore, most pseudo-reference electrodes work over a limited range of conditions such as pH or temperature; outside of this range the electrodes’ behavior becomes unpredictable.⁵²

Thereby, in order to insure that the potential ranges at which we were measuring CVs are the appropriated ones, it was necessary to evaluate the behavior of the Pt electrode by inserting an internal electrochemical reference. Such internal reference was a stable redox couple used to calibrate the potential when comparing with *ex situ* measurements. We applied a procedure proposed by Unocic *et al.*⁵³ who used a reversible ferricyanide/ferrocyanide redox couple. The electrolyte was composed with potassium ferricyanide [$\text{K}_3\text{Fe}(\text{CN})_6$] (6.7mg, 0.02mmol) and potassium ferrocyanide [$\text{K}_4\text{Fe}(\text{CN})_6 \cdot 3\text{H}_2\text{O}$] (8.4 mg, 0.02 mmol) added to a 10 mL supporting electrolyte, which consisted of a mixture of potassium chloride (KCl) (0.75 g, 10.00mmol) and sodium cyanide (NaCN) (6.00 mg, 0.12mmol). The latter is added in order to avoid the formation of Prussian blue at the surface of the Pt electrode. The electrolyte containing the internal reference was introduced in the cell at a flow rate of 25 $\mu\text{L}/\text{min}$ using the micropump system described above.

CV cycles obtained using the *in situ* TEM holder are presented figure 1.18. The anodic and cathodic peaks from the redox couple $[\text{Fe}(\text{CN})_6]^{3-/4-}$ appear between -50 to 50 mV vs. Pt, in agreement with Unocic *et al.*⁵³ A slight anodic shift after the first cycle occurs and stabilizes between the second and third cycle. We observe a deviation from the ideal reversible character of the reaction since the difference between the anodic and cathodic peaks is over 59 mV s^{-1} .⁵⁴ Nonetheless, because the position of these waves was stable and reproducible, the redox couple $[\text{Fe}(\text{CN})_6]^{3-/4-}$ could be used as an internal reference.

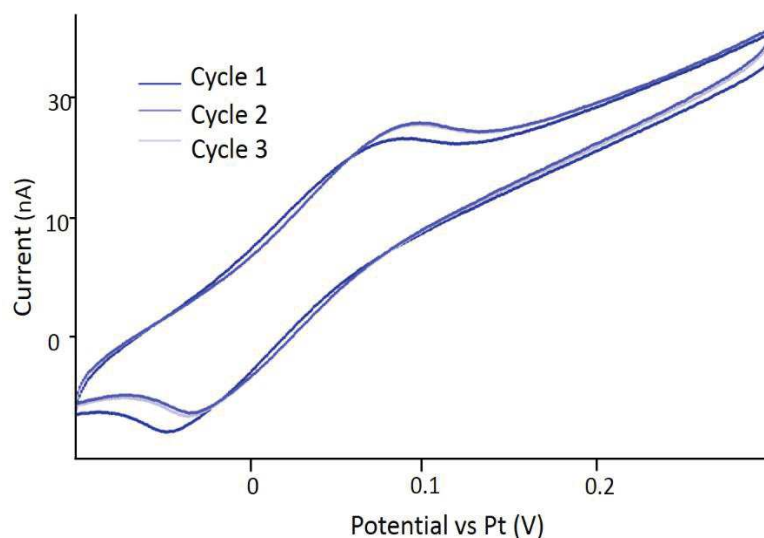


Figure 1.18. Cyclic voltammograms of a glassy carbon electrode within a 2 mM $\text{K}_3\text{Fe}(\text{CN})_6$ and 2 mM $\text{K}_4\text{Fe}(\text{CN})_6 \cdot 3\text{H}_2\text{O}$, 1 M KCl and 10 mM NaCN electrolyte. Cyclic voltammetry scans were acquired at a scan rate of 250 mV/s and at an electrolyte flow rate of 25 $\mu\text{L}/\text{min}$.

OER and ORR are performed in basic electrolytes, such as KOH solutions, to make the reactions more favorable thermodynamically⁵⁵. Since the Pt electrode is a pseudo-reference, it is necessary to verify the stability of the internal reference in basic media. The previous mixture was then modified to insure this requirement: 100 mL of 2 mM $\text{K}_3\text{Fe}(\text{CN})_6$ and 2 mM $\text{K}_4\text{Fe}(\text{CN})_6$ in a 0.1 KOH/10 mM NaCN electrolyte solution. This solution was stored in a polymer bottle to avoid silicate contamination from a glass bottle. Using the basic electrolyte generates an anodic shift in the redox couple vs. Pt, without changing its reversibility, as can be seen in figure 1.19. As in the neutral supporting electrolyte, the potential remains stable upon cycling. Preparation of the reference electrolyte can be found in annexes.

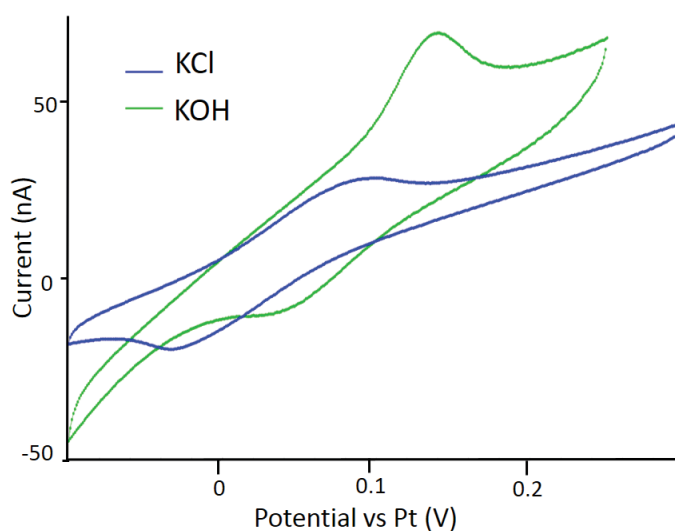


Figure 19. Cyclic voltammograms of a glassy carbon electrode within a 2 mM $\text{K}_3\text{Fe}(\text{CN})_6$ and 2 mM $\text{K}_4\text{Fe}(\text{CN})_6 \cdot 3\text{H}_2\text{O}$ electrolyte with 10mM NaCN, 1 M KCl (green) and 0.1 M KOH (blue) at a scan rate of 250 mV s^{-1} . Electrolyte flow rate of $25 \mu\text{L min}^{-1}$.

Typical electrocatalytic measurements in three-electrodes rotating disc cells are performed at $10\text{-}20 \text{ mV s}^{-1}$. However, with the miniaturized cell, at such slow scan rates, the curves have a sigmoidal shape with peaks that vary significantly in each cycle (annex 2). This behavior is characteristic of microelectrodes with conditions such that the smallest dimension of the electrode and the diffusion distance are comparable on the time scale of the experiment. Under these conditions, the anodic and cathode wave potentials are no longer measurable and instead the limiting current values are often extracted from these plots for analysis⁵³. Hence, we have assessed the impact on the scan rate on the electrochemical response, as shown in figure 1.20. At 250 mV s^{-1} the cathodic and anodic waves are clearly measurable. These waves start to separate and the redox behavior becomes irreversible when increasing the scan rate. In this regard, it is worth mentioning that at slower scan rates it was not possible to observe the waves and the repeatability was not satisfying. Finally, the *operando* and *ex situ* measurements were performed both at 100 mV s^{-1} as will be shown in chapter 2. In chapter 2, the use of this internal reference will be shown when studying Co_3O_4 during the oxygen evolution reaction.

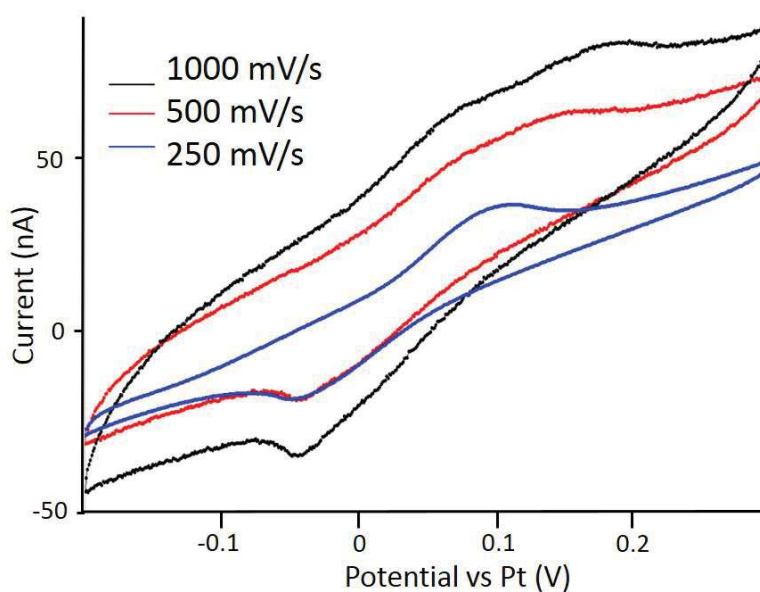


Figure 1.20. Cyclic voltammograms of a glassy carbon electrode within a 2 mM $K_3Fe(CN)_6$ and 2 mM $K_4Fe(CN)_6 \cdot 3H_2O$, 10mM NaCN electrolyte with 0.11 M KOH .Cyclic voltammetry scans were acquired at different scan rates between 250 and 1000 $mV s^{-1}$. Electrolyte flow rate of 25 $\mu L min^{-1}$.

However, the internal reference has some drawbacks. Indeed, iron ions can alter the catalytic activity, particularly, of cobalt oxide-based electrocatalytic materials.⁵⁶ To solve this problem, we have tested an organic redox couples as potential reference. In figure 1.21, the hydroquinone redox couple was tested as a metal-free internal reference. By using a solution of 0.5 mmol in 0.1 M KOH we measured a shift of the potential first with respect to the reversible hydrogen electrode (RHE) and then to the ferric/ferrous internal reference. Thus, organic water-soluble compounds could also be useful as internal references. Nevertheless, this strategy would have required further testing of decomposition events or transformation under the beam, as the polymer could passivate the surface of the working electrode.

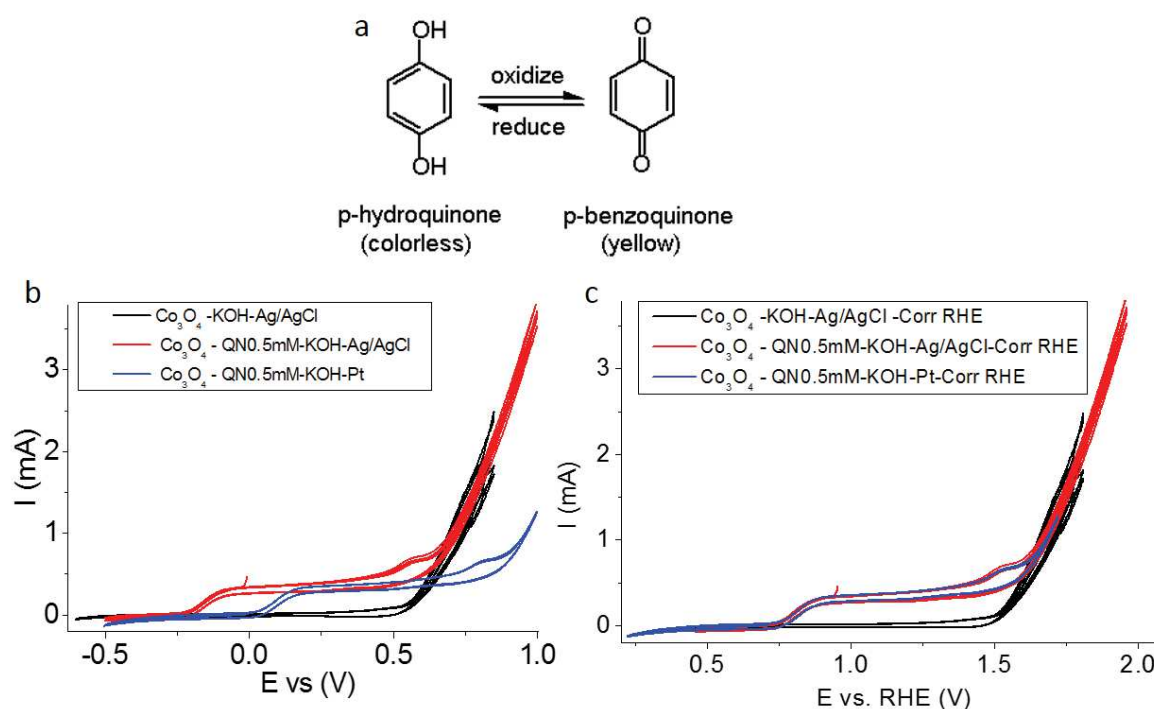


Figure 1.21. a) Hydroquinone redox reaction. b) A solution of 0.5 mM was used as metal-free internal reference in a 0.1 M KOH solution. The Co_3O_4 ‘only catalyst ink’ was used to test OER. Electrochemical measurements were performed in a three electrodes cell with a rotating glassy carbon disc as a working electrode at 1600 rpm. Reference electrodes were a $\text{Ag}/\text{AgCl}_{\text{sat}}$ and a Pt wire. c) curves from b) corrected vs RHE.

1.5.3. Beam effect and grounding

The choice of the imaging mode has an impact not only on beam damage effects, as detailed in section 1.4, but also on the electrochemical measurements, particularly in the case of TEM. Indeed, figure 22a shows that when the beam is on in TEM mode, artifacts on the CV curves appear, as current peaks and other unusual features. On the other hand, the focused beam in the STEM mode does not significantly impact the electrochemical measurements (figure 1.22b). This smaller impact of the beam in STEM mode is ascribed, as beam damage effects, to the shorter time that the beam probe spends on a given area, compared to the TEM mode. For instance, for a pixel dwell time of 40 μs producing an image of 512x512 pixels, the probe would take around 10 s to return to the same area, opposite to the continuous illumination in TEM.

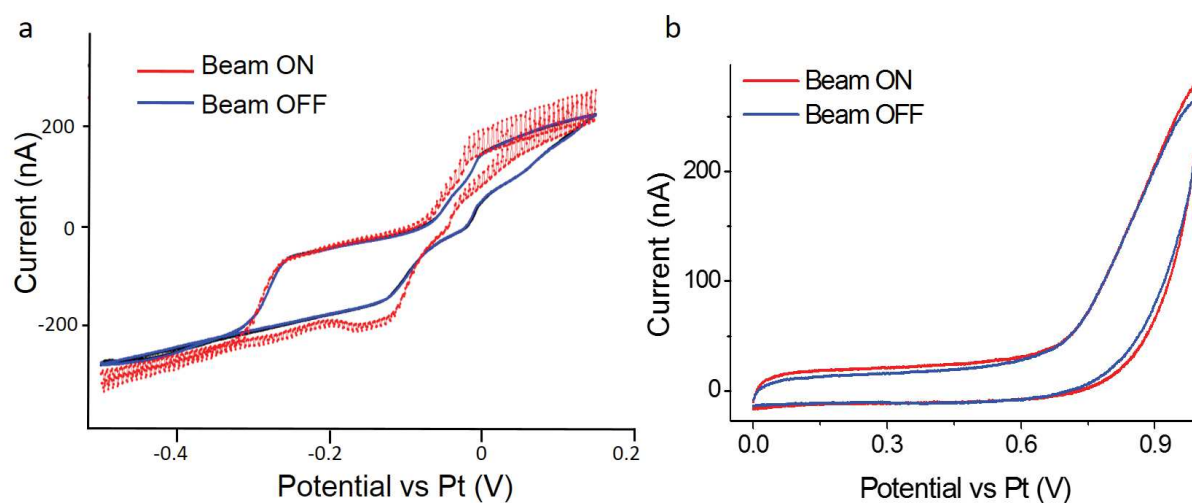


Figure 1.22. a) *Operando* cyclic voltammograms at 100 mV s^{-1} of Co_3O_4 in TEM mode while having the beam off (blue) and on (red). The impact of the beam on the voltammetric measurements is significant, leading to large current instability and shift of the potential scale. b) *Operando* cyclic voltammograms at 100 mV s^{-1} of Co_3O_4 in STEM mode while having the beam off (blue) and on (red). No significant difference in the curves was observed in the presence of the STEM beam.

Another aspect that can impact the stability of the electrochemical signal is the ground connection. Throughout the different experiments, we experienced strong difficulties in obtaining reproducibility CV curves. These troubles occurred because of the different

grounding of the electron microscope, the ample holder and the potentiostat. It appeared necessary for reproducibility purpose to remove any ground connection from the holder and the potentiostat, while the holder was inside of the microscope, thus keeping only the ground of the microscope. This problem, although trivial, was not known by the company Protochips before we experienced it. Such effects were however already shown by Fahrenkrug *et al.*⁵⁷ (figure 1.23). In contrast, when the measurements were performed out of the microscope but within the *in situ* holder, the external ground connection of the potentiostat and of the holder was necessary.

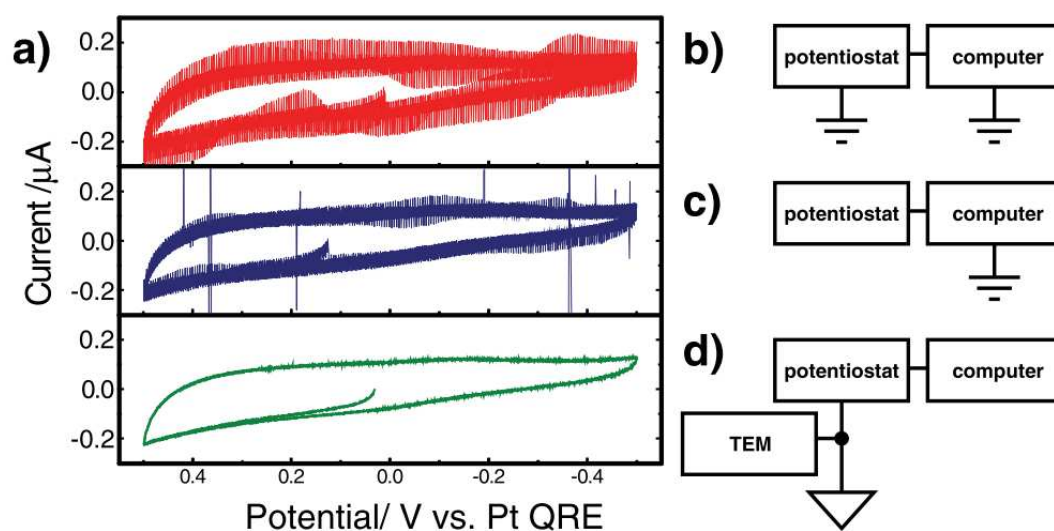


Figure 1.23. a) Current-voltage characteristics with respect to a platinum quasi-reference electrode (QRE) of the assembled electrochemical-TEM cell measured *ex situ* with different grounding configurations. (Top) The potentiostat and controlling computer were kept at earth ground as shown in (b). (Middle) The potentiostat was not grounded but the controlling computer was connected to earth ground as shown in (c). (Bottom) The controlling computer was not grounded and the potentiostat was grounded to the TEM chassis as shown in (d). Electrolyte: 1 mM $\text{Ru}(\text{NH}_3)_6\text{Cl}_3$ and 1 M KCl in water. Chip spacer: 250 nm. Taken from ref ⁵⁷

1.6. Additional considerations for data acquisition

1.6.1. Post-mortem analysis

As mentioned at the beginning of this chapter, the electron-matter interaction produces multiple signals. Among those, the X-rays and electrons coming from the sample are characteristic of the elements present in the material and can be used to identify its composition and electronic structure through spectroscopic and diffraction techniques.⁵⁸ In order to enhance the comprehension of the phenomena observed *in situ*, such

spectroscopic and diffraction techniques were used to analyze the samples once the liquid medium was removed. The methods used in this work are listed and described below:

- Energy dispersive X-ray spectroscopy (EDS) is a standard method for identifying and quantifying elemental compositions in the sample. The atoms on the surface are excited by the electron beam, emitting specific wavelengths of X-rays that are characteristic of the atomic structure of the elements. A solid-state device that discriminates among X-ray energies can analyze these X-ray emissions. Appropriate elements are assigned, yielding the composition of the atoms on the specimen surface.⁵⁹ This was used to determine the initial and final composition of the electrocatalyst as well as the crystallization products of the colloidal and biomimetic synthesis.
- Electron energy loss spectroscopy (EELS) uses the characteristic energy loss spectrum of electrons that have been transmitted through the sample. Since the amount of electron energy loss is related directly to the ionization energy, which has a well-known characteristic behavior for any given element, information can be obtained about elemental composition, chemical bonding and electronic structure.⁶⁰
- Selected area electron diffraction (SAED) patterns are a projection of the reciprocal lattice, with lattice reflections showing as sharp diffraction spots. By tilting a crystalline sample to low-index zone axes, SAED patterns can be used to identify crystal structures and measure lattice parameters. SAED of multiple nanocrystals gives ring patterns analogous to those from X-ray powder diffraction, and can be used to identify texture and discriminate nanocrystalline from amorphous phases.⁶¹

In this work, these measurements were performed once the liquid was removed from the *in situ* holder as well as in the samples recovered from conventional *ex situ* measurements. High-resolution imaging (especially in oxides and low contrasting elements-based materials), electron energy loss spectroscopy (EELS), energy dispersive spectroscopy (EDS) mapping or selected area electron diffraction (SAED) are particularly challenging in liquid media. For instance, EELS is routinely used to determine the thickness of the liquid throughout the observation window⁴² but not to determine the electronic structure of the materials within the liquid because the energy resolution of EELS acquisition is strongly deteriorated by diffusion in the liquid. Few examples of *in situ* liquid EDS measurements can be found in the literature.^{20,62} Due to the multiple inelastic scattering induced by the liquid, the resolution is highly degraded. With SiN windows the resolution has been found to be 10 nm.⁶² Improved resolution has been achieved

with a graphene membrane.²⁰ Similarly, diffraction patterns recorded *in situ* require precession of the electron beam⁶³ or the implementation of very fast cameras permitting a reduced exposure time⁶⁴.

Typically, when an observation is over, the cell is carefully disassembled and both chips are cleaned by submerging them in ethanol. Then they are dried using compressed air. Given the dimensions of the miniaturized electrochemical cell, the *post mortem* studies in the chip surfaces required a modified support depicted in figure 1.23. The support was designed to insure that the top chip could fit, and the observation window was free to be analyzed by all the spectroscopic and diffraction techniques available within the microscope.

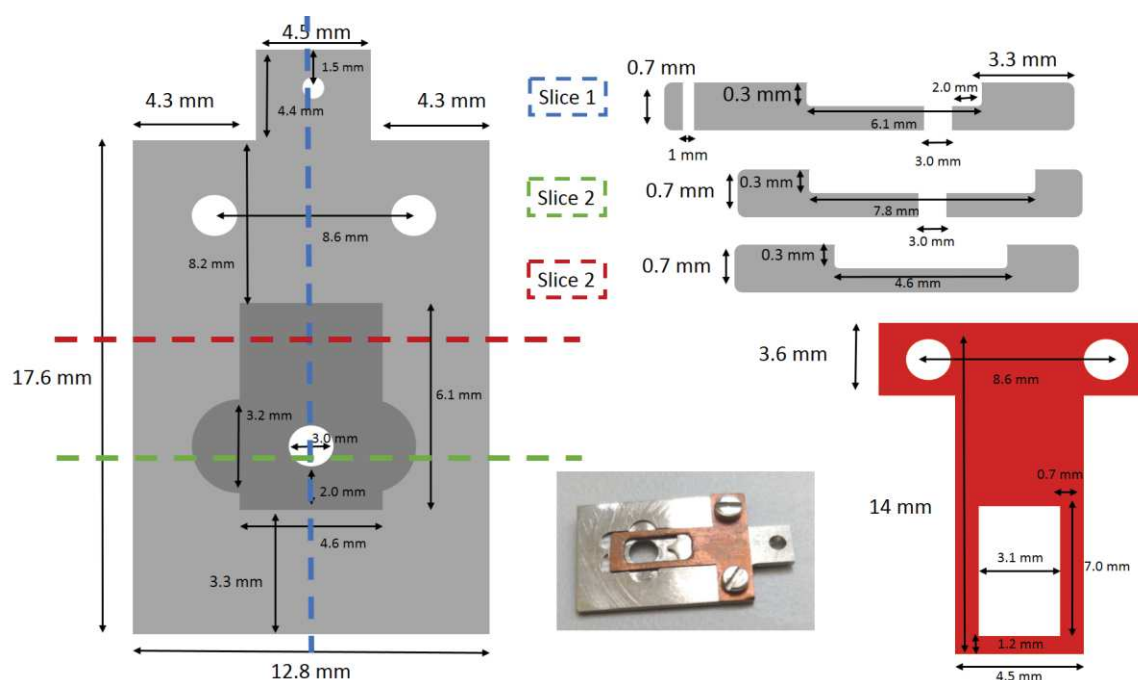


Figure 1.23. Modified support designed to perform *post mortem* analysis on the top chip.

Finally, for clarity, throughout this document, “*in situ*” TEM analyses refer to the samples observed in the e-chips in contact with the liquid. “*operando*” refers to the measurements made during electrochemical measurements. “*Post in situ*” TEM analyses refer to the samples observed in the chips after the end of the experiment and the removal of the liquid media, “*Ex situ post mortem*” TEM analyses refer to the samples observed on a common carbon-coated carbon grid after retrieval of the material from a classical utilization or preparation set-up.

1.7. Perspectives and future improvements

The use of direct electron detectors can help to improve the limited resolution offered in liquid-cell TEM. Direct electron detectors capable of directly detecting high energy electrons with a high signal to noise ratio, ensuring single electron sensitivity.⁶⁵ This type of detectors collect and essentially amplify electrons from specimens with much weaker signal to noise ratios⁶⁶. Further improvement could be achieved by the utilization of sophisticated imaging processing algorithms for signal enhancement.⁶⁷

1.8. Concluding remarks

The goal of this chapter will help the reader to navigate without trouble through this document. Most of the considerations examined when performing *in situ* and/or *operando* observations have been summarized here. Thus, when considering performing *in situ* and *operando* measurements remember:

- Sample preparation: Translate the typical sample preparation to a suitable procedure for *in situ* liquid experiments. Question yourself about possible interferences that might arise from that preparation.
- Sample deposition: Determine if the sample should be deposited on the top or bottom window or if it should be send through the microfluidic system. In the case of the *in situ* nucleation and growth of nanoparticles wonder about the speed of the reaction.
- Imaging mode, resolution and electron dose: Remember to align the microscope before introducing the *in situ* holder with your sample. Depending on the samples position within the observation chamber, one of TEM or STEM modes can be more convenient. Far from the beam entrance, TEM tend to yield better results. Close to the beam entrance, STEM can yield better results. Stablish the electron dose that gives you the best compromise between spatial and temporal resolution, SNR, radiolysis species production, charge accumulation and particles detachment.
- Electrochemical measurements: When studying electrochemical reactions consider the effect of the beam in addition to the electrochemical stimuli. Make sure that the electrochemical behavior that you observe *operando* is representative of the behavior *ex situ*. If there is not a reference electrode, you can introduce an internal reference. Verify the behavior of your internal reference in

the conditions that you wish to use, both *in situ* and *ex situ*. Determine the influence of your internal reference in the phenomena you want to observe.

- Post mortem observations: Remember that you can employ complementary studies as EELS, EDS or SAED to enhance your comprehension of the processes observed *in situ*. If you decide to observe *post in situ* samples take special care when disassembling the chips to avoid breaking the window and losing your sample.

1.9. References

- (1) Freundlich, M. M. Origin of the Electron Microscope. *Science (80-.)*. **1963**, *142*, 185–188.
- (2) Inkson, B. J. *Scanning Electron Microscopy (SEM) and Transmission Electron Microscopy (TEM) for Materials Characterization*; Elsevier Ltd, 2016.
- (3) Williams, D.; Carter, B. *Transmission Electron Microscopy*, 2nd ed.; Springer: New York, 2009.
- (4) Schneider, N. M.; Norton, M. M.; Mendel, B. J.; Grogan, J. M.; Frances, M.; Bau, H. H. Electron - Water Interactions and Implications for Liquid Cell Electron Microscopy – Supporting Information. *J. Phys. Chem. C* **2014**, *118*, 22373–22382.
- (5) Lassalle-Kaiser, B.; Gul, S.; Kern, J.; Yachandra, V. K.; Yano, J. In Situ/Operando Studies of Electrocatalysts Using Hard X-Ray Spectroscopy. *J. Electron Spectros. Relat. Phenomena* **2017**, *221*, 18–27.
- (6) Ruska, E. Beitrag Zur Übermikroskopischen Abbildung Bei Höheren Drucken. *Kolloid-Zeitschrift* **1942**, *100*, 212–219.
- (7) von Ardenne, M. Über Ein 200 KV-Universal-Elektronenmikroskop Mit Objektabschattungsvorrichtung. *Zeitschrift für Phys.* **1941**, *117*, 657–688.
- (8) Parsons, D. F. Structure of Wet Specimens in Electron Microscopy. *Science (80-.)*. **1974**, *186*, 407–414.
- (9) Ruska, E. The Development of the Electron Microscope and of Electron Microscopy (Nobel Lecture). *Angew. Chemie Int. Ed. English* **1987**, *26*, 595–605.
- (10) Ruska, H. Die Sichtbarmachung Der Bakteriophagen Lyse Im Übermikroskop. *Naturwissenschaften* **1940**, *28*, 45–46.

- (11) Krause, F. Das Magnetische Elektronenmikroskop Und Seine Anwendung in Der Biologie. *Naturwissenschaften* **1937**, *25*, 817–825.
- (12) Adrian, M.; Dubochet, J.; Lepault, J.; McDowell, A. W. Cryo-Electron Microscopy of Viruses. *Nature* **1984**, *308*, 32–36.
- (13) Kesselman, E.; Talmon, Y.; Bang, J.; Abbas, S.; Li, Z.; Lodge, T. P. Cryogenic Transmission Electron Microscopy Imaging of Vesicles Formed by a Polystyrene-Polyisoprene Diblock Copolymer. *Macromolecules* **2005**, *38*, 6779–6781.
- (14) Cressey, D.; Callaway, E. Cryo-Electron Microscopy Wins Chemistry Nobel. *Nature* **2017**, *550*, 167–167.
- (15) Dubochet, J.; Knapek, E. Ups and Downs in Early Electron Cryo-Microscopy. *PLoS Biol.* **2018**, *16*, 4–7.
- (16) D.F.Parsons. Structure of Wet Specimens in Electron Microscopy. *Science* (80-.). **1974**, *186*, 407–414.
- (17) Stokes, D. J. General Principles of VP-ESEM: Utilising a Gas. In *Principles and Practice of Variable Pressure/Environmental Scanning Electron Microscopy (VP-ESEM)*; John Wiley & Sons, Ltd: Chichester, UK, 2008; pp 63–92.
- (18) Abrams, I. M.; McBain, J. W. A Closed Cell for Electron Microscopy. *J. Appl. Phys.* **1944**, *15*, 607–609.
- (19) Ring, E. A.; Peckys, D. B.; Dukes, M. J.; Baudoin, J. P.; de Jonge, N. Silicon Nitride Windows for Electron Microscopy of Whole Cells. *J. Microsc.* **2011**, *243*, 273–283.
- (20) Kelly, D. J.; Zhou, M.; Clark, N.; Hamer, M. J.; Lewis, E. A.; Rakowski, A. M.; Haigh, S. J.; Gorbachev, R. V. Nanometer Resolution Elemental Mapping in Graphene-Based TEM Liquid Cells. *Nano Lett.* **2018**, *18*, 1168–1174.
- (21) Williamson, M. J.; Tromp, R. M.; Vereecken, P. M.; Hull, R.; Ross, F. M. Dynamic Microscopy of Nanoscale Cluster Growth at the Solid–Liquid Interface. *Nat. Mater.* **2003**, *2*, 532–536.
- (22) de Jonge, N.; Ross, F. M. Past, Present, and Future Electron Microscopy of Liquid Specimens. In *Liquid Cell Electron Microscopy*; Ross, F. M., Ed.; Advances in Microscopy and Microanalysis; Cambridge University Press: Cambridge, 2016; Vol. 350, pp 3–34.

- (23) Thanh, N. T. K.; Maclean, N.; Mahiddine, S. Mechanisms of Nucleation and Growth of Nanoparticles in Solution. *Chem. Rev.* **2014**, *114*, 7610–7630.
- (24) Nguyen, K. X.; Holtz, M. E.; Richmond-Decker, J.; Muller, D. A. Spatial Resolution in Scanning Electron Microscopy and Scanning Transmission Electron Microscopy Without a Specimen Vacuum Chamber. *Microsc. Microanal.* **2016**, *22*, 754–767.
- (25) Woehl, T. J.; Evans, J. E.; Arslan, I.; Ristenpart, W. D.; Browning, N. D. Direct in Situ Determination of the Mechanisms Controlling Nanoparticle Nucleation and Growth. *ACS Nano* **2012**, *6*, 8599–8610.
- (26) Woehl, T. J.; Abellan, P. Defining the Radiation Chemistry during Liquid Cell Electron Microscopy to Enable Visualization of Nanomaterial Growth and Degradation Dynamics. *J. Microsc.* **2017**, *265*, 135–147.
- (27) Liu, Y.; Tai, K.; Dillon, S. J. Growth Kinetics and Morphological Evolution of ZnO Precipitated from Solution. *Chem. Mater.* **2013**, *25*, 2927–2933.
- (28) Kimura, Y.; Niinomi, H.; Tsukamoto, K.; García-Ruiz, J. M. In Situ Live Observation of Nucleation and Dissolution of Sodium Chlorate Nanoparticles by Transmission Electron Microscopy. *J. Am. Chem. Soc.* **2014**, *136*, 1762–1765.
- (29) Yuan, Y.; Amine, K.; Lu, J.; Shahbazian-Yassar, R. Understanding Materials Challenges for Rechargeable Ion Batteries with in Situ Transmission Electron Microscopy. *Nat. Commun.* **2017**, *8*, 15806.
- (30) Smeets, P. J. M.; Cho, K. R.; Kempen, R. G. E.; Sommerdijk, N. A. J. M.; De Yoreo, J. J. Calcium Carbonate Nucleation Driven by Ion Binding in a Biomimetic Matrix Revealed by in Situ Electron Microscopy. *Nat. Mater.* **2015**, *14*, 394–399.
- (31) Woehl, T. J.; Kashyap, S.; Firlar, E.; Perez-Gonzalez, T.; Faivre, D.; Trubitsyn, D.; Bazylnski, D. A.; Prozorov, T. Correlative Electron and Fluorescence Microscopy of Magnetotactic Bacteria in Liquid: Toward In Vivo Imaging. *Sci. Rep.* **2015**, *4*, 6854.
- (32) Firlar, E.; Ouy, M.; Bogdanowicz, A.; Covnot, L.; Song, B.; Nadkarni, Y.; Shahbazian-Yassar, R.; Shokuhfar, T. Investigation of the Magnetosome Biomineralization in Magnetotactic Bacteria Using Graphene Liquid Cell-Transmission Electron Microscopy. *Nanoscale* **2019**, *11*, 698–705.
- (33) de Jonge, N.; Pfaff, M.; Peckys, D. B. Practical Aspects of Transmission Electron

- Microscopy in Liquid. In *Advances in Imaging and Electron Physics*; Elsevier, 2014; Vol. 186, pp 1–37.
- (34) Zhu, G.; Prabhudev, S.; Yang, J.; Gabardo, C. M.; Botton, G. A.; Soleymani, L. In Situ Liquid Cell TEM Study of Morphological Evolution and Degradation of Pt – Fe Nanocatalysts During Potential Cycling. *J. Phys. Chem. C* **2014**, *118*, 22111–22119.
- (35) Poseidon liquid holder <https://www.protochips.com/products/poseidon-select/> (accessed Nov 21, 2018).
- (36) Jakubowski, U.; Baumeister, W.; Glaeser, R. M. Evaporated Carbon Stabilizes Thin, Frozen-Hydrated Specimens. *Ultramicroscopy* **1989**, *31*, 351–356.
- (37) Pennycook, S. J.; Nellist, P. D.; Midgley, P. A.; Weyland, M. *Scanning Transmission Electron Microscopy*; 2011.
- (38) de Jonge, N. Theory of the Spatial Resolution of (Scanning) Transmission Electron Microscopy in Liquid Water or Ice Layers. *Ultramicroscopy* **2018**, *187*, 113–125.
- (39) De Jonge, N.; Ross, F. M. Electron Microscopy of Specimens in Liquid. *Nature Nanotechnology*. 2011, pp 695–704.
- (40) Grogan, J. M.; Schneider, N. M.; Ross, F. M.; Bau, H. H. Bubble and Pattern Formation in Liquid Induced by an Electron Beam. *Nano Lett.* **2014**, *14*, 359–364.
- (41) de Jonge, N.; Houben, L.; Dunin-Borkowski, R. E.; Ross, F. M. Resolution and Aberration Correction in Liquid Cell Transmission Electron Microscopy. *Nat. Rev. Mater.* **2019**, *4*, 61–78.
- (42) Keskin, S.; Kunnas, P.; Jonge, N. De. Liquid-Phase Electron Microscopy with Controllable Liquid Thickness. **2019**.
- (43) de Jonge, N.; Browning, N. D.; Evans, J. E.; Chee, S. W.; Ross, F. M. Resolution in Liquid Cell Experiments. In *Liquid Cell Electron Microscopy*; Cambridge University Press: Cambridge, 2016; pp 164–188.
- (44) Protochips. *Poseidon™ Introduction Application Note. EELS and EDS*; 2017.
- (45) Grogan, J. M.; Schneider, N. M. N. M.; Ross, F. M.; Bau, H. H. Bubble and Pattern Formation in Liquid Induced by an Electron Beam. *Nano Lett.* **2014**, *14*, 359–364.
- (46) Verch, A.; Pfaff, M.; De Jonge, N. Exceptionally Slow Movement of Gold

- Nanoparticles at a Solid/Liquid Interface Investigated by Scanning Transmission Electron Microscopy. *Langmuir* **2015**, *31*.
- (47) Hauwiller, M. R.; Ondry, J. C.; Chan, C. M.; Khandekar, P.; Yu, J.; Alivisatos, A. P. Gold Nanocrystal Etching as a Means of Probing the Dynamic Chemical Environment in Graphene Liquid Cell Electron Microscopy. *J. Am. Chem. Soc.* **2019**, jacs.9b00082.
- (48) Abellan, P.; Woehl, T. J.; Parent, L. R.; Browning, N. D.; Evans, J. E.; Arslan, I. Factors Influencing Quantitative Liquid (Scanning) Transmission Electron Microscopy. *Chem. Commun.* **2014**, *50*, 4873–4880.
- (49) Schneider, N. M.; Norton, M. M.; Mendel, B. J.; Grogan, J. M.; Ross, F. M.; Bau, H. H. Electron-Water Interactions and Implications for Liquid Cell Electron Microscopy. *J. Phys. Chem. C* **2014**, *118*, 22373–22382.
- (50) Jiang, N. Note on in Situ (Scanning) Transmission Electron Microscopy Study of Liquid Samples. *Ultramicroscopy* **2017**, *179*, 81–83.
- (51) Suen, N.-T.; Hung, S.-F.; Quan, Q.; Zhang, N.; Xu, Y.-J.; Chen, H. M. Electrocatalysis for the Oxygen Evolution Reaction: Recent Development and Future Perspectives. *Chem. Soc. Rev.* **2017**, *46*, 337–365.
- (52) Inzelt, G. Pseudo-Reference Electrodes. In *Handbook of Reference Electrodes*; Springer Berlin Heidelberg: Berlin, Heidelberg, 2013; pp 331–332.
- (53) Unocic, R. R.; Sacci, R. L.; Brown, G. M.; Veith, G. M.; Dudney, N. J.; More, K. L.; Li, F. S. W.; Gardiner, D. S.; Damiano, J.; Nackashi, D. P. Quantitative Electrochemical Measurements Using In Situ Ec-S / TEM Devices. *Microsc. Microanal.* **2014**, *20*, 452–461.
- (54) Bard, A. J.; Faulkner, L. R.; Bagotsky, V. S. *Electrochemical Methods Fundamentals of Electrochemistry*, 2nd ed.; John Wiley and sons, inc: New York, 2001.
- (55) McCrory, C. C. L.; Jung, S.; Peters, J. C.; Jaramillo, T. F. Benchmarking Heterogeneous Electrocatalysts for the Oxygen Evolution Reaction. *J. Am. Chem. Soc.* **2013**, *135*, 16977–16987.
- (56) Gong, L.; Chng, X. Y. E.; Du, Y.; Xi, S.; Yeo, B. S. Enhanced Catalysis of the Electrochemical Oxygen Evolution Reaction by Iron(III) Ions Adsorbed on

- Amorphous Cobalt Oxide. *ACS Catal.* **2017**, No. Iii, 807–814.
- (57) Fahrenkrug, E.; Alsem, D. H.; Salmon, N.; Maldonado, S. Electrochemical Measurements in In Situ TEM Experiments. *J. Electrochem. Soc.* **2017**, *164*, H358–H364.
- (58) Su, D. Advanced Electron Microscopy Characterization of Nanomaterials for Catalysis. *Green Energy Environ.* **2017**, *2*, 70–83.
- (59) Ebnesajjad, S. *Surface Treatment of Materials for Adhesive Bonding*, 2nd ed.; William Andrew Publishing: Oxford, 2014.
- (60) Smith, D. J.; McCartney, M. R. MICROSCOPY APPLICATIONS | Semiconductors. In *Reference Module in Chemistry, Molecular Sciences and Chemical Engineering*; Worsfold, P., Poole, C., Townshend, A., Miró, M. B. T.-E. of A. S. (Third E., Eds.; Elsevier: Oxford, 2013; pp 89–97.
- (61) Nayfeh, M. Characterization and Simulation Technologies of Nanomaterial. In *Fundamentals and Applications of Nano Silicon in Plasmonics and Fullerenes*; Nayfeh, M. B. T.-F. and A. of N. S. in P. and F., Ed.; Elsevier, 2008; pp 153–167.
- (62) Lewis, E. A.; Haigh, S. J.; Slater, T. J. A.; He, Z.; Kulzick, M. A.; Burke, M. G.; Zaluzec, N. J. Real-Time Imaging and Local Elemental Analysis of Nanostructures in Liquids. *Chem. Commun.* **2014**, *50*, 10019–10022.
- (63) Taylor, C. A.; Nenoff, T. M.; Pratt, S. H.; Hattar, K. Synthesis of Complex Rare Earth Nanostructures Using in Situ Liquid Cell Transmission Electron Microscopy. *Nanoscale Adv.* **2019**, 2229–2239.
- (64) Karakulina, O. M.; Demortière, A.; Dachraoui, W.; Abakumov, A. M.; Hadermann, J. In Situ Electron Diffraction Tomography Using a Liquid-Electrochemical Transmission Electron Microscopy Cell for Crystal Structure Determination of Cathode Materials for Li-Ion Batteries. *Nano Lett.* **2018**, *18*, 6286–6291.
- (65) Jin, L. Direct Electron Detection in Transmission Electron Microscopy, UC San Diego, 2009.
- (66) Taheri, M. L.; Stach, E. A.; Arslan, I.; Crozier, P. A.; Kabius, B. C.; LaGrange, T.; Minor, A. M.; Takeda, S.; Tanase, M.; Wagner, J. B.; et al. Current Status and Future Directions for in Situ Transmission Electron Microscopy. *Ultramicroscopy* **2016**, *170*, 86–95.

- (67) Schneider, N. M.; Park, J. H.; Norton, M. M.; Ross, F. M.; Bau, H. H. Automated Analysis of Evolving Interfaces during in Situ Electron Microscopy. *Adv. Struct. Chem. Imaging* **2017**, *2*.

Chapter II

Chapter II. Spying on electrocatalysts

2.1. *In situ* and *operando* measurements for electrocatalysts.

2.2. Cobalt oxide electrocatalysis: a “not so model” system.

2.2.1. Morphological evolution monitored by *operando* STEM during cyclic voltammetry.

2.2.2. Morphological evolution monitored by *operando* STEM during chronopotentiometry.

2.2.3. Structural evolution: post-mortem study

2.3. Concluding remarks

2.4. References

2.1. *In situ* and *operando* measurements for electrocatalysts

Fossil fuel energy production is no longer sustainable.¹ Exploitation of these nonrenewable resources is problematic not only because the quantity is limited but also because the byproducts resulting from their use are detrimental for the environment, fact evidenced in the greenhouse effect among others. As reported by the Economic World Forum in their 2019 report, the failure to adapt or mitigate the climate change is the very second item in the risks list for the near future.²

Thus, the need of efficient, clean and sustainable energy production methods has been clear for the past few decades³. Although the panorama looks brighter with solar, tidal, hydro or wind based energies, their intermittent character limits the applicability in a more extended manner. Thereby, developing efficient ways to store energy for periods of no-production is crucial to improve the current energetic scenario.

In this regard, conversion of energy into chemical bonds is a very attractive option. For instance, water splitting devices electrolyze water to form O₂ and H₂. These gases can be later recombined in fuel cells, recovering simultaneously water and the majority of the

energy invested to break the initial bond. In figure 2.1, we find a schematic representation of an electrolyzer and a fuel cell. In the former, two half reactions are involved in the breakage of water: (1) the oxygen evolution reaction (OER) at the anode (same as in metal-air batteries during charging) and (2) the hydrogen evolution reaction (HER) at the cathode. Inversely, in a fuel cell, the oxygen reduction reaction (ORR) and the hydrogen oxidation reaction (HOR) occur.

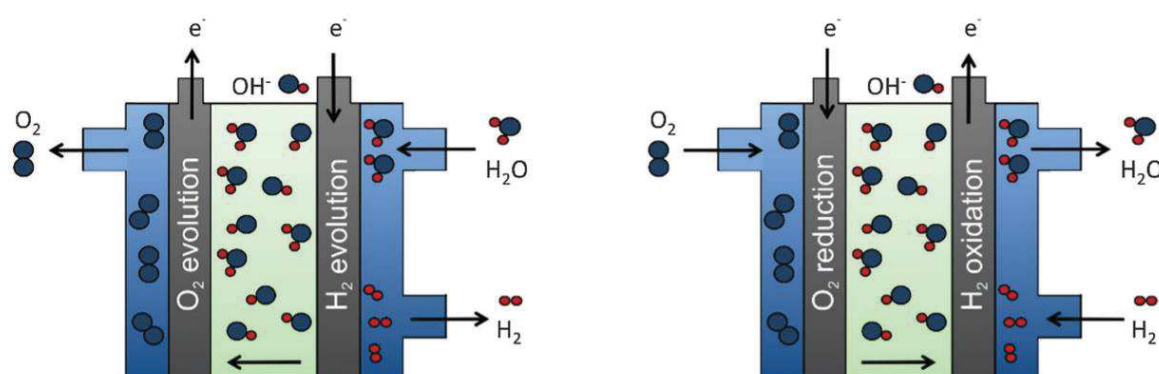


Figure 2.1. Schematic representation of the processes within a) water splitting device and b) fuel cell. Adapted from ref ⁴

Whether energy is stored or produced, the half reactions involved in the overall process take place at the electrodes of an electrochemical cell. The major energy losses are due to the sluggish kinetics of the four electrons electrochemical reactions involving oxygen species (OER and ORR). Hence, these reactions must be fastened by judicious choice of electrocatalysts in order to decrease overpotentials. The current operating devices use Pt as HER catalyst, while the OER catalysts are based on Ir, Ni or Co oxides and ORR ones on Pt or Pd. In their large majority, these metals are scarce, expensive and irregularly distributed on the earth crust. Therefore, in the last decade, research focusing on electrode materials based on earth-abundant elements have increased significantly⁵. Transition metal oxides based on earth-abundant elements are attracting major attention in the field, since some of them present remarkable activity towards the OER and ORR⁵⁻⁷ at lower costs than precious metals. They also offer a wide spectrum of compositions allowing fine tuning of their catalytic properties.⁸ Despite the great

fundamental and technological interest of metal oxide electrocatalysts, their evolution in electrocatalytic conditions remains elusive.

In heterogenous electrocatalysis, catalytic properties are related to the surface chemistry of the electrode material. Thereby, structural, compositional and morphological characteristics determine the performance of the material. Understanding structural, compositional and morphological changes would pave the way to improvement of activity, selectivity and stability.⁹ A wide variety of characterization techniques are employed to evaluate the materials as soon as they are prepared, and sometimes *post mortem* after several cycles of use in a device. However, chemical and physical properties evolve during electrocatalysis, so that electrocatalytically active species may be only present in the conditions of catalysis, during operation of the device. Identification of electrocatalytically active species requires focus on the interface between the catalytic material and the electrolyte containing the reactants. Indeed, during catalysis, bonds are formed and broken at the surface of the electrocatalyst.¹⁰ This corresponds to a sub-nanometer-thick layer at the surface of the catalyst.^{11,12} These interfaces are complex and dynamic, extremely difficult to reconstruct from *post mortem* analysis, where the electrolyte is not present anymore. Hence, the transformations occurring at these interfaces must be probed *in situ* and *operando*.

As opposed to conventional characterization, *operando* analysis requires adapting the techniques to the detection of phenomena in a suitable timeframe. Although applied to rechargeable batteries, figure 2.2 resumes the time and length scales that are also relevant in electrocatalytic processes. Such techniques have been adapted in the last decades to perform *in situ* and *operando* studies during HER, OER and/or ORR, relying mostly,¹³ but not exhaustively, on X-ray absorption (XAS),¹⁴ X-ray emission,¹⁵ X-ray photoelectron,^{16,17} Mossbauer¹⁸ and Raman¹⁹ spectroscopies.

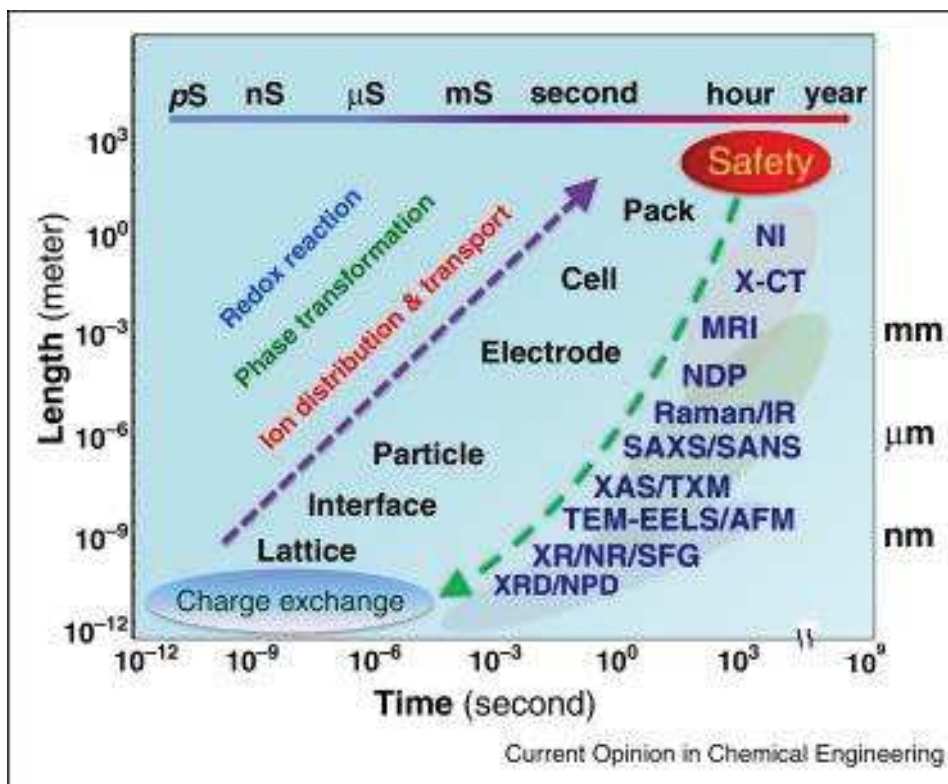


Figure 2.2. Time and length scales relevant to address rechargeable batteries issues. Taken from ref ²⁰

These techniques are useful to detect structural and electronic changes during electrocatalysis (see details in Table 1). They are probing different space- and time-scales, so that combining several *in situ* and *operando* measurements with complementary temporal and spatial resolutions is a fruitful strategy. For instance, eventual leaching of cations from the electrocatalysts to the electrolyte may be readily accessible by transmission electron microscopy (shape changes, chemical mapping by STEM-EDX in vacuum or liquid media) at the nanoscale, and by synchrotron-based radiation spectroscopies on the local atomic environment of overall samples (X-ray absorption spectroscopy and X-ray Raman spectroscopy).

Table 1. Some *in situ* and *operando* techniques used to study electrocatalysts for electrolyzers or fuel cells.

<i>In Situ</i> and/or <i>Operando</i> Technique	What Can Be Measured	Timescale	Pros Cons	References
Vibrational spectroscopies				

Infrared and Raman spectroscopy	Specific bond formation or breaking	~ seconds	<ul style="list-style-type: none"> -Simple implementation -Penetrability (~mm) - Non-destructive 	21–25
X-ray based methods				
XAS (X-ray absorption spectroscopies) XANES (X-ray absorption near edge spectroscopy) EXAFS (extended x-ray absorption fine structure)	<ul style="list-style-type: none"> -Average oxidation state. -Nature neighboring atoms -Local symmetry - Spin state of the excited atom -Number and distance of neighbors around central atom - Crystallinity 	Several minutes-hours when applied to electrocatalysis in liquids	<ul style="list-style-type: none"> -Dimension of the cell close to conventional cell dimensions -Penetrability (~mm) 	26–32
XES (X-ray Emission Spectroscopy)	- Electronic structural information pertinent to bound ligands		<ul style="list-style-type: none"> -Probes multiple metal centers simultaneously -XES measurements can be performed in parallel with XRD measurements using the same photon energy for the incident X-ray pulses 	33
XRD (X-ray diffraction)	--Structural (surface or bulk crystallography, roughness) and chemical (layer composition) information	Seconds (synchrotron) to several minutes	<ul style="list-style-type: none"> -Low absorption of light elements (aqueous solvents/electrolytes), less. Less interferences 	34–36
Microscopies				
AFM (Atomic Force Microscopy)	Surface morphology with nanometric resolution and correlated potential	seconds-hours	Restricted to model systems supported on flat electrodes	37–40
TEM (Transmission electron microscopy)	Morphological changes at nm scale Phase transformations	~ seconds	<ul style="list-style-type: none"> -Good temporal-spatial resolution -Local, single particle observation -Complementary EELS, 	41–43

	(precession) Chemical distribution		EDS and SAED	
			-Very thin samples -Miniaturized e-cells -Electron beam influence	

In situ electrochemical transmission electron microscopy (EC-TEM) brings very attractive perspectives to the panorama of *in situ* and *operando* techniques for nanostructured electrocatalysts. This methodology is among the most recent ones that have been implemented as *in situ* techniques for studying electrochemical processes.¹³ It can provide morphological information with nanometric resolution and in shorter delays compared with the synchrotron-based spectroscopies when using a direct detection camera. Another advantage is the fact that EC-TEM uses dedicated sample holders enabling performing electrochemical studies in any conventional microscopes. Its relatively scarce use for studying electrocatalytic materials is related to the technical challenges described in chapter 1.

All in all, *in situ* EC-TEM is widely used to study the structural evolution of Li-ion batteries electrodes during cycling.^{44–46} In these devices, Li (de)insertion occurs in the whole volume of the particles making the related structural and morphological changes relatively easy to track. In contrast, electrocatalytic events do often occur on the surface of the materials, where a small geometrical area, possibly a few nanometer-thick layer is involved during the process, thus pushing further the requirements in terms of sensitivity and spatial resolution, among others. The sparse reported works on *in situ* EC-TEM for electrocatalysis have focused on electrocatalysts made out of relatively stable precious metals,^{42,47,48} especially for the oxygen reduction reaction (ORR), where particles etching has been evidenced. Materials with a more complex structure and free of precious metals are sought for^{6,8} but may show deeper transformations under electrocatalytic conditions. Hence, more intricate evolution processes are still to be discovered. Besides, while several works have addressed ORR electrocatalysts^{49,50}, there is no report on *in situ* EC-TEM for OER electrocatalysts.

In this chapter, a description of the study of Co₃O₄ as a model for OER electrocatalysis is given. As a first instance, a complementary description of the *in situ* EC-TEM

methodology is given in resonance with what was described in section 1.5. We then apply *in situ* electrochemical TEM to water oxidation electrocatalysis over Co_3O_4 nanoparticles in alkaline and neutral electrolytes under various electrochemical conditions. Finally, the nanocatalysts morphological and structural modifications taking place during OER are discussed. Lastly, preliminary results from the study of $\text{La}_{2/3}\text{Sr}_{1/3}\text{MnO}_3$ perovskite (LSMO) nanocrystals for the ORR will be presented along with some perspectives.

2.2. Cobalt oxide electrocatalysis: A “not so model” system

The spinel Co_3O_4 crystal is a case study of low-cost and efficient electrocatalyst towards the OER in alkaline media, where structural evolution involves multiple phenomena beyond simple etching of the surface. Several authors have pointed out that the actual active species are Co^{4+} cations, which appear only above the onset potential and get reduced upon return to non-catalytic conditions.^{51–55} Despite the various examples of OER electrocatalysts based on Co_3O_4 nanoparticles, there is no insight on the evolution of the morphology of the particles and on the reversibility of these structural and morphological transformations. One of the clearest attempts to solve this question was done by Bergmann *et al.*⁵⁶ who used a combination of XAS performed on quenched electrodes, and *in situ* grazing-incident X-ray diffraction (GIXRD). In their work, the appearance of the active Co^{4+} species was related to a reversible formation of an amorphous sub-nanometer shell of $\text{CoO}_x(\text{OH})_y$ on Co_3O_4 . Although this approach provided the first insights into the changes that Co_3O_4 nanoparticles do experience during OER, no information on the morphological evolutions could be retrieved. Hence, Co_3O_4 nanoparticles appear as an ideal candidate for *in situ* EC-TEM in OER conditions. Such a new analytical approach should complete the knowledge acquired with previous spectroscopic studies⁵⁶ by providing a direct view, in real time and real space, of both morphological and structural changes during OER.

Catalyst nanoparticles synthesis

The Co_3O_4 nanoparticles were produced through a microwave-assisted hydrothermal synthesis by modifying a protocol reported recently.⁵⁷ $\text{Co}(\text{NO}_3)_2 \cdot 6\text{H}_2\text{O}$ was solubilized in 35 mL at a concentration of 0.02 mol L^{-1} . The pH was then adjusted to 11.5 by addition of an ammonia solution at 28 wt. %. The reaction medium was aged by stirring under air for 1 h. The suspension was then divided into 2 aliquots of ca. 20 mL. Each of these aliquots was heated into a monomode microwave oven (Anton Paar Monowave 300) with

a 10 s heating ramp at 800 W followed by a 10 min dwell time. Each aliquot was then washed by 5 cycles of centrifugation-redispersion into milliQ water. The recovered powders were dried overnight under vacuum at 40 °C.

Catalyst ink preparation

As mentioned in Section 1.6, two types of ink composition were tested *ex situ*. The first one contained 10 mg of Co₃O₄, Acetylene Black (AB, Alfa Aesar) (99.9+ %, 75 m² g⁻¹) and 10 mL of absolute ethanol. This mixture was sonicated during 2 h. Then, the dispersion was cooled down to room temperature and 435 μL of ion-exchanged Nafion© solution (5 wt. % in aliphatic alcohols, Aldrich) was added immediately. The mixture was then sonicated again until a stable dispersion was reached. This is a classical composition to test electrocatalytic OER properties.⁵⁸ A second ink was tested, comprising only 10 mg of Co₃O₄ and 10 mL of absolute ethanol, without any additives. For the *in situ* EC-TEM experiments, only the second carbon-free ink was used to avoid decomposition of Nafion© under the beam and to avoid the dilution of Co₃O₄ nanoparticles by AB particles.

Electrode preparation and electrochemistry

***Ex situ* electrochemistry.** An electrochemical workstation VPS Biologic potentiostat equipped with a rotating disk working electrode (1600 rpm) was used to evaluate *ex situ* the OER properties of a thin-layer film of Co₃O₄ nanoparticles. The working electrode consisted of a 3 mm diameter glassy carbon (GC) disk covered by a thin-layer film of electrocatalyst obtained by drop casting of the inks described above. The counter electrode was a Pt wire. An Ag/AgCl/saturated KCl electrode was used as a reference. Prior to the deposition of the ink, the GC electrodes (0.07 cm², Radiometer Analytical) were sequentially polished using diamond paste (1 μm, BAS inc.) followed by alumina paste (0.05 μm, BAS inc.) to reach mirror grade. After polishing, the electrodes were sonicated in water and ethanol 10 min each. Then, 2 μL of the additive-free ink (10 mg Co₃O₄/10 mL ethanol) were drop-casted over the GC disk and dried under static air for 1h. The maximum load (Co₃O₄) over the GC electrode would be 28.5 μg cm_{GC}⁻². A 0.1 M KOH, a 0.1 M KCl, and a pH 7 phosphate buffer aqueous solutions were used as electrolytes. The buffer solution was obtained by mixing of 0.1 M K₂HPO₄ and 0.1 M KH₂PO₄ aqueous solutions until pH 7 was reached.

***In situ* electrochemical TEM.** For the *in situ* liquid TEM analysis, the methodology is described in chapter 1. First, the e-chips were cleaned. Thereafter, a 2-5 nm carbon layer

was deposited on the e-chip with the electrodes (top chip) using a carbon evaporator. The carbon layer was introduced to reduce the drift of the nanoparticles during observation. This layer helped to the better fixation of the nanoparticles over the observation window. Alternatively, plasma cleaning with Ar/O₂ during 30 s was also tested to improve the fixation, but the carbon layer proved to be better for this end. Then, a drop of the Co₃O₄ ink was deposited over the silicon nitride observation window through the mask. The chip was dried under air during 1 h before closure of *in situ* cell. The maximum load over the GC electrode collector was 342 μg cm_{GC}⁻². The electrolytes were flushed into the *in situ* cell after its introduction into the microscope at a constant 25 μL min⁻¹ flow. The dynamical processes at the surface of the nanoparticles were best observed within the formed bubbles since only a thin layer of electrolyte is preserved, improving the resolution. The use of a flow of electrolyte helped to insure the wetness of the surface. No evidence of full dewetting was observed in the electrochemical measurements.

2.2.1. Morphological evolution monitored by operando STEM during cyclic voltammetry

First, we observed the Co₃O₄ nanoparticles (Figure 2.3a) drop-casted on the observation window of the chip, without any liquid. The nanoparticles with diameter between 10 and 15 nm formed 100 nm-scale agglomerates over the glassy carbon electrode. Thereafter, the 0.1 M KOH electrolyte solution was continuously flowed into the chip (Figure 2.3b). The conditions of electron illumination were optimized in STEM mode in order to set the appropriate conditions for minimizing the beam effect on the particles and electrochemical measurements as described in section 1.4. No modification of the morphology of the nanoparticles was observed after they were set in contact with the flow of electrolyte (Figure 2.3b). Furthermore, additional EELS and electron diffraction analysis of nanoparticles that were not subjected to any electrochemical measurement showed no beam-induced modifications (Figure 2.4). The same electrode area described above (Figure 2.3a and 2.3b) was observed during cyclic voltammetry (Figure 2.3c) within the liquid. Remarkably, after 25 cycles at 20 mV s⁻¹, the diameter of the Co₃O₄ nanoparticles decreased to around 5 nm (Figure 2.3c). The lighter contrast around the nanoparticles after cycling indicates the presence of a low electron density matrix embedding the particles. ([Annex movie M1](#))

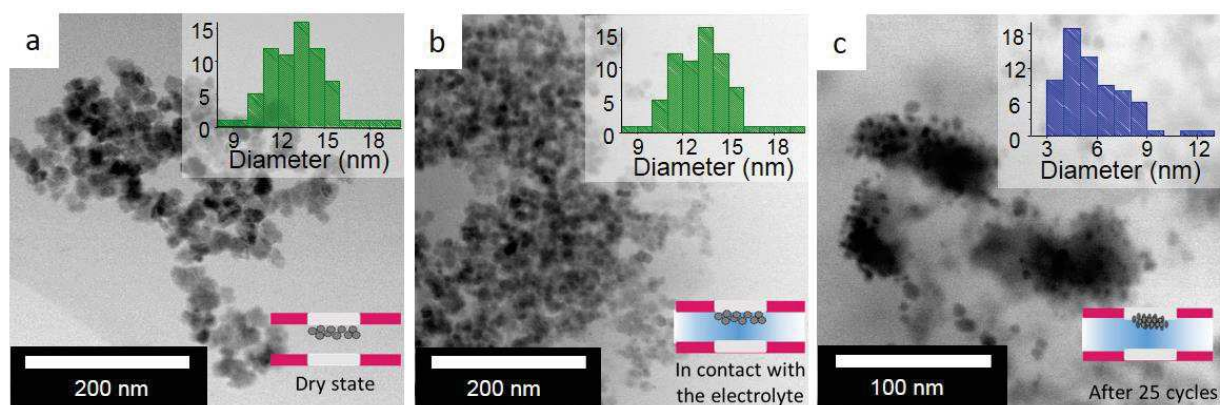


Figure 2.3. *In situ* STEM images of Co_3O_4 nanoparticles deposited over the glassy carbon electrode in the observation window of the electrochemical TEM sample holder: particles a) as-prepared in the dry state, b) in contact with a 0.1 M KOH electrolyte before electrochemical measurements, c) after 25 voltammetric cycles from 0.6 V to 1.8 V vs. RHE in a 0.1 M KOH aqueous electrolyte at 20 mV s^{-1} . Top insets in a, b and c show the corresponding size distributions. Lower insets schematize the *in situ* EC-TEM cell and the location of the sample on the cell window.

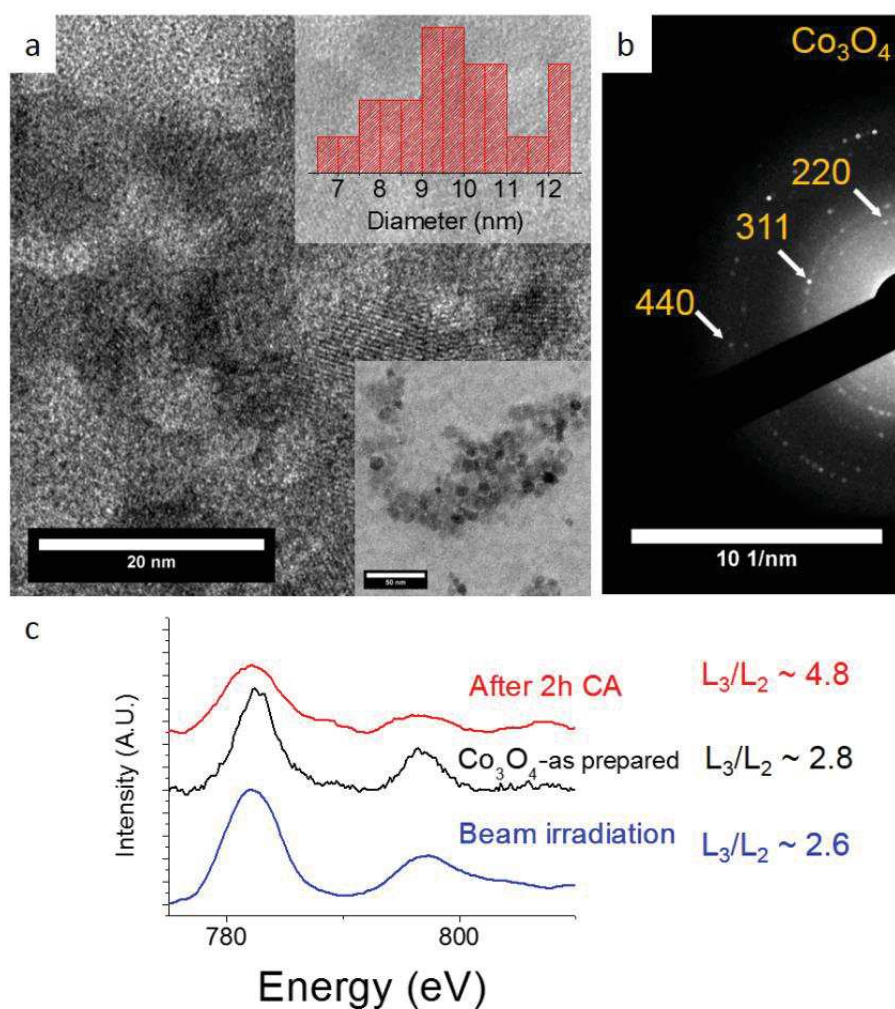


Figure 2.4. a) HR-TEM images from Co_3O_4 after 2 h of electron beam irradiation within the KOH 0.1 M electrolyte without electrochemical measurements. (Inset: size distribution). b) Diffraction pattern recorded after removal of the electrolyte, displaying the main reflexions of Co_3O_4 . c) EEL spectra of the recovered nanoparticles. Compared with the as-prepared Co_3O_4 , the smaller L_3/L_2 ratio reflects a higher oxidation induced by the electrolyte. No beam-induced changes were found

Chemical mapping by Energy Dispersive X-Ray spectroscopy-coupled STEM (STEM-EDX) was performed on the electrode material before cycling and after the 125 cycles at 100 mV s^{-1} . A verification of the uniform composition of the nanocatalyst during CV was obtained through the analysis of 9 nm nanoparticles after 125 CV cycles at 100 mV s^{-1} . It showed particles size decrease and growth of a low contrast matrix (Figure 2.5). It indicated that the particles as well as the surrounding matrix are made of both cobalt and oxygen (Figures 2.5c-d and 2.5g-h).

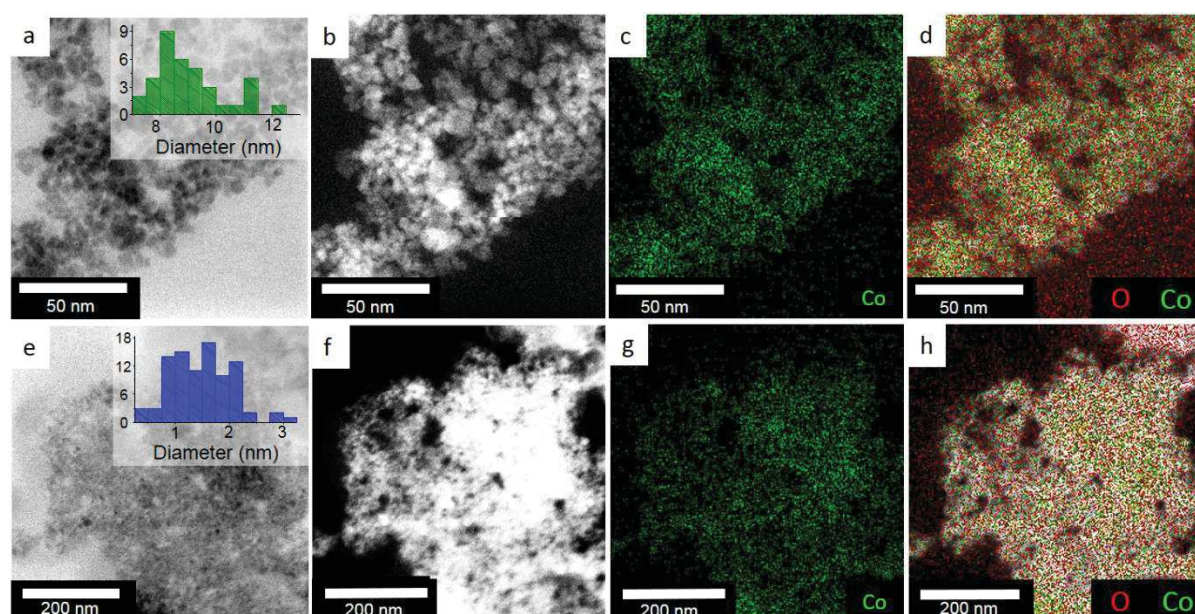


Figure 2.5. Analytical study of Co_3O_4 nanoparticles deposited on the electrode of the *in situ* electrochemical TEM holder (a-d) in the dry state, (e-h) after 125 cycles from 0.6 V/RHE to 1.8 V/RHE in a 0.1 M KOH aqueous electrolyte at 100 mV s^{-1} . Bright field STEM images (a) before and (e) after cycling. STEM images recorded in High Angular Annular Dark Field (HAADF) mode of the same regions (b) before and (f) after cycling. (c, g) Corresponding elemental maps of Co (K α). (d, h) Corresponding composite maps of Co (green) and O (red) superimposed to the STEM-HAADF images. Insets in (a) and (e) show the size distributions of the nanoparticles before and after cycling.

In order to ensure that the electrochemical potential window within the miniaturized cell corresponds to the same range into a typical *ex situ* three-electrodes set-up, the reference redox couple $\text{Fe}(\text{CN})_6^{3-}/\text{Fe}(\text{CN})_6^{4-}$ (1.2 V vs. RHE) was introduced in the electrolyte as

internal reference, curve (a). The potential was recalibrated using the $\text{Fe}(\text{CN})_6^{3-}/\text{Fe}(\text{CN})_6^{4-}$ redox potential with respect to an Ag/AgCl reference electrode and a Pt wire. The cyclic voltammograms (CV) recorded at 100 mV s^{-1} (Figure 2.6) show that the redox waves of the reference couple *in situ* and *ex situ* are shifted by 0.3 V. After realignment of the potential scales by taking into account this shift, the CV curves are very close. They span a potential range between 0.6V and 1.8 V/RHE and exhibit similar shapes. After correction of the *in situ* potential scale, the most important difference between *ex situ* and *in situ* recorded CV curves is the higher polarization in the *in situ* cell, which may account for the impossibility to polish the electrode in the *in situ* set-up and the heterogeneous dispersion of the nanoparticles in the surface of the working electrode.

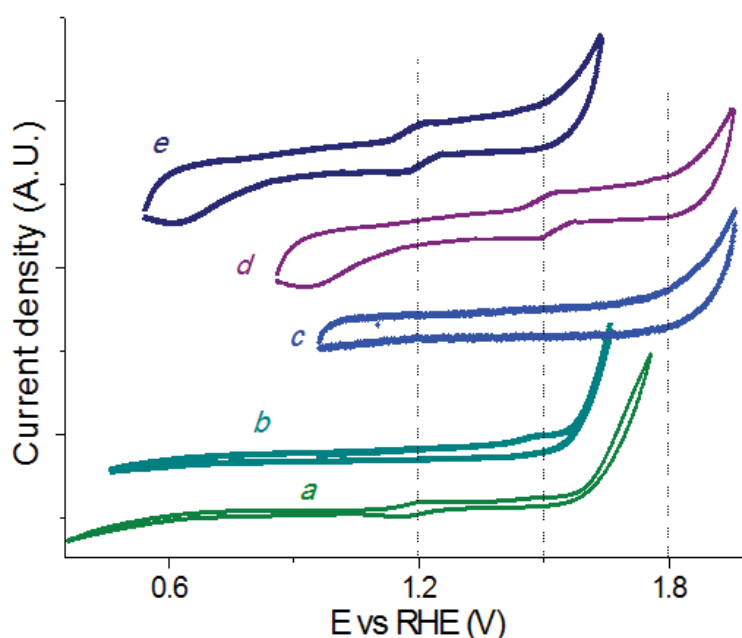


Figure 2.6. Voltammetry cycles (2nd cycle) recorded at 100 mV s^{-1} *ex situ* and *in situ* by using electrodes of Co_3O_4 nanoparticles with (a) and without (b) the $\text{Fe}(\text{CN})_6^{3-}/\text{Fe}(\text{CN})_6^{4-}$ couple as internal reference in a 0.1 M KOH aqueous electrolyte, in a classical three-electrodes electrochemical cell with a Pt pseudo-reference electrode (“*ex situ*” curves), and in the *in situ* electrochemical TEM holder, without (c) and with (d) the internal reference, respectively. The curve (e) “*in situ* internal reference corrected” corresponds to the curve (d) “*in situ* internal reference” which was shifted in order to align the redox wave of the reference couple with the one measured *ex situ*.

Overall, direct observation by *in situ* electrochemical STEM of the formation of the matrix and of the particle diameter decrease suggests a structural modification of the outer part of the initial nanoparticles into a less dense cobalt oxide arrangement. No hint of atom-scale ordering within this matrix could be retrieved after cycling using high

resolution TEM (HRTEM) *post in situ*, thus suggesting an amorphous character. The observed composition and atom-scale disorder of the matrix are in agreement with previous reports suggesting the formation of an amorphous cobalt (oxyhydr)oxide-like phase during OER with Co_3O_4 materials.^{34,56} Such a restructuration occurs when the material is repeatedly exposed to potentials high enough to trigger OER, in agreement with the conclusions of Bergmann *et al.*⁵⁶ who proposed a surface amorphization of Co_3O_4 nanoparticles above the OER onset potential in a neutral phosphate buffer (KPi) aqueous electrolyte. However, a significant difference arises between the previous observations made from *in situ* grazing-incident X-ray diffraction (GIXRD) and from quenched- X-ray absorption edge spectroscopy (XAS)⁵⁶ on the one side, and our *in situ* TEM results on the other side. While the formers report amorphization at high potential that is fully reversible when the electrode goes back at its resting state, we observed an irreversible growth of the amorphous layer upon voltammetric cycling, leading to the formation of an amorphous matrix embedding the remaining crystalline fractions. To probe the extent of such irreversible amorphization in basic KOH aqueous electrolyte, we have submitted a Co_3O_4 nanoparticles-based electrode to some more severe OER conditions, by using chronopotentiometry in the OER conditions in aqueous 0.1M KOH electrolyte in the *in situ* electrochemical TEM holder.

2.2.2. Morphological evolution monitored by operando STEM during chronopotentiometry

The morphological evolution of Co_3O_4 nanoparticles was monitored while applying a 10 mA $\text{cm}_{\text{GC}}^{-2}$ current density during 10 min (Figure 2.7). The chronopotentiometry curve is similar to those previously reported in the literature,^{59,60} with a steep increase of the potential over the first 30 s, followed by a slower increase. Over a period of around 120 s, STEM images show the growth of a matrix embedding smaller crystalline nanoparticle ([Annex movie M2](#)). As mentioned above, this matrix is assigned to an amorphous cobalt (oxyhydr)oxide-like phase. The overall area of the chosen agglomerate increased by 8% up to 120 s and then reached a steady state. The persistence of bright areas in the STEM-HAADF images shows that dense nano-domains were maintained and that the amorphization process of the particles into a lesser density solid is not complete. The *in situ* STEM chronopotentiometry experiment (Figure 2.7) is consistent with the *operando* STEM CV study (Figure 2.4), showing extended amorphization of the spinel nanoparticles in the course of OER. The resulting amorphous cobalt (oxyhydr)oxide-like phase is then exposed to the electrolyte and is probably at the origin of the

electrocatalytic activity,⁶¹ with the formation of Co^{4+} species according to the literature.^{51,61,62}

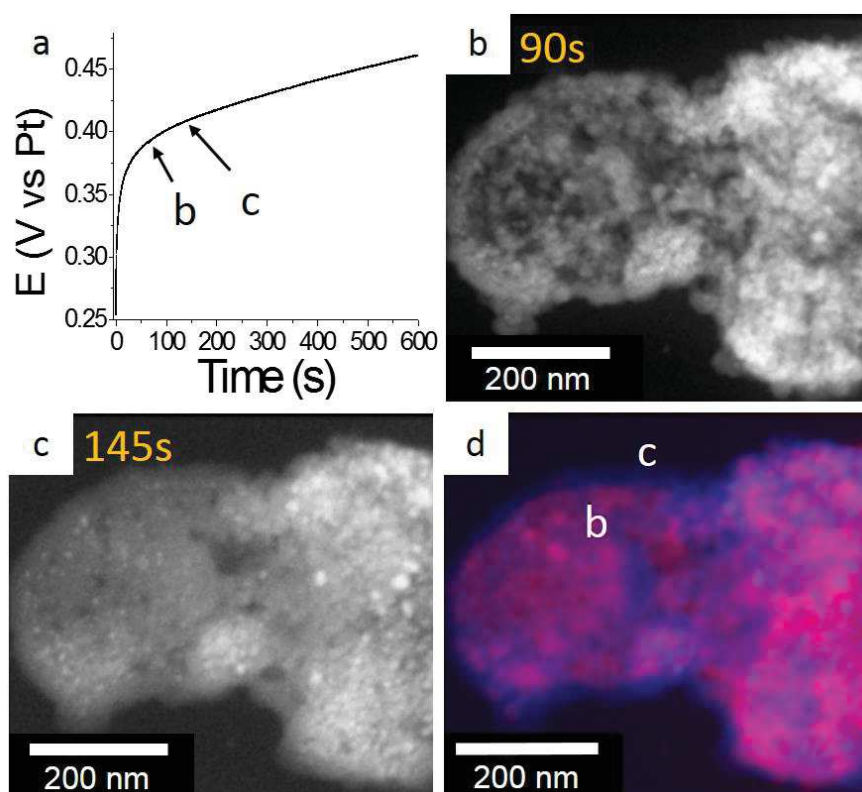


Figure 2.7. a) *In situ* electrochemical TEM chronopotentiometry experiment at 10 mA cm^{-2} in aqueous 0.1 M KOH electrolyte for 10 min: time evolution of the electrode potential vs. RHE and of the area of a nanoparticles agglomerate. STEM-HAADF images recorded at 90 s b) and 145 s c). d) Superposition of b and c evidencing the evolution of the area of the agglomerate at 90 s (red) and 145 s (blue).

The fact that amorphous/crystalline components are also present in regions away from the illuminated area further indicates that the amorphization is not caused by the electron beam. To confirm this statement and rule out any synergistic effect between electrochemistry and the extended exposition to the electron beam, chronopotentiometry and CV experiments were performed *ex situ* in the same conditions as *in situ*. Then, both electrode materials were observed *post mortem* in STEM (Figure 2.8). Similar amorphous/crystalline composite containing smaller particles embedded into a less dense matrix were observed both *in situ* and *ex situ*. The electrodes were further analyzed to get deeper understanding of the nature of this matrix and of the remaining nanoparticles.

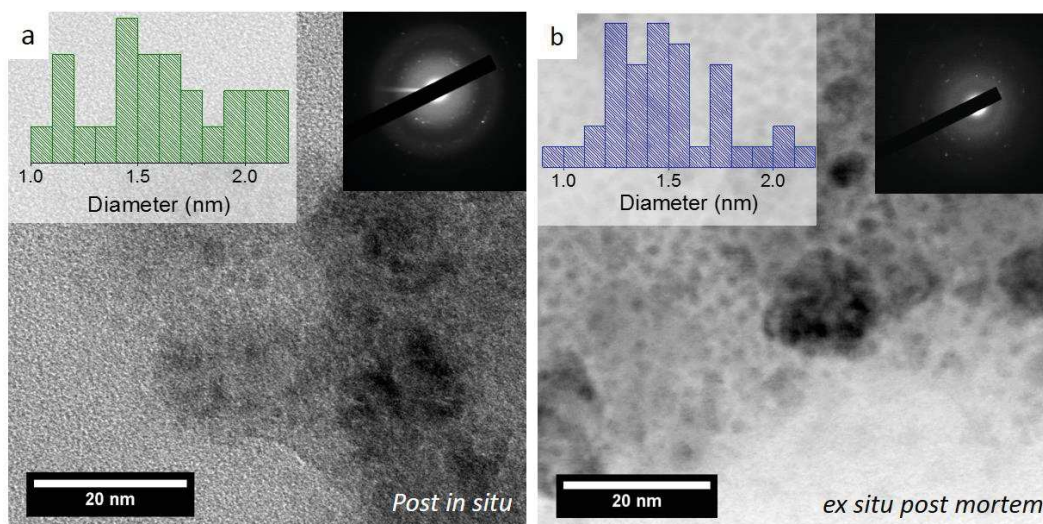


Figure 2.8. STEM *post mortem* images of Co_3O_4 nanoparticles a) deposited over the glassy carbon electrode in the observation window of the electrochemical TEM sample holder b) recovered from a rotating glassy carbon disk electrode of a typical 3-electrodes set-up. Both images have been acquired after 2 h chronopotentiometry measurements at $10 \text{ mA cm}^{-2}_{\text{GC}}$. Top insets in A and B show the corresponding size distributions

2.2.3 Structural evolution: post mortem study

Electron diffraction (ED) performed on the electrode material after chronopotentiometry in aqueous 0.1 M KOH electrolyte for 2h, using the *in situ* set-up as well as the classical three electrode cell, (Figure 2.9B) shows that the Co_3O_4 structure has disappeared. Instead, the observed diffraction spots are assigned to a mixture of CoO , CoOOH and $\text{Co}(\text{OH})_2$ phases, thus indicating that the initial Co_3O_4 particles have transformed after prolonged OER into other cobalt-oxo phases and an amorphous (oxyhydr)oxide-like matrix.

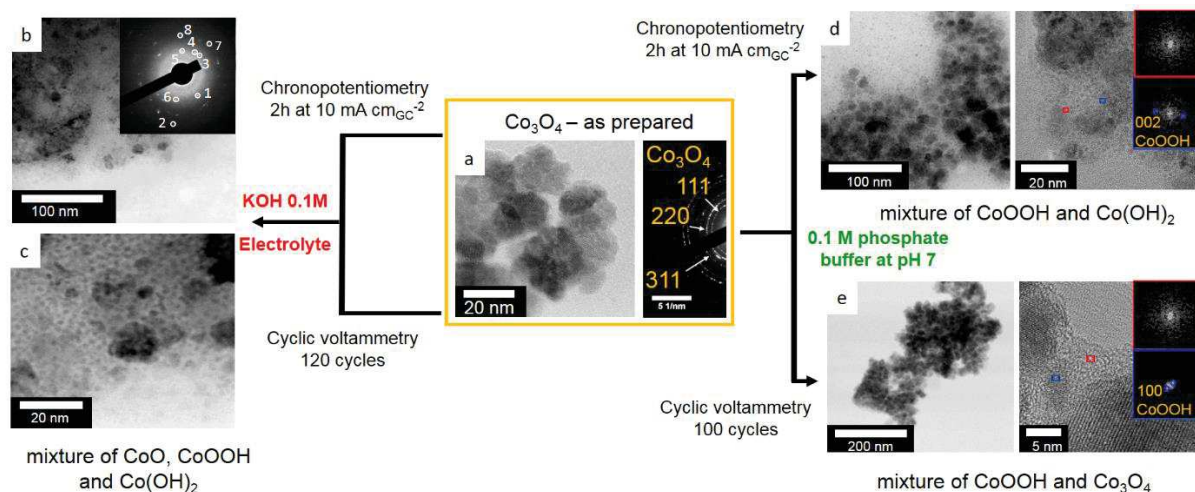


Figure 2.9. Bright field STEM images and diffraction patterns of a) as prepared Co_3O_4 , b) Co_3O_4 after 2 h of chronopotentiometry at 10 mA cm^{-2} in aqueous 0.1 M KOH electrolyte (inset: diffraction pattern displaying a mixture of CoOOH (1-[100]; 2-[200]; 3-[100]), $\text{Co}(\text{OH})_2$ (4-[101]; 5-[100]) and CoO (6-[111]; 7,8-[220])). c) Co_3O_4 after 120 CV cycles from 0.6 to 1.8 V vs RHE in aqueous 0.1 M KOH electrolyte. d) Co_3O_4 after 100 CV from 0.6 to 1.8 V vs RHE in KPi as electrolyte. e) Co_3O_4 after 2 h of chronopotentiometry at 10 mA cm^{-2} in neutral KPi aqueous electrolyte.

Electron energy loss spectroscopy (EELS) performed on the electrode in the miniaturized EC-TEM cell before and after chronopotentiometry confirms this observation (Figure 2.10), with a significant change in the cobalt L_3/L_2 intensity ratio from the initial electrode to the *post-mortem* electrode. The “as prepared” Co_3O_4 nanoparticles displayed an L_3/L_2 ratio of *ca.* 2.8 in agreement with the mixed valence $\text{Co}^{\text{II}}/\text{Co}^{\text{III}}$ expected in Co_3O_4 .⁶³ After chronopotentiometry, a L_3/L_2 ratio of *ca.* 4.8 was observed, suggesting Co^{2+} species as the major component. This result confirms the assignment of the remaining nanoparticles to CoO , CoOOH and $\text{Co}(\text{OH})_2$, and strongly supports the presence of Co^{2+} species also in the amorphous phase after electrochemical experiments. Hence, the electrode analyzed *post-mortem* comprises CoO , CoOOH and $\text{Co}(\text{OH})_2$ nanoparticles embedded into an amorphous CoO_xH_y matrix containing Co^{2+} species. Overall, consistent observations between *in situ* and *ex situ* studies show that in aqueous 0.1 M KOH electrolyte, Co_3O_4 nanoparticles decompose irreversibly into smaller Co^{2+} -based (CoO and $\text{Co}(\text{OH})_2$) and Co^{3+} -based (CoOOH) nanoparticles within an extended amorphous cobalt (oxy)hydroxide matrix. The latter contains Co^{2+} when isolated *post mortem*, but is most probably oxidized into $\text{Co}^{3+}/\text{Co}^{4+}$ species under the OER conditions, according to previous results.^{51–55} This would also agree with a recent report that has accounted for a similar behavior in alkaline OER conditions of the spinel NiCo_2O_4 ,²¹ for which *in situ* Raman measurements showed that the initial spinel irreversibly transforms into a poorly ordered (oxyhydr)oxide-like phase and rock salt CoO in alkaline OER conditions. Further *in situ* investigations will be necessary to assess *in situ* the electronic state of Co during OER, especially with *in situ* XAS to avoid the limitations of EELS, which can only be performed in the dried cell.

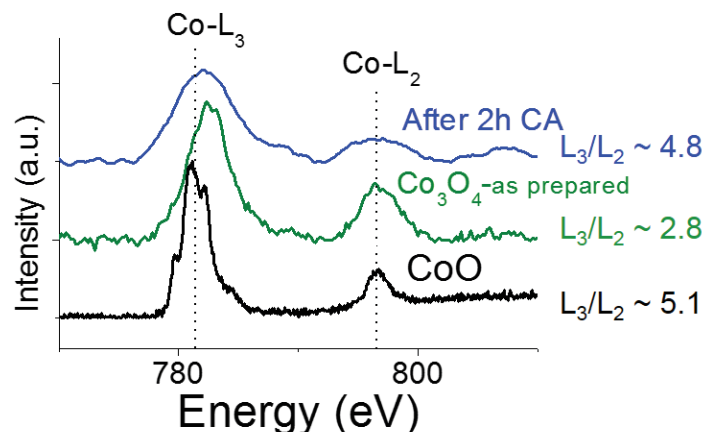


Figure 2.10. Co K edge EEL spectra of CoO (black), “as prepared” Co_3O_4 (green) and catalyst after 2h of chronopotentiometry measurements (blue) at 10 mA cm^{-2} in aqueous 0.1 M KOH . CoO spectra was taken from the EELS database.⁶⁴

Although we have obtained consistent evidences of extended and irreversible amorphization of the Co_3O_4 nanoparticles surface, this observation appears in contradiction with other reports mentioning reversible structural modifications of Co_3O_4 materials.^{34,56} The reversibility of this transformation may be impacted by the crystallographic facets exposed by the material.⁶⁵ This could explain the discrepancy between our observation of irreversible amorphization of nanoparticles and the reversible surface amorphization of an oriented $\text{Co}_3\text{O}_4(111)$ thin film.³⁴

Another factor possibly influencing the surface amorphization is the nature of the aqueous electrolyte, including pH and counter ions. Previous *in situ* measurements of reversible amorphization of Co_3O_4 nanoparticles have been performed in a neutral phosphate buffer (KPi) electrolyte.⁵⁶ In order to assess the influence of the electrolyte, we have studied by STEM and EDX the electrode after *ex situ* cyclic voltammetry (**Figures 2.11, 2.12** and **Figure 2.13**) and chronopotentiometry in the KPi electrolyte. As in alkaline medium, the particles average diameter decreased during OER, down to 1-2 nm under chronopotentiometry conditions after 2 h (Figure 2.9d). Lattice planes typical of the interlayer distance (002) of CoOOH were observed in some $\sim 2 \text{ nm}$ nanoparticles. In figure 13, sheet-like nanostructures were detected, typical of lamellar phases like CoOOH and $\text{Co}(\text{OH})_2$ with interlayer distance of about 1 nm, in agreement with the presence of cobalt (oxy)hydroxide and/or hydroxide phases.⁶⁶

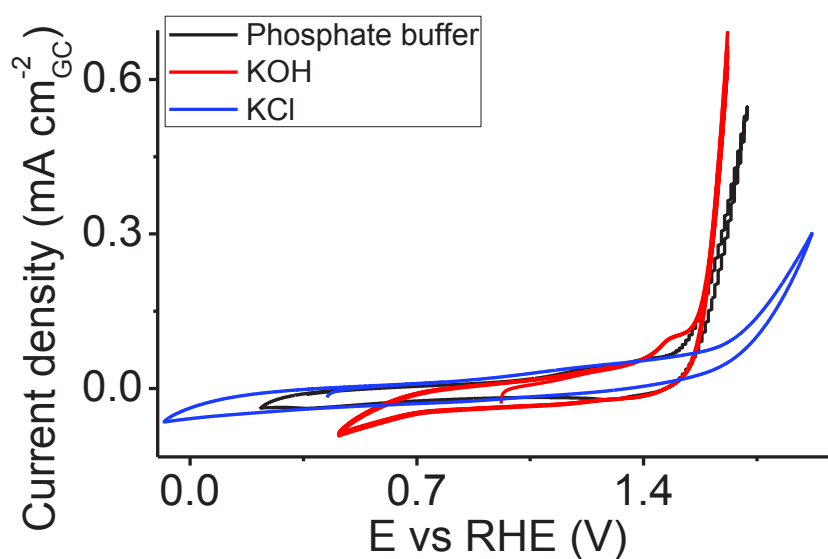


Figure 2.11. Cyclic voltammograms recorded *ex situ* at 100 mV s⁻¹ for Co₃O₄ nanoparticles within 0.1 M KOH (red), 0.1 M KPi phosphate buffer at pH 7 (black) and 0.1 M KCl (blue) aqueous electrolytes in a classical 3 electrodes electrochemical cell, with a working disk electrode rotating at 1600 rpm.

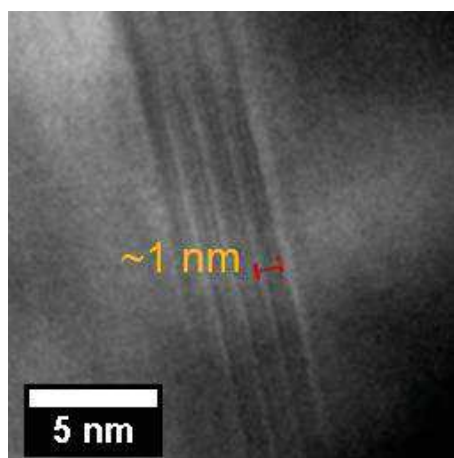


Figure 2.12. Bright field-STEM image of a Co₃O₄ electrode material recovered from the working electrode after chronopotentiometry of 2 h at 10 mA cm_{GC}⁻² in a classical *ex situ* electrochemical set-up in a 0.1 M KPi phosphate buffer electrolyte at pH 7.

Some areas from the surrounding phase showed no evidence of structuration, thus suggesting that the matrix is again amorphous, as in basic medium (Figure 10E). Chemical mapping did not evidence the presence of phosphorus (Figure 14). Thus, the matrix is an amorphous cobalt (oxyhydr)oxide-like phase, as in the alkaline KOH electrolyte. When using the same KPi electrolyte but under cyclic voltammetry (Figure 10E), morphological changes are less apparent, with no significant change in the particle size. Some 1-2 nm crystalline domains were nevertheless observed with d-

spacing typical of CoOOH. They are embedded in a 3 nm-thick amorphous layer. These TEM observations complete the structural information reported by Bergmann *et al.*⁵⁶ under cyclic voltammetry. Indeed, although Co₃O₄ appears in TEM as the main phase, thus confirming that structural changes are limited, we observe the formation of a thin amorphous layer in an irreversible manner that was not detected by structural studies,⁵⁶ which appear not sensitive enough to surface states. Chronopotentiometry under OER conditions implies larger charge transfer per experimental time unit than cyclic voltammetry ones. These more stringent conditions yield extended and irreversible amorphization, as it was the case in the alkaline electrolyte.

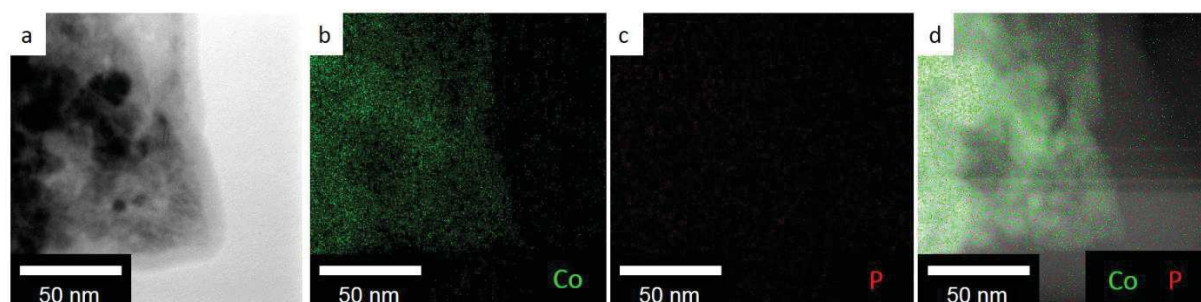


Figure 2.13. Compositional study of Co₃O₄ nanoparticles recovered from the rotating glassy carbon electrode of the classical electrochemical set-up after 2h CP at 10 mA cm⁻²_{GC} in a 0.1 M KPi phosphate buffer electrolyte at pH 7. a) Bright field-STEM image after chronopotentiometry. Corresponding elemental maps of b) Co (K α), c) P (K α). d) Corresponding composite maps of Co (green) and P (red) superimposed to the STEM-HAADF images. This compositional analysis shows that phosphates are not inserted in a detectable amount in the structure of the catalyst after the electrocatalysis.

In a phosphate-free KCl electrolyte with the same pH as the KPi electrolyte, more important structural and morphological changes were observed after 2h of chronopotentiometry (Figure 2.14), including extended crystallization of Co(OH)₂, CoOOH and Co₃O₄, with no evidence of potassium insertion in the final material (Figure 2.15). As in the case of KOH and KPi electrolytes, evolutions are less marked in CV conditions. At the same pH the phosphate buffer provides higher OER activity than the KCl electrolyte (Figure 2.11). In addition, the amorphous matrix grown around the initial Co₃O₄ particles appears mandatory to trigger high OER activity. This corroborates the hypothesis that this amorphous cobalt (oxyhydr)oxide-like phase is the actual electrocatalytic material in the material studied herein, initially made of sole Co₃O₄ nanoparticles. The difference in reactivity in KPi and KCl at the same pH is not ascribed to the presence of phosphates in the material obtained in KPi, as phosphorus could not be detected by EDS in the electrode material.

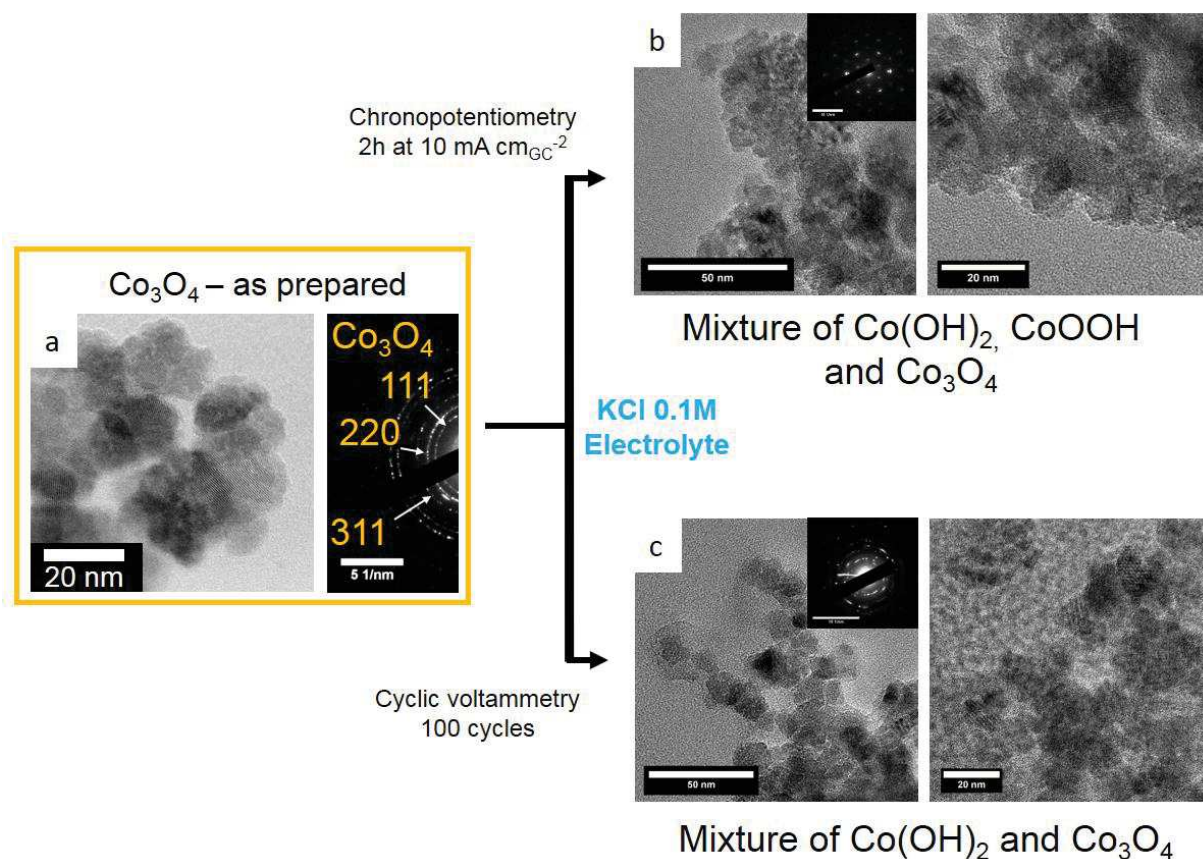


Figure 2.14. Bright field electron micrographs and diffraction patterns of a) “as-prepared” Co₃O₄, b) Co₃O₄ after 2 h of chronopotentiometry at $10 \text{ mA cm}_{\text{GC}}^{-2}$ in aqueous 0.1 M KCl electrolyte. In the case of KCl as the electrolyte, the initial structure of the nanoparticles is deeply changed. There is an extended crystallization and the diffraction patterns show the coexistence of different phases Co(OH)₂, CoOOH and Co₃O₄. c) Electrode material recovered after 100 CV cycles from 0.2 to 2 V vs RHE in aqueous 0.1 M KCl electrolyte. In this neutral electrolyte, when the potential is cycled, the size of the nanoparticles remains unchanged and there is no evidence of amorphous regions. However the reticular distances indicate the presence of a mixture of Co(OH)₂ and Co₃O₄.

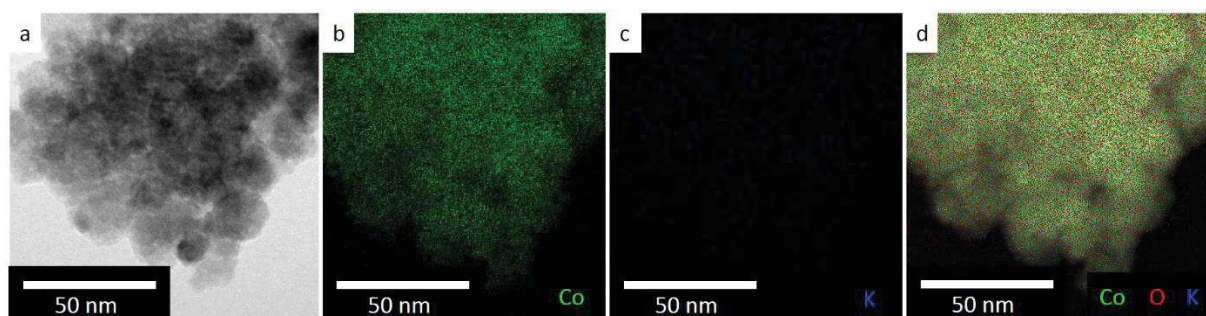


Figure 2.15. Compositional study of Co_3O_4 nanoparticles recovered from the working electrode of an *ex situ* electrochemical set-up after 2h chronopotentiometry at 10 mA cm^{-2} in a 0.1 M KCl electrolyte. (a) Bright field-STEM image. Corresponding EDS elemental maps of (b) Co (K α), (c) K (K α). (d) Corresponding EDS composite map of Co (green), K (blue) and O (red) superimposed to the STEM-HAADF images. This compositional analysis shows that potassium is not inserted in a detectable amount in the structure of the material.

This suggests that the amorphous cobalt (oxyhydr)oxide-like phase forming during OER at the surface of the Co_3O_4 nanoparticles is not subjected to the self-healing mechanism evidenced by Nocera *et al.* for the electrodeposited electrocatalyst Co-Pi, a phosphate-containing amorphous cobalt (oxyhydr)oxide-like phase.^{67–69} On the contrary, phosphates into the KPi electrolyte can act as proton acceptors to fasten OER compared to the KCl electrolyte.⁷⁰ Likewise, Cl^- ions can trigger larger morphological changes by nucleophilic catalysis of oxide restructuring.⁷¹ Furthermore, morphological and structural changes are less marked in KPi with neutral conditions than in basic KOH electrolyte, where cobalt-oxo species are however less soluble.^{71,72} Therefore, extensive restructuring in aqueous KOH is not related to dissolution-reprecipitation of the Co-based material, but can be traced back to the OER process, in agreement with previous reports that ascribe the formation of a layered cobalt oxyhydroxide-like phase to the transition of initial $\text{Co}^{2+_{Td}}$ species into Co_3O_4 , $\text{Co}^{3+_{Oh}}$ species into the layered phase.^{56,73} The cyclic voltammograms recorded in the different electrolytes show that at a given potential vs. RHE, higher current and hence higher OER rate are reached in KOH than in KPi, which exemplifies the more favorable kinetics of OER in the basic electrolyte. The faster OER would in turn trigger faster structural evolution and amorphization in KOH than in the phosphate buffer, thus suggesting that the OER rate and the amorphization rate are related, presumably through the amount of transferred charges.

Overall, under operation of the Co_3O_4 -based electrodes, surface amorphization occurs to an extent that depends on the nature of the electrolyte and on the electrochemical conditions. In some of the most common conditions (alkaline electrolyte and/or chronopotentiometry), the amorphous phase becomes the major component of the electrode. Its formation is not reversible but it is also responsible for the water oxidation activity.

Finally, this study shows the suitability of *in situ* electrochemical TEM to address morphological transformations of electrocatalysts in *operando* conditions. The choice of Co_3O_4 as a model system, allowed to verify the *in situ* observations not only with data reported in the literature but with our own *post mortem* analysis. Moreover, we show the

advantage of analyzing locally a small amount of catalyst really participating in the reaction in contrast with other techniques where only the average activity is accounted for, including those that are not directly involved. Thus, this allows understanding the real impact of the electrocatalytic process on the evolution of the catalyst. Furthermore, the direct local observation benefits as well of the *post mortem* search for morphological changes, permitting a more targeted search. The latter was particularly evidenced in samples recovered after *ex situ* conventional electrocatalysis where a large amount of catalyst was unchanged. While this study was largely supported by *post mortem in situ* and *ex situ* data, we firmly believe that it will help in future implementation of *in situ* electrochemical TEM in other electrocatalytic systems more complex and less explored.

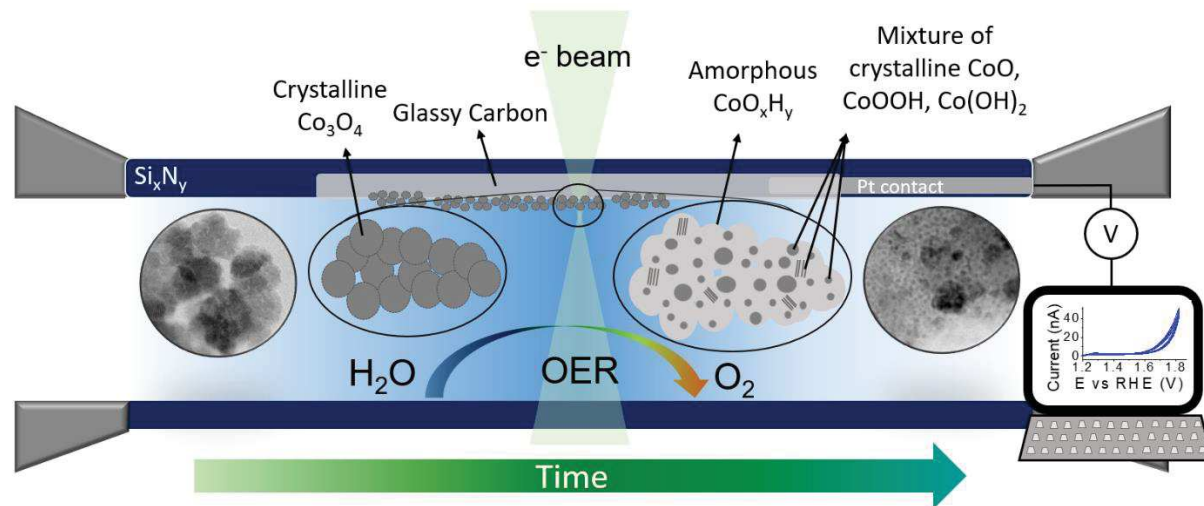


Figure 2.16. Scheme of the evolution of Co_3O_4 nanoparticles during oxygen evolution, as revealed by *in situ* electrochemical STEM.

In summary, we have assessed the structural and morphological transformations of cobalt oxide spinel nanoparticles in operation conditions for the oxygen evolution reaction. The study was performed by *in situ* electrochemical transmission electron microscopy after thorough evaluation of the role of the observation conditions, including electron dose, electrochemical conditions and electrolyte's nature. Optimized conditions allow direct tracking of the catalyst nanostructure in relation with the electrochemical measurements within the electrolyte. In addition to the imaging modes, the *in situ* cell can also be conveniently used for other complementary structural and chemical analyses, including selected area diffraction, energy dispersive and electron energy loss spectroscopies performed *post-mortem*, on the used electrodes after removal of the electrolyte. Electrodes studied electrochemically *in situ* as well as *ex situ* can then be

analyzed by STEM, yielding a more complete picture of the composition, microstructure and phase transformations induced by the electrocatalytic process.

Therefore, we could directly observe the gradual amorphization of Co_3O_4 nanoparticles during water oxidation process. Such amorphization reaches a plateau after a couple of minutes in the observation conditions, whatever the electrolyte used (basic KOH or neutral phosphate buffer). This restructuration appears beneficial to the water oxidation electrocatalytic activity and demonstrates that the amorphous phase formed in the course of the reaction is the active species for electrocatalytic OER on Co_3O_4 nanoparticle-based materials, as previously mentioned by other groups.⁵⁶ However, contrary to some previous reports, our observations unambiguously show that the material amorphization is not reversible in the electrochemical conditions studied, especially under constant current, which corresponds to the most operational conditions of water splitting electrochemical cells. All in all, the work reported herein sets the basic experimental parameters in order to use *in situ* electrochemical TEM for highlighting structural changes in electrocatalytic materials, using conditions as close as possible to that encountered in regular lab bench set-ups, and closer to more advanced electrocatalysis devices.

2.3. Concluding remarks

In situ electrochemical TEM provides specific advantages to assess electrocatalysts:

(i) *In situ* observation ensure that the compositional, structural and morphological analyzes are performed on nanoparticles actually involved in the electrochemical reactions, while *post mortem* analyzes cannot warrant that the materials analyzed were indeed involved in the reaction. In this work, we have especially ensured that the nanoparticles studied were in contact with the electrode and involved in electrocatalytic processes.

(ii) Likewise, *in situ* electrochemical TEM can be used to validate or improve a protocol for less time demanding *post mortem* analysis, once the data obtained by both approaches have been shown to be consistent. In this direction, we have used *in situ* studies to ensure that structural and morphological evolutions were occurring because of the electrocatalytic process, and not because of exposure to the electrolyte or because of post mortem drying of the electrode material, for instance.

(iii) Like many other *in situ* techniques, *in situ* electrochemical TEM can be used to detect steady states not stable after drying for *post mortem* observation, or elusive states difficult to quench. This track will be followed in the near future for non-model electrocatalysts such as the LSMO, LSCO and other mixed oxides. (Annex 3)

2.4. References

- (1) Hirlimann, C. *La Révolution CO2!*, 2nd ed.; Charles Hirlimann: La Wantzenau, 2018.
- (2) World Economic Forum. Marsh & McLennan Companies.; Insurance, Z. *Global Risks Report 2019*; World Economic Forum, 2019.
- (3) Obama, B. The Irreversible Momentum of Clean Energy. *Science* (80-.). **2017**, *355*, 126–129.
- (4) Hong, W. T.; Risch, M.; Stoerzinger, K. A.; Grimaud, A.; Suntivich, J.; Shao-Horn, Y. Toward the Rational Design of Non-Precious Transition Metal Oxides for Oxygen Electrocatalysis. *Energy Environ. Sci.* **2015**, *8*, 1404–1427.
- (5) Yan, Y.; Xia, B. Y.; Zhao, B.; Wang, X. A Review on Noble-Metal-Free Bifunctional Heterogeneous Catalysts for Overall Electrochemical Water Splitting. *J. Mater. Chem. A* **2016**, *4*, 17587–17603.
- (6) Roger, I.; Shipman, M. A.; Symes, M. D. Earth-Abundant Catalysts for Electrochemical and Photoelectrochemical Water Splitting. *Nat. Rev. Chem.* **2017**, *1*, 1–14.
- (7) McCrory, C. C. L.; Jung, S.; Peters, J. C.; Jaramillo, T. F. Benchmarking Heterogeneous Electrocatalysts for the Oxygen Evolution Reaction. *J. Am. Chem. Soc.* **2013**, *135*, 16977–16987.
- (8) Burke, M. S.; Enman, L. J.; Batchellor, A. S.; Zou, S.; Boettcher, S. W. Oxygen Evolution Reaction Electrocatalysis on Transition Metal Oxides and (Oxy)Hydroxides: Activity Trends and Design Principles. *Chem. Mater.* **2015**, *27*, 7549–7558.
- (9) Suen, N.-T.; Hung, S.-F.; Quan, Q.; Zhang, N.; Xu, Y.-J.; Chen, H. M. Electrocatalysis for the Oxygen Evolution Reaction: Recent Development and Future Perspectives.

- Chem. Soc. Rev.* **2017**, *46*, 337–365.
- (10) Suntivich, J.; May, K. J.; Gasteiger, H. A.; Goodenough, J. B.; Shao-Horn, Y. A Perovskite Oxide Optimized for Oxygen Evolution Catalysis from Molecular Orbital Principles. *Science*. **2011**, *334*, 1383–1385.
- (11) Garlyyev, B.; Fichtner, J.; Piqué, O.; Schneider, O.; Bandarenka, A. S.; Calle-Vallejo, F. Revealing the Nature of Active Sites in Electrocatalysis. *Chem. Sci.* **2019**, *10*, 8060–8075.
- (12) Wei, C.; Sun, S.; Mandler, D.; Wang, X.; Qiao, S. Z.; Xu, Z. J. Approaches for Measuring the Surface Areas of Metal Oxide Electrocatalysts for Determining Their Intrinsic Electrocatalytic Activity. *Chem. Soc. Rev.* **2019**, *48*, 2518–2534.
- (13) Li, X.; Wang, H.-Y.; Yang, H.; Cai, W.; Liu, S.; Liu, B. In Situ/Operando Characterization Techniques to Probe the Electrochemical Reactions for Energy Conversion. *Small Methods* **2018**, *2*, 1700395 (1-14).
- (14) Fabbri, E.; Nachttegaal, M.; Binninger, T.; Cheng, X.; Kim, B.-J.; Durst, J.; Bozza, F.; Graule, T.; Schäublin, R.; Wiles, L.; et al. Dynamic Surface Self-Reconstruction Is the Key of Highly Active Perovskite Nano-Electrocatalysts for Water Splitting. *Nat. Mater.* **2017**, *16*, 925–931.
- (15) Gul, S.; Ng, J. W. D.; Alonso-Mori, R.; Kern, J.; Sokaras, D.; Anzenberg, E.; Lassalle-Kaiser, B.; Gorlin, Y.; Weng, T.-C.; Zwart, P. H.; et al. Simultaneous Detection of Electronic Structure Changes from Two Elements of a Bifunctional Catalyst Using Wavelength-Dispersive X-Ray Emission Spectroscopy and in Situ Electrochemistry. *Phys. Chem. Chem. Phys.* **2015**, *17*, 8901–8912.
- (16) Paloukis, F.; Papazisi, K. M.; Balomenou, S. P.; Tsiplakides, D.; Bournel, F.; Gallet, J. Applied Surface Science In Situ X-Ray Photoelectron Spectroscopy Study of Complex Oxides under Gas and Vacuum Environments. *Appl. Surf. Sci.* **2017**, *423*, 1176–1181.
- (17) Favaro, M.; Drisdell, W. S.; Marcus, M. A.; Gregoire, J. M.; Crumlin, E. J.; Haber, J. A.; Yano, J. An Operando Investigation of (Ni–Fe–Co–Ce)O_x System as Highly Efficient Electrocatalyst for Oxygen Evolution Reaction. *ACS Catal.* **2017**, *7*, 1248–

1258.

- (18) Chen, J. Y. C.; Dang, L.; Liang, H.; Bi, W.; Gerken, J. B.; Jin, S.; Alp, E. E.; Stahl, S. S. Operando Analysis of NiFe and Fe Oxyhydroxide Electrocatalysts for Water Oxidation: Detection of Fe 4+ by Mössbauer Spectroscopy. *J. Am. Chem. Soc.* **2015**, *137*, 15090–15093.
- (19) Trześniewski, B. J.; Diaz-Morales, O.; Vermaas, D. A.; Longo, A.; Bras, W.; Koper, M. T. M.; Smith, W. A. In Situ Observation of Active Oxygen Species in Fe-Containing Ni-Based Oxygen Evolution Catalysts: The Effect of PH on Electrochemical Activity. *J. Am. Chem. Soc.* **2015**, *137*, 15112–15121.
- (20) Wang, H.; Wang, F. In Situ, Operando Measurements of Rechargeable Batteries. *Curr. Opin. Chem. Eng.* **2016**, *13*, 170–178.
- (21) Chen, Z.; Cai, L.; Yang, X.; Kronawitter, C.; Guo, L.; Shen, S.; Koel, B. E. Reversible Structural Evolution of NiCoO_xH_y during the Oxygen Evolution Reaction and Identification of the Catalytically Active Phase. *ACS Catal.* **2018**, *8*, 1238–1247.
- (22) An, H.; Chen, Z.; Yang, J.; Feng, Z.; Wang, X.; Fan, F.; Li, C. An Operando-Raman Study on Oxygen Evolution of Manganese Oxides: Roles of Phase Composition and Amorphization. *J. Catal.* **2018**, *367*, 53–61.
- (23) Toparli, C.; Sarfraz, A.; Wieck, A. D.; Rohwerder, M.; Erbe, A. In Situ and Operando Observation of Surface Oxides during Oxygen Evolution Reaction on Copper. *Electrochim. Acta* **2017**, *236*, 104–115.
- (24) Zandi, O.; Hamann, T. W. Determination of Photoelectrochemical Water Oxidation Intermediates on Haematite Electrode Surfaces Using Operando Infrared Spectroscopy. *Nat. Chem.* **2016**, *8*, 778–783.
- (25) Dutta, A.; Kuzume, A.; Rahaman, M.; Veszteg, S.; Broekmann, P. Monitoring the Chemical State of Catalysts for CO₂ Electroreduction: An In Operando Study. *ACS Catal.* **2015**, *5*, 7498–7502.
- (26) Carraro, F.; Vozniuk, O.; Calvillo, L.; Nodari, L.; La Fontaine, C.; Cavani, F.; Agnoli, S. In Operando XAS Investigation of Reduction and Oxidation Processes in Cobalt and

- Iron Mixed Spinels during the Chemical Loop Reforming of Ethanol. *J. Mater. Chem. A* **2017**, *5*, 20808–20817.
- (27) Zhou, J.; Wang, Y.; Su, X.; Gu, S.; Liu, R.; Huang, Y.; Yan, S.; Li, J.; Zhang, S. Electrochemically Accessing Ultrathin Co (Oxy)-Hydroxide Nanosheets and Operando Identifying Their Active Phase for the Oxygen Evolution Reaction. *Energy Environ. Sci.* **2019**, *12*, 739–746.
- (28) Song, S.; Zhou, J.; Su, X.; Wang, Y.; Li, J.; Zhang, L.; Xiao, G.; Guan, C.; Liu, R.; Chen, S.; et al. Operando X-Ray Spectroscopic Tracking of Self-Reconstruction for Anchored Nanoparticles as High-Performance Electrocatalysts towards Oxygen Evolution. *Energy Environ. Sci.* **2018**, *11*, 2945–2953.
- (29) Fabbri, E.; Nachttegaal, M.; Binniger, T.; Cheng, X.; Kim, B.; Durst, J.; Bozza, F.; Graule, T.; Schäublin, R.; Wiles, L.; et al. Dynamic Surface Self-Reconstruction Is the Key of Highly Active Perovskite Nano-Electrocatalysts for Water Splitting. *Nat. Mater.* **2017**, *16*, 925–931.
- (30) Pedersen, A. F.; Escudero-Escribano, M.; Sebok, B.; Bodin, A.; Paoli, E.; Frydendal, R.; Friebel, D.; Stephens, I. E. L.; Rossmeisl, J.; Chorkendorff, I.; et al. Operando XAS Study of the Surface Oxidation State on a Monolayer IrO_x on RuO_x and Ru Oxide Based Nanoparticles for Oxygen Evolution in Acidic Media. *J. Phys. Chem. B* **2017**, *Submitted*.
- (31) Risch, M.; Stoerzinger, K. A.; Han, B.; Regier, T. Z.; Peak, D.; Sayed, S. Y.; Wei, C.; Xu, Z.; Shao-Horn, Y. Redox Processes of Manganese Oxide in Catalyzing Oxygen Evolution and Reduction: An in Situ Soft X-Ray Absorption Spectroscopy Study. *J. Phys. Chem. C* **2017**, *121*, 17682–17692.
- (32) Enman, L. J.; Stevens, M. B.; Dahan, M. H.; Nellist, M. R.; Toroker, M. C.; Boettcher, S. W. Operando X-Ray Absorption Spectroscopy Shows Iron Oxidation Is Concurrent with Oxygen Evolution in Cobalt–Iron (Oxy)Hydroxide Electrocatalysts. *Angew. Chemie - Int. Ed.* **2018**, *57*, 12840–12844.
- (33) Gul, S.; Ng, J. W. D.; Alonso-Mori, R.; Kern, J.; Sokaras, D.; Anzenberg, E.; Lassalle-Kaiser, B.; Gorlin, Y.; Weng, T.-C.; Zwart, P. H.; et al. Simultaneous Detection of

- Electronic Structure Changes from Two Elements of a Bifunctional Catalyst Using Wavelength-Dispersive X-Ray Emission Spectroscopy and in Situ Electrochemistry. *Phys. Chem. Chem. Phys.* **2015**, *17*, 8901–8912.
- (34) Reikowski, F.; Maroun, F.; Pacheco, I.; Wiegmann, T.; Allongue, P.; Stettner, J.; Magnussen, O. M. Operando Surface X-Ray Diffraction Studies of Structurally Defined Co₃O₄ and CoOOH Thin Films during Oxygen Evolution. *ACS Catal.* **2019**, *9*, 3811–3821.
- (35) Nelson, J.; Misra, S.; Yang, Y.; Jackson, A.; Liu, Y.; Wang, H.; Dai, H.; Andrews, J. C.; Cui, Y.; Toney, M. F. In Operando X-Ray Diffraction and Transmission X-Ray Microscopy of Lithium Sulfur Batteries. *J. Am. Chem. Soc.* **2012**, *134*, 6337–6343.
- (36) Li, Z.; Ganapathy, S.; Xu, Y.; Heringa, J. R.; Zhu, Q.; Chen, W.; Wagemaker, M. Understanding the Electrochemical Formation and Decomposition of Li₂O₂ and LiOH with Operando X-Ray Diffraction. *Chem. Mater.* **2017**, *29*, 1577–1586.
- (37) Deng, J.; Nellist, M. R.; Stevens, M. B.; Dette, C.; Wang, Y.; Boettcher, S. W. Morphology Dynamics of Single-Layered Ni(OH)₂/NiOOH Nanosheets and Subsequent Fe Incorporation Studied by in Situ Electrochemical Atomic Force Microscopy. *Nano Lett.* **2017**, *17*, 6922–6926.
- (38) Khalakhan, I.; Vorokhta, M.; Kúš, P.; Dopita, M.; Václavů, M.; Fiala, R.; Tsud, N.; Skála, T.; Matolín, V. In Situ Probing of Magnetron Sputtered Pt-Ni Alloy Fuel Cell Catalysts during Accelerated Durability Test Using EC-AFM. *Electrochim. Acta* **2017**, *245*, 760–769.
- (39) Khalakhan, I.; Vorokhta, M.; Václavů, M.; Šmíd, B.; Lavková, J.; Matolínová, I.; Fiala, R.; Tsud, N.; Skála, T.; Matolín, V. In-Situ Electrochemical Atomic Force Microscopy Study of Aging of Magnetron Sputtered Pt-Co Nanoalloy Thin Films during Accelerated Degradation Test. *Electrochim. Acta* **2016**, *211*, 52–58.
- (40) Nellist, M. R.; Laskowski, F. A. L.; Qiu, J.; Hajibabaei, H.; Sivula, K.; Hamann, T. W.; Boettcher, S. W. Potential-Sensing Electrochemical Atomic Force Microscopy for in Operando Analysis of Water-Splitting Catalysts and Interfaces. *Nat. Energy* **2018**, *3*, 46–52.

- (41) Beermann, V.; Holtz, M. E.; Padgett, E.; de Araujo, J. F.; Muller, D. A.; Strasser, P. Real-Time Imaging of Activation and Degradation of Carbon Supported Octahedral Pt–Ni Alloy Fuel Cell Catalysts at the Nanoscale Using in Situ Electrochemical Liquid Cell STEM. *Energy Environ. Sci.* **2019**, *12*, 2476–2485.
- (42) Zhu, G.; Prabhudev, S.; Yang, J.; Gabardo, C. M.; Botton, G. A.; Soleymani, L. In Situ Liquid Cell TEM Study of Morphological Evolution and Degradation of Pt – Fe Nanocatalysts During Potential Cycling. *J. Phys. Chem. C* **2014**, *118*, 22111–22119.
- (43) Holtz, M. E.; Yu, Y.; Gunceler, D.; Gao, J.; Sundararaman, R.; Schwarz, K. A.; Arias, T. A.; Abruña, H. D.; Muller, D. A. Nanoscale Imaging of Lithium Ion Distribution during in Situ Operation of Battery Electrode and Electrolyte. *Nano Lett.* **2014**, *14*, 1453–1459.
- (44) Wheatcroft, L.; Özkaya, D.; Cookson, J.; Inkson, B. J. Towards In-Situ TEM for Li-Ion Battery Research. *Energy Procedia* **2018**, *151*, 163–167.
- (45) Yuan, Y.; Amine, K.; Lu, J.; Shahbazian-Yassar, R. Understanding Materials Challenges for Rechargeable Ion Batteries with in Situ Transmission Electron Microscopy. *Nat. Commun.* **2017**, *8*, 15806.
- (46) Wu, F.; Yao, N. Advances in Sealed Liquid Cells for In-Situ TEM Electrochemical Investigation of Lithium-Ion Battery. *Nano Energy* **2015**, *11*, 196–210.
- (47) Claudel, F.; Dubau, L.; Berthomé, G.; Sola-Hernandez, L.; Beauger, C.; Piccolo, L.; Maillard, F. Degradation Mechanisms of Oxygen Evolution Reaction Electrocatalysts: A Combined Identical-Location Transmission Electron Microscopy and X-Ray Photoelectron Spectroscopy Study. *ACS Catal.* **2019**, *9*, 4688–4698.
- (48) Beermann, V.; Holtz, M. E.; Padgett, E.; de Araujo, J. F.; Muller, D. A.; Strasser, P. Real-Time Imaging of Activation and Degradation of Carbon Supported Octahedral Pt–Ni Alloy Fuel Cell Catalysts at the Nanoscale Using in Situ Electrochemical Liquid Cell STEM. *Energy Environ. Sci.* **2019**, *12*, 2476–2485.
- (49) Liu, Q.; Yang, T.; Du, C.; Tang, Y.; Sun, Y.; Jia, P.; Chen, J.; Ye, H.; Shen, T.; Peng, Q.; et al. In Situ Imaging the Oxygen Reduction Reactions of Solid State Na–O₂

- Batteries with CuO Nanowires as the Air Cathode. *Nano Lett.* **2018**, *18*, 3723–3730.
- (50) Gocyla, M.; Kuehl, S.; Shviro, M.; Heyen, H.; Selve, S.; E. Dunin-Borkowski, R.; Heggen, M.; Strasser, P. Shape Stability of Octahedral PtNi Nanocatalysts for Electrochemical Oxygen Reduction Reaction Studied by in Situ Transmission Electron Microscopy. *ACS Nano* **2018**, *12*, 5306–5311.
- (51) Risch, M.; Ringleb, F.; Kohlhoff, M.; Bogdanoff, P.; Chernev, P.; Zaharieva, I.; Dau, H. Water Oxidation by Amorphous Cobalt-Based Oxides : In Situ Tracking of Redox Transitions and Mode of Catalysis. *Energy Environ. Sci.* **2015**, *8*, 661–674.
- (52) Zhang, M.; de Respinis, M.; Frei, H. Time-Resolved Observations of Water Oxidation Intermediates on a Cobalt Oxide Nanoparticle Catalyst. *Nat. Chem.* **2014**, *6*, 362–367.
- (53) Klingan, K.; Ringleb, F.; Zaharieva, I.; Heidkamp, J.; Chernev, P.; Gonzalez-Flores, D.; Risch, M.; Fischer, A.; Dau, H. Water Oxidation by Amorphous Cobalt-Based Oxides: Volume Activity and Proton Transfer to Electrolyte Bases. *ChemSusChem* **2014**, *7*, 1301–1310.
- (54) Friebel, D.; Bajdich, M.; Yeo, B. S.; Louie, M. W.; Miller, D. J.; Sanchez Casalongue, H.; Mbuga, F.; Weng, T.-C.; Nordlund, D.; Sokaras, D.; et al. On the Chemical State of Co Oxide Electrocatalysts during Alkaline Water Splitting. *Phys. Chem. Chem. Phys.* **2013**, *15*, 17460–17467.
- (55) Han, Y.; Axnanda, S.; Crumlin, E. J.; Chang, R.; Mao, B.; Hussain, Z.; Ross, P. N.; Li, Y.; Liu, Z. Observing the Electrochemical Oxidation of Co Metal at the Solid/Liquid Interface Using Ambient Pressure X-Ray Photoelectron Spectroscopy. *J. Phys. Chem. B* **2018**, *122*, 666–671.
- (56) Bergmann, A.; Martinez-Moreno, E.; Teschner, D.; Chernev, P.; Gliech, M.; de Araújo, J. F.; Reier, T.; Dau, H.; Strasser, P. Reversible Amorphization and the Catalytically Active State of Crystalline Co₃O₄ during Oxygen Evolution. *Nat. Commun.* **2015**, *6*, 8625.
- (57) Abidat, I.; Cazayus, E.; Loupiau, L.; Morais, C.; Comminges, C.; Napporn, T. W.; Portehault, D.; Durupthy, O.; Mamede, A.-S.; Chanéac, C.; et al. Co₃O₄/RGO

- Catalysts for Oxygen Electrocatalysis: On the Role of the Oxide/Carbon Interaction. *J. Electrochem. Soc.* **2019**, *166*, H94–H102.
- (58) Suntivich, J.; Gasteiger, H. A.; Yabuuchi, N.; Shao-Horn, Y. Electrocatalytic Measurement Methodology of Oxide Catalysts Using a Thin-Film Rotating Disk Electrode. *J. Electrochem. Soc.* **2010**, *157*, B1263–B1268.
- (59) Chen, Z.; Kronawitter, C. X.; Koel, B. E. Facet-Dependent Activity and Stability of Co₃O₄ Nanocrystals towards the Oxygen Evolution Reaction. *Phys. Chem. Chem. Phys.* **2015**, *17*, 29387–29393.
- (60) Potvin, E.; Brossard, L. Oxygen Evolution on Electrochemically Generated Cobalt Spinel Coating. *J. Appl. Electrochem.* **1955**, *25*, 462–471.
- (61) Kanan, M. W.; Yano, J.; Surendranath, Y.; Dinca, M.; Yachandra, V. K.; Nocera, D. G. Structure and Valency of a Cobalt-Phosphate Water Oxidation Catalyst Determined by in Situ X-Ray Spectroscopy. *J. Am. Chem. Soc.* **2010**, *132*, 13692–13701.
- (62) Surendranath, Y.; Dincă, M.; Stich, T. A.; Britt, R. D.; Stoian, S. A.; McAlpin, J. G.; Nocera, D. G.; Casey, W. H. EPR Evidence for Co(IV) Species Produced During Water Oxidation at Neutral PH. *J. Am. Chem. Soc.* **2010**, *132*, 6882–6883.
- (63) Wang, Z. L.; Yin, J. S.; Jiang, Y. D. EELS Analysis of Cation Valence States and Oxygen Vacancies in Magnetic Oxides. *Micron* **2000**, *31*, 571–580.
- (64) Ewels, P.; Sikora, T.; Serin, V.; Ewels, C. P.; Lajaunie, L. A Complete Overhaul of the Electron Energy-Loss Spectroscopy and X-Ray Absorption Spectroscopy Database: Eelsdb.Eu. *Microsc. Microanal.* **2016**, *22*, 717–724.
- (65) Gupta, S.; Yadav, A.; Bhartiya, S.; Singh, M. K.; Miotello, A.; Sarkar, A.; Patel, N. Co Oxide Nanostructures for Electrocatalytic Water-Oxidation: Effects of Dimensionality and Related Properties. *Nanoscale* **2018**, *10*, 8806–8819.
- (66) Jayashree, R. S.; Kamath, P. V. Electrochemical Synthesis of α -Cobalt Hydroxide. *J. Mater. Chem.* **1999**, *9*, 961–963.
- (67) Kanan, M. W.; Surendranath, Y.; Nocera, D. G. Cobalt-Phosphate Oxygen-Evolving

- Compound. *Chem. Soc. Rev.* **2009**, *38*, 109–114.
- (68) Lutterman, D. A.; Surendranath, Y.; Nocera, D. G. A Self-Healing Oxygen-Evolving Catalyst. *J. Am. Chem. Soc.* **2009**, *131*, 3838–3839.
- (69) Costentin, C.; Nocera, D. G. Self-Healing Catalysis in Water. *Proc. Natl. Acad. Sci.* **2017**, *114*, 13380–13384.
- (70) Surendranath, Y.; Kanan, M. W.; Nocera, D. G. Mechanistic Studies of the Oxygen Evolution Reaction by a Cobalt-Phosphate Catalyst at Neutral PH. *J. Am. Chem. Soc.* **2010**, *132*, 16501–16509.
- (71) Jolivet, J.-P.; Henry, M.; Livage, J. *Metal Oxide Chemistry and Synthesis: From Solution to Solid State*; Wiley: Michigan, 2000.
- (72) Pourbaix, M. J. N.; Zoubov, N. de. *Atlas d'Equilibres Electrochimiques*; Gauthier-Villars: Paris, 1963.
- (73) Wang, H.; Hung, S.; Chen, H.; Chan, T.; Chen, H. M.; Liu, B. In Operando Identification of Geometrical-Site-Dependent Water Oxidation Activity of Spinel Co₃O₄. *J. Am. Chem. Soc.* **2016**, *138*, 36–39.

Chapter III

CHAPTER III: Monitoring nucleation and growth mechanisms *in situ*

3.1. Ending the guessing game

3.2. The case-study of iron oxide

3.2.1. Thermal decomposition

3.2.2. Triggering thermal decomposition *in situ*

3.2.3. Electron dose impact on the nanoparticle growth

3.2.3.1. TEM illumination mode

3.2.3.2. STEM illumination mode

3.3. Concluding remarks

3.4. References

3.1. Ending the guessing game

Ngo and collaborators¹ have called “ending the guessing game” when it comes to tracking the dynamics of nucleation and growth of nanoparticles in solution by using liquid phase TEM. Indeed, as mentioned in previous chapters, among the multiple opportunities provided by the *in situ* liquid TEM, one can find the visualization of intermediate and/or metastable states in the formation and degradation of materials in liquids, that are not accessible by other characterization techniques. The comprehension of such mechanistic pathways permits to tune reaction parameters in order to obtain materials with specific properties.

Along these lines, direct observation of crystallization processes at the nanoscale has been the dream of chemists and physicists interested in multiple geological, biological and synthetic systems. Beyond mere curiosity, the understanding of nucleation and growth of crystals is important in enabling the precise design of complex inorganic and hybrid structures. Classical nucleation models have described the nucleation as the aggregation monomer-by-monomer of nuclei in a supersaturated solution.²⁻⁴ To minimize the surface free energy, the nuclei has to overcome a critical size or else it is re-dissolved

into the medium. Crystals over this critical size then grow to form the final particle. After monomer-by-monomer growth, ageing takes place, often through coalescence or Ostwald ripening. Even if some systems are well described by these models, this formulation has proven to be insufficient for a large variety of materials.^{5,6}

In figure 3.1, de Yoreo and collaborators⁷ summarized some of the alternative intermediate stages that can take place in the nucleation and subsequent growth of crystalline particles. Pre-crystallization routes can include the aggregation of poorly ordered precursors, or even the liquid-liquid phase separation to form solute-rich dense liquid phases where the solid phase can nucleate. Furthermore, insights in growth processes made clear the existence of co-alignment of primary crystalline particles (so-called oriented attachment) or the recrystallization *via* dislocation and grain boundary migrations beyond classical monomer-by-monomer reactions. Deciphering the intermediate stages of such processes has been particularly challenging for colloidal synthesis due to the limitations of the characterization devices to track in real time the mechanisms occurring at the nanoscale within a liquid reaction mixture.

The appearance of *in situ* liquid phase TEM filled the gap that other *in situ* techniques had left.⁸ The combined temporal and spatial resolution has allowed to tackle fundamental questions about the formation, growth and structural modifications of metallic and metal oxide nanostructures,⁹ biological minerals, proteins, macromolecules viruses^{10,11} along with vesicles¹², self-assembling organic systems¹³, and so on.

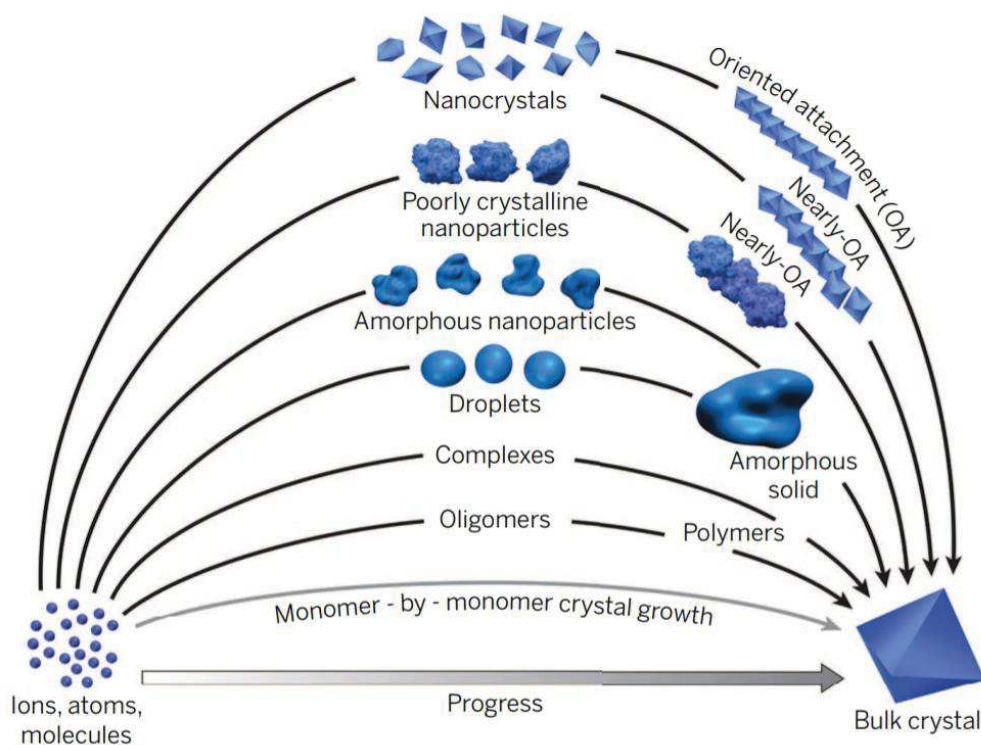


Figure 3.1. Pathways to crystallization by particle attachment. In contrast to monomer-by-monomer addition as envisioned in classical models of crystal growth (gray curve), CPA occurs by the addition of higher-order species ranging from multi-ion complexes to fully formed nanocrystals. (The final faceted bulk crystal is a schematic representation of a final single-crystal state. Taken from⁷

Herein, the case of the crystallization of iron oxide nanoparticles within a thermal decomposition reaction mixture in an organic solvent will be addressed. The pre-nucleation stages as well as the subsequent growth and aging will be studied by *in situ* liquid phase TEM in order to determine if they follow the classical nucleation models. Furthermore, we studied the impact of the electron dose in the final morphology of the nanoparticles. The electron dose will serve as energy source comparable with the thermal energy in a conventional set-up. The analysis of different electron doses will permit to distinguish between reaction and diffusion limited growth mechanisms as a function of the energy input.

3.2 The case-study of iron oxide

Whereas there is an enormous interest in the production and implementation of metal-based nanoparticles for different applications, there are still a lot of questions regarding their nucleation and growth mechanisms. For instance, the parameters governing the

formation of specific morphologies or determining the size distribution. Furthermore, a tailored preparation of monodispersed iron oxide-based nanoparticles is central for their implementation as Magnetic Resonance Imaging contrast agents^{14–16} or for hyperthermia cancer treatment^{17–19}. Thus, it is especially interesting to look into organo-metallic precursors mixtures for thermal decomposition since this method have proved to provide narrow size distribution nanoparticles with handpicked morphologies following rather simple and scalable procedures.^{20–23} Although there is a good understanding of how a high supersaturation regime drives monodispersity in the hot-injection method²⁴, the atom-scale and nanoscale mechanisms governing size selection in the thermal decomposition method are still a black box. The mechanisms of synthesis have been typically deduced by indirect means or *ex situ* stationary analysis²⁵. *Post mortem* analyses have left a gap in the comprehension of the pre-nucleation processes. More recently, *in situ* SAXS studies²⁰ have proven the importance of addressing pre-nucleation processes by demonstrating that the final particle size is directly related such processes, including the formation of inorganic clusters that takes place after precursor decomposition and before particle nucleation. The size and concentration of clusters were shown to be dependent on the precursor-to-surfactant ratio and heating rate, which in turn led to differences in the onset of nucleation and the concentration of nuclei after the nucleation burst step.

In this context, we decided to tackle the lack of information by following in real time the dynamical changes happening within a reaction mixture typically used to synthesize iron nanoparticles by thermal decomposition in organic precursors. Thanks to the ability of the *in situ* liquid phase TEM imaging to enable the observation within a real reaction mixture, the behavior of the precursors and the formation of the reaction products have been monitored.

3.2.1 Thermal decomposition

The synthesis of iron oxide nanoparticles by thermal decomposition flourished after Hyeon²⁶ et al. achieved highly monodispersed nanoparticles batches following a relatively simple and scalable method. In a typical set up, an organometallic precursor, like iron stearate, iron oleate or iron pentacarbonyl, among others, is dispersed in a high boiling point solvent. Surfactants, like oleic acid, are also added to the reaction mixture to fine-tune growth kinetics and customize particle size and distribution²². For activating the nucleation and growth of the nanoparticles, the temperature is raised in a controlled

manner up to the decomposition temperature of the precursors (Figure 3.2). In our case, we used a dispersion of iron stearate with oleic acid and sodium oleate in octadecene as a solvent. Differently from the conventional set-up, the amount of energy mandatory for triggering the decomposition is provided by the electron beam irradiation in the microscope.

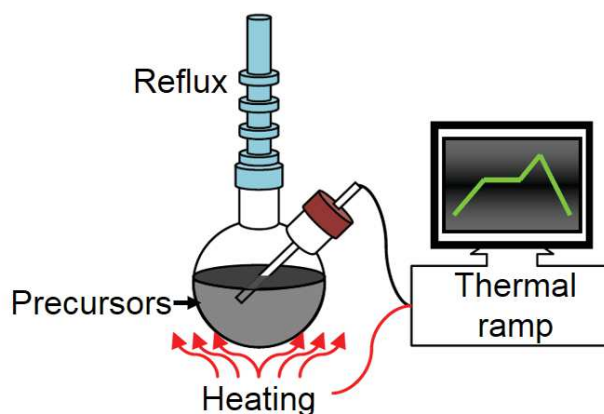


Figure 3.2. Typical thermal decomposition set-up

The reaction mixtures used in these experiments were the ones usually employed for thermal decomposition synthesis of iron oxide Fe_3O_4 nanoparticles in organic media in the group of Prof. Sylvie Begin at IPCMS. First, 2.32 mmol of iron stearate were mixed with 3 mmol of the ligands, oleic acid and sodium oleate, in 15 mL octadecene used as a solvent. The mixture was stirred and heated at 120 °C for 60 min without reflux condenser in order to dissolve the reactants and remove the water residues. A similar procedure was followed using octylether as a solvent. The sample was deposited as described in section 1.2 (figure 3).

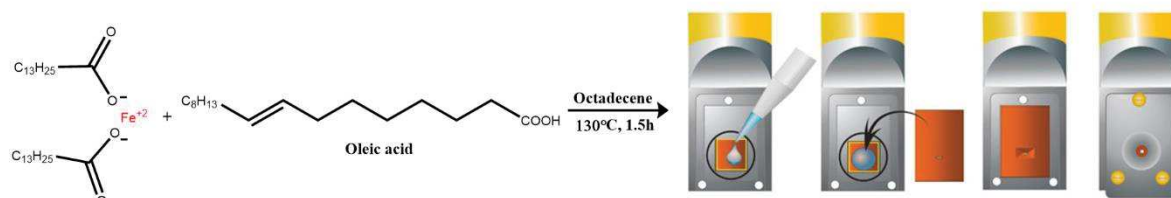


Figure 3.3. Schematic representation of the reaction mixture preparation and loading in the *in situ* set-up.

3.2.2 Triggering the thermal decomposition *in situ*

The formation of the monomer in the typical thermal decomposition or heating up method is driven by the increase in temperature, which activates the formation of intermediary oxygenated species²⁷. Although, the *in situ* set-up we used was not adapted to an increase of the temperature, the reaction was triggered by the electron beam irradiation. The temperature rise of a liquid irradiated by the electron beam depends on the stopping power of the medium and the thickness of the liquid, as described by Schneider et al.²⁸ The temperature rise due to the beam calculated for octadecene is negligible in this case (annex 4).²⁹

Therefore, the *in situ* decomposition does not arise from an increase in the temperature. Hence, we propose two processes that might take place to decompose the precursors, probably simultaneously: 1) electron beam-induced reduction and 2) direct cleavage of the precursor. Figure 3.4 shows an image sequence acquired at the beginning of the *in situ* analysis showing that the nucleation does not occur immediately after the electron irradiation has started ([annex movie M3](#)). Moreover, before nucleation takes place, the presence of globule-like structures in the solution is observed. Figure 3.4a-g illustrates the general behavior of these structures, in particular the yellow circles highlights the fast way in which they move around in the mixture and undergo coalescence and Ostwald-like ripening until they burst to form the nuclei and finally the nanocrystals.

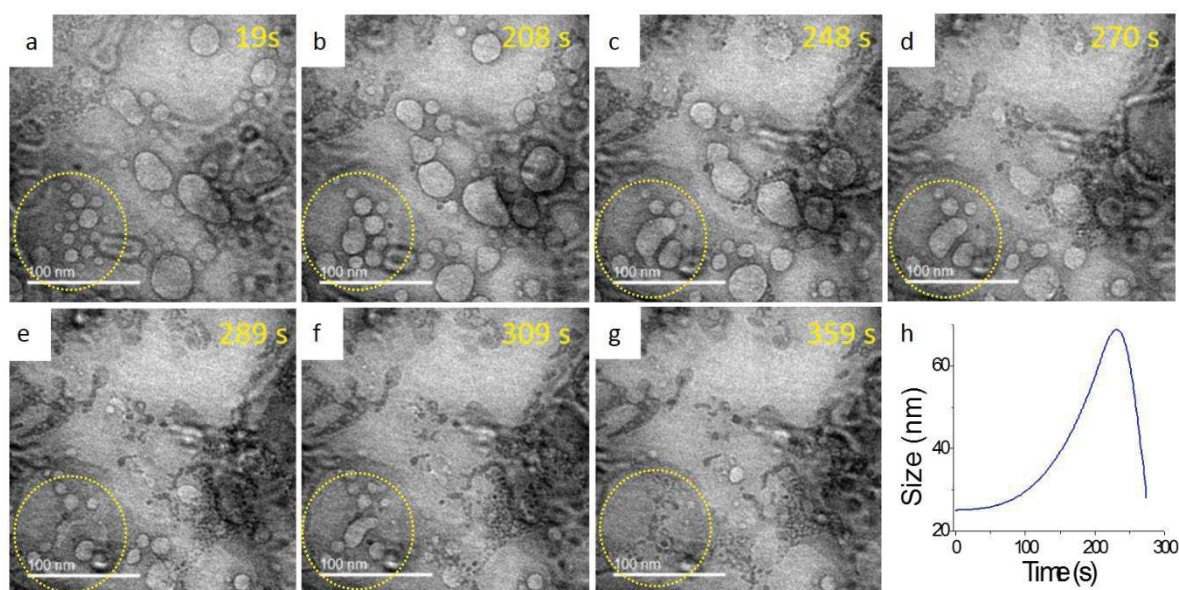


Figure 3.4. (a-g) *In situ* TEM image sequence from the reaction mixture in octadecene. (h) Evolution of the globules diameter within the yellow circle over time.

The presence of these globular structures has not been described before. It is unexpected since the nucleation of iron nanoparticles following the decomposition method is usually described by the LaMer mechanism³. According to this mechanism, monomers coming from the decomposition of precursor molecules would circulate randomly in the medium, react together or with already formed clusters until the nucleation would be triggered when a critical concentration is reached. However, what we observe is that the monomer organizes itself in globular structures before the nucleation takes place.

The observed behavior could be explained by a previously proposed pre-nucleation process, thus adopting a two steps mechanism³⁰. This mechanism suggests that there is an intermediate state between the homogenous solution and the final crystal corresponding to a particle in its incipient growth state. Such a mechanism has been already mentioned for the crystallization of proteins and of some organic molecules³⁰⁻³². Nonetheless, there are few examples of minerals and metallic nanoparticles that are thought to behave similarly.³³ This state would be a mesophase called in some cases “dense liquid”. It would be formed of saturated droplets where the crystal seeds start to grow. This mesophase can be quite stable depending on the medium and the precursors. For instance, Lenhoff et al. have tracked *in situ* using confocal microscopy the crystallization of glucose isomerase within dense droplets³⁴. Later on, the same type of behavior was detected in the nucleation of gold nanoparticles in solution with citrate, where Zaikovski et al.³³ studied the formation of intermediate states. Using *in situ* liquid AFM they observed the presence in an intermediate step of 200-300 nm aggregates of 30-50 nm globules. Moreover, both the globules and their aggregates consisted largely of a liquid or a soft matter since they were easily stretched by moving the cantilever and flattened on a highly oriented pyrolytic graphite (HOPG) support. Additionally, the authors showed using DLS measurements that the hydrodynamic diameter of the globules depended on the citrate/Au ratio, varying from 60 to 125 nm.

Among the very few examples of *in situ* liquid phase TEM in organic media, the formation of nanorods of Pt₃Fe in pentadecene allowed to observe three different crystallization stages: first the monomer aggregation and coalescence forming spherical particles, then a second stage of particles interactions forming a chain with a twisted morphology that ends up by relaxing into the final nanorod in the final stage.³⁵ Although in this case, the pre-nucleation stages were not deeply analyzed, the study showed the

feasibility of *in situ* liquid phase-TEM in an organic solvent using metallorganic precursors. More recently, Smeets et al.³⁶ have shown, by using *in situ* LP-TEM as well, that the presence of a biomimetic matrix, namely polystyrene sulfonate, leads to the formation of amorphous CaCO₃ globules where the crystallization of vaterite takes place only over the surface of the globules and not elsewhere in the solution. This intermediate state might be an example of a two steps pre-nucleation mechanism enabled by the organic medium in the biomimetic matrix. However, *in situ* studies regarding the nucleation and growth of iron oxide nanoparticles like the one from Lassenberger et al.²⁰, using SAXS tracking of thermal decomposition in solution, still fail to confirm the presence of such intermediate state, dense liquid or otherwise. Our observation demonstrates the presence of globule-like structures prior the nucleation burst. This structure seems to be a stable mesophase conforming a vesicular arrangement. Such organization can come from the strong interaction between water molecules coming from the precursors.³⁷

Vesicular mesophase

Figure 3.5 displays a sequence from a typical movie of the pre-nucleation processes. Vesicles ranging from 10 to 20 nm in diameter interact and are formed continuously ([annex movie M4](#)). Their diameter increases up to several tens of nanometers once the globules coalesce. Looking closely to the walls of the globular structures, we can observe some more contrasted, darker areas within. These darker areas can be associated to the nucleation seeds. Once several nuclei appear, the vesicular mesophase dissociates and the resulting grains aggregate to form the nanoparticles. The fact that the nucleation occurs only in the walls of the globule corroborates that it behaves as vesicles, where only the walls contain hydrated precursor that nucleates. The resulting nanoparticles then grow following classical growth mechanisms widely discussed in several review papers.^{3,38-42}

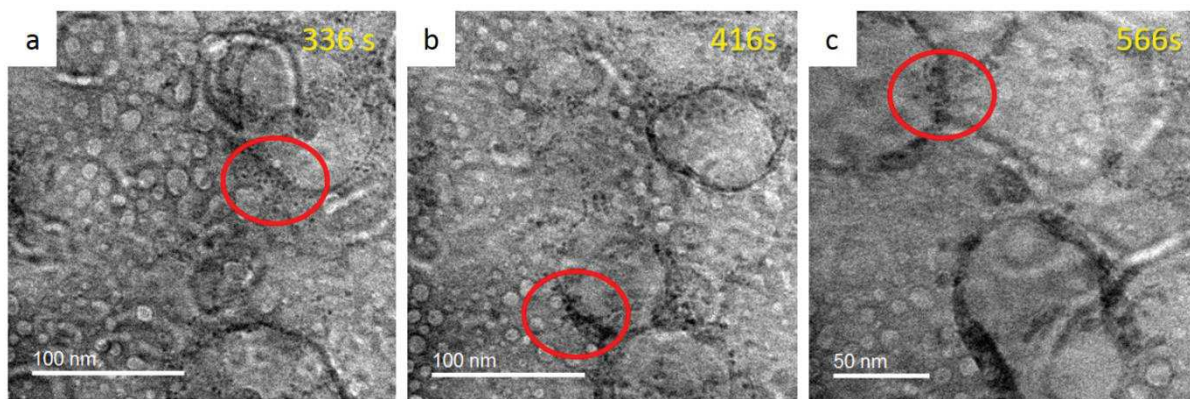


Figure 3.5. a) *In situ* TEM images sequence of the reaction mixture in octadecene. Red circles highlight the walls of the vesicles where the nuclei formed.

In order to verify that this behavior is typical of the pre-nucleation process as implemented in the *ex situ* reaction for a thermal decomposition synthesis, we also tested octylether as a solvent for the same reaction mixture. In contrast with octadecene, octylether has a lower boiling point and has been proven to yield smaller nanoparticles⁴³. In this case, a similar behavior was observed as in the previous reaction mixture, although there were two different types of globular shaped structures, the “vesicular” ones as before and what we have called the “reverse micellar” structures. Those are the focus of the next section. A reverse micelle in this case would be form by the long chained precursor trapping the water available in the media.

Reverse micellar mesophase

In Figure 3.6, the simultaneous presence of vesicular (light contrast) and inverse micellar (dark contrast) structures is observed. The vesicles go through coalescence and their size increases while the reverse micelles coalesce but their size remains almost identical ([annex movie M5](#)).

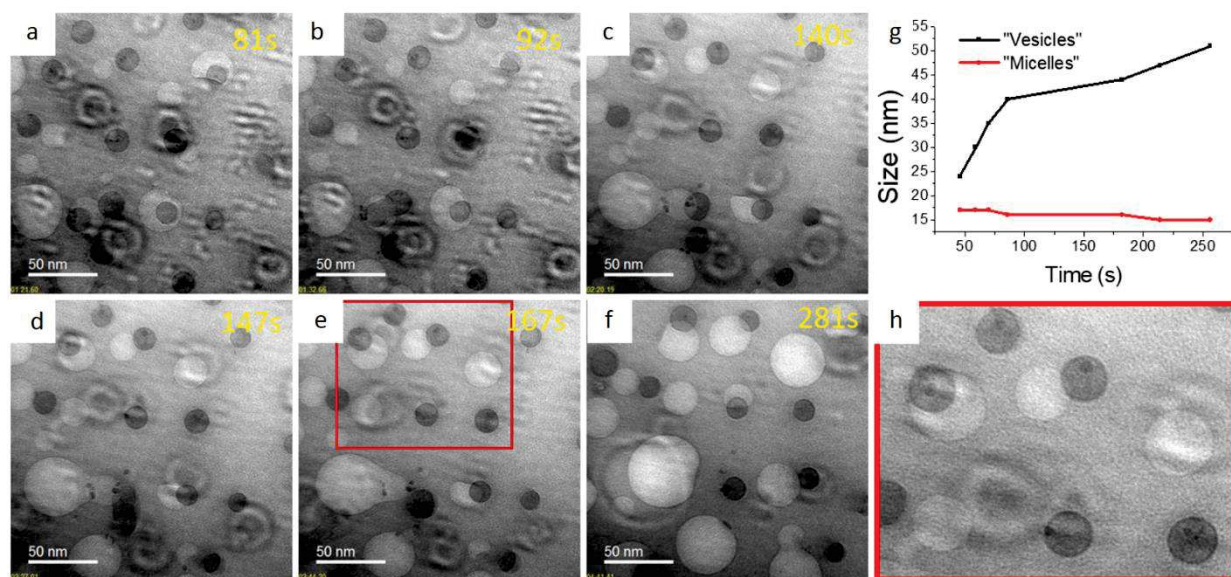


Figure 3.6. a-f) *In situ* TEM images sequence from the reaction mixture in octylether. g) Size evolution of the vesicular-like and micellar-like mesophases. h) Close-up of the nucleation seeds inside the micellar structures.

Even though the reverse micelles undergo a coalescence process, their size remains close to their initial size of around 15 nm. The fact that they combine without changing size implies that the concentration of monomer inside them increases until it reaches the critical point to form a crystal seed. Differently from the vesicles, the nucleation grains formed within the reverse micelles and several crystals seeds can agglomerate inside a single reverse micelle and form a nanoparticle, as shown in figure 3.7 ([annex movie M6](#)). The nuclei from either vesicles or reverse micelles have a diameter around 2 to 3 nm.

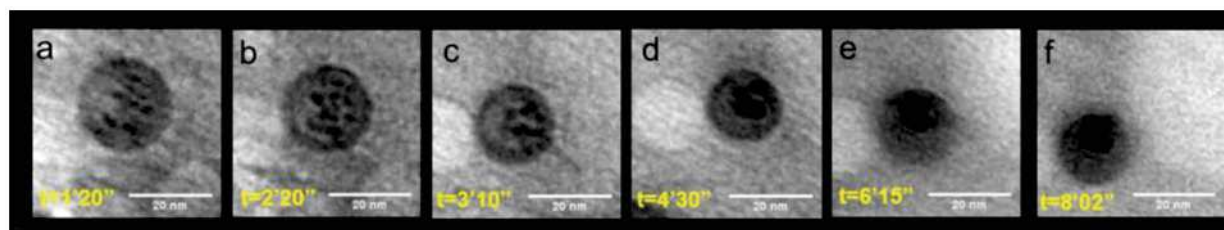


Figure 3.7. *In situ* TEM images sequence showing a close-up of nuclei aggregating within a reverse micelle.

Our findings lead us to think that the walls of the globules with vesicular structure are formed by monomers stabilized by the ligand (in this case oleate chains), most likely as polyiron-oxo clusters²⁷. These clusters remain stable until the supersaturation regime is reached and the nucleation starts. Hence, our observations validate the two steps mechanism, involving an assembly of the precursor previous to the burst, for the nucleation of iron oxide nanoparticles in organic media. Thus, providing unprecedented

information on the microstructure of the reaction media before the particles nucleation, in relation with the localization and the characteristics of the nuclei. The propose mechanism is depicted in Figure 3.8, including two different types of mesophases, “vesicular” and “reverse micellar”, which were observed in different reaction mixtures. In contrast with the hot-injection synthesis where the supersaturation regime can be reached almost instantaneously, by the thermal decomposition method, the precursors and/or monomers tend to organize themselves in a mesophase until the supersaturation regime is reached. The presence of different pre-nucleation arrangements depending on the solvent might be due to the hydration level of the solvents.

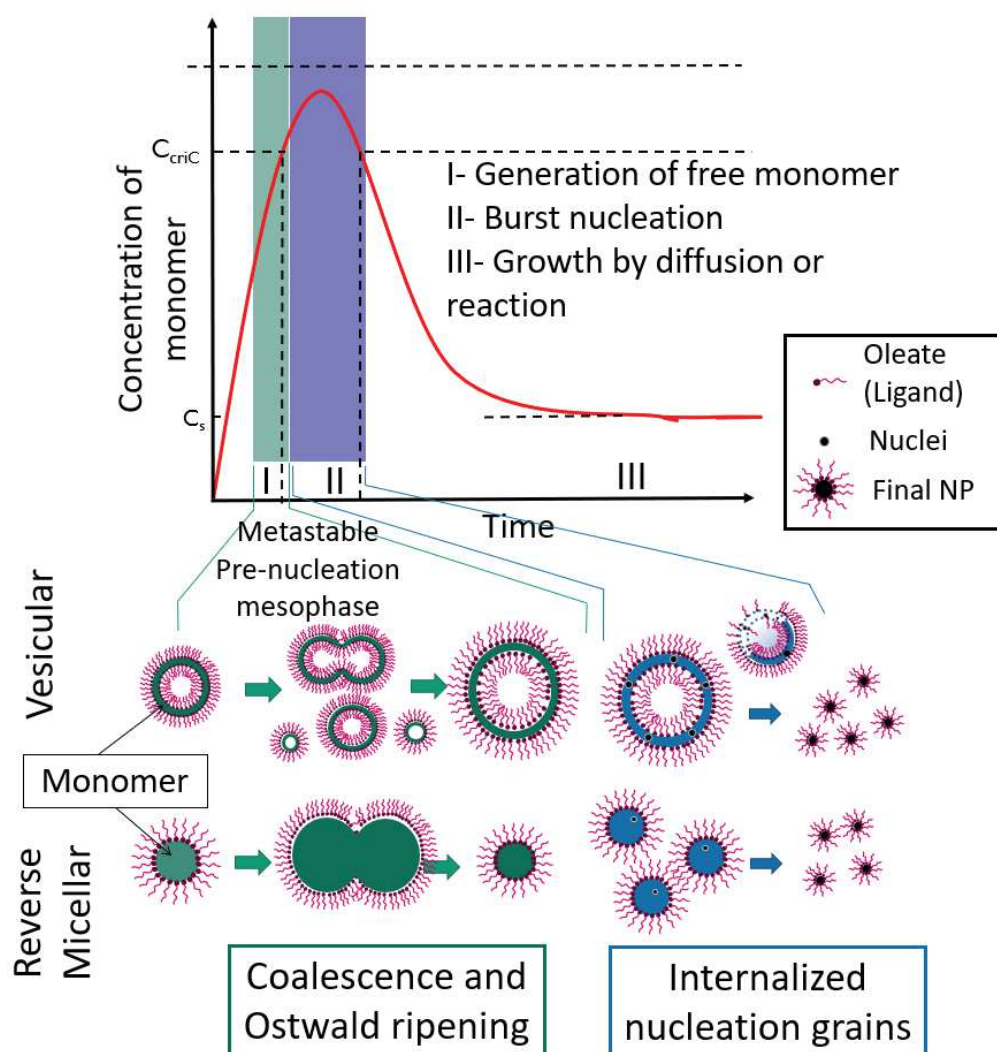


Figure 3.8. Schematic representation of the pre-nucleation and nucleation processes. In the initial pre-nucleation phase, the presence of metastable vesicular and micellar structures was observed in our experiments depending on the nature of the solvent. Such structures can interact between them and later on enable the burst of nucleation of the iron oxide crystal seeds.

To rule out any artifact that could arise from the solvents in the liquid cell or their interaction with the electron beam, we also evaluated under the microscope a cell filled up only with octylether. As expected, octylether by itself does not form any globular-like structure ([annex movie M7](#)).

Finally, after stopping the synthesis by ceasing the irradiation, the product of the reaction was analyzed by HR-TEM. Iron oxide nanoparticles of around 7 nm were obtained. The interplanar distances highlighted in figure 3.9b correspond to Fe_3O_4 (JCPDS Card No. 19-629).

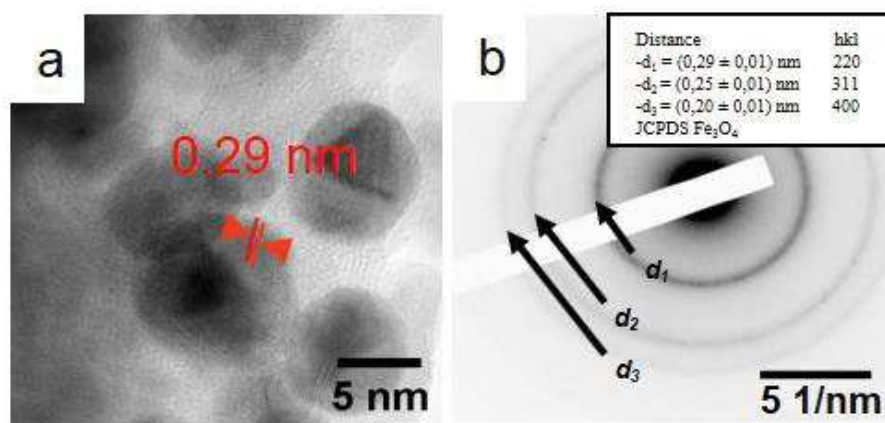


Figure 3.9. a) *Post mortem* HR-TEM images of iron-based nanoparticles produced in the *in situ* synthesis. b) Diffraction pattern of Fe_3O_4 nanoparticles in a (inset lattice parameters)

3.2.3 Electron dose impact in the nanoparticle growth

Once the "dense liquid" reaches a critical size (critical radius), the globules (inverted micelles and vesicles) "explode" by releasing the crystal nuclei. After this nucleation step, we followed the growth of the nuclei into nanoparticles of iron oxide. It has already been observed that the electron dose has a significant influence on the kinetics of formation and the morphology of nanoparticles grown *in situ.*, with e.g Au, Ag, Pt and mixed oxides in aqueous solutions.^{39,40,44,45} The electron dose provides a direct control of the growth rate.

As mentioned in section 1.4.3 the electron dose can greatly influence the observed reaction. Hence, while in previous chapters we have looked for means to minimize this influence, in the case of the crystallization triggered by the beam, the electron dose can be used to impact the amount of energy in the final product. Thus, in this section will be

described the differences induced in the final nanoparticles as a function of the electron dose.

3.2.3.1 TEM illumination mode

High electron dose ($d = 9364 \text{ e}^- / \text{nm}^2\text{s}$)

When using the parallel TEM mode, the dose of electrons can be large since the liquid is irradiated continuously. The beam current used is 150 pA, which corresponds to an electron dose of $9364 \text{ e}^- / \text{nm}^2\text{s}$. Under this electron dose, the growth of the nanoparticles is very fast. In fact, the nucleation step takes place in less than 10 s as evidenced in figure 3.10a ([annex movie M8](#)). Rapidly the nanoparticles grow until reaching a critical radius. This critical radius is described by the LaMer model.³ Above that critical radius, the growth continues and aging processes takes place. Finally, the second plateau corresponds to the size at which the growth stops and the size is stabilized (figure 3.10b). The final stop of the growth can be attributed to the depletion of monomers within the reactional mixture. It should be noted that with this amount of energy, neither the morphology nor the size dispersion can be controlled.

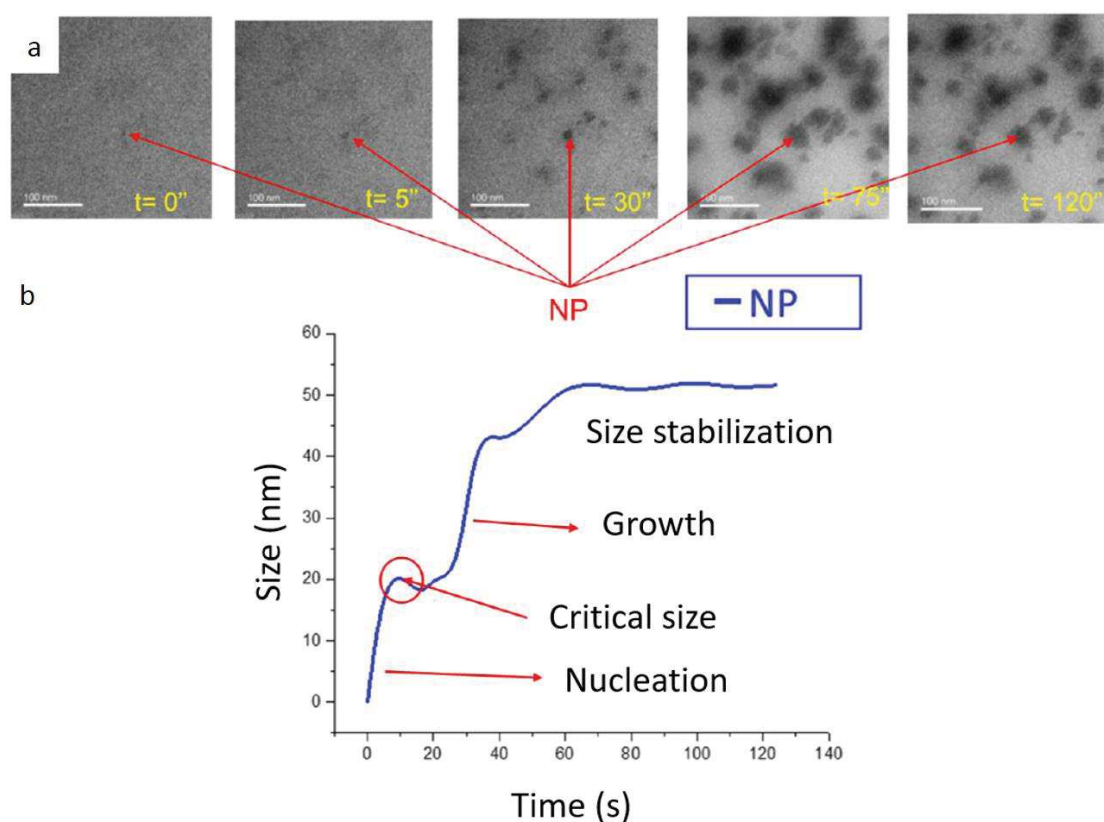


Figure 3.10. a) Sequence from an *in situ* recording under an electron dose of $9364 \text{ e}^- / \text{nm}^2\text{s}$. b) Evolution of the particle size (red arrow) upon time. It is possible to determine the

different growth regimes, from the nucleation burst until reaching the critical size after which the growth continues until reaching the final size of around 50 nm. The measurements were done manually over the particle pointed by the red arrow.

Medium electron dose ($d = 6870 \text{ e}^- / \text{nm}^2\text{s}$)

In the second growth study, the electron dose was decreased to a value of $6870 \text{ e}^- / \text{nm}^2\text{s}$, almost a third less than previously. Under this irradiation conditions, it is possible to evidence the increase in the nucleation duration ([annex movie M9](#)). Again, the energy input produces growth as described by the LaMer's model. Indeed in figure 3.11, starting from a globule (a vesicle) we can follow in real time the formation of monomers that coalesce to form larger particles until reaching the critical radius.

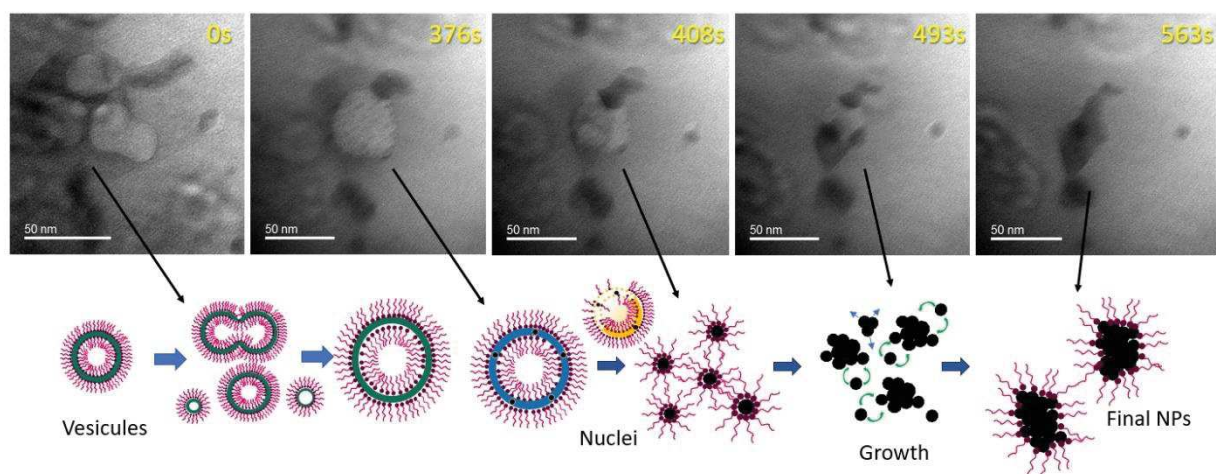


Figure 3.11. *In situ* sequence under an electron dose of $6870 \text{ e}^- / \text{nm}^2\text{s}$. Schematic representation of the nucleation within a vesicle. The nucleation takes place over the surface of the vesicle until the nuclei aggregate to form the nanoparticles.

Low electron dose ($d=2500 \text{ e}^- / \text{nm}^2\text{s}$)

In this case, the electron dose used was three times lower than previously. This lower energy condition allowed the observation of the Ostwald ripening described in the classical growth model. In figure 3.12, the evolution of two nanoparticles as a function of time is compared ([annex movie M10](#)). The curves representing this evolution show three regimes. In the first period the two nanoparticles (NP1 and NP2) see their sizes increase, however the NP2 one growth faster than the NP1 one. The second period shows a relative stability while in the last stage the NP2 particle size rapidly increases benefiting from the NP1 nanoparticle volume decrease. This observation is in agreement with the classical Ostwald ripening mechanism caused by the change in solubility of nanoparticles dependent on their size. Due to the high surface energy of smaller

particles, they show a high solubility and re-dissolve within the solution, which allow in turn the larger particles to grow even more.²⁵

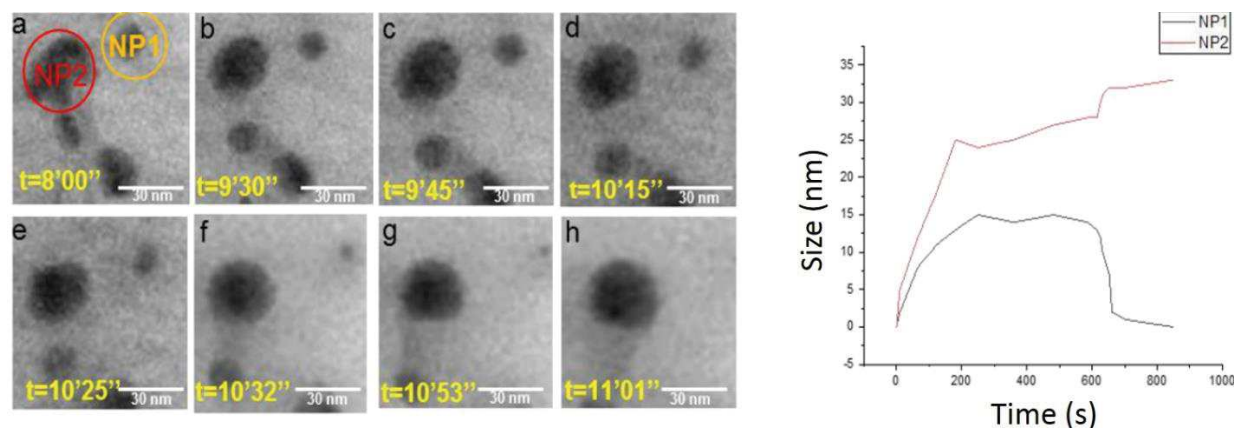


Figure 3.12. a-h) Sequence from a video *in situ* under an electron dose of $2500 \text{ e}^- / \text{nm}^2 \cdot \text{s}$. Evolution of NP 1 (black) and NP2 (red) particle size upon time measured manually. Only the nuclei that reaches the critical size continues growing, contrary to the nucleus under that size that re-dissolves in the solution, to feed the growth of other surrounding particles.

3.2.3.2 STEM illumination mode

As mentioned in section 1.4, the STEM mode in principle allows for a better control of the electron dose. Furthermore, it is characterized by a better theoretical spatial resolution for materials close to the beam entrance.⁴⁶ However, when using the STEM mode directly, even after two hours of irradiation, the reaction does not take place. This is due to the fact that the energy provided by the probe during the sweep is rapidly dissipated and therefore insufficient to exceed the threshold of the thermal decomposition reaction of iron stearate. Thusly, to trigger the reaction, we use the spot mode, meaning that the beam is blocked in a single position without scanning. This mode allows concentrating the current in the chosen location. As so, the beam is placed for a few seconds in the center of the observation area. Thanks to this highly concentrated small area beam, it is possible to trigger the reaction.

Since, the beam current can be better controlled, the STEM mode permitted a clearer understanding of the impact of the amount of energy input. In figure 3.13, when the electron dose was $900 \text{ e}^- / \text{nm}^2 \cdot \text{s}$ the nanoparticle grew into a polyhedral morphology ([annex movie M11](#)). In contrast, at a lower dose of $230 \text{ e}^- / \text{nm}^2 \cdot \text{s}$ anisotropic growth was favored ([annex movie M12](#)). Moreover, in contrast with the TEM mode, in the STEM mode only the region observed is illuminated and hence the nucleation and growth only took place in the region of interest. This means that when the reaction starts at the

chosen location, only the nuclei created in this place grows. The morphology appears also to be dictated by the electron dose.

Furthermore, this study shows that a large energy supply (whether by the electron beam or the thermal energy) generates larger amounts of monomer, so that the growth is diffusion-limited, generally with spherical morphology. Whereas at a low energy dose, the growth is rather reaction limited, hence the formation of anisotropic nanoparticles is favored. The fact that the structure can be tailored as a function of the energy input, without the addition of capping agents, opens exciting paths in the development of nanoparticles with specific morphologies.

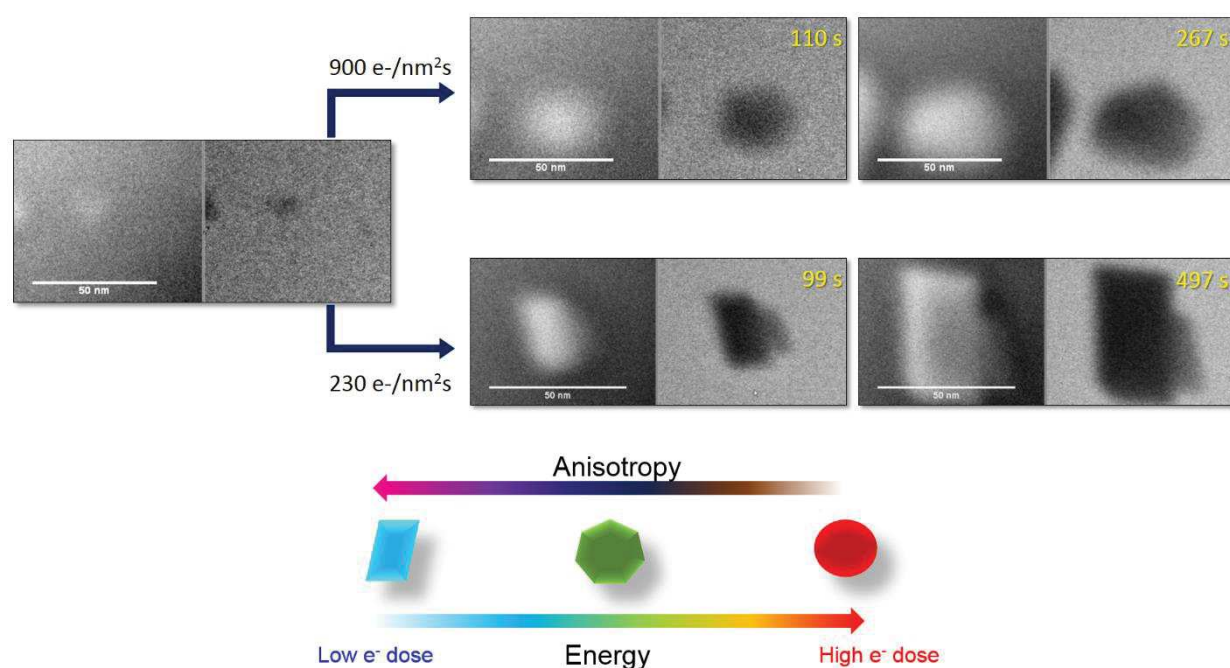


Figure 3.13. *In situ* TEM observation and crystallization: 900 e-/ nm²s (top) and 230 e-/ nm²s (bottom). Effect of the amount of energy provided on the growth of nanoparticles. At higher electron dose the nanoparticles tend to be polyhedral and spherical. On the other hand, at lower electron dose certain faces are favored.

Further analysis evaluating the hydration degree in the media, the type of precursor employed and the presence of multiple metallic centers should be pursued. Future work would help to understand what is the impact of the two pre-nucleation structures (vesicles and reverse micelles) on the size distribution and determining what is driving the formation of only one structure or of the two structures depending on the solvent.

3.3. Conclusion

We have succeeded in synthesizing iron oxide nanoparticles from a thermal decomposition reaction mixture within the *in situ* liquid phase TEM set-up. The direct observation of the formation pathways has shown that the nucleation follows a non-classical route. Globular-like pre-nucleation assemblies of the molecular precursor were observed. These pre-nucleation globules are vesicles and/or inverse micelles where the nucleation takes place. Two different behaviors were observed depending on the pre-nucleation structure: On one hand, after nucleation burst, the vesicles disintegrate and the nuclei aggregate to form the nanoparticles grains. On the other hand, the nuclei formed within the inverse micelles aggregate and ages within them.

Additionally, we have shown the impact of the electron dose on the growth of the nanoparticles. We have directly observed that at high electron dose the morphology of the nanoparticles tends to be spherical or polyhedral (isotropic). Oppositely, at lower electron doses, anisotropic structures are formed.

From a more general point of view, these striking results confirm the strong benefit of *in situ* transmission electron microscopy methods for the elucidation of dynamical processes in the incipient steps of nucleation and growth in the synthesis of inorganic and even hybrids structures. Furthermore, it opens the way towards a better control of nanoparticles properties by a full understanding of their nucleation and growth mechanisms involving kinetically unfavored paths.

3.4. References

- (1) Ngo, T.; Yang, H. Toward Ending the Guessing Game: Study of the Formation of Nanostructures Using *in situ* Liquid Transmission Electron Microscopy. *J. Phys. Chem. Lett.* **2015**, *6*, 5051–5061.
- (2) Chu, D. B. K.; Owen, J. S.; Peters, B. Nucleation and Growth Kinetics from LaMer Burst Data. *J. Phys. Chem. A* **2017**, *121*, 7511–7517.
- (3) LaMer, V. K.; Dinigar, R. H. Theory, Production and Mechanism of Formation of Monodispersed Hydrosols. *J. Am. Chem. Soc.* **1950**, *72*, 4847.
- (4) Mehranpour, H.; Askari, M.; Sasani Ghamsari, M. LaMer Theory Approach to Study the Nucleation and Growth of Sol-Gel Derived TiO₂ Nanoparticles. In *I.R.*

- Iran*; 2012; pp 1710–1712.
- (5) Thanh, N. T. K.; Maclean, N.; Mahiddine, S. Mechanisms of Nucleation and Growth of Nanoparticles in Solution. *Chemical Reviews*. 2014, pp 7610–7630.
 - (6) Lee, J.; Yang, J.; Kwon, S. G.; Hyeon, T. Nonclassical Nucleation and Growth of Inorganic Nanoparticles. *Nat. Rev. Mater.* **2016**, *1*.
 - (7) De Yoreo, J. J.; Gilbert, P. U. P. A.; Sommerdijk, N. A. J. M.; Penn, R. L.; Whitelam, S.; Joester, D.; Zhang, H.; Rimer, J. D.; Navrotsky, A.; Banfield, J. F.; et al. Crystallization by Particle Attachment in Synthetic, Biogenic, and Geologic Environments. *Science (80-.)*. **2015**, *349*.
 - (8) De Yoreo, J. J. In-Situ Liquid Phase TEM Observations of Nucleation and Growth Processes. *Prog. Cryst. Growth Charact. Mater.* **2016**, *62*, 69–88.
 - (9) Liu, Y.; Tai, K.; Dillon, S. J. Growth Kinetics and Morphological Evolution of ZnO Precipitated from Solution. *Chem. Mater.* **2013**, *25*, 2927–2933.
 - (10) He, K.; Shokuhfar, T.; Shahbazian-Yassar, R. Imaging of Soft Materials Using in Situ Liquid-Cell Transmission Electron Microscopy. *Journal of Physics Condensed Matter*. 2019.
 - (11) Cameron Varano, A.; Rahimi, A.; Dukes, M. J.; Poelzing, S.; M. McDonald, S.; Kelly, D. F. Visualizing Virus Particle Mobility in Liquid at the Nanoscale. *Chem. Commun.* **2015**, *51*, 16176–16179.
 - (12) Ianiro, A.; Wu, H.; van Rijt, M. M. J.; Vena, M. P.; Keizer, A. D. A.; Esteves, A. C. C.; Tuinier, R.; Friedrich, H.; Sommerdijk, N. A. J. M.; Patterson, J. P. Liquid–Liquid Phase Separation during Amphiphilic Self-Assembly. *Nat. Chem.* **2019**, *11*, 320–328.
 - (13) Touve, M. A.; Figg, C. A.; Wright, D. B.; Park, C.; Cantlon, J.; Sumerlin, B. S.; Gianneschi, N. C. Polymerization-Induced Self-Assembly of Micelles Observed by Liquid Cell Transmission Electron Microscopy. *ACS Cent. Sci.* **2018**, *4*, 543–547.
 - (14) Lartigue, L.; Hugounenq, P.; Alloyeau, D.; Clarke, S. P.; Lévy, M.; Bacri, J. C.; Bazzi, R.; Brougham, D. F.; Wilhelm, C.; Gazeau, F. Cooperative Organization in Iron Oxide Multi-Core Nanoparticles Potentiates Their Efficiency as Heating Mediators and MRI Contrast Agents. *ACS Nano* **2012**, *6*, 10935–10949.
 - (15) Boni, A.; Basini, A. M.; Capolupo, L.; Innocenti, C.; Corti, M.; Cobianchi, M.;

- Orsini, F.; Guerrini, A.; Sangregorio, C.; Lascialfari, A. Optimized PAMAM Coated Magnetic Nanoparticles for Simultaneous Hyperthermic Treatment and Contrast Enhanced MRI Diagnosis. *RSC Adv.* **2017**, *7*, 44104–44111.
- (16) Li, L.; Jiang, W.; Luo, K.; Song, H.; Lan, F.; Wu, Y.; Gu, Z. Superparamagnetic Iron Oxide Nanoparticles as MRI Contrast Agents for Non-Invasive Stem Cell Labeling and Tracking. *Theranostics*. 2013, pp 595–615.
- (17) Espinosa, A.; Di Corato, R.; Kolosnjaj-Tabi, J.; Flaud, P.; Pellegrino, T.; Wilhelm, C. Duality of Iron Oxide Nanoparticles in Cancer Therapy: Amplification of Heating Efficiency by Magnetic Hyperthermia and Photothermal Bimodal Treatment. *ACS Nano* **2016**, *10*, 2436–2446.
- (18) Bañobre-López, M.; Teijeiro, A.; Rivas, J. Magnetic Nanoparticle-Based Hyperthermia for Cancer Treatment. *Reports Pract. Oncol. Radiother.* **2013**, *18*, 397–400.
- (19) Martinez-Boubeta, C.; Simeonidis, K.; Makridis, A.; Angelakeris, M.; Iglesias, O.; Guardia, P.; Cabot, A.; Yedra, L.; Estradé, S.; Peiró, F.; et al. Learning from Nature to Improve the Heat Generation of Iron-Oxide Nanoparticles for Magnetic Hyperthermia Applications. *Sci. Rep.* **2013**, *3*, 1–8.
- (20) Lassenberger, A.; Grünwald, T. A.; Van Oostrum, P. D. J.; Rennhofer, H.; Amenitsch, H.; Zirbs, R.; Lichtenegger, H. C.; Reimhult, E. Monodisperse Iron Oxide Nanoparticles by Thermal Decomposition: Elucidating Particle Formation by Second-Resolved in Situ Small-Angle X-Ray Scattering. *Chem. Mater.* **2017**, *29*, 4511–4522.
- (21) Park, J.; An, K.; Hwang, Y.; Park, J. E. G.; Noh, H. J.; Kim, J. Y.; Park, J. H.; Hwang, N. M.; Hyeon, T. Ultra-Large-Scale Syntheses of Monodisperse Nanocrystals. *Nat. Mater.* **2004**, *3*, 891–895.
- (22) Hufschmid, R.; Arami, H.; Ferguson, R. M.; Gonzales, M.; Teeman, E.; Brush, L. N.; Browning, N. D.; Krishnan, K. M. Synthesis of Phase-Pure and Monodisperse Iron Oxide Nanoparticles by Thermal Decomposition. *Nanoscale* **2015**, *7*, 11142–11154.
- (23) Baaziz, W.; Pichon, B. P.; Fleutot, S.; Liu, Y.; Lefevre, C.; Greneche, J. M.; Toumi, M.; Mhiri, T.; Begin-Colin, S. Magnetic Iron Oxide Nanoparticles: Reproducible Tuning of the Size and Nanosized-Dependent Composition, Defects, and Spin

- Canting. *J. Phys. Chem. C* **2014**, *118*, 3795–3810.
- (24) Kwon, S. G.; Hyeon, T. Formation Mechanisms of Uniform Nanocrystals via Hot-Injection and Heat-Up Methods. *Small* **2011**, *7*, 2685–2702.
- (25) Thanh, N. T. K.; Maclean, N.; Mahiddine, S. Mechanisms of Nucleation and Growth of Nanoparticles in Solution. *Chem. Rev.* **2014**, *114*, 7610–7630.
- (26) Park, J.; An, K.; Hwang, Y.; Park, J.-G.; Noh, H.-J.; Kim, J.-Y.; Park, J.-H.; Hwang, N.-M.; Hyeon, T. Ultra-Large-Scale Syntheses of Monodisperse Nanocrystals. *Nat. Mater.* **2004**, *3*, 891–895.
- (27) Soon, G. K.; Piao, Y.; Park, J.; Angappane, S.; Jo, Y.; Hwang, N. M.; Park, J. G.; Hyeon, T. Kinetics of Monodisperse Iron Oxide Nanocrystal Formation by “Heating-up” Process. *J. Am. Chem. Soc.* **2007**, *129*, 12571–12584.
- (28) Schneider, N. M.; Norton, M. M.; Mendel, B. J.; Grogan, J. M.; Frances, M.; Bau, H. H. Electron - Water Interactions and Implications for Liquid Cell Electron Microscopy – Supporting Information. *J. Phys. Chem. C* **2014**, *118*, 22373–22382.
- (29) Schneider, N. M. Electron Beam Effects in Liquid Cell TEM and STEM. In *liquid cell electron microscopy*; 2017; pp 140–163.
- (30) Vekilov, P. G. Nucleation. *Cryst. Growth Des.* **2010**, *10*, 5007–5019.
- (31) Vekilov, P. G. Dense Liquid Precursor for the Nucleation of Ordered Solid Phases from Solution. *Cryst. Growth Des.* **2004**, *4*, 671–685.
- (32) Sauter, A.; Roosen-Runge, F.; Zhang, F.; Lotze, G.; Jacobs, R. M. J.; Schreiber, F. Real-Time Observation of Nonclassical Protein Crystallization Kinetics. *J. Am. Chem. Soc.* **2015**, *137*, 1485–1491.
- (33) Mikhlin, Y.; Karacharov, A.; Likhatski, M.; Podlipskaya, T.; Zubavichus, Y.; Veligzhanin, A.; Zaikovski, V. Submicrometer Intermediates in the Citrate Synthesis of Gold Nanoparticles: New Insights into the Nucleation and Crystal Growth Mechanisms. *J Colloid Interface Sci* **2011**, *362*, 330–336.
- (34) Vivarès, D.; Kaler, E. W.; Lenhoff, A. M. Quantitative Imaging by Confocal Scanning Fluorescence Microscopy of Protein Crystallization via Liquid-Liquid Phase Separation. *Acta Crystallogr. Sect. D Biol. Crystallogr.* **2005**, *61*, 819–825.
- (35) Liao, H. G.; Cui, L.; Whitlam, S.; Zheng, H. Real-Time Imaging of Pt₃Fe Nanorod

- Growth in Solution. *Science (80-.)*. **2012**, *336*, 1011–1014.
- (36) Smeets, P. J. M.; Cho, K. R.; Kempen, R. G. E.; Sommerdijk, N. A. J. M.; De Yoreo, J. J. Calcium Carbonate Nucleation Driven by Ion Binding in a Biomimetic Matrix Revealed by in Situ Electron Microscopy. *Nat. Mater.* **2015**, *14*, 394–399.
- (37) Cotin, G.; Kiefer, C.; Perton, F.; Boero, M.; Özdamar, B.; Bouzid, A.; Ori, G.; Massobrio, C.; Begin, D.; Pichon, B.; et al. Evaluating the Critical Roles of Precursor Nature and Water Content When Tailoring Magnetic Nanoparticles for Specific Applications. *ACS Appl. Nano Mater.* **2018**, *1*, 4306–4316.
- (38) Baumgartner, J.; Dey, A.; Bomans, P. H. H.; Coadou, C. Le; Fratzl, P.; Sommerdijk, N. A. J. M.; Faivre, D. Nucleation and Growth of Magnetite from Solution. *Nat. Mater.* **2013**, *12*, 310–314.
- (39) Woehl, T. J.; Evans, J. E.; Arslan, I.; Ristenpart, W. D.; Browning, N. D. Direct in Situ Determination of the Mechanisms Controlling Nanoparticle Nucleation and Growth. *ACS Nano* **2012**, *6*, 8599–8610.
- (40) Alloyeau, D.; Dachraoui, W.; Javed, Y.; Belkahla, H.; Wang, G.; Lecoq, H.; Ammar, S.; Ersen, O.; Wisnet, A.; Gazeau, F.; et al. Unravelling Kinetic and Thermodynamic Effects on the Growth of Gold Nanoplates by Liquid Transmission Electron Microscopy. *Nano Letters*. 2015, pp 2574–2581.
- (41) Dinh, C. T.; Nguyen, T. D.; Kleitz, F.; Do, T. O. *Shape-Controlled Synthesis of Metal Oxide Nanocrystals*; Stanford, P., Ed.; Singapore, 2012; Vol. 3.
- (42) Mehranpour, H.; Askari, M.; Ghamsari, M. S.; Farzalibeik, H. Study on the Phase Transformation Kinetics of Sol-Gel Drived TiO Nanoparticles. *J. Nanomater.* **2010**, *2010*, 1–5.
- (43) Demortière, a; Panissod, P.; Pichon, B. P.; Pourroy, G.; Guillon, D.; Donnio, B.; Bégin-Colin, S. Size-Dependent Properties of Magnetic Iron Oxide Nanocrystals. *Nanoscale* **2011**, *3*, 225–232.
- (44) Ge, M.; Lu, M.; Chu, Y.; Xin, H. Anomalous Growth Rate of Ag Nanocrystals Revealed by in Situ STEM. *Sci. Rep.* **2017**, *7*.
- (45) Beermann, V.; Holtz, M. E.; Padgett, E.; de Araujo, J. F.; Muller, D. A.; Strasser, P. Real-Time Imaging of Activation and Degradation of Carbon Supported Octahedral Pt–Ni Alloy Fuel Cell Catalysts at the Nanoscale Using in Situ

Electrochemical Liquid Cell STEM. *Energy Environ. Sci.* **2019**, *12*, 2476–2485.

- (46) de Jonge, N. Theory of the Spatial Resolution of (Scanning) Transmission Electron Microscopy in Liquid Water or Ice Layers. *Ultramicroscopy* **2018**, *187*, 113–125.

Chapter IV

CHAPTER IV: Biomineralization processes *in situ*

4.1 Non-classical nucleation in biological systems

4.2 Calcium phosphate

4.2.1 *Ex situ* synthesis

4.2.2 Cryo-electron microscopy

4.2.3 *In situ* synthesis methodology

4.2.3.1 Flow mode results

4.2.3.2 Static mode results

4.3 Calcite

4.3.1 CaCO₃ *ex situ* synthesis

4.3.2 Synthesis on a copper grid: control

4.3.3 *In situ* synthesis methodology

4.3.3.1 Synthesis without additives

4.3.3.2 Evaluation of CaCO₃ crystals formed in the presence of L-aspartic acid

4.3.3.3 Evaluation of CaCO₃ crystals formed in the presence of glycine

4.4. Concluding remarks

4.5. References

4.1. Non-classical nucleation in biological systems

Biomimetic minerals are widely studied and used for pharmaceutical purposes, tissue regeneration, and understanding environmental processes, among other areas.¹ A better understanding of how mineralization occurs in a biological environment could allow the production of bio-inspired materials with special properties and thus ensure safe and reliable production.² Crystallization is a phase transition in which the material changes

from a more disordered liquid, gaseous or amorphous solid state to a more orderly solid state. Insights in the crystallization of minerals in biological matrices is key in the comprehension of the formation of bones (and diseases), shells and geological deposits. This is particularly important for the comprehension of the apparition of hierarchical architectures present in a variety of natural systems as shown in figure 4.1.

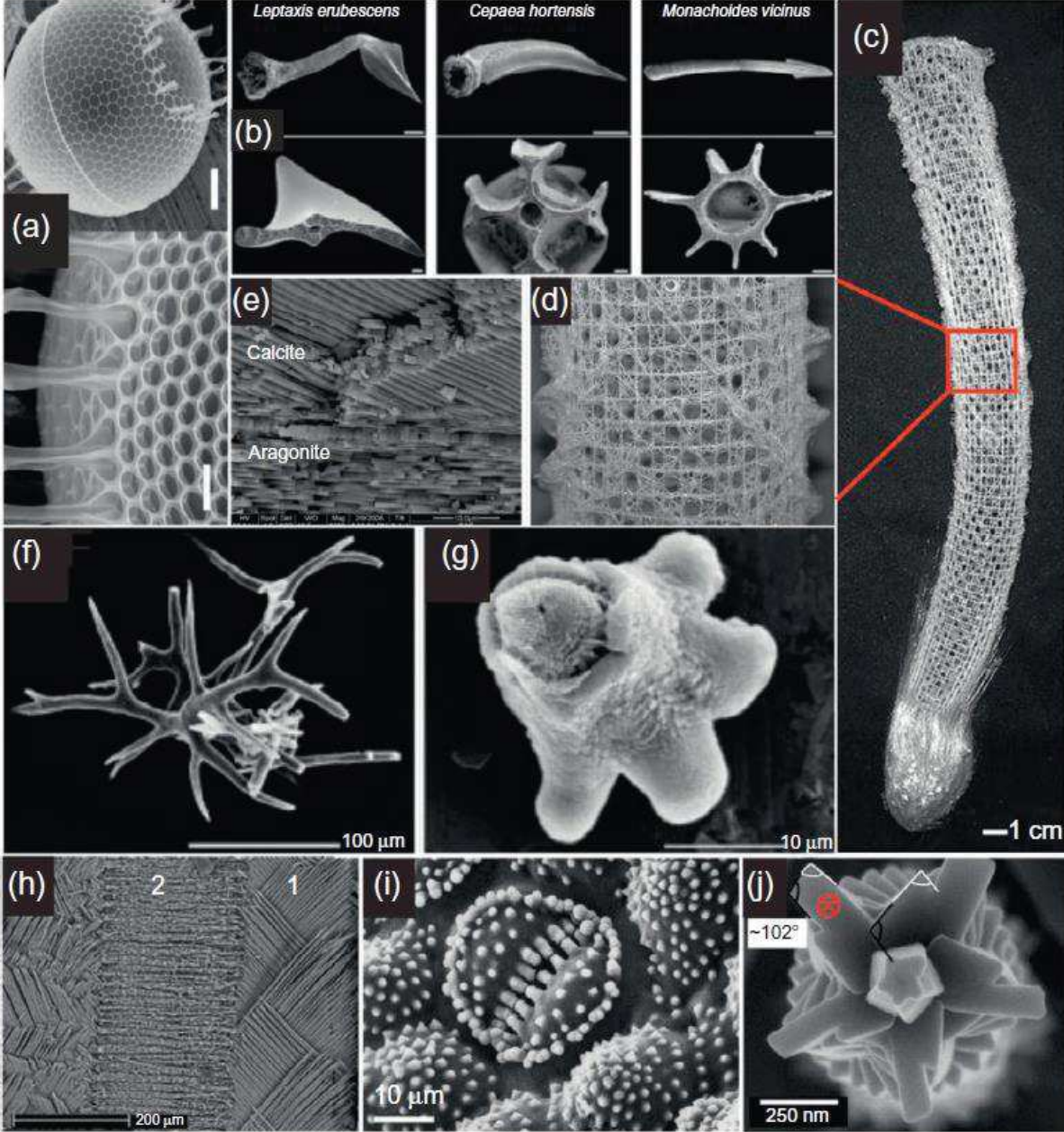


Figure 4.1. Compositional and structural diversity at different length scales illustrated by: (a) the patterned siliceous cell wall of a diatom *Stephanopyxis turris*, (b) calcareous love darts in certain species of land snails, (c and d) the siliceous cylindrical skeletal lattice of the sponge *Euplectella aspergillum* with arrays of vertical, horizontal, and diagonal struts, (e) a backscattered electron image of the fractured shell of the bivalve *Mytilus edulis* calcite prisms and aragonite nacre, (f and g) amorphous skeletal elements from *Pyura pachydermatina*, (h) cross-lamellar layers in the shell of gastropod *Strombus decorus persicus*, (i) cell surface stomata decorated with silicon oxide structures in the common horsetail (*Equisetum arvensis*), and (j) tip of a spine from the coccolith *Rhabdosphaera clavigera*. Taken from ref ³

Multiple examples of microstructures or textural patterns that cannot be readily interpreted within the frame of classical monomer-by-monomer addition can be found in nature.⁴ For instance, calcite crystals found in sea urchin spine,⁵ embryonic spicules⁶ and teeth,⁷ mammalian tooth enamel,⁸ vertebrate bones⁹ among others, are formed by the accumulation of amorphous calcium carbonate precursors that subsequently crystallized into calcite. Besides amorphous precursor phases, intermediate stages of crystallization may occur as dense liquid droplets,¹⁰ oligomers, polymers, gels ^{11,12} or even other crystalline phases of the material.¹³ Direct observation at the nanometric scale of those intermediate stages has unveiled unknown thermodynamic and kinetic aspects of the biomineralization processes.¹⁴ Particularly, implementation of *in situ* liquid phase TEM (LP-TEM) has been key for the comprehension of mineralization processes in biological and biomimetic systems.¹⁵

In this chapter, the mineralization pathways of calcium phosphate and calcium carbonate will be addressed by LP-TEM. These two compounds are basic building blocks in most biological and geological mineralization processes. First, we analyze the crystallization of calcium phosphate for the production of hydroxyapatite. Then, the precipitation of calcite from CaCl_2 and NaCO_3 is examined. Finally, the effect of specific aminoacid in the crystallization is studied. Differently from previous *in situ* TEM studies addressing the biomineralization for these two cases, here the crystallization takes place without the presence of a biomimetic matrix. This approach is implemented in view of reducing the complexity of the system and help the discernment of the role of each component.

4.2. Calcium phosphate

Materials based on calcium phosphates, and particularly hydroxyapatite ($\text{Ca}_{10}(\text{PO}_4)_6(\text{OH})_2$), are biocompatible materials and can be used for orthopedic and dental implants with excellent results in osteointegration.¹⁶ Furthermore, hydroxyapatite

(HAP) is the main constituent of bone mineral in vertebrates and is widely used as a model biomaterial in biomedical studies and medical clinics.

Thereby, the synthesis of HAP is the starting point of various applications.¹⁷ HAP is also used as a model to understand the nucleation, the growth and the presence of possible precursor phases in the biological mineralization processes such as those involved in bone formation.^{18,19} The hierarchical HAP structures encountered in natural samples and the mechanical properties and physiological functions of these structures have motivated decades of research on its mineralization processes.²⁰ Moreover, studying the nucleation and growth mechanisms of calcium phosphate contributes to the understanding of diseases caused by pathological mineralization and to the design of biomimetic materials with properties suitable for bone regeneration and preservation.^{21,22}

According to recent studies,^{14,23} crystallization of HAP (including biological studies) may occur through multistep nucleation and different precursor phases may exist before the final structure: clusters aggregation, larger amorphous particles formation then HAP crystallization. Thus, we addressed this subject by *in situ* liquid TEM to identify at a nanometric scale the intermediate phases present during the reaction of calcium hydroxide ($\text{Ca}(\text{OH})_2$) and phosphoric acid (H_3PO_4) towards HAP.

4.2.1 *Ex situ* synthesis

Calcium and phosphate ions react to form calcium phosphate (CaP). $\text{Ca}(\text{OH})_2$ was obtained by hydration of calcium oxide. Calcium oxide was obtained from the calcination of calcium carbonate (Synthy 99% concentration) at 900 °C (5 °C min^{-1}) for 3 h. Calcium oxide (28 g) was maintained for 1 h in MilliQ water (500 ml) to react exothermically and to form calcium dihydroxide under continuous stirring. The same volume (500 ml) containing 34.52 g of phosphoric acid (Sigma- Aldrich 85% concentration) in MilliQ water was added dropwise at a rate of $\sim 3\text{ mL min}^{-1}$ for $\sim 2.5\text{ h}$ into the solution containing 500 mL of calcium hydroxide and maintained under agitation (aging). The synthesis of HAP was performed by dropwise addition of phosphoric acid (H_3PO_4) to a calcium dihydroxide ($\text{Ca}(\text{OH})_2$) solution in order to obtain a final solution with a Ca/P ratio of 1.67. The whole synthesis (dropwise addition and aging) occurred over a period of 24 h. The reaction was performed at room temperature ($\sim 25\text{ °C}$), and the pH was not kept constant.

4.2.2 Cryo-electron microscopy

This work was precedent by studies carried out through a cooperation program with Brazil using cryo-electron microscopy.²⁴ Here, we recapitulate some of their results that served as referent for the *in situ* experiments.²⁴ Aliquots were taken from the reaction mixture at different periods of time (5 min, 10 min, 30 min, 1 h, 2 h, 7 h, 11 h, 15 h, 19 h and 24 h) to monitor the process of HAP crystallization and growth. Figure 4.2 shows dark field STEM images of nanoparticles immersed in their original frozen solution after 5 min, 10 min, 30 min, 1 h, 11 h and 24 h of reaction. After 5 min of reaction, some agglomerates of CaP nanoparticles (composition determined by EDS) with a ~200 nm size that had irregular contours were detected and showed a low contrast. Some nanoparticles observed after 5 min of synthesis were encapsulated within an external layer (~15 nm) less dense than the bulk region (see ref ²⁴). After 10 min of synthesis, other types of agglomerates of CaP nanoparticles (<100 nm) having a more defined contour were observed, and the presence of many calcium hydroxide particles was also evidenced. After 30 min of synthesis, a few plate-like CaP nanoparticles appeared (figure 4.2, arrow), in addition to the CaP nanoparticles with irregular shapes and calcium hydroxide particles, highlighted by the * at 30 min in figure 4.2. They observed that at 1 h of synthesis contained pre-dominantly CaP particles (~150 nm) formed by parallel assemblies of needles (figure 4.2, arrow). After 1 h, only plate-like CaP nanoparticles were observed in solution. The nanoparticles at 24 h of synthesis (final sample) were similar to those at 1 h and 11 h but were slightly larger (~200nm).²⁴

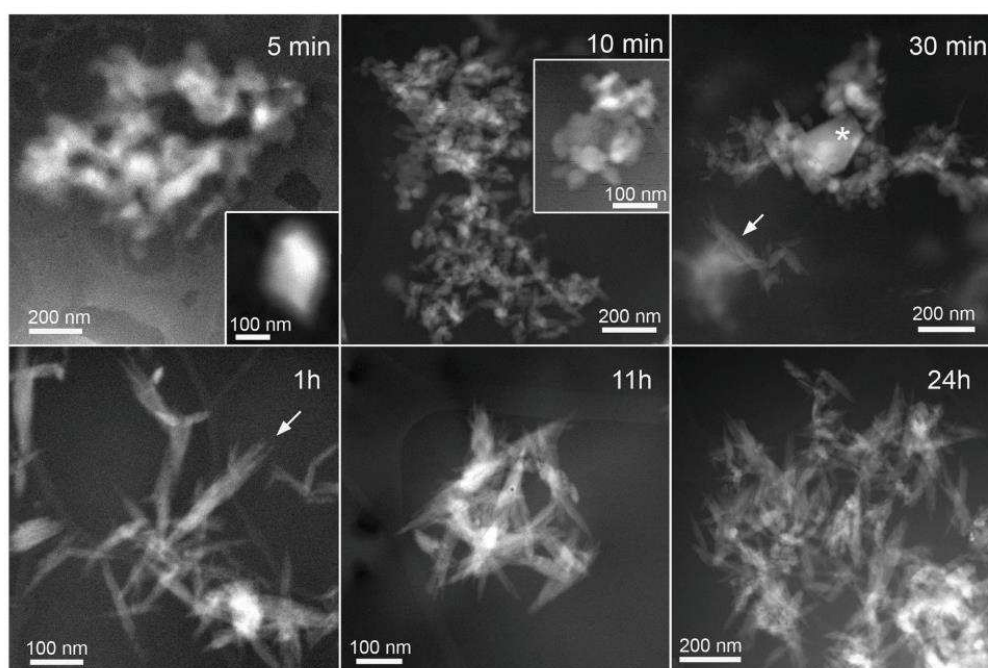


Figure 4.2. Cryo-TEM images obtained in STEM-DF mode of the synthesis products in the 5, 10, and 30 min and 1, 11 and 24 h samples. Small volumes (2 μl) of the reaction solution were collected, immediately ultrafast-frozen and transferred to the TEM. The arrows at 30 min and 1 h indicate the typical needle-like shape of HAP. The asterisk on the 30 min sample indicates a calcium hydroxide nanoparticle. Taken from ²⁴

4.2.3 *In situ* synthesis methodology

It is worth reminding that the holder used for these studies possesses only one inlet and one outlet. Thereby, the simultaneous addition of two reagents in the observation chamber is not possible. This is particularly inconvenient for the study of very fast reactions such as the biomimetic crystallization of calcite or HAP. Considering that between assembling the holder and finally observing the sample in the microscope, there are some tens of minutes, it is possible that the processes that we hope to see will be over.

Hence, two approaches were used to perform *in situ* observations: “static” and “flow” modes. When working in the static mode, the reaction mixture is prepared out of the microscope mixing $\text{Ca}(\text{OH})_2$ with H_3PO_4 . Immediately after mixing, a drop of the mixture was deposited over the observation window of the chip. The excess of liquid was removed with a filter paper and the cell was closed and load into the holder. No further addition of precursors could be done after closing. Oppositely, in the flow mode a drop of $\text{Ca}(\text{OH})_2$ solution was deposited over the e-chip and the cell was assembled and inserted in the microscope. The solution of H_3PO_4 was flushed through the microfluidic circuit. Both modes are represented in figure 4.3.

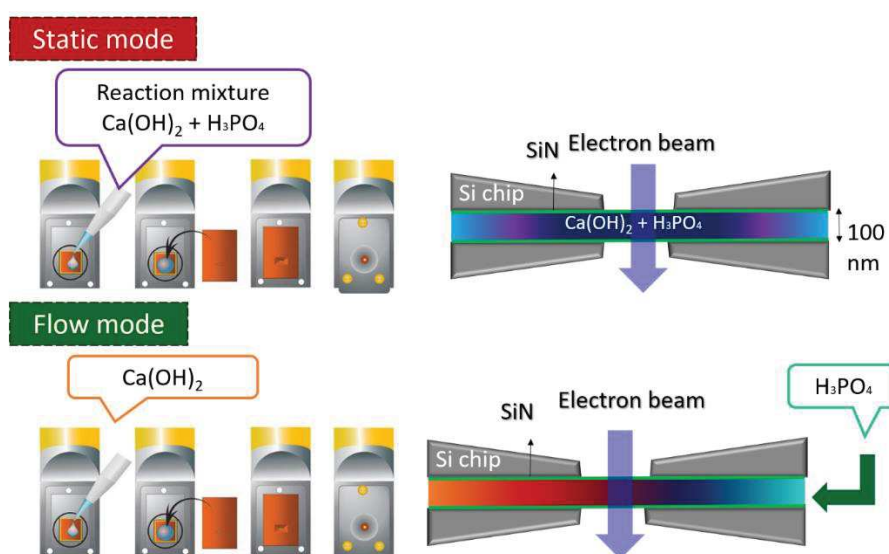


Figure 4.3. Schematic representation of the static (top) and flow (bottom) modes used to synthesize HAP within the *in situ* set-up.

4.2.3.1 Flow mode results

In this case the $\text{Ca}(\text{OH})_2$ solution is deposited over the window. Beforehand, the H_3PO_4 was introduced to the edge of the entrance of the observation region, in order to avoid replacing the deposited solution and delays in the reaction. In figure 4.4, it is possible to distinguish the region where the initial hydroxide solution comes in contact with the phosphoric acid flow, next to the region where only the hydroxide resides. The apparition of globular structures is the result of the mixing of the two solutions on the mixing front edge. Unfortunately, it was not possible to observe further stages in the crystallization. After few minutes of observation the window broke due probably to the internal pressure within the observation chamber. However, complementary observations in static mode allowed us to complete the panorama of the crystallization.

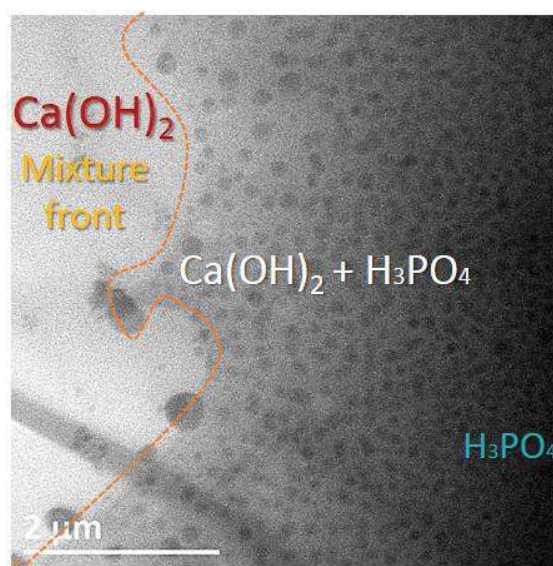


Figure 4.4. Front of phosphoric acid coming in contact with the $\text{Ca}(\text{OH})_2$.

4.2.3.2 Static mode results

Cryo-microscopy²⁴ and previous *in situ* studies²⁵ gave hints about the presence of pre-nucleation clusters of calcium triphosphate ions as nanometer-sized building blocks for CaP. , Our *in situ* observation in static mode to displayed a variety of structures that we think correspond to different stages in the crystallization (figure 5).

First, spherical-shaped structure in figure 4.5(1) might be a droplet of ‘ionic dense liquid’. Such liquid-liquid phase separation has been previously described in the

literature in the crystallization of calcium phosphate.²⁶ The ionic dense liquid is described as a pre-nucleation cluster exists as a separate amorphous liquid-like precursor phase distinct from either the supersaturated solution or crystal phases. The dense liquid has a defined interface, and is more dense than the surrounding solution, but less dense than the crystal form, what explains the darker contrast in the TEM image compared with the surrounding media. The dense liquid can be composed of ions, molecules, and/or prenucleation clusters. The dense liquid is larger than a crystal nucleus having a diameter close to 100 nm. Crystal nuclei of around 2-3 nm in diameter seems to be the darker spots within the dense liquid. In a following stage (figure 4.5(2)) various ionic dense droplets appear to interact between them, some of the nuclei have grown and display a much darker contrast. Next stage, observe in figure 4.5(3) appears similar to amorphous precursors reported for various biominerals,^{8,27,28} as mention at the beginning of this chapter. Such amorphous spherical precursors are few tens of nanometer in diameter, much smaller than the initial dense liquid droplets. In figure 4.5 (3) and (4) is evidenced that these amorphous precursors form branched 'polymeric' structures. Final stage (5) would be the transition to the the needle-like structure.

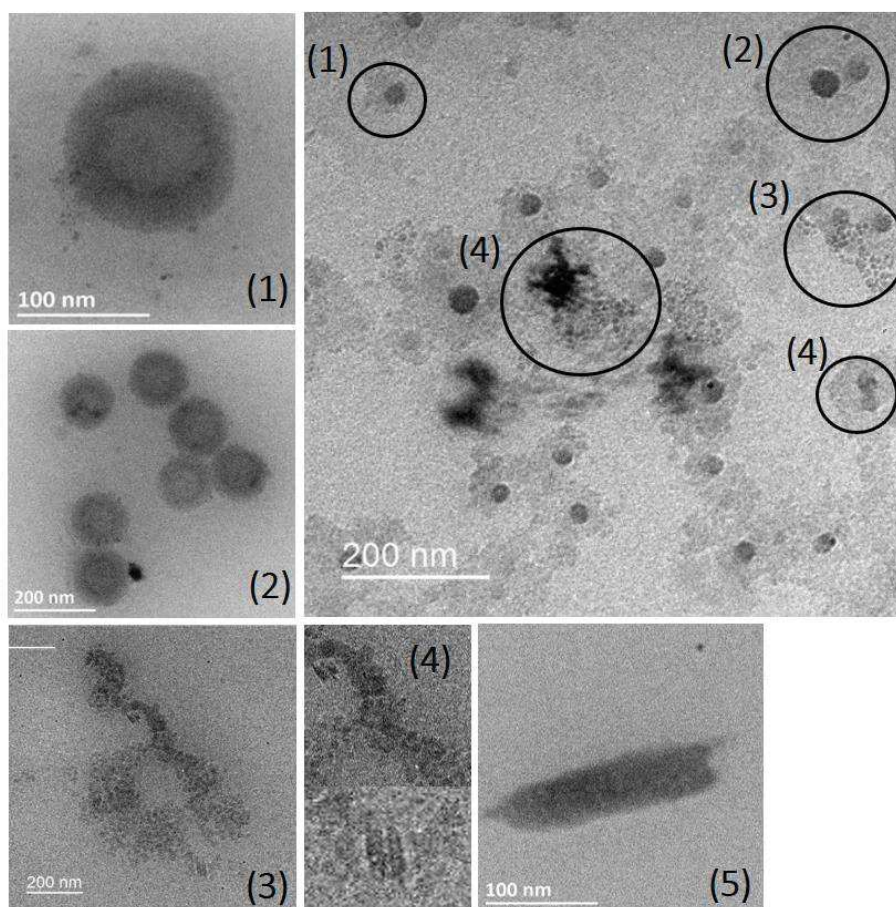


Figure 5. The five stages of pre-nucleation, nucleation and growth of HAP needles. (1) The ionic dense liquid (pre-nucleation clusters formed within and around the globules). (2) Aggregation of the ionic dense spheres. (3) Amorphous precursors aligning and agglomerating. (4) Reorganization. (5) Final needle morphology.

Further insight in stages (3), (4) and (5) can be attained by close inspection of image sequence in figure 5.6 ([annex movie M13](#)). The yellow circle highlights how several amorphous precursors interact and form particles with morphologies other than needles, (figure 5.6 at 49s). Mostly, isotropic structures that re-dissolve into the media. Furthermore, these intermediate structures are observed all along the reaction time. The needle-like structure appear in the vicinity of the isotropic structures, yet remain stable and continue growing throughout the observation period.

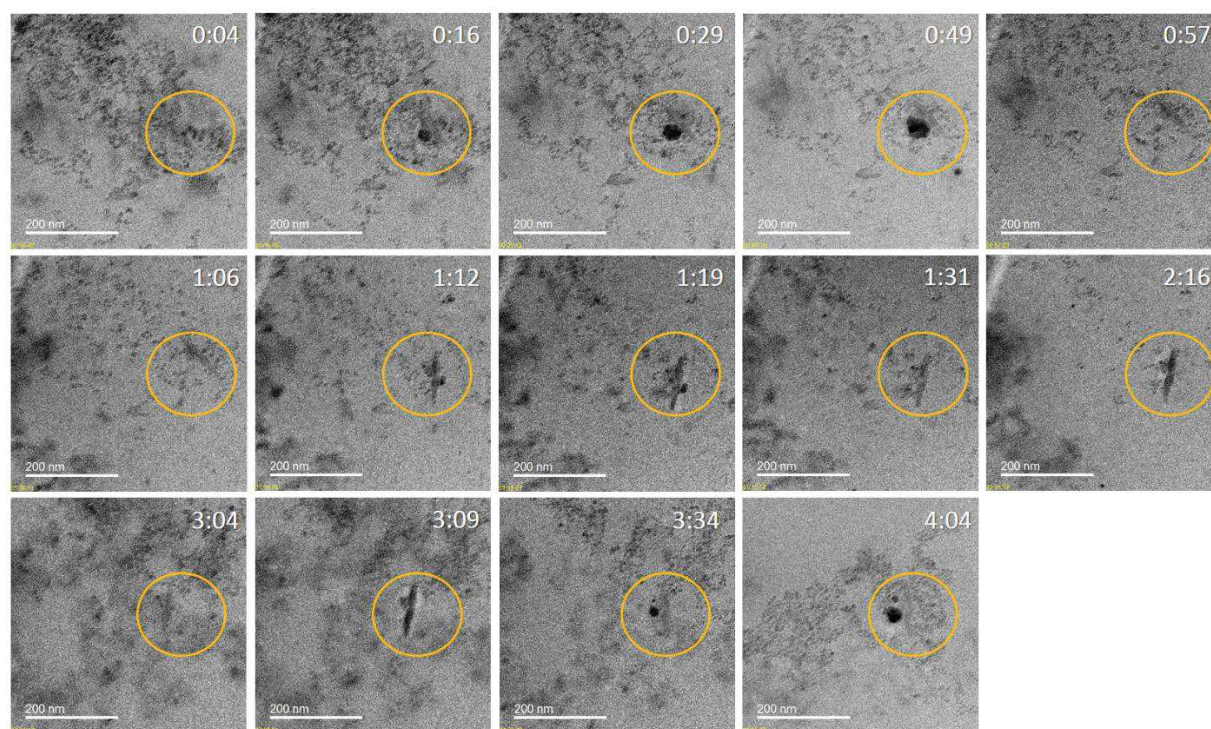


Figure 4.6. *In situ* TEM images sequence from the reaction mixture displaying stages (3) and (4) and (5). This sequence shows several amorphous precursors aligning and agglomerating. The yellow circle shows a needle forming and structures with other morphologies forming a disappearing.

The *post in situ* analysis of the structures formed over the observation window corresponded as well to the needle-like structure expected for the HAP. Nonetheless, it was possible to find some regions where the crystallization was not totally over. Amorphous precursors, similar to those observed *in situ*, were found near crystalline needles (figure 4.7). This suggests that the formed needles do continue growing by the addition of the amorphous precursors. Final needle-like crystals tended to aggregate as

can be seen in figure 4.7b-c. The inset on the figure shows the diffraction pattern of the needles displaying (211) reflections²⁹.

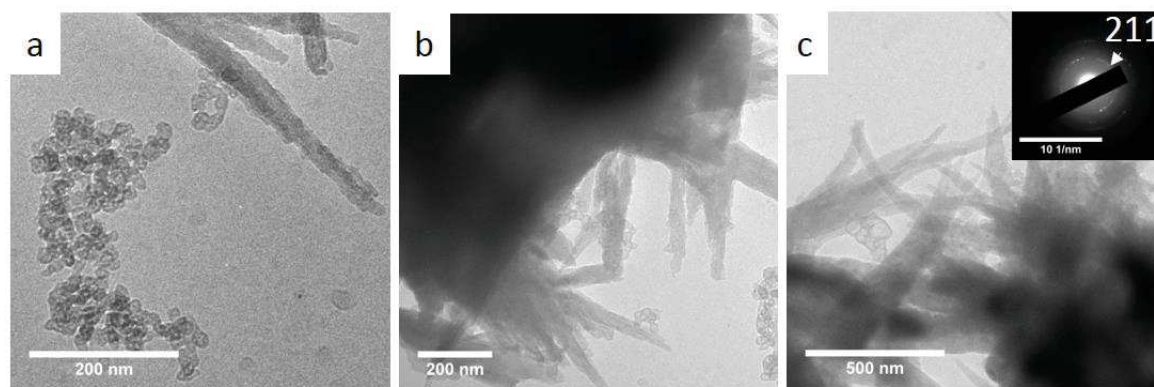


Figure 4.7. *Post in situ* images of the structures obtained within the microscope.

Habraken et al.²³ have studied the precipitation of calcium phosphate in a biomimetic solution (buffered solution) and described the formation of similar pre-nucleation clusters that aggregate to form branched polymeric networks. The branches develop nodules that further condense, transforming into spheres that subsequently coagulate and precipitate. Then, coagulated spheres transform, producing a thin ribbon-like morphology. In the course of the reaction, the ribbons evolve into their final shape that consists of elongated plates. In our case, we demonstrate that the crystallization of hydroxyapatite from the addition of phosphoric acid (H_3PO_4) to calcium hydroxide ($\text{Ca}(\text{OH})_2$) in an aqueous medium without any biomimetic matrix shows a very similar multi-stage crystallization process. The major difference between crystallization pathways with and without biomimetic additives is the presence of an ionic dense liquid stage that is only observed in the initial stage of the crystallization in the absence of biomimetic additives. This ionic dense liquid phase has been previously discussed in the case of CaCO_3 by Wolf et al.³⁰ and was described as a metastable liquid-like cluster formation generated by density fluctuations in the inorganic ions in the bulk. All in all, the presence of any pre-nucleation stages is a strategy of the system to decrease the energy barrier for nucleation.^{11,31}

Finally, the compositional analysis by EDS of the needles formed *in situ* (figure 8) shows a Ca/P ratio of ~ 1.3 . Stoichiometric HAP is composed of calcium and phosphorus with molar ratio of Ca/P equal to 1.67.³² Thus, *in situ* synthesis leads to calcium-deficient crystals. This compositional difference might be related to the unhomogeneous distribution of precursors and the absence of stirring during *in situ* experiments. Further

analysis of the composition of the pre-nucleation ionic dense liquids and the amorphous precursor is envisioned to enhance the comprehension of the precipitation mechanism in non-biomimetic media.

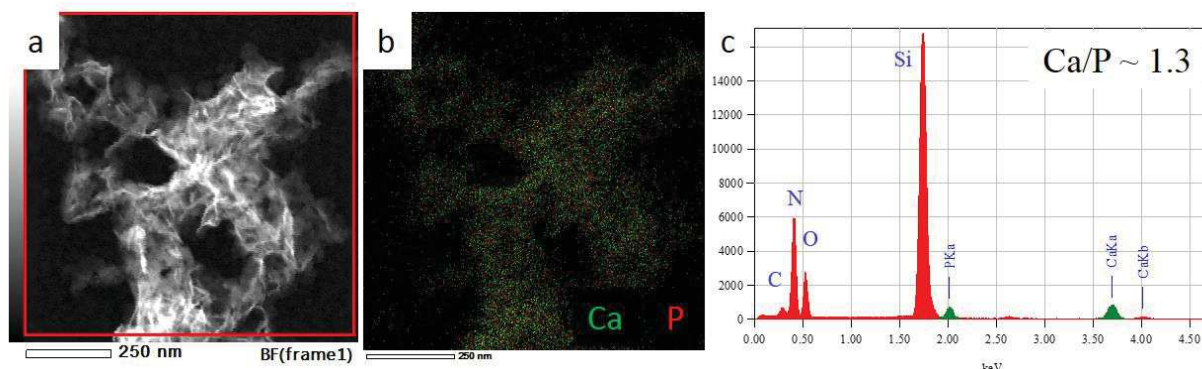


Figure 8. a) *Post in situ* TEM image of final HAP needles synthesized *in situ*. b) Compositional mapping of the calcium (green) and phosphor (red) of a. c) ED spectra recorded on the squared area in a.

4.3. Calcite

Calcium carbonate (CaCO_3) is the most abundant biomineral in nature, consisting of calcareous sponge spicules, rigid structures of marine species, hard invertebrate tissues, eggshell, and inner ear otoliths. Thus, calcium carbonate is a material of great interest for fundamental studies as a nucleation and crystallization model.^{33–35} CaCO_3 three main polymorphs are³³: vaterite, the less stable polymorph with a hexagonal unit cell that typically forms “flower” shaped crystals with hexagonal contours; aragonite, a metastable and second most abundant polymorph with orthorhombic structure that crystallizes in the form of needle-shaped clusters growing along the c-axis, or pseudohexagonal prisms by cyclic twinning in {110}; and triclinic calcite, the most stable polymorph typically forming rhombohedral crystals that express faces of the family {104}.³³ According to the Ostwald-Lussac law, before reaching the crystalline final state, the material goes through less stable forms that, in the case of calcium carbonate, would go from the amorphous state, to the vaterite and aragonite polymorphs and, finally, to the more stable state: calcite.

Studies on calcium carbonate nucleation show that both classical and non-classical crystallization coexist. Besides, the existence of more than one amorphous phase has been reported.^{36,37} However, little is known about how organic compounds interfere with the stability of amorphous calcium carbonate (ACC - Amorphous Calcium Carbonate)

and the formation of calcium carbonate polymorphs.^{38,39} The influence of organic compounds on calcium carbonate crystallization has been studied through the formation of biogenic and non-biogenic calcites. Both kinds of samples differ in exposed facets, hardness and morphology. These differences are related to macromolecules that are present during the formation of the biogenic mineral. These macromolecules may be present as layers interspersed with the mineral and filling occlusions^{2,40} or even dispersed within the crystalline mineral.⁴¹ Such interactions between macromolecules and biominerals are still poorly understood.

Specific properties of the amino acids present in proteins involved in biomineralization, such as polarity, presence of nucleophilic and electrophilic groups, presence of phosphates and sulfates are directly linked to the reaction kinetics and the orientation of the resulting crystals.^{2,27,40,42} Thereby, in this section will be explained how we approach the impact of amino acids on calcium carbonate biomineralization, especially in the crystallization of calcite, leading to specific crystalline phases.

4.3.1. *CaCO₃ ex situ synthesis*

The synthesis in water of calcium carbonate crystals was based on a method already described in the literature, taking into consideration the stoichiometric ratio of the reagents and the formation of the most stable polymorph, calcite.^{35,43,44} The synthesis was carried out without pH control, temperature or changes in the concentrations, in order to resembles *in situ* experiments.

Calcium carbonate was synthesized using 100 mM CaCl₂ and 100 mM Na₂CO₃, final pH = 8-9. In a beaker containing 100 mL of Na₂CO₃, 100 mL of CaCl₂ were added using a 1.5 mL min⁻¹ flow from a peristaltic pump. The reaction was constantly mixed using a tip sonicator (UP200S - HIELSCHER) with 80% amplitude. After the addition of calcium chloride was completed, the reaction medium was stirred for a further 30 min. After the synthesis phase, the sample was centrifuged 3 times at 6000 rpm for 15 min. At each cycle, the supernatant was replaced with distilled water so that sodium chloride formed during the reaction could be completely removed. Then the precipitate recovered by centrifugation was lyophilized for further analysis.

4.3.2. *Synthesis in a copper grid: control*

During the *in situ* experiments, the electron beam may impact nucleation rates and dissolution processes.¹⁵ Therefore, it is essential to have a reference in order to identify

the events related to the chemical synthesis and those related to beam damage artifacts. This control synthesis was carried over copper grids. Copper grids with a carbon film were plasma cleaned using an oxygen plasma to increase hydrophilicity. The grids were placed in a petri dish and 5 μL of Na_2CO_3 solution containing one of the amino acids at one of the concentrations described below was drop-casted. Then, 5 μL of CaCl_2 solution were added and after 1, 5, 10 and 30 min, the crates were washed three times by dripping distilled water. The amino acids tested are L-aspartic acid and glycine. Both were used at concentrations of 50 and 10 mM.

4.3.3. *In situ* synthesis methodology

The reagents were used with a concentration of 10 mM calcium chloride (CaCl_2) and of 10 mM sodium carbonate (Na_2CO_3). Amino acids were solubilized in Na_2CO_3 solution. For the experiment without amino acid addition, 5 μL of a 10 mM Na_2CO_3 solution was drop-casted onto the bottom chip of the TEM cell. The spacing between the top and the bottom chips of the *in-situ* cell was 150 nm. The excess liquid was removed with a paper filter, the chip was sealed with the top chip and the sample holder was inserted into the microscope. Then, the CaCl_2 solution was inserted with a continuous flow of 10 $\mu\text{L min}^{-1}$. For the amino acid addition experiment, the static and the flow mode were both tested.

4.3.3.1 Synthesis without additives

The copper grid control experiment yields after 30 s of reaction crystalline nanoparticles of around 2 μm (Figure 4.9). Interplanar distances consistent with the calcite structure were found in the diffraction pattern (Figure 4.9a -inset).

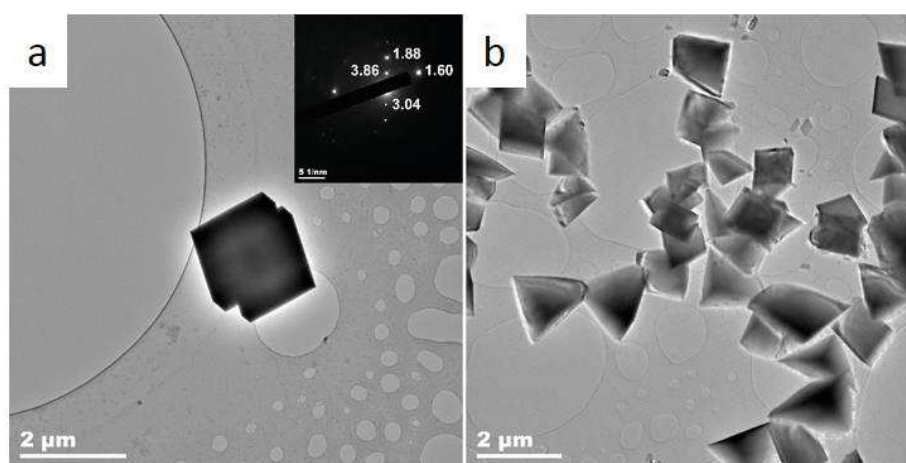


Figure 4.9. TEM images of CaCO_3 synthesis without additives interrupted after 30 s. Inset in a is an SAED of the observed crystal.

The *in situ* sequence in figure 4.10 shows the precipitation of polyhedral particles between 5 and 50 nm within a dense liquid droplet ([annex movie M14](#)). Nielsen et al.³⁷ have studied similar precipitation processes in the presence of a biomimetic matrix. According to their studies, faceted particles can undergo oriented attachment to continue the growth. Figure 4.10 at 70 s might reflect this observation. After 128 s, the particles re-dissolve. According to Dey, de With and Sommerdijk,³³ crystallization only occurs after nanoparticles reach about 70 to 120 nm. Fast ion-depletion or electron beam-induced radiolysis can be the reason for the re-dissolution.⁴⁵

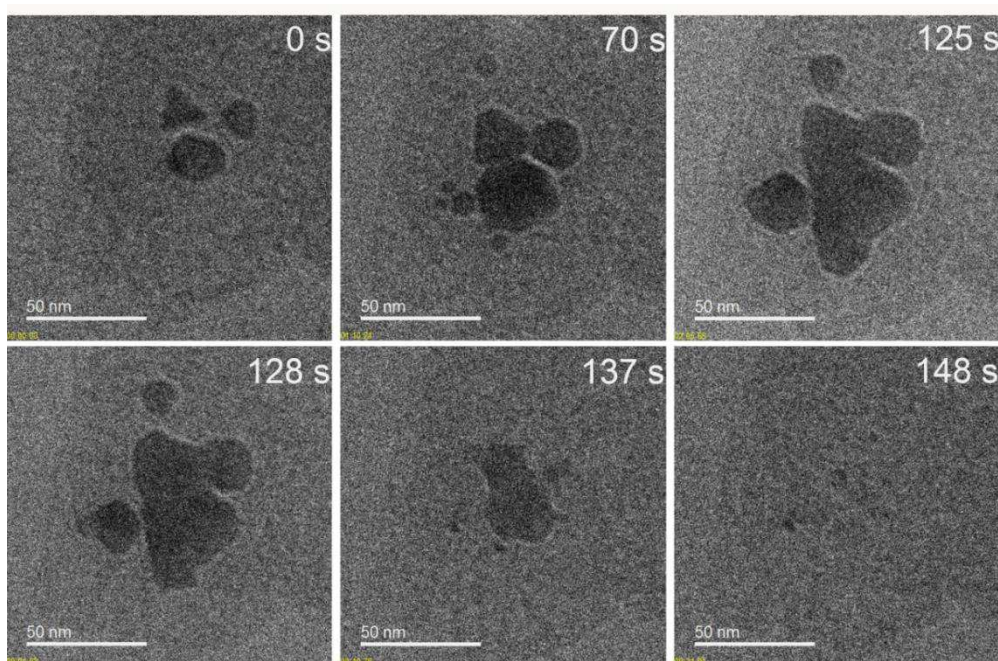


Figure 10. Sequence of video recorded during *in situ* synthesis of CaCO_3 without addition of amino acids. Flow = $10 \mu\text{L min}^{-1}$.

4.3.3.2 Study of CaCO_3 crystals formed in the presence of L-aspartic acid

Through the control grid synthesis, it was possible to determine that the growth of CaCO_3 crystals is slower in the presence of aspartic acid (Asp). Indeed, 1 min after mixing, no particles could be detected in the presence of Asp (50mM and 10mM), microscale crystals were observed after 30 seconds without additives. Furthermore, at a concentration of 10 mM of Asp, nano clusters arranged in globular structures were detected at 5 min (Figure 4.11). After 10 min, these clusters had evolved in faceted crystals of approximately 2 μm . Figure 4.12 shows that such crystals were surrounded by starting materials, as if migrating to the crystal. EDS confirms the presence of calcium

in the crystal, and of the other chemical elements introduced, C, N, O, Na, Cl in the material dispersed around the crystal (Figure 4.12c).

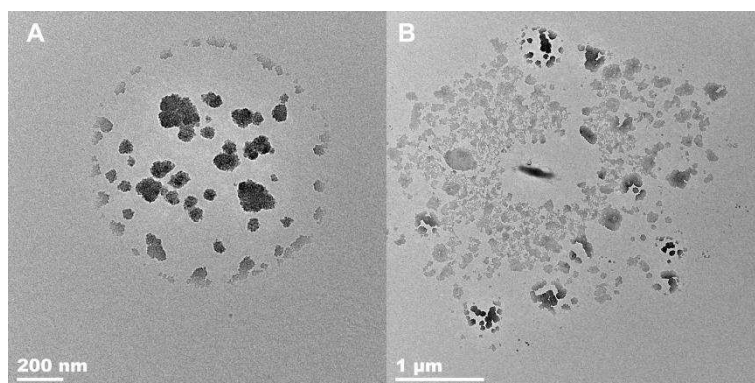


Figure 4.11. TEM image of control copper grid experiment after 5 min using 10 mM Asp.

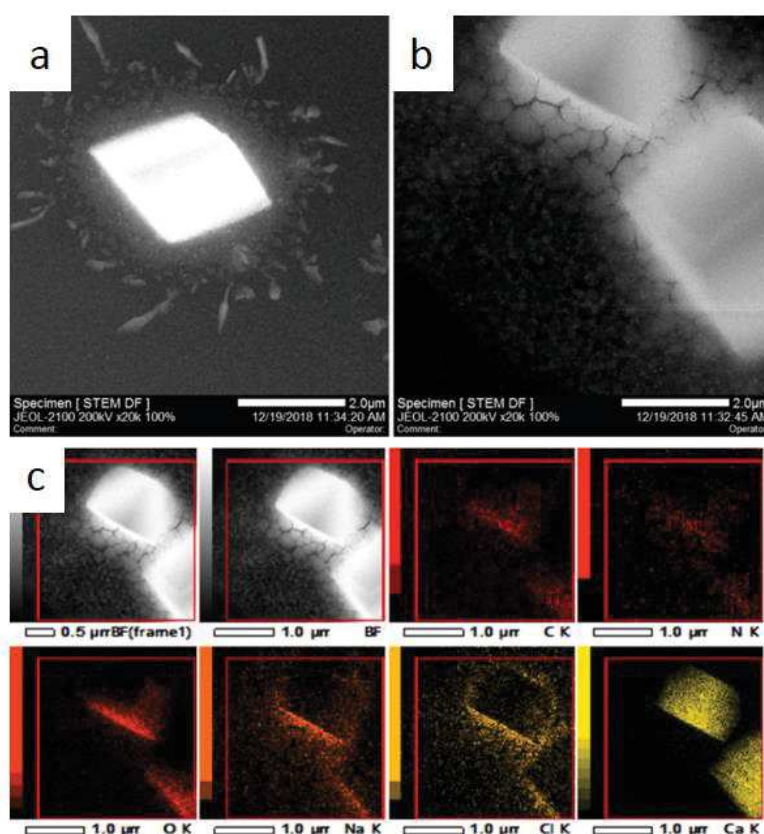


Figure 4.12. a) and b) STEM-DF images of crystals obtained by synthesis interrupted after 10 min using 10 mM Asp. c) EDS mapping of the crystal observed in b).

Interestingly, the control experiments in the presence of 10 mM Asp samples after 10 min and 50 mM Asp after 5 min showed the presence of spherical structures with crystalline material inside (Figure 4.13). Such spherical structures were also observed during the *in situ* experiment using 10 mM Asp (Figure 4.14). Furthermore, figure 13d

shows the accumulation of calcium in the crystalline material within the globule. The pH of the reaction medium is strongly basic, close to 11. In these conditions, Asp is deprotonated and negatively charged as aspartate anions. These anions probably bind strongly to calcium cations.

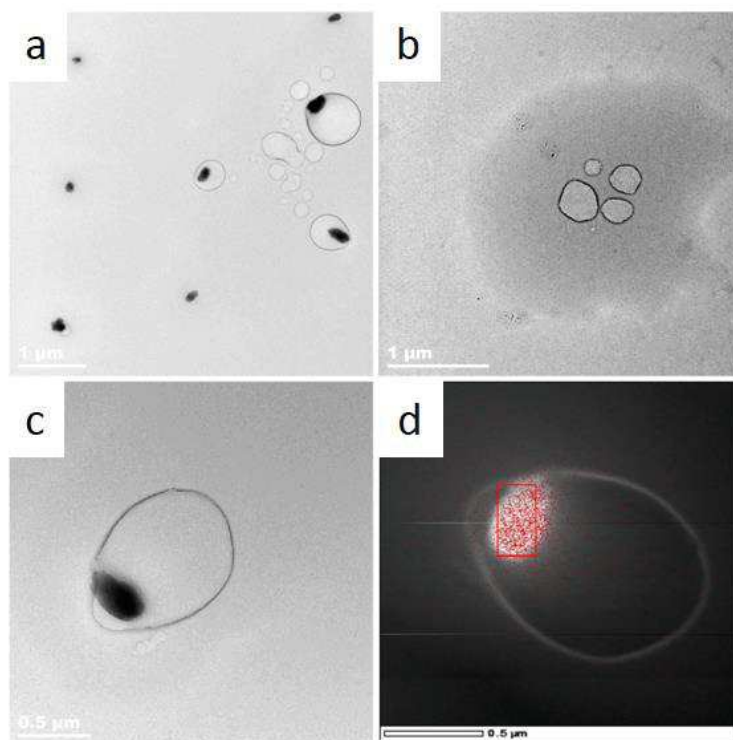


Figure 13. a) and b) TEM image of vesicles formed during interrupted synthesis using 50 mM Asp after 5 min of synthesis. c) TEM image of vesicles formed using Asp 10 mM after 10 min of synthesis, d) -EDS mapping of calcium from image c.

Gower and Odom⁴⁶ described the use of poly L-aspartic acid in an *in situ* optical microscopy experiment. Such vesicular structures are comparable to those formed by poly L-aspartic acid when it is used as a polymer-induced liquid precursor (PILP). They observed small isotropic droplets formed by PILP. After some time, they report a granular carbonate film formed by the coalescence of the PILP droplets.

During the *in situ* experiment displayed in figure 4.14, globular structures, as those observed in the control experiment, were detected. There were multiple crystallites of around 20-30 nm within each globule, differently from the couple hundreds nm cumulus detected in the control experiment shown in figure 4.13. After several minutes, there was no precipitation. This might be linked to the continuous flow of the reagents through the cell, leading to the migration of the vesicles out of the observation window.

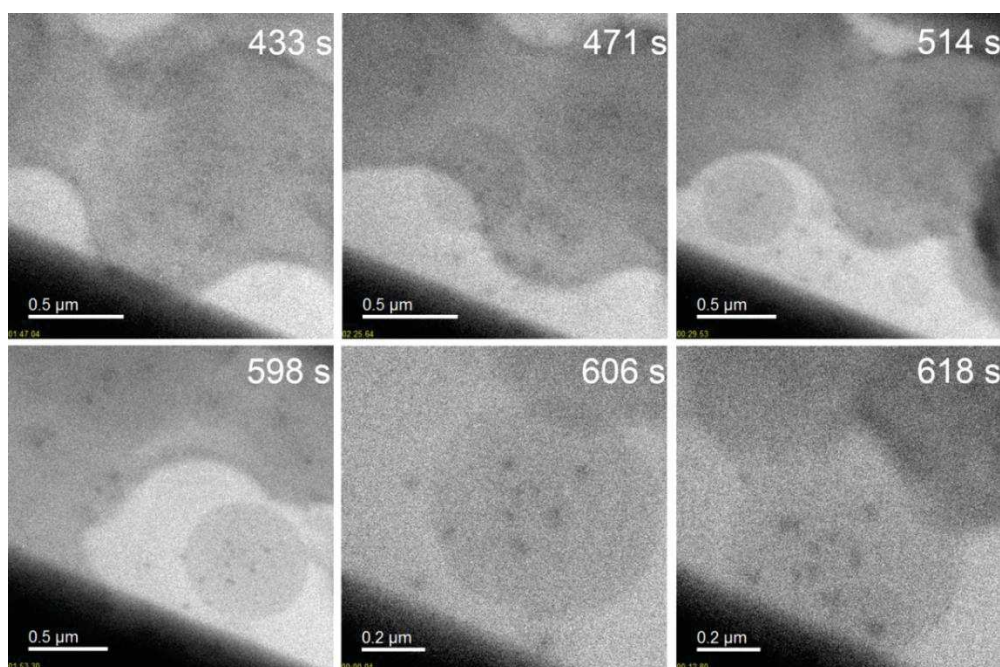


Figure 4.14. Sequence recorded *in situ* during the continuous flow experiment of CaCO_3 synthesis with the addition of 10 mM Asp. Flow = $10 \mu\text{L min}^{-1}$.

The delaying effect of Asp is due to the strong electrostatic interaction between aspartate and calcium ions, which sequesters Ca^{2+} cations into self-organizing globular structures. Note that Asp and L-glutamic acid are present in larger amounts in proteins associated with the biogenic formation of calcite^{38,40}. Furthermore, previous studies have confirmed the influence of Asp on calcite morphology during its formation.^{35,47,48}

4.3.3.3 Evaluation of CaCO_3 crystals formed in the presence of glycine

In addition to aspartic and glutamic acids, glycine (Gly) is one of the most abundant soluble amino acids involved in calcium carbonate crystallization.^{38,49} Štajner and colleagues³⁵ studied the influence of various amino acids on CaCO_3 crystallization. They observed that nonpolar amino acids do not significantly influence crystallization kinetics when testing L-alanine and L-phenylalanine. Since the objective of this study is to evaluate how functional groups and polarity of different amino acids interfere in CaCO_3 crystallization, glycine (Gly) was selected as a model nonpolar amino acid.

The control grid synthesis showed exclusively crystals with the typical morphology of calcite for both 10 mM Gly and 50 mM Gly samples (Figure 4.15).

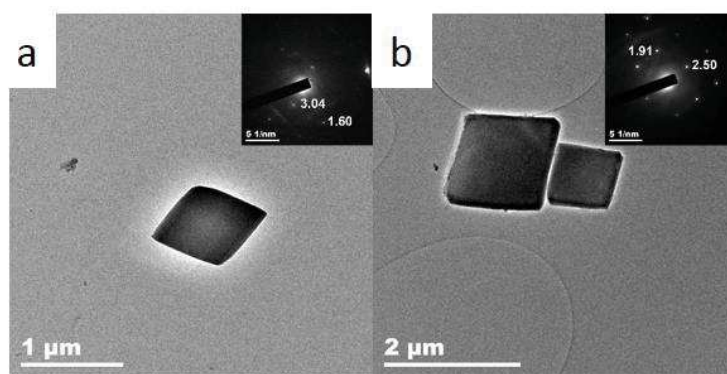


Figure 4.15. TEM images of crystals obtained after 30 min of reaction using a) 10 mM Gly, b) 50 mM Gly. Insets in a and b SAED of observed crystals.

However, the static *in situ* experiment demonstrated that in the presence of 10 mM Gly two types of solids are formed: calcite-like rhombohedral and vaterite-like spherical crystals (Figure 4.16a). This is consistent with the literature, which points out that in the presence of both low and high concentrations of glycine, both calcite and vaterite crystals are formed.^{49,50} The coexistence of both crystal structures was confirmed by SAED in a *post mortem* analysis (Figure 4.16b), confirming that in addition to promoting vaterite nucleation, Gly may also be responsible for vaterite stabilization (metastable polymorph).

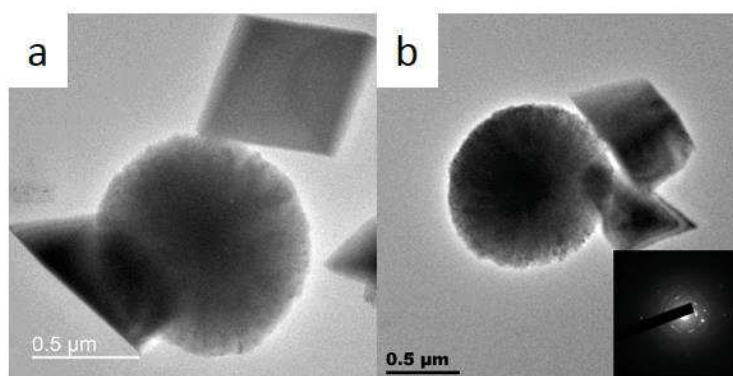


Figure 4.16. TEM images of recorded a) during the static *in situ* in experiment of CaCO_3 synthesis with the addition of 10 mM Gly, and b) *post in situ* condition from a. Inset in b shows an SAED pattern of the observed crystals with characteristic interplanar distances of vaterite (0.28 nm) and calcite (0.22; 0.19; 0.18 and 0.16 nm).

Besides the formation of calcite and vaterite crystals in the presence of glycine during the static *in situ* experiment, two processes were observed. Figures 4.17 and 4.18 show the growth of an amorphous sphere in which the center dissolves while the walls start to show diffraction contrast. Then, the object breaks down (Figure 4.18) into small crystallites that tend to reassemble in the course of the reaction. A similar behavior has been described by Nielsen, Aloni and Yoreo³⁷ in an *in situ* TEM experiment without

addition of additives, where vaterite formation was observed probably through dissolution of the core of an amorphous solid and recrystallization on the edges.

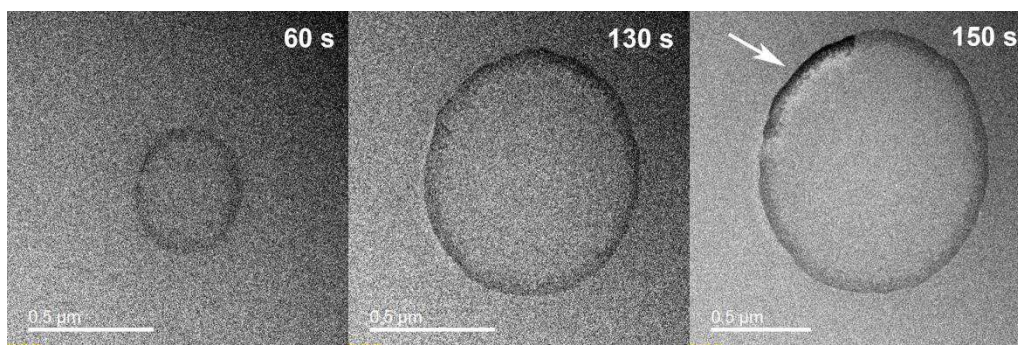


Figure 4.17. Sequence recorded *in situ* during the static experiment of CaCO_3 synthesis with 10 mM Gly. The arrow indicates diffraction contrast at the border of the sphere.

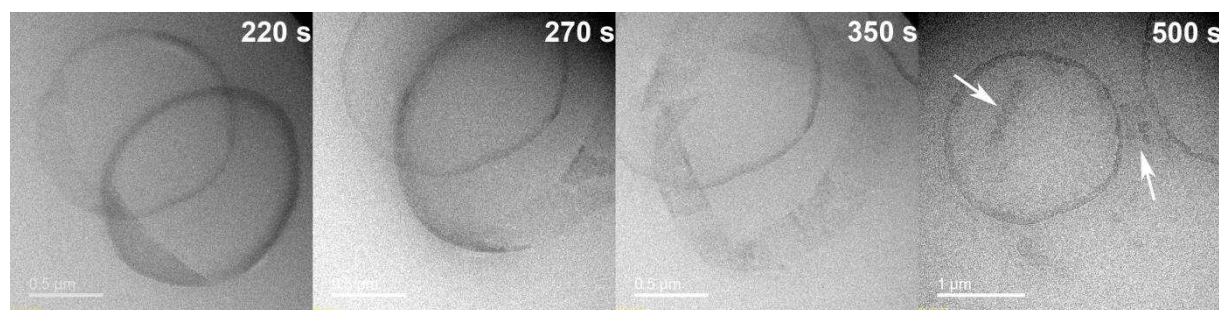


Figure 4.18. Sequence recorded *in situ* during the static experiment of CaCO_3 synthesis with 10 mM Gly. Arrows indicate the crystallites formed after breaking down of the sphere.

4.4. Conclusions

Herein, two different cases of mineralization processes for calcium carbonate and calcium phosphate have been reported. In all cases, evidences of non-classical nucleation processes was found. Furthermore, we show that the non-classical crystallization routes take place even in non-biomimetic conditions. Both mineralization pathways several stages including in first instance the formation of what we propose to be ionic dense liquids, which tend to self-organize in globular structure. Nucleation of the solid takes place within the ionic dense liquid, leading to amorphous pre-crystallization objects. Such amorphous precursors aggregate to form the crystals. The crystal can go through phase transformations until reaching the most stable phase.

Taking into account the results from the previous chapter, the implementation of *in situ* liquid phase TEM allowed to observe the pre-nucleation stages for all the systems, demonstrating the versatility of this technique to address unsolved questions in the formation of crystals in both, aqueous and organics solvents. Our observations show that

the reactions analyzed presented a two-step evolution to metastable phases, as presented in figure 4.19C and extensively explained by de Yoreo et al.⁴. In the case of the iron oxide synthesis discussed in the previous chapter, vesicular and reverse micellar metastable arrangements were at the origin of the nucleation grains. Similarly, ionic dense liquids were found in the pre-nucleation stages of the mineralization of both calcium derivatives.

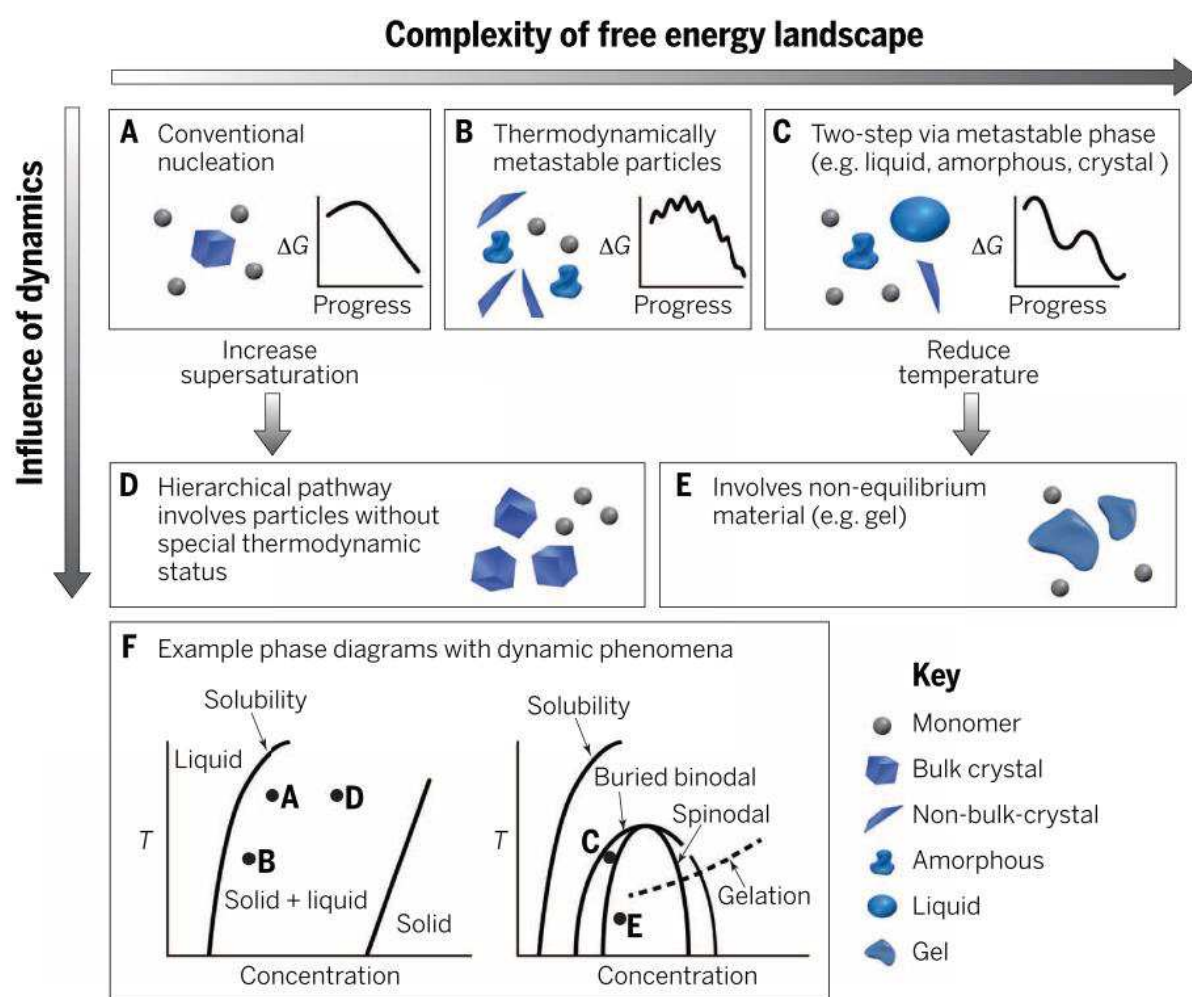


Figure 4.19. Crystallization through a wide variety of pathways. The possible pathways by which monomers form a stable bulk crystal, and the physical mechanisms that give rise to them, can have thermodynamic (A to C) and kinetic (D and E) origins. (A) Classical monomer-by-monomer addition. (B) Aggregation of metastable particles, such as liquid, amorphous, or poorly crystalline particles, or of oriented (and nearly oriented) attachment of metastable nanocrystals. (C) Crystallization via the formation of a metastable bulk phase, such as a liquid or solid polymorph. (D) Kinetically dominated aggregation of clusters or oligomers. (E) Aggregation of unstable particles whose internal structures are not those of equilibrium phases. The phase diagrams (F), with or without a spinodal region, reflect a thermodynamical controls on assembly. As indicated, each pathway in (A) through (E) corresponds to a similarly labeled point in these phase diagrams. Taken from ⁴

Furthermore, this is a clear example of the possibilities offered by *in situ* liquid TEM for deepening our comprehension at the nanoscale of all the processes that a material

undergoes from its very formation, to its use (as describe in chapter 2) and its degradation routes.

4.5. References

- (1) Sommerdijk, N. A. J. M.; Cölfen, H. L. Lessons from Nature — Biomimetic Approaches to Minerals with Complex Structures. **2019**, *35*.
- (2) Green, D. C.; Ihli, J.; Thornton, P. D.; Holden, M. A.; Marzec, B.; Kim, Y.-Y.; Kulak, A. N.; Levenstein, M. A.; Tang, C.; Lynch, C.; et al. 3D Visualization of Additive Occlusion and Tunable Full-Spectrum Fluorescence in Calcite. *Nat. Commun.* **2016**, *7*, 13524.
- (3) Rao, A.; Cölfen, H. *Morphology Control and Molecular Templates in Biomineralization*; Elsevier Ltd., 2015.
- (4) De Yoreo, J. J.; Gilbert, P. U. P. A.; Sommerdijk, N. A. J. M.; Penn, R. L.; Whitelam, S.; Joester, D.; Zhang, H.; Rimer, J. D.; Navrotsky, A.; Banfield, J. F.; et al. Crystallization by Particle Attachment in Synthetic, Biogenic, and Geologic Environments. *Science (80-.)*. **2015**, *349*.
- (5) Politi, Y.; Arad, T.; Klein, E.; Weiner, S.; Addadi, L. Sea Urchin Spine Calcite Forms via a Transient Amorphous Calcium Carbonate Phase. *Science (80-.)*. **2004**, *306*, 1161–1164.
- (6) Beniash, E.; Aizenberg, J.; Addadi, L.; Weiner, S. Amorphous Calcium Carbonate Transforms into Calcite during Sea Urchin Larval Spicule Growth. *Proc. R. Soc. B Biol. Sci.* **1997**, *264*, 461–465.
- (7) Killian, C. E.; Metzler, R. A.; Gong, Y. U. T.; Olson, I. C.; Aizenberg, J.; Politi, Y.; Wilt, F. H.; Scholl, A.; Young, A.; Doran, A.; et al. Mechanism of Calcite Co-Orientation in the Sea Urchin Tooth. *J. Am. Chem. Soc.* **2009**, *131*, 18404–18409.
- (8) Beniash, E.; Metzler, R. A.; Lam, R. S. K.; Gilbert, P. U. P. A. Transient Amorphous Calcium Phosphate in Forming Enamel. *J. Struct. Biol.* **2009**, *166*, 133–143.
- (9) Mahamid, J.; Sharir, A.; Addadi, L.; Weiner, S. Amorphous Calcium Phosphate Is a Major Component of the Forming Fin Bones of Zebrafish: Indications for an Amorphous Precursor Phase. *Proc. Natl. Acad. Sci. U. S. A.* **2008**, *105*, 12748–

12753.

- (10) Galkin, O.; Chen, K.; Nagel, R. L.; Hirsch, R. E.; Vekilov, P. G. Liquid-Liquid Separation in Solutions of Normal and Sickle Cell Hemoglobin. *Proc. Natl. Acad. Sci. U. S. A.* **2002**, *99*, 8479–8483.
- (11) Dey, A.; Bomans, P. H. H.; Müller, F. A.; Will, J.; Frederik, P. M.; de With, G.; Sommerdijk, N. A. J. M. The Role of Prenucleation Clusters in Surface-Induced Calcium Phosphate Crystallization. *Nat. Mater.* **2010**, *9*, 1010–1014.
- (12) Mikhlin, Y.; Karacharov, A.; Likhatski, M.; Podlipskaya, T.; Zubavichus, Y.; Veligzhanin, A.; Zaikovski, V. Submicrometer Intermediates in the Citrate Synthesis of Gold Nanoparticles: New Insights into the Nucleation and Crystal Growth Mechanisms. *J Colloid Interface Sci* **2011**, *362*, 330–336.
- (13) Van Driessche, A. E. S.; Benning, L. G.; Rodriguez-Blanco, J. D.; Ossorio, M.; Bots, P.; García-Ruiz, J. M. The Role and Implications of Bassanite as a Stable Precursor Phase to Gypsum Precipitation. *Science (80-.)*. **2012**, *335*, 69–72.
- (14) Kim, D.; Lee, B.; Thomopoulos, S.; Jun, Y.-S. In Situ Evaluation of Calcium Phosphate Nucleation Kinetics and Pathways during Intra- and Extrafibrillar Mineralization of Collagen Matrices. *Cryst. Growth Des.* **2016**, *16*, 5359–5366.
- (15) De Yoreo, J. J. In-Situ Liquid Phase TEM Observations of Nucleation and Growth Processes. *Prog. Cryst. Growth Charact. Mater.* **2016**, *62*, 69–88.
- (16) Łukaszewska-Kuska, M.; Krawczyk, P.; Martyla, A.; Hędzerek, W.; Dorocka-Bobkowska, B. Hydroxyapatite Coating on Titanium Endosseous Implants for Improved Osseointegration: Physical and Chemical Considerations. *Adv. Clin. Exp. Med.* **2018**, *27*, 1055–1059.
- (17) Gomes, D. S.; Santos, A. M. C.; Neves, G. A.; Menezes, R. R. A Brief Review on Hydroxyapatite Production and Use in Biomedicine. *Ceramica* **2019**, *65*, 282–302.
- (18) Kattimani, V. S.; Kondaka, S.; Lingamaneni, K. P. Hydroxyapatite—Past, Present, and Future in Bone Regeneration. *Bone Tissue Regen. Insights* **2016**, *7*, BTRI.S36138.
- (19) Siddiqui, H. A.; Pickering, K. L.; Mucalo, M. R. A Review on the Use of Hydroxyapatite- Carbonaceous Structure Composites in Bone Replacement Materials for Strengthening Purposes. *Materials (Basel)*. **2018**, *11*, 1–32.

- (20) Zhou, C.; Ye, X.; Fan, Y.; Ma, L.; Tan, Y.; Qing, F.; Zhang, X. Biomimetic Fabrication of a Three-Level Hierarchical Calcium Phosphate/Collagen/Hydroxyapatite Scaffold for Bone Tissue Engineering. *Biofabrication* **2014**, *6*, 035013.
- (21) Dorozhkin, S. V.; Epple, M. Biological and Medical Significance of Calcium Phosphates. *Angew. Chemie Int. Ed.* **2002**, *41*, 3130–3146.
- (22) Yiu, A.; Callaghan, D.; Sultana, R.; Bandyopadhyay, B. Vascular Calcification and Stone Disease: A New Look towards the Mechanism. *J. Cardiovasc. Dev. Dis.* **2015**, *2*, 141–164.
- (23) Habraken, W. J. E. M.; Tao, J.; Brylka, L. J.; Friedrich, H.; Bertinetti, L.; Schenk, A. S.; Verch, A.; Dmitrovic, V.; Bomans, P. H. H.; Frederik, P. M.; et al. Ion-Association Complexes Unite Classical and Non-Classical Theories for the Biomimetic Nucleation of Calcium Phosphate. *Nat. Commun.* **2013**, *4*, 1507.
- (24) Dalmônico, G. M. L.; López, E. O.; Longuinho, M. M.; Checca, N. R.; Farina, M.; Ersen, O.; Rossi, A. M.; Rossi, A. L. Insight by Cryo-TEM into the Growth and Crystallization Processes of Calcium Phosphate Nanoparticles in Aqueous Medium. *Mater. Chem. Phys.* **2019**, *237*, 121862.
- (25) Su, X.; Wang, Y.; Zhou, J.; Gu, S.; Li, J.; Zhang, S. Operando Spectroscopic Identification of Active Sites in NiFe Prussian Blue Analogues as Electrocatalysts: Activation of Oxygen Atoms for Oxygen Evolution Reaction. *J. Am. Chem. Soc.* **2018**, *140*, 11286–11292.
- (26) Veis, A.; Dorvee, J. R. Biomineralization Mechanisms: A New Paradigm for Crystal Nucleation in Organic Matrices. *Calcif. Tissue Int.* **2013**, *93*, 307–315.
- (27) Bentov, S.; Weil, S.; Glazer, L.; Sagi, A.; Berman, A. Stabilization of Amorphous Calcium Carbonate by Phosphate Rich Organic Matrix Proteins and by Single Phosphoamino Acids. *J. Struct. Biol.* **2010**, *171*, 207–215.
- (28) Sauter, A.; Roosen-Runge, F.; Zhang, F.; Lotze, G.; Jacobs, R. M. J.; Schreiber, F. Real-Time Observation of Nonclassical Protein Crystallization Kinetics. *J. Am. Chem. Soc.* **2015**, *137*, 1485–1491.
- (29) Rincón-López, J. A.; Hermann-Muñoz, J. A.; Giraldo-Betancur, A. L.; De Vizcaya-Ruiz, A.; Alvarado-Orozco, J. M.; Muñoz-Saldaña, J. Synthetic and Bovine-Derived Hydroxyapatite Ceramics : A Comparison. *Materials (Basel)*. **2018**, *11*, 17.

- (30) Wolf, S. E.; Leiterer, J.; Kappl, M.; Emmerling, F.; Tremel, W. Early Homogenous Amorphous Precursor Stages of Calcium Carbonate and Subsequent Crystal Growth in Levitated Droplets. *J. Am. Chem. Soc.* **2008**, *130*, 12342–12347.
- (31) Tao, J.; Nielsen, M. H.; De Yoreo, J. J. Nucleation and Phase Transformation Pathways in Electrolyte Solutions Investigated by in Situ Microscopy Techniques. *Curr. Opin. Colloid Interface Sci.* **2018**, *34*, 74–88.
- (32) Mohd Pu'ad, N. A. S.; Koshy, P.; Abdullah, H. Z.; Idris, M. I.; Lee, T. C. Syntheses of Hydroxyapatite from Natural Sources. *Heliyon* **2019**, *5*, e01588.
- (33) Dey, A.; De With, G.; Sommerdijk, N. A. J. M. In Situ Techniques in Biomimetic Mineralization Studies of Calcium Carbonate. *Chem. Soc. Rev.* **2010**, *39*, 397–409.
- (34) Hariharan, M.; Varghese, N.; Cherian, A. B.; Sreenivasan, P. V; Paul, J.; Benny Cherian, A.; Sreenivasan, P. V; Paul, J.; Antony, A. K. Synthesis and Characterisation of CaCO₃ (Calcite) Nano Particles from Cockle Shells Using Chitosan as Precursor. *Int. J. Sci. Res. Publ.* **2014**, *4*, 1–5.
- (35) Štajner, L.; Kontrec, J.; Njegić Džakula, B.; Maltar-Strmečki, N.; Plodinec, M.; Lyons, D. M.; Kralj, D. The Effect of Different Amino Acids on Spontaneous Precipitation of Calcium Carbonate Polymorphs. *J. Cryst. Growth* **2018**, *486*, 71–81.
- (36) Gebauer, D.; Völkel, A.; Cölfen, H. Stable Prenucleation Calcium Carbonate Clusters. *Science (80-.)*. **2008**, *322*, 1819–1822.
- (37) Nielsen, M. H.; Aloni, S.; De Yoreo, J. J. In Situ TEM Imaging of CaCO₃ Nucleation Reveals Coexistence of Direct and Indirect Pathways. *Science (80-.)*. **2014**, *345*, 1158–1162.
- (38) Hamm, L. M.; Giuffre, A. J.; Han, N.; Tao, J.; Wang, D.; De Yoreo, J. J.; Dove, P. M. Reconciling Disparate Views of Template-Directed Nucleation through Measurement of Calcite Nucleation Kinetics and Binding Energies. *Proc. Natl. Acad. Sci.* **2014**, *111*, 1304–1309.
- (39) Tobler, D. J.; Blanco, J. D. R.; Dideriksen, K.; Sand, K. K.; Bovet, N.; Benning, L. G.; Stipp, S. L. S. The Effect of Aspartic Acid and Glycine on Amorphous Calcium Carbonate (ACC) Structure, Stability and Crystallization. *Procedia Earth Planet. Sci.* **2014**, *10*, 143–148.

- (40) Aizenberg, J.; Addadi, L.; Weiner, S.; Lambert, G. Stabilization of Amorphous Calcium Carbonate by Specialized Macromolecules in Biological and Synthetic Precipitates. *Adv. Mater.* **1996**, *8*, 222–226.
- (41) Rossi, A. L.; Barreto, I. C.; Maciel, W. Q.; Rosa, F. P.; Rocha-Leão, M. H.; Werckmann, J.; Rossi, A. M.; Borojevic, R.; Farina, M. Ultrastructure of Regenerated Bone Mineral Surrounding Hydroxyapatite-Alginate Composite and Sintered Hydroxyapatite. *Bone* **2012**, *50*, 301–310.
- (42) Freeman, C. L.; Harding, J. H.; Quigley, D.; Rodger, P. M. Structural Control of Crystal Nuclei by an Eggshell Protein. *Angew. Chemie - Int. Ed.* **2010**, *49*, 5135–5137.
- (43) Kirboga, S.; Öner, M. Application of Experimental Design for the Precipitation of Calcium Carbonate in the Presence of Biopolymer. *Powder Technol.* **2013**, *249*, 95–104.
- (44) Rieger, J.; Frechen, T.; Cox, G.; Heckmann, W.; Schmidt, C.; Thieme, J. Precursor Structures in the Crystallization/Precipitation Processes of CaCO₃ and Control of Particle Formation by Polyelectrolytes. *Faraday Discuss.* **2007**, *136*, 265–277.
- (45) Kröger, R.; Verch, A. Liquid Cell Transmission Electron Microscopy and the Impact of Confinement on the Precipitation from Supersaturated Solutions. *Minerals* **2018**, *8*.
- (46) Gower, L. B.; Odom, D. J. Deposition of Calcium Carbonate Films by a Polymer-Induced Liquid-Precursor (PILP) Process. *J. Cryst. Growth* **2000**, *210*, 719–734.
- (47) Kim, Y. Y.; Carloni, J. D.; Demarchi, B.; Sparks, D.; Reid, D. G.; Kunitake, M. E.; Tang, C. C.; Duer, M. J.; Freeman, C. L.; Pokroy, B.; et al. Tuning Hardness in Calcite by Incorporation of Amino Acids. *Nat. Mater.* **2016**, *15*, 903–910.
- (48) Orme, C. A.; Noy, A.; Wierzbicki, A.; McBride, M. T.; Grantham, M.; Teng, H. H.; Dove, P. M.; Deyoreo, J. J. Formation of Chiral Morphologies through Selective Binding of Amino Acids to Calcite Surface Steps. *Nature* **2001**, *411*, 775–779.
- (49) Hou, W.; Feng, Q. Morphology and Formation Mechanism of Vaterite Particles Grown in Glycine-Containing Aqueous Solutions. *Mater. Sci. Eng. C* **2006**, *26*, 644–647.
- (50) Gan, X.; He, K.; Qian, B.; Deng, Q.; Lu, L.; Wang, Y. The Effect of Glycine on the

Growth of Calcium Carbonate in Alkaline Silica Gel. *J. Cryst. Growth* **2017**, *458*, 60–65.

Chapter V

CHAPTER V: New roads, ongoing work and perspectives

5.1. Electrodeposition of pyrocatechol

5.1.1. About graphene production

5.1.2 Building from the scratch: pyrocatechol

5.1.2. *Post-mortem* sample after classical *ex situ* electrochemistry

5.1.3 *In situ* and identical location microscopy observations

5.2. Magnetotactic bacteria

5.3. Concluding remarks and perspectives

5.1 Electrodeposition of pyrocatechol

Electrochemically triggered reactions are of great interest for the production of a great variety of materials. Electrochemical synthesis is a well-established method to produce coatings, nanoparticles, composites and other nanostructured materials in a simple and efficient manner. However, *in-situ* characterization of the electrochemically produced coatings has rarely been addressed. This was a challenge fitted perfectly in the scope of this PhD project. This chapter will be devoted to one of the studies that are in early stages but have left very promising perspectives in the use of our *in situ* set-up to study the evolution of electrochemical reactions by identical location TEM. The case-study is the electrodeposition of pyrocatechol to potentially form graphene-like structures.

5.1.1. *About graphene production*

Carbon-based nanostructured materials, such as graphene, nanotubes and fullerenes have attracted a wide attention of the scientific community thanks to their unique electrochemical, chemical and physical properties.¹⁻³ For instance, graphene is largely studied for its high electrical conductivity, extraordinary mechanical strength and high young modulus.⁴ Its characteristics make it a great candidate for different applications in electronics,⁵ sensing devices,⁶⁻⁸ and catalysis.⁹ This is a quasi 2D platform suitable to be functionalized, either covalently or non-covalently, with different functional groups.

One of the most significant challenges is the production of graphene at large scale in a reproducible and simple way. Furthermore, production methods should allow the preservation of the striking graphene's physical and chemical properties. Since, the refinement of electrochemical responses and selectivity of the devices based on carbon nanostructures is greatly affected by their synthesis route and their subsequently purification and functionalization, overcoming the synthesis challenges would allow the production of more compact, programmable and inexpensive devices.

Among the most popular synthesis methods to obtain graphene sheets or few layers graphene, we find chemical vapor deposition (CVD),¹⁰ the scotch-tape method,¹¹ or electrochemical and chemical exfoliation¹⁵ from graphite.¹² Although these methods are extensively used, they present multiple limitations. For instance, CVD requires ultrahigh vacuum conditions, the selection of a metallic highly oriented substrate as well as very specific deposition conditions implying very high costs and many steps. On the other hand, the scotch-tape method, consists in the mechanical exfoliation or shedding layers of bulk graphite pieces. Even though this is not expensive the yields are significantly low and crystalline quality of graphene is relatively poor. Some other methodologies are based on the chemical or electrochemical exfoliation of graphene to form colloidal suspensions. These strategies generally give rise to graphene oxides or some similar species with reduced mechanical and electrochemical properties and require further steps of reduction and purification, decreasing the global yield of the reactions. More recently, techniques involving ultrasonic cavitation have become very important in the obtention of Single-Layer Graphene (SLG) or Few-Layers Graphene (FLG), among other nanostructured materials.¹³ These methods harness the energy derived from the implosions in the solvent to disperse the graphitic sheets forming colloidal-like solutions that can be stabilized with the use of surfactants and/or polymers and can be intercalated or functionalized.¹⁴⁻¹⁶

Thus, the development of simple, repeatable and scalable production methods is of great interest. In this regard, the bottom-up production of nano platelets and nanoribbons of graphene has gained interest given the control over the surfaces formed. Typically, the fusion of organic fragments to produce 2D graphenic surfaces, requires multiple synthesis steps.¹⁷ However, the use of organic redox couples could yield the desired structures. This is aim of the work developed by Prof. Vincent Ball from the University of Strasbourg, who has been evaluating the types of structures that can be obtained by

the electrochemical polymerization of simple bioderived building blocks like catecholamines (dopamine for instance) or catechols/polyphenols.

5.1.2 Building from the scratch: Pyrocatechol

The 1,2-dihydroxybenzene, also known as pyrocatechol, is a diol derived from the metabolism of multiple natural products (figure 5.1). This type of molecules, catechols, are good models to study more complex biological structures, like dopamine. A redox equilibrium occurs between the reduced form catechol, and the oxidized form ketone (molecule 2 in figure 5.1). The carbons in the opposite side of the ring can be attacked nucleophilically and polymerize.

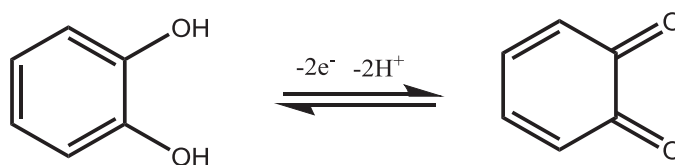


Figure 5.1. Structure of 1,2-dihydroxybenzene or pyrocatechol and its equilibrium with the quinone.

In this study, a solution of pyrocatechol at $1\text{ mg}\cdot\text{mL}^{-1}$ was prepared in a 50 mM sodium acetate buffer at $\text{pH} = 5.0$. This solution was used as the electrolyte in a three electrodes electrochemical cell (Chi 604B, ChInstruments), with a glassy carbon disc as the working electrode, an Ag/AgCl reference electrode and a Pt wire as the counter electrode..

Amorphous carbon electrodes (ref Chi 104, ChInstruments) were successively polished on SiC cloth with two different mesh Al_2O_3 slurries (1 and $0.1\mu\text{m}$, Escil, Villeurbanne, France) before sonication in two water baths for 2 min each. The electrodeposition of pyrocatechol on such an electrode was performed from the $1\text{ mg}\cdot\text{mL}^{-1}$ pyrocatechol buffered electrolyte by sweeping the potential at $20\text{ mV}\cdot\text{s}^{-1}$ between -0.6 and 1.0 V versus Ag/AgCl using an Ag/AgCl reference electrode (ref ChI 111) and a Pt wire counter electrode (ref. ChI 115).

The current density decreases upon each voltammetry cycle (Figure 5.2), which indicates the electrodeposition of a less conductive material on the anode.

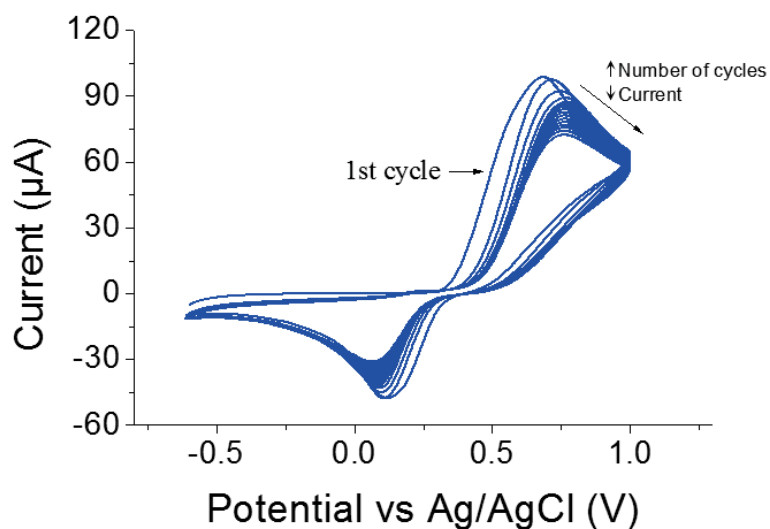


Figure 5.2. 50 voltammetry cycles performed in a 1 mg mL^{-1} pyrocatechol at buffered electrolyte at 20 mV s^{-1} between -0.6 and 1.0 V versus Ag/AgCl.

5.1.2. Post-mortem sample after classical ex situ electrochemistry

When the sample was scratched from the glassy carbon electrode and observed *post mortem* by STEM. After 50 voltammetric cycles platelets of few micron wide were found. Additionally, EDS mapping in figure 5.3, the platelets are uniformly composed of C, N and O. However, there is a difference in contrast at different regions of the resulting platelets. This indicates unhomogeneous crystalline ordering. Furthermore, we found diffracting nano-platelets presented in figure 5.4.

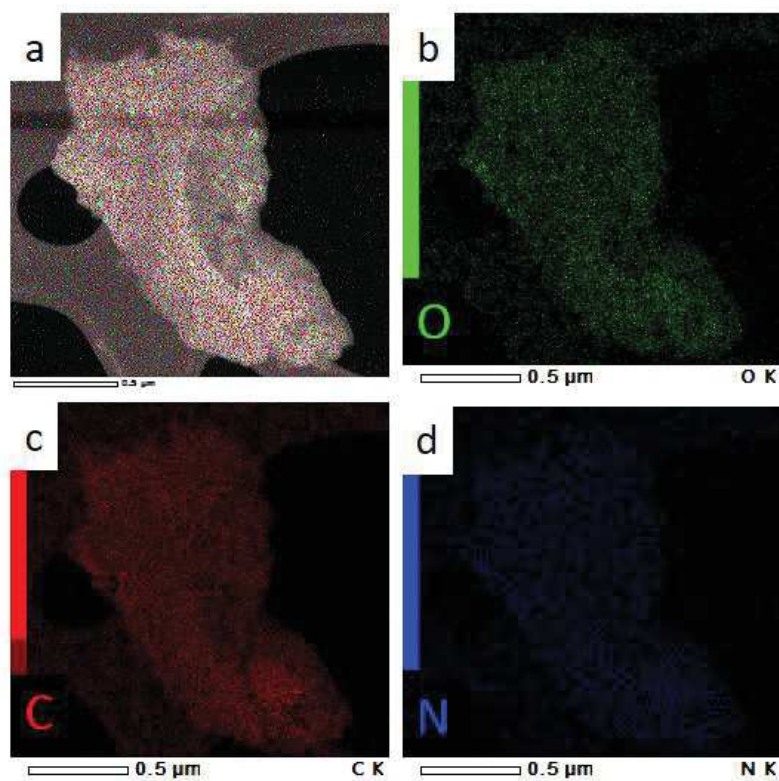


Figure 5.3. a) Dark field- STEM image of the graphene-like platelets formed over glassy carbon after 50 voltammetric cycles in a three electrodes classical electrochemical cell at a potential sweep rate of 20 mV/s. Chemical distribution of b) oxygen, c) carbon and d) nitrogen over the sheet.

As in the case of cobalt oxide in chapter 2, the less contrasting regions are probably amorphous. Furthermore, the more contrasted regions are small platelets. The fourier transform of the figure 5.4c present diffraction spots that can correspond to a graphene-like structure.

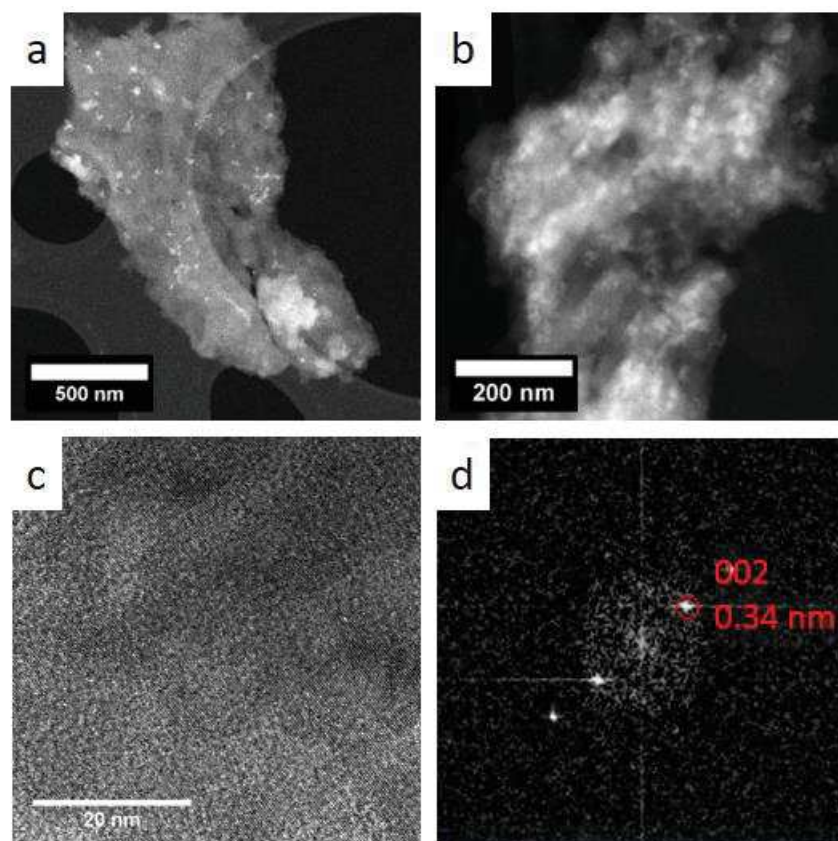


Figure 4. a-b) STEM dark-field image from a sample recovered from the amorphous carbon electrode after 50 cycles performed in 1 mg mL^{-1} pyrocatechol at buffered electrolyte at 20 mV s^{-1} between -0.6 and 1.0 V versus Ag/AgCl . c) high-resolution TEM image displaying lattice orientations on the recovered nano-plates d) shows an FFT of the area shown in (c).

The formation of graphene platelets from the electrochemical oxidation of pyrocatechol in a aqueous electrolyte is rather unexplored but would be a breakthrough in the bottom-up obtention of graphenic structures. Our observation suggests that the electrochemical oxidation drives the growth of a polycyclic structure. Figure 5.5 shows the known oxidation pathways of catechol to form triphenylenes derivatives, that could be the result of the reaction.

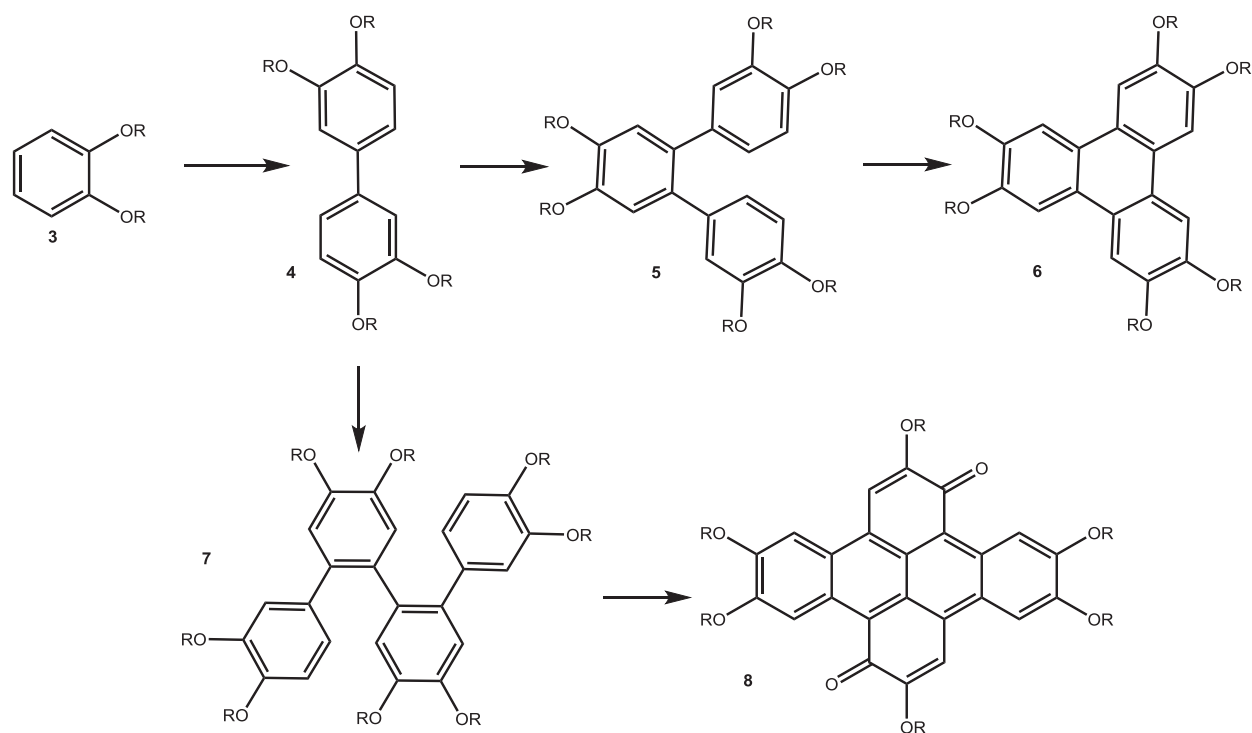


Figure 5.5. Known oxidation pathways of catechol.¹⁸

5.1.3 *In situ* and identical location microscopy observations

The 1 mg mL^{-1} pyrocatechol solution in a 50 mM sodium acetate buffer at $\text{pH} = 5.0$ was prepared right before every experiment. The pyrocatechol can get oxidized by the environmental oxygen in basic conditions which justifies the use of an acetate buffer at $\text{pH} = 5$ ensuring the stability of the solute in the absence of an exogenous oxidant. This solution was flushed into the miniaturized EC cell at $25 \text{ } \mu\text{L min}^{-1}$. Cyclic voltammetry experiments were then performed at 20 mV/s from -0.6 V to 1.0 V vs Pt pseudo-reference electrode, in order to mimic as closely as possible the *ex situ* conditions. Note however that the electric field lines are not the same in the *ex-situ* and in the *in-situ* electrochemical cell. It cannot be excluded that the difference in the experimental cell design may have an influence on the oxidation of pyrocatechol and its subsequent polymerization even if the potential range and the potential sweep rate were the same in both experiments.

In order to verify that the formation of such structures do not arise as a consequence of the electron beam, the solution was irradiated over 15 to 20 min before launching the cyclic voltammetry. After several minutes of exposure without any electrochemical stimuli, there was no sign of growth ([annex movie M15](#)). Once the cyclic voltammetry

was launched, it was possible to observe sheet-like structures within the liquid ([annex movie M16](#)). In spite of the continuous vigilance over the electrode and its vicinity, it was not possible to observe in real time the formation of such structures. However, as can be seen in figure 5.6, after 25 CV cycles, the *post in situ* analysis of the chip showed that the electrochemical oxidation of pyrocatechol forms fewmicrons-wide sheets. These structures were not found in regions apart from the electrode as at the edge of the observation window. This latter fact, shows that the polymerization of the catechol units is triggered by the potential sweep and not by the e⁻ beam, since only the regions in the reach of the electric field permitted the growth of the crystalline carbon-based sheets.

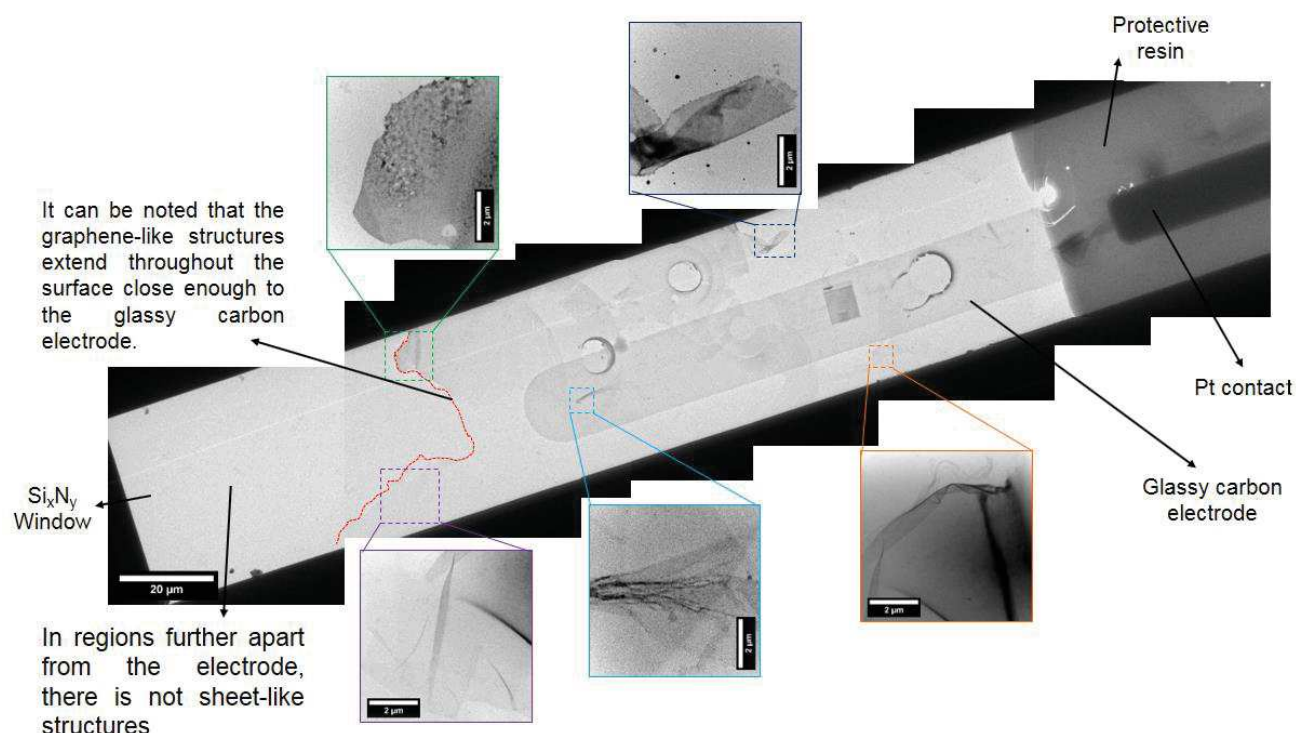


Figure 5.6. *Post in situ* low magnification image of the observation window after 25 CV cycles at 20 mV.s⁻¹ between -0.6 and 1.0 V versus the Pt counterelectrode.

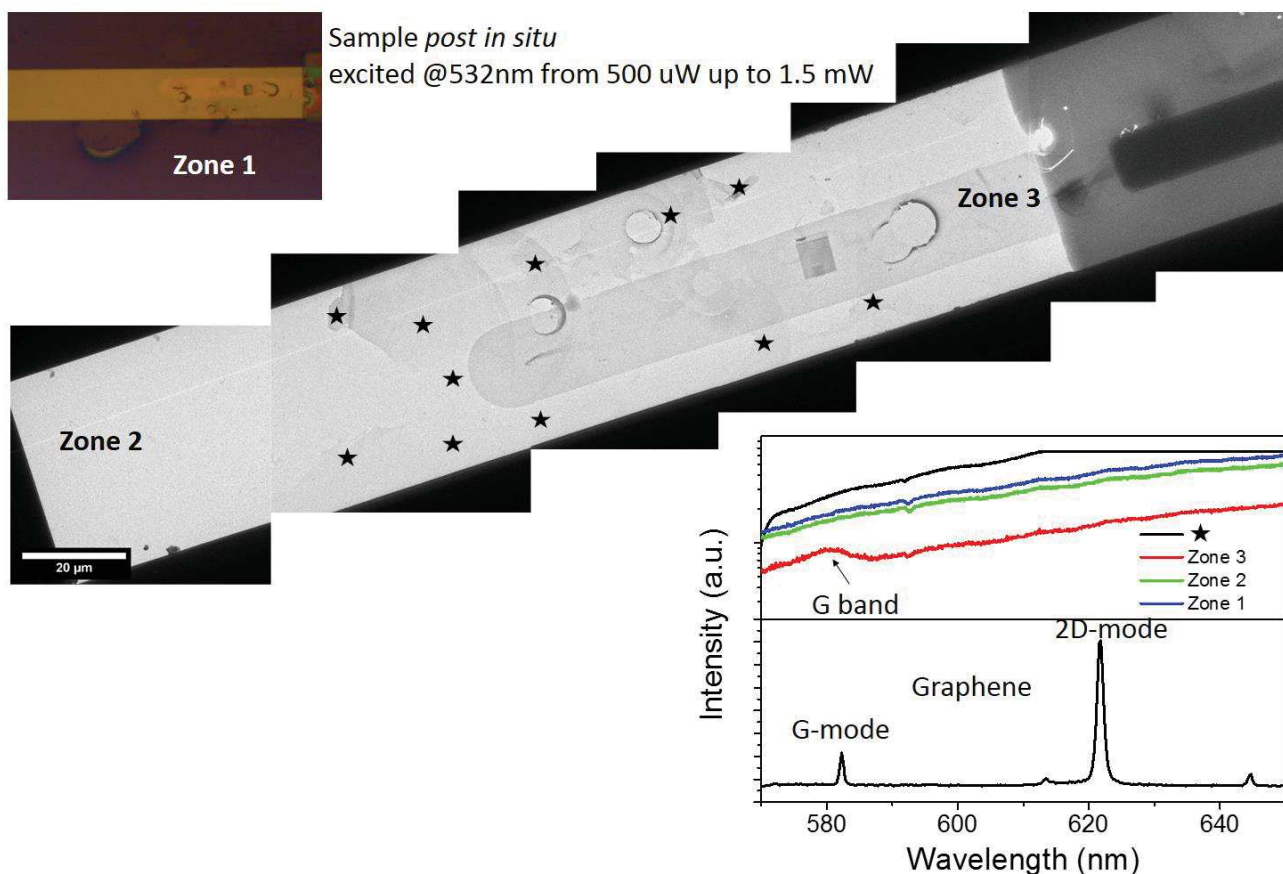


Figure 5.7. *Post in situ* Raman spectra of different regions in the observation window after 25 CV cycles at $20 \text{ mV}\cdot\text{s}^{-1}$ between -0.6 and 1.0 V . It is only possible to detect the G band in the zone where the carbon electrode is placed.

Raman spectroscopy is an important characterization technique for graphene-like structures.¹⁹ Extensive studies combined with Atomic Force Microscopy (AFM) and Scanning Electron Microscopy (SEM) have shown that the Raman shift of the typical signals for graphitic compounds changes depending on the thickness (number of layers) present in the sample^{19,20}. Carbon-derived materials are characterized by the G and D bands, corresponding to the stretching and breathing modes of sp^2 carbons, respectively^{21,22}. Thus, Raman spectroscopy was used to analyse different regions of the *post in situ* sample (figure 5.7). The presence of the characteristic G band is only detectable over the glassy carbon electrode. The regions where the sheets are observed by electron microscopy do not present neither the G or D bands. Although, this is troublesome, it might be due to the fluorescence produced by the silicon nitride window that is several times thicker than a graphene layer or even few layers graphene.²³ Thereby future complementary measurements will require the use of different laser

wavelengths allowing shifting the peaks of interest while decreasing the effect of the background.²⁴

The *in situ* liquid phase TEM observation of the electrodeposition process is extremely difficult in real time due to the very poor contrast of the organic material within the “very thick” liquid layer. However, the miniaturized cell, allows to track a specific ROI from the beginning and after each cycle, by extracting the chip and removing the liquid. Hence, we started by introduce the pyrocatechol solution through the microfluidic system to a pristine chip. Then, we launched the cyclic voltammetry. In figure 5.8, the chip is observed after having performed 2, 4 and 8 voltammetric cycles. Already from the second cycle, we found a nanoplatelet close to the electrode. The diffraction patterns of the platelet displayed its crystallinity and how it evolved over further potential cycling.

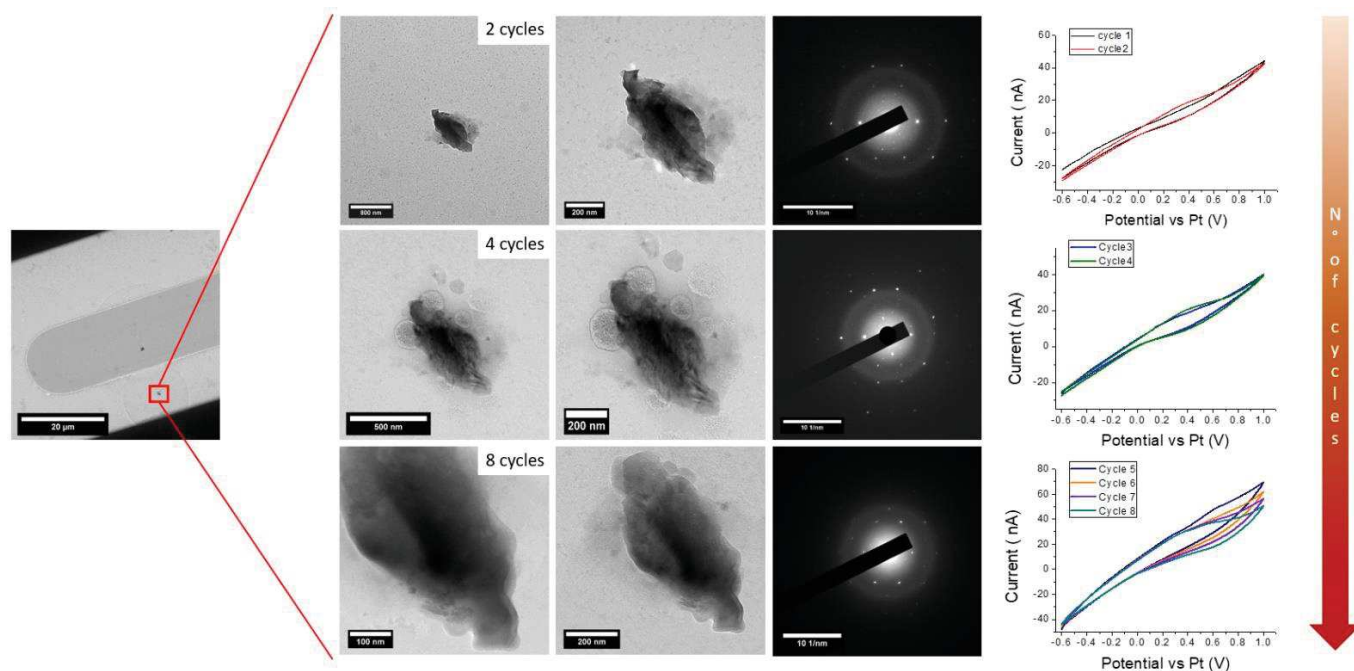


Figure 5.8. Identical location TEM images and its corresponding SAED pattern after 2, 4 and 8 cycles at $20 \text{ mV}\cdot\text{s}^{-1}$ between -0.6 and 1.0 V in the presence of pyrocatechol at $1 \text{ mg}\cdot\text{mL}^{-1}$.

The evolution of the electron diffraction patterns is presented in figure 5.9. From the very first 2 cycles a very intense diffraction spot at lattice spacing of 0.24 nm characteristic of the interplanar distance between graphitic planes is observed.^{17,25} Nevertheless, this pattern presents also less intense diffraction rings, circled in figure 5.9a, evidencing the polycrystalline character of the deposit. After 4 cycles, the rings become almost imperceptible although different spots of various intensities in the

background are still distinguishable. Very close spots might arise probably from pillared-up graphene-like platelets. Finally, after 8 cycles much less diffraction spots in the background can be detected, indicating possibly a tendency towards a higher monocrystalline character of the deposit.

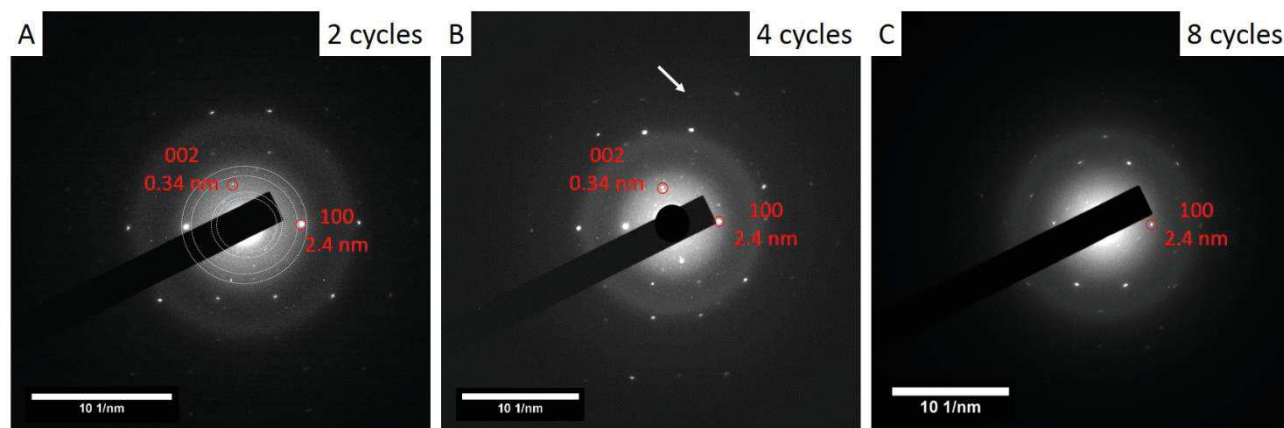


Figure 5.9. SAED patterns after 2, 4 and 8 cycles at $20 \text{ mV}\cdot\text{s}^{-1}$ between -0.6 and 1.0 V in the presence of pyrocatechol at $1 \text{ mg}\cdot\text{mL}^{-1}$.

Next steps will include a more extended identical location study to determine if the relatively small graphene-like plates can grow to a few micrometers-wide sheet with a precise crystalline organization. Furthermore, other *in situ* techniques, such as SAXS, should be used to determine the evolution in the electronic structure during the electrodeposition.

5.2. Magnetotactic bacteria

In chapter 4, the interest on mineralization in biological and biomimetic systems was discussed. Two cases of study concerning the mineralization of calcium phosphates and carbonates were analyzed. Along those lines, and in the frame of the same collaboration with Brazil, we have initiated the study of the biomineralization of iron oxide nanoparticles within magnetotactic bacteria. Magnetotactic bacteria are aquatic prokaryotic microorganisms able to orient and migrate along a magnetic field lines.²⁶ This unique ability arises from the presence of nanoscopic particle chains of magnetite (Fe_3O_4) or greigite (Fe_3S_4) within internal vesicles.²⁷ The nanocrystals, called magnetosomes, have nearly perfect mineral crystal structures with consistent species-specific morphologies, leading to well-defined magnetic properties.^{28–30} As mentioned in chapter 3, magnetic nanoparticles are widely studied for multiple applications.

Therefore, the comprehension of the biological formation mechanism of such nanoparticles withdraws major attention in the biomimetic materials field. Furthermore, these single-cell micro-organism are great candidates to serve as a model for other biomineralization processes.

Magnetite biomineralization in these bacteria is a multistep process involving a number of stages including cellular uptake and reduction of ferric ions, complexation of the iron with membrane proteins, and nucleation and growth of mature magnetosomes. In figure 10 is a schematic representation of the stages involve in the mineralization within the bacteria. Despite decades of intense research, this process is still not fully understood.^{29,31,32} It is known that a variety of biological macromolecules are involved in the mineralization process, specifically membrane bound proteins which play an important role in templating biomineralized magnetosome magnetite crystals, although their exact role remains unclear.³³

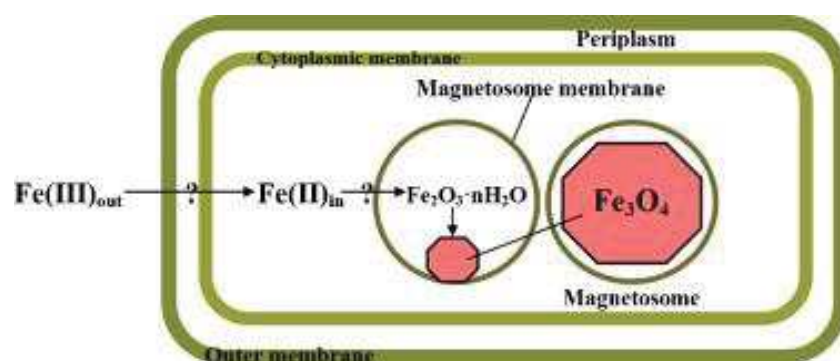


Figure 5.10. Proposed model for magnetite biomineralization in Magnetospirillum species. Fe(III) is actively taken up by the cell, possibly via a reductive step. Iron is then thought to be reoxidized. In the last step, one-third of the Fe(III) ions are reduced, and magnetite is produced within the magnetosome vesicle. The magnetosome membrane contains specific Mam proteins, which are thought to have crucial functions in the accumulation of iron, nucleation of minerals, and redox and pH control. Adapted from ref ³⁴

The implementation of *in situ* liquid phase TEM experiments is pivotal to address the questions regarding the biomineralization process within the bacteria. Thus, Woehl, et al.²⁷ have used correlated fluorescence microscopy and *in situ* liquid phase TEM showing that it is possible visualizing magnetosome structures while retaining an intact bacterial cell membrane. Moreover, Shokuhfar, et al.³² have shown the viability of observing *in situ* living magnetotactic bacteria carrying out the biomineralization process within a graphene pocket.

Magnetotactic bacterium strain MV-1^T ('magnetic vibrio 1') was cultivated in an iron-depleted medium in order to have magnetosome-free cells following Bazylinski, et al. protocol.³⁶ A drop of bacteria-containing solution was drop-casted over a poly-L-lysine coated chip. The poly-L-lysine was previously deposited over the chip as described in the literature.³⁰ This was done in order to facilitate the fixation of the bacteria over the chip. The excess of liquid was removed and the cell was closed. Once the holder was introduced in the microscope, an iron-rich solution was flowed through the microfluidic system in order to feed the bacteria. The magnetosome-free cells have a very poor contrast within the liquid, which makes the observation very challenging. Nonetheless, we succeeded in observing the iron-enrichment of the magnetosome membrane (Figure 5.11). Multiple regions within the bacteria were observed to accumulate the iron. No further changes were observed in the bacteria in the figure 11, probably due to an electron beam-induced death.

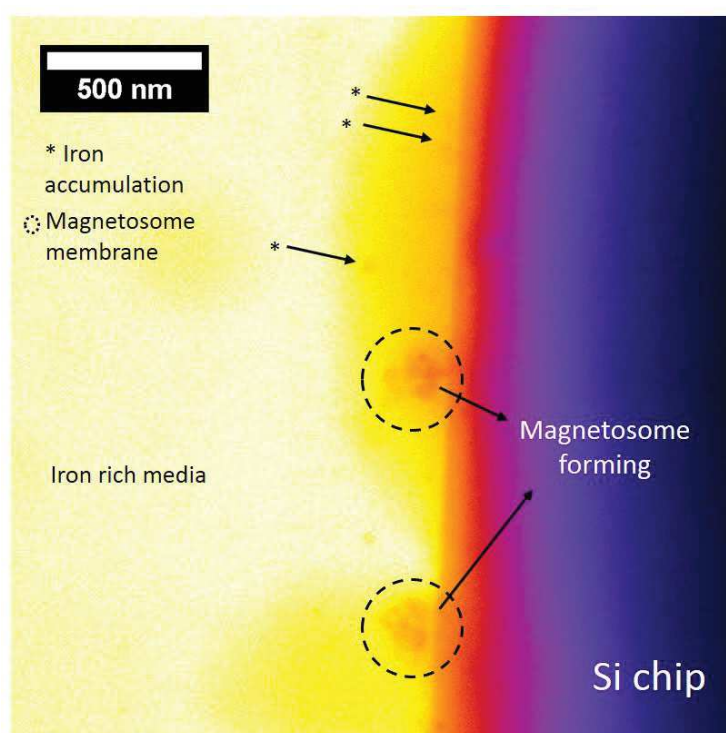


Figure 5.11. *In situ* liquid TEM image of the iron enrichment of the magnetosome membrane in the MV-1^T bacteria.

The *post in situ* analysis of figure 12a showed cases where there is no presence of magnetite nanoparticles but it is possible to distinguish accumulated iron-islands. Such accumulated iron displayed some diffraction contrast. Furthermore, in figure 12b typical

iron oxide magnetosomes were found. In the extremity of the bacteria, smaller developing magnetosome can be observed.

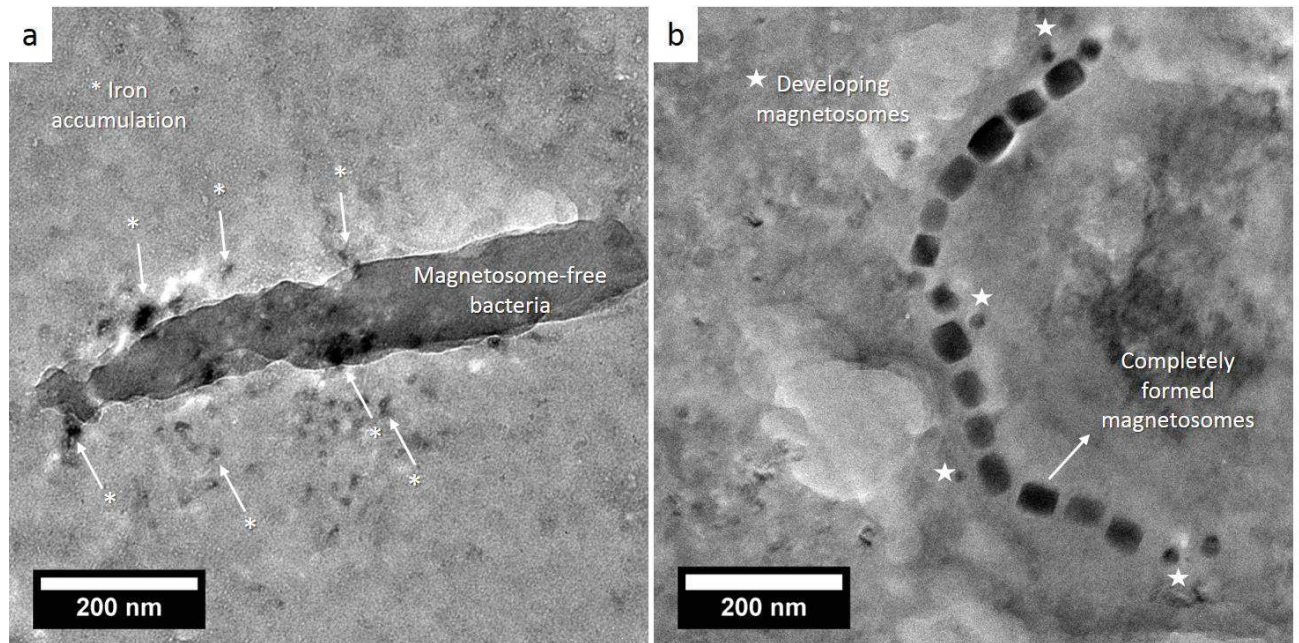


Figure 12. *Post in situ* images of the growth of magnetosomes in MV-1T bacteria. a) Magnetosome-free bacterium surrounded by iron-enriched islands. b) Completely formed and developing magnetosomes.

Thus, this preliminary results shows that the poly-l-lysine coating of the *in situ* chip surface allows attaching and observing iron-starved MV1 bacterium cells. In addition, we determined that one of the main requirements to help the success of this challenging experiment is to start flowing through the cell a liquid without iron and, only after the holder has been inserted into the microscope, to change the flowing medium with an iron rich one. However, the experiment duration should be optimized in order to be able to observe living bacteria. The next step will be to repeat the last experiment by using chips with a thin liquid space, in order to maximize the signal-to-noise ratio on the *in situ* liquid TEM videos to be acquired.

5.3. Concluding remarks and perspectives

The formation of carbon-based sheets from the electrochemical oxidation of pyrocatechol in solution promises to be a noticeable development in the fabrication of graphene layers. Furthermore, the insight that *in situ* electrochemical and identical location transmission

electron microscopy can give insights in the mechanisms governing this reaction should be highly beneficial for the rapid progress of the method.

Regarding the observation of living microorganisms and cells within the liquid TEM set-up, major challenges concerning the electron beam effect and the immobilization of the cells have to be overcome.³⁷ Nonetheless, the implementation of this technique opens exciting paths in the comprehension of the most impressive machines in the universe: living organisms!

New projects harnessing the possibilities brought by the *in situ* liquid set-up are starting in the group. A PhD project continuing with the study of biomineralization processes over different substrates and in different biomimetic matrixes. In addition, the study of the oriented attachment of aluminum oxide to form bohemite needles is starting this year.

5.4. References

- (1) Allen, M. J.; Tung, V. C.; Kaner, R. B. Honeycomb Carbon: A Review of Graphene. *Chem. Rev.* **2010**, *110*, 132–145.
- (2) Ren, S.; Rong, P.; Yu, Q. Preparations, Properties and Applications of Graphene in Functional Devices: A Concise Review. *Ceram. Int.* **2018**, *44*, 11940–11955.
- (3) Zhong, Y.; Zhen, Z.; Zhu, H. Graphene: Fundamental Research and Potential Applications. *FlatChem* **2017**, *4*, 20–32.
- (4) Geim, A. K. Graphene: Status and Prospects. *Science (80-.)*. **2009**, *324*, 1530–1534.
- (5) Avouris, P. Graphene: Electronic and Photonic Properties and Devices. *Nano Lett.* **2010**, *10*, 4285–4294.
- (6) Amin, K. R.; Bid, A. Graphene as a Sensor. *Curr. Sci.* **2014**, *107*, 430–436.
- (7) Shao, Y.; Wang, J.; Wu, H.; Liu, J.; Aksay, I. A.; Lin, Y. Graphene Based Electrochemical Sensors and Biosensors: A Review. *Electroanalysis* **2010**, *22*, 1027–1036.
- (8) Galpaya, D. Recent Advances in Fabrication and Characterization of Graphene-Polymer Nanocomposites. *Graphene* **2012**, *01*, 30–49.

- (9) Fan, X.; Zhang, G.; Zhang, F. Multiple Roles of Graphene in Heterogeneous Catalysis. *Chem. Soc. Rev.* **2015**, *44*, 3023–3035.
- (10) Park, S.; Ruoff, R. S.; Engineering, M. Chemical Methods for the Production of Graphenes. *Nat. Nanotechnol.* **2009**, *4*, 217–224.
- (11) Novoselov, K. S.; Geim, A. K.; Morozov, S. V.; Jiang, D.; Zhang, Y.; Dubonos, S. V.; Grigorieva, I. V.; Firsov, A. A. Electric Field Effect in Atomically Thin Carbon Films. *Science (80-.)*. **2004**, *306*, 666–669.
- (12) Wei, D.; Grande, L.; Chundi, V.; White, R.; Bower, C.; Andrew, P.; Ryhänen, T. Graphene from Electrochemical Exfoliation and Its Direct Applications in Enhanced Energy Storage Devices. *Chem. Commun.* **2012**, *48*, 1239.
- (13) Bang, J. H.; Suslick, K. S. Applications of Ultrasound to the Synthesis of Nanostructured Materials. *Adv. Mater.* **2010**, *22*, 1039–1059.
- (14) Ciesielski, A.; Samorì, P. Supramolecular Approaches to Graphene: From Self-Assembly to Molecule-Assisted Liquid-Phase Exfoliation. *Adv. Mater.* **2016**, *28*, 6030–6051.
- (15) Narayan, R.; Kim, S. O. Surfactant Mediated Liquid Phase Exfoliation of Graphene. *Nano Converg.* **2015**, *2*, 1–20.
- (16) Ihiawakrim, D.; Ersen, O.; Melin, F.; Hellwig, P.; Janowska, I.; Begin, D.; Baaziz, W.; Begin-Colin, S.; Pham-Huu, C.; Baati, R. A Single-Stage Functionalization and Exfoliation Method for the Production of Graphene in Water: Stepwise Construction of 2D-Nanostructured Composites with Iron Oxide Nanoparticles. *Nanoscale* **2013**, *5*, 9073–9080.
- (17) Jordan, R. S.; Wang, Y.; McCurdy, R. D.; Yeung, M. T.; Marsh, K. L.; Khan, S. I.; Kaner, R. B.; Rubin, Y. Synthesis of Graphene Nanoribbons via the Topochemical Polymerization and Subsequent Aromatization of a Diacetylene Precursor. *Chem* **2016**, *1*, 78–90.
- (18) Voisin, E.; Williams, V. E. Do Catechol Derivatives Electropolymerize? *Macromolecules* **2008**, *41*, 2994–2997.
- (19) Mak, K. F.; Shan, J.; Heinz, T. F. Electronic Structure of Few-Layer Graphene: Experimental Demonstration of Strong Dependence on Stacking Sequence. *Phys. Rev. Lett.* **2010**, *104*, 1–4.

- (20) Ferrari, A. C.; Meyer, J. C.; Scardaci, V.; Casiraghi, C.; Lazzeri, M.; Mauri, F.; Piscanec, S.; Jiang, D.; Novoselov, K. S.; Roth, S.; et al. Raman Spectrum of Graphene and Graphene Layers. *Phys. Rev. Lett.* **2006**, *97*, 187401.
- (21) Castiglioni, C.; Tommasini, M.; Zerbi, G. Raman Spectroscopy of Polyconjugated Molecules and Materials: Confinement Effect in One and Two Dimensions. *Phil. Trans. R. Soc. Lond. A* **2004**, *362*, 2425.
- (22) Castiglioni, C.; Negri, F.; Rigolio, M.; Zerbi, G. Raman Activation in Disordered Graphites of the A₁ Symmetry Forbidden K \neq 0 Phonon: The Origin of the D Line. *J. Chem. Phys.* **2001**, *115*, 3769–3778.
- (23) Wei, D.; Chen, S.; Liu, Q. Review of Fluorescence Suppression Techniques in Raman Spectroscopy. *Appl. Spectrosc. Rev.* **2015**, *50*, 387–406.
- (24) Martins, M. A. da S.; Ribeiro, D. G.; Pereira dos Santos, E. A.; Martin, A. A.; Fontes, A.; Martinho, H. da S. Shifted-Excitation Raman Difference Spectroscopy for in Vitro and in Vivo Biological Samples Analysis. *Biomed. Opt. Express* **2010**, *1*, 617.
- (25) Bordes, E.; Morcos, B.; Bourgogne, D.; Andanson, J.-M.; Bussière, P.-O.; Santini, C. C.; Benayad, A.; Costa Gomes, M.; Pádua, A. A. H. Dispersion and Stabilization of Exfoliated Graphene in Ionic Liquids. *Front. Chem.* **2019**, *7*, 1–14.
- (26) Prozorov, T. Magnetic Microbes: Bacterial Magnetite Biomineralization. *Semin. Cell Dev. Biol.* **2015**, *46*, 36–43.
- (27) Bazylizinki, D. A.; Heywood, B. R.; Mann, S.; Frankel, R. B. Fe₃O₄ and Fe₃S₄ in a Bacterium. *Nature* **1993**, *366*, 218–218.
- (28) Bazylinski, D. A.; Frankel, R. B. Magnetosome Formation in Prokaryotes. *Nat. Rev. Microbiol.* **2004**, *2*, 217–230.
- (29) Bazylinski, D. A. Synthesis of the Bacterial Magnetosome: The Making of a Magnetic Personality. *Int. Microbiol.* **1999**, *2*, 71–80.
- (30) Woehl, T. J.; Kashyap, S.; Firlar, E.; Perez-Gonzalez, T.; Faivre, D.; Trubitsyn, D.; Bazylinski, D. A.; Prozorov, T. Correlative Electron and Fluorescence Microscopy of Magnetotactic Bacteria in Liquid: Toward In Vivo Imaging. *Sci. Rep.* **2015**, *4*, 6854.
- (31) Frankel, R. B.; Bazylinski, D. A. Magnetosomes: Nanoscale Magnetic Iron

Minerals in Bacteria. *Nanobiotechnology* **2005**, No. May 2018, 136–145.

- (32) Komeili, A.; Vali, H.; Beveridge, T. J.; Newman, D. K. Magnetosome Vesicles Are Present before Magnetite Formation, and MamA Is Required for Their Activation. *Proc. Natl. Acad. Sci.* **2004**, *101*, 3839–3844.
- (33) Prozorov, T.; Mallapragada, S. K.; Narasimhan, B.; Wang, L.; Palo, P.; Nilsen-Hamilton, M.; Williams, T. J.; Bazylinski, D. A.; Prozorov, R.; Canfield, P. C. Protein-Mediated Synthesis of Uniform Superparamagnetic Magnetite Nanocrystals. *Adv. Funct. Mater.* **2007**, *17*, 951–957.
- (34) Schuler, D. The Biomineralization of Magnetosomes in *Magnetospirillum Gryphiswaldense*. *Int. Microbiol.* **2002**, *5*, 209–214.
- (35) Firlar, E.; Ouy, M.; Bogdanowicz, A.; Covnot, L.; Song, B.; Nadkarni, Y.; Shahbazian-Yassar, R.; Shokuhfar, T. Investigation of the Magnetosome Biomineralization in Magnetotactic Bacteria Using Graphene Liquid Cell-Transmission Electron Microscopy. *Nanoscale* **2019**, *11*, 698–705.
- (36) Bazylinski, D. A.; Williams, T. J.; Lefèvre, C. T.; Trubitsyn, D.; Fang, J.; Beveridge, T. J.; Moskowicz, B. M.; Ward, B.; Schübbe, S.; Dubbels, B. L.; et al. *Magnetovibrio Blakemorei* Gen. Nov., Sp. Nov., a Magnetotactic Bacterium (Alphaproteobacteria: Rhodospirillaceae) Isolated from a Salt Marsh. *Int. J. Syst. Evol. Microbiol.* **2013**, *63*, 1824–1833.
- (37) De Jonge, N.; Peckys, D. B. Live Cell Electron Microscopy Is Probably Impossible. *ACS Nano* **2016**, *10*, 9061–9063.

Conclusion

Conclusion

Enhancing the comprehension of dynamical processes at the nanoscale, such as the formation and the degradation of solids, as well as the mechanisms of heterogeneous catalysis, is pivotal to improve production methods and/or to identify the suitable conditions of implementation of a material into functional devices. Characterization techniques must evolve to reach this level of understanding, especially through real time monitoring of the evolution of materials in synthesis or operational environments. The development of *in situ* liquid transmission electron microscopy fits in this frame, by enabling monitoring changes at the nanometer scale in real time and conditions close to those applied for synthesis for actual use of the materials. In this thesis, we have focused on harnessing *in situ* liquid transmission electron microscopy to address electrocatalysts in operation, inorganic nanoparticles, biomimetic crystals and electroactive materials in the course of their formation.

In order to obtain reliable and representative data, *in situ* liquid TEM requires thoughtful planning of the experiment and careful analysis of the results in comparison to conventional experiments. Therefore, in chapter 1, we have focused on practical aspects of the implementation of *in situ* liquid TEM. We have presented an inventory of elements to consider before, during and after performing *in situ* experiments: Sample preparation and deposition, choice of the imaging mode, of the electron dose and factors influencing the resolution. Then, specific considerations for the study of electrocatalytic materials were presented. Final considerations for *post in situ* analysis were also discussed. These practical notes were formulated based on various reports from the literature and our own experiments presented in the subsequent chapters. Overall, we have shown that each sample requires a specific set of conditions to be properly studied.

Then, in chapter 2, we have used cobalt oxide nanoparticles during oxygen evolution reaction as a case-study to demonstrate the benefits of tracking in real time the nanoscale transformations of electrocatalysts. Simultaneous recording of images and electrochemical measurements allowed relating *in operando* surface amorphization of the nanocatalyst surface with the catalytic activity. Moreover, this study showed that such amorphization is irreversible contrary to previous reports from *in situ* experiments that used characterization techniques not suitable to assess the nanoscale. The

differences of the *in situ* set-up with a conventional electrochemical cell were taken into account to insure that the morphological changes observed *in situ* were representative of typical electrocatalytic events. We expect that the methodological steps developed herein will help for a more extended application of this technique in the study of other electrocatalytic materials.

In chapter 3, we studied nucleation and growth of nanocrystals in a typical colloidal synthesis. *In situ* liquid phase TEM provided valuable information about the pre-nucleation stages of iron oxide nanoparticles formed by thermal decomposition. The detection of pre-nucleation assemblies, vesicles and reverse micelles, revealed that crystallization occurs in a non-classical fashion. We showed that nucleation takes place inside the pre-nucleation assemblies. This observation suggests that the hydration of the precursors can influence the nucleation pathway. Thereafter, we studied the influence of the amount of energy input on the final morphology of the nanoparticles. By varying the electron dose, we showed that the particle anisotropy is directly link to the energy input. At high electron doses, the morphology tends to be spherical and, inversely, a lower electron doses favors anisotropic morphologies. Such a direct evidence of the electron dose influence on the final shape is very significant, since fine-tuning of the morphology of magnetic nanoparticles is key for their implementation in different applications.

A different case of crystallization was considered in chapter 4. Biomimetic mineral formation of calcium phosphate and calcium carbonate was addressed. Both systems, of great interest for the comprehension of biomineral-based materials, were studied to scrutinize their crystallization pathway in non-biomimetic conditions. Differently from the previous chapter, the presence of pre-nucleation stages was attributed to the formation of ionic dense liquids. The existence of such ionic dense liquids indicated that the crystallization occurs again through non-classical pathways. We propose five crystallization stages, more clearly observed in the case of calcium carbonate: (1) ionic dense liquid droplets, (2) aggregation of the ionic dense liquids, (3) amorphous precursors aligning and agglomerating to form chains and branches, (4) reorganization of some of the branches aligned and sticked to other crystallites while some other appeared and disappeared, (5) final morphology. Latter steps of this study included evaluating the influence of different aminoacids in the biomineralization. Additional insight was achieved by direct observation of the intermediate states formed in the presence of aspartic acid and glycine, known to slow down the crystallization of calcium carbonate. Following this first research track, a PhD project has been launched in order

to definitively identify the nature of the different stages along with the thermodynamic and kinetic implications of the presence of aminoacids during the crystallization.

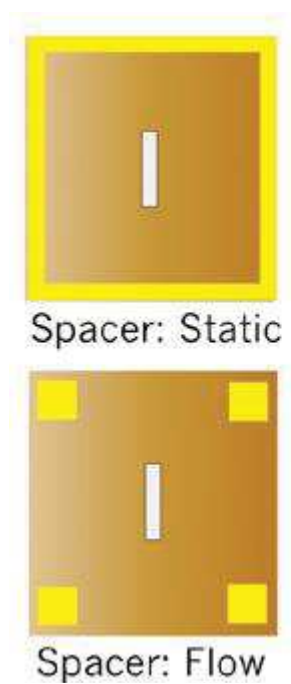
Finally, we ended by exploring the electrodeposition of electroactive films from basic organic building blocks. We were able to track the progressive growth of carbon-based platelets with crystallinity gradually increasing. Future studies should enable determining the formation and crystallization mechanisms in such systems. Studies involving living micro-organisms and cells are also envisioned in forthcoming applications of *in situ* liquid phase TEM.

Although there is still a lot of work to be done in order to deliver routine *in situ* liquid TEM experiments, the implementation of this technique definitely complements the information brought by other *in situ* techniques and contributes to a better understanding of the dynamic processes at the nanoscale in liquids.

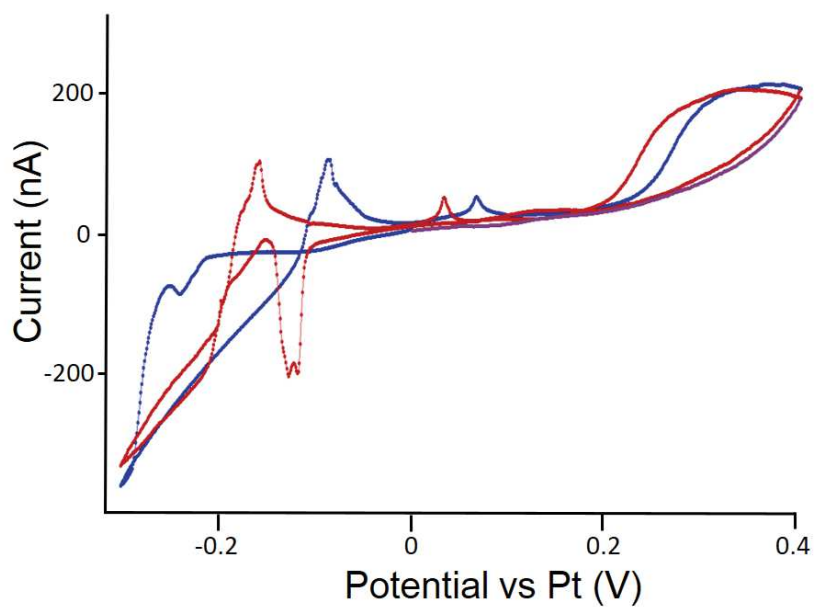
Annexes

Annexes

Annex 1. Bottom chip spacer design. Taken from ref ¹

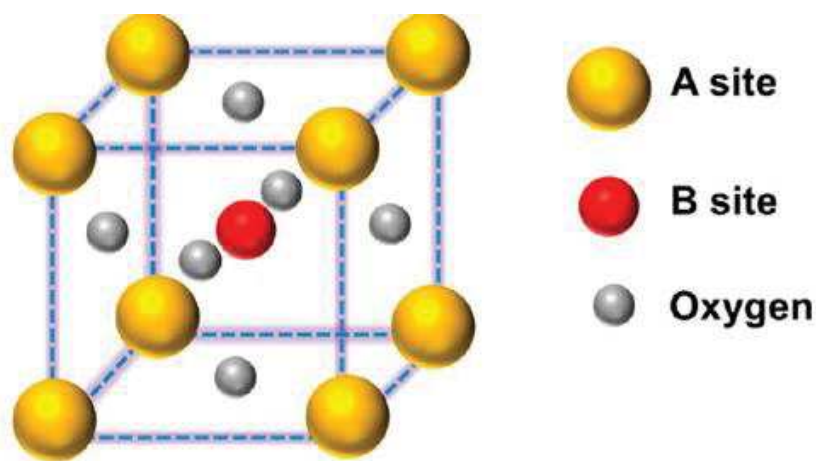


Annex 2. Cyclic voltammetry measurements at 20 mV/s of $\text{La}_{0.7}\text{Sr}_{0.3}\text{MnO}_4$ within the *in situ* set-up 2 mM $\text{K}_3\text{Fe}(\text{CN})_6$ and 2 mM $\text{K}_4\text{Fe}(\text{CN})_6 \cdot 3\text{H}_2\text{O}$, 0.1 M KOH as electrolyte. Cyclic voltammetry scans were acquired at a flow rate of 25 $\mu\text{L}/\text{min}$.



Annex 3. Perovskites: preliminary results

Perovskite oxides are mixed metal oxides with a general formula ABO_3 with a cubic structure as depicted in figure 17. Typically, they are composed by lanthanides, alkaline or alkaline-earth cations in the position A and transition metal cations, such as Co, Fe, Ni, Cr or Mn in the position B. These compounds withdraw major attention in the field of electrocatalysts thanks to their excellent thermal stability and tunable electronic structure, ionic conductivity, electron mobility and redox behavior properties, which provide remarkable activity and stability in OER and/or ORR. Their properties can be largely tailored, since there is a large flexibility to choose the cations in the A and B sites. Moreover, multiple cations can be inserted in the different sites leading to a more general formula $A_{1-x}A'_xB_{1-y}B'_yO_{3\pm\delta}$, and hence to even more variations of physical-chemical properties.



Sub-annex 3.1. Schematic representation of the structure of a perovskite

Perovskites manganites and cobaltites are attracting increasing interest since a few years, especially since the seminal works of Shao-Horn *et al.* on manganites for ORR and cobaltites for OER.² The electrocatalytic activity of these materials is among the highest reported for precious-metal free catalysts. However, their synthesis as nanoparticles with high surface-to-volume ratio is much more difficult than for spinels, as high temperatures (>600°C) are required by usual methods that result in large grain growth. Hence, retrieving high surface area nanoparticles of these perovskites is an arduous task. The LCMCP recently developed an innovative method based on the use of

thermally stable inorganic molten salts as media for the precipitation of nanoparticles at 600°C.³ Because nucleation kinetics are enhanced in liquids, a larger number of particles is formed at a constant amount of matter, resulting in smaller particles with high crystallinity. The nanoparticles obtained in molten salts expose well defined {100}_{cubic} facets.

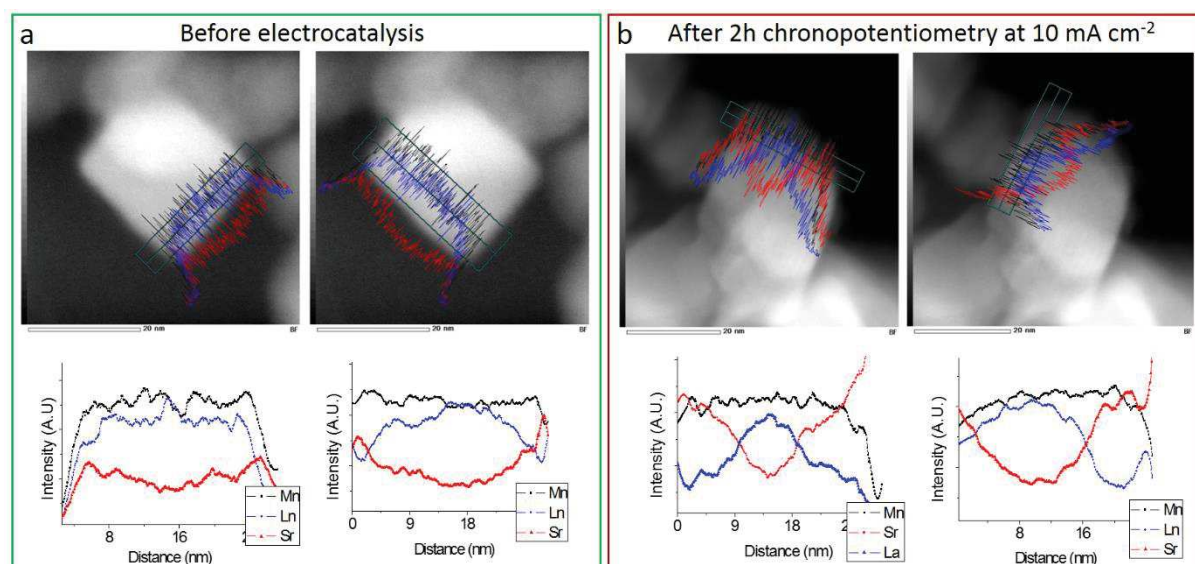
The comprehension of the nature of the active species and of the structural evolution of perovskite nanocrystals involved in electrocatalytic processes would be a breakthrough for the conception of new perovskite-based devices with enhanced efficiency and stability. As so, the nanoparticles produced at LCMCP are the subject of the present studies implementing the methodology described for Co₃O₄.

As in the case of cobalt oxide, the impact of the electrocatalyst ink composition on the electrochemical behavior during ORR was tested. The first ink tested was the classical composition containing carbon black and Nafion was assessed, and the second one was containing only the La_{2/3}Sr_{1/3}MnO₃ (LSMO) nanoparticles. The efficiency of the attachment of the particles to the surface of the electrode without Nafion has been shown in section 1.5. The current density decreased when the carbon black was removed from the ink, as could be expected, although electron percolation in the electrode and at the current collector/nanoparticle interface was sufficient to ensure electrocatalysis, even if not with the optimized activity. Given the difficulties raised by TEM imaging of nanoparticles embedded in Nafion and surrounded by carbon black particles, the additive-free ink was used for the *in situ* EC-TEM tests.

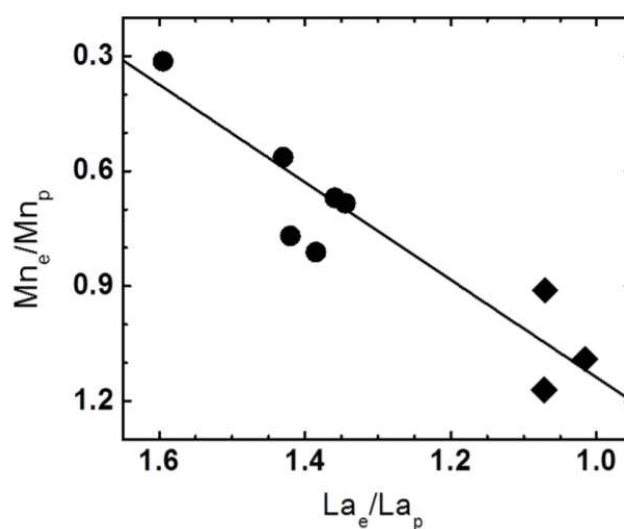
Composition redistribution hints

A first attempt to determine the nature of the possible transformations occurring in LSMO during ORR was done by *post mortem* analysis of a sample recovered from a regular glassy carbon electrode after 2 h chronopotentiometry at 10 mA cm⁻²_{GC}. The compositional profile (figure 20) of a nanoparticle corresponds to the Mn, La and Sr relative contents of 1.0, 0.7 and 0.3 in the center of the particles, while the La/Sr ratio is slightly increased at the edges of particles, with La/Sr = 0.6/0.4. However, when a similar nanoparticle was analyzed after chronopotentiometry, a depletion of La is observed at the surface of the nanoparticles, which agrees with an increase of the relative amount of Sr. According to Shao-Horn, et. al.⁴ the Mn over-stoichiometry correlates to a drop of surface La and vice versa. This was observed for LSMO epitaxial

films used as electrodes for the OER. In that case the dissolution of Mn induced the enrichment in La to preserve the structure. They have described the relation in figure 21. Thus, it is possible that in the case of the ORR, an inverse process where this depletion in La can be a sign of an enrichment in Mn. Further studies will be pursued in order to verify this hypothesis.



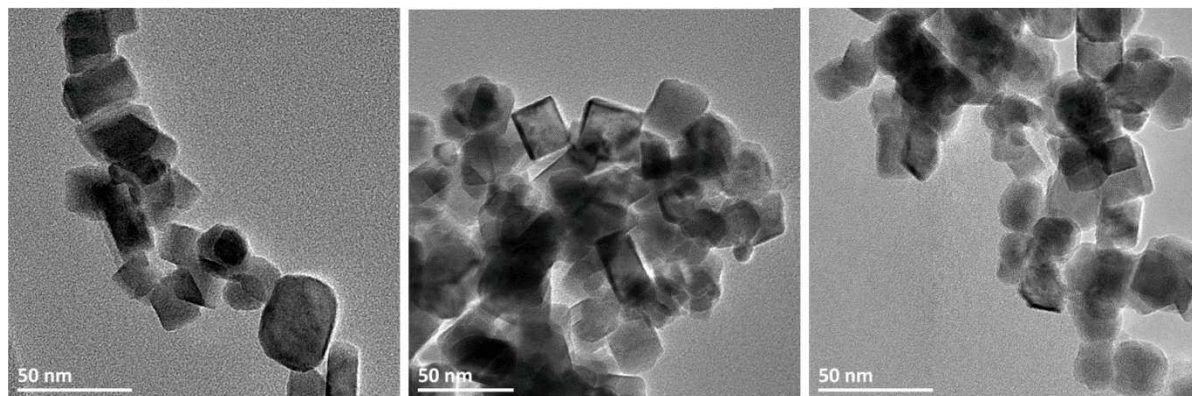
Sub-annex 3.2. Dark field images and (left) transversal and (right) longitudinal compositional profile showing the relative amounts of Mn, La and Sr of LSMO nanoparticle a) before electrochemistry and b) after 2 h chronopotentiometry at 10 mA cm⁻² *ex situ* in a classical 3 electrodes rotating disc cell at 1600 rpm.



Sub-annex figure 3.3. Correlation between changes in the surface stoichiometric ratio of electrolyzed (after 1 h CA at 1.7 V vs RHE) to pristine manganese (Mn_e/Mn_p) and lanthanum (La_e/La_p) determined by XPS. Electrolysis was either performed on pristine surfaces (circles) or repeated measurements (diamonds). Taken from ref ⁴

Can we see oxygen vacancies migrating?

As mentioned above, synthesis of perovskites in molten salts yields ligand-free surfaces with particle sizes below 100 nm. This is very useful to harness the properties of LSMO for electrocatalysis. Figure 22 shows that the synthesized LSMO nanoparticles size ranges from 20 to 60 nm. The wide size dispersion of the nanoparticles represents a difficulty to determine the changes induced by the electrocatalysis only with *post mortem* analysis. Thereby, *in situ* analysis is key in the comprehension of the catalytic mechanisms in these systems.



Sub-annex 3.4. TEM images of pristine LSMO nanoparticles synthesized in molten salts.

Kan *et al.* have shown that in LSMO thin films, ORR electrocatalysis might be driven by migrations of oxygen vacancies from the core to the lattice surface and *vice versa*.⁵ Such a migration would be caused by the change in the oxidation state of Mn during ORR. A similar behavior has been observed for magnetoresistive applications through *in situ* TEM by applying a voltage causing phase transitions that alter the resistivity of the material.⁶ Note that such *in situ* experiment was carried out in UHV conditions. Thus, the question to raise is the following: would we be able to observe such lattice distortion due to the oxygen vacancies migrating in the materials while in contact with the electrolyte? So far it seems unlikely with our *in situ* set-up, as described in section 1.4, since the resolution that can be reached within the liquid electrolyte ranges from 1-8 nm as a function of the thickness and of the composition, which is much larger than any

atom-scale change. However, the small amounts of catalyst used, along with the ease to identify a ROI in an e-chip, allows to perform identical location observations. Identical localization of a region would enable analysis without the electrolyte before and after the electrochemical measurements. This methodology could help to observe progressive phase transformations or changes in compositions the at sub-nanometric scale. Further improvements in the *in situ* set-up could also allow to reduce the liquid thickness and hence improve the resolution enough to access these types of processes. Consequently, final remarks about LSMO behavior during ORR studied by *in situ* electrochemical TEM come more as a short-term perspective.

Annex 4. Maximum temperature rise calculation due to the electron beam⁷

$$\Delta T_{max} = \frac{S 10^2}{\pi \alpha_{th} C_p} I \left(1 + \frac{t}{\lambda} \right) \left(\frac{1}{4} + \frac{1}{2} \text{Ln} \left[\frac{L}{a} \right] \right)$$

I = beam current; a= beam radius; t = thickness; L = Window size; λ = Mean free path

Parameter	Water	Organic solvent
S = stopping power (MeV cm ² g ⁻¹) (200 kV)	2.79 ⁸	2.99 (paraffin wax) ⁸
C _p = specific heat at constant pressure (J mol ⁻¹ K ⁻¹) (300 K)	75.28	564.4 (octadecane) ⁹
α_{th} = thermal diffusivity (10 ⁻⁶ m ² s ⁻¹) (300 K)	0.148 ¹⁰	0.06 (octadecane) ¹¹

Hence,

$$\Delta T_{maxWater} < 4 K$$

$$\Delta T_{maxOctadecane} < 10 K$$

References

- (1) Protochips. *Sample Preparation Guide*; 2016.
- (2) Suntivich, J.; Gasteiger, H. A.; Yabuuchi, N.; Nakanishi, H.; Goodenough, J. B.; Shao-Horn, Y. Design Principles for Oxygen-Reduction Activity on Perovskite Oxide Catalysts for Fuel Cells and Metal–Air Batteries. *Nat. Chem.* **2011**, *3*, 546–550.
- (3) Gonell, F.; Alem, N.; Dunne, P.; Crochet, G.; Beaunier, P.; Méthivier, C.; Montero, D.; Laberty-Robert, C.; Doudin, B.; Portehault, D. Versatile Molten Salt Synthesis of Manganite Perovskite Oxide Nanocrystals and Their Magnetic Properties. *ChemNanoMat* **2019**, *5*, 358–363.
- (4) Scholz, J.; Risch, M.; Stoerzinger, K. A.; Wartner, G.; Shao-Horn, Y.; Jooss, C. Rotating Ring-Disk Electrode Study of Oxygen Evolution at a Perovskite Surface: Correlating Activity to Manganese Concentration. *J. Phys. Chem. C* **2016**, *120*,

- 27746–27756.
- (5) Kan, D.; Orikasa, Y.; Nitta, K.; Tanida, H.; Kurosaki, R.; Nishimura, T.; Sasaki, T.; Guo, H.; Ozaki, Y.; Uchimoto, Y.; et al. Overpotential-Induced Introduction of Oxygen Vacancy in $\text{La}_{0.67}\text{Sr}_{0.33}\text{MnO}_3$ Surface and Its Impact on Oxygen Reduction Reaction Catalytic Activity in Alkaline Solution. *J. Phys. Chem. C* **2016**, *120*, 6006–6010.
 - (6) Yao, L.; Inkinen, S.; Dijken, S. Van. Direct Observation of Oxygen Vacancy-Driven Structural and Resistive Phase Transitions in $\text{La}_{2/3}\text{Sr}_{1/3}\text{MnO}_3$. *Nat. Publ. Gr.* **2017**, *8*, 1–9.
 - (7) Schneider, N. M. Electron Beam Effects in Liquid Cell TEM and STEM. In *liquid cell electron microscopy*; 2017; pp 140–163.
 - (8) Berger, M. J.; Seltzer, S. M. *Stopping Powers and Ranges of Electrons and Positrons*; 1983.
 - (9) U.S. Secretary of Commerce on behalf of the United States of America. Octadecane <https://webbook.nist.gov/cgi/cbook.cgi?ID=C593453&Units=SI&Mask=FFF> (accessed Oct 14, 2019).
 - (10) Water - Thermal Diffusivity https://www.engineeringtoolbox.com/water-steam-thermal-diffusivity-d_2058.html (accessed Oct 14, 2004).
 - (11) Vélez, C.; Khayet, M.; Ortiz De Zárate, J. M. Temperature-Dependent Thermal Properties of Solid/Liquid Phase Change Even-Numbered n-Alkanes: N-Hexadecane, n-Octadecane and n-Eicosane. *Appl. Energy* **2015**, *143*, 383–394.

Annexed movies

[Annex movie M1. Co₃O₄ during Cyclic Voltammetry in 0.1 M KOH](#)

[Annex movie M2. Co₃O₄ during Chronoamperometry at 10 mA cm² in 0.1M KOH](#)

[Annex movie M3. Thermal decomposition iron oxide](#)

[Annex movie M4. Thermal decomposition vesicles](#)

[Annex movie M5. Thermal decomposition inverse micelles](#)

[Annex movie M6. Thermal decomposition inverse micelles -2](#)

[Annex movie M7. Octadecene](#)

[Annex movie M8. Thermal decomposition high electron dose TEM](#)

[Annex movie M9. Thermal decomposition medium electron dose TEM](#)

[Annex movie M10. Thermal decomposition low electron dose TEM](#)

[Annex movie M11. Thermal decomposition STEM-1](#)

[Annex movie M12. Thermal decomposition STEM-2](#)

[Annex movie M13. Hydroxyapatite stages 3-4-5](#)

[Annex movie M14. Calcium carbonate nucleation-dissolution](#)

[Annex movie M15. Beam irradiation before EC in pyrocatechol](#)

[Annex movie M16. Electrodeposited sheets within the electrolyte](#)

***In situ* liquid phase transmission electron microscopy: from electrocatalysts to biomaterials**

Résumé

La microscopie électronique à transmission en phase liquide offre une opportunité unique d'explorer le comportement dynamique des matériaux synthétiques et biologiques à l'échelle nanométrique dans des conditions *in situ* et opérationnelles. Ainsi, dans un premier temps, on a déterminé l'ensemble de paramètres d'observation le mieux adapté en fonction de la nature du matériau analysé; l'effet de faisceau d'électrons; la procédure de dépôt de l'échantillon ainsi que le mode d'observation. La méthodologie développée a ensuite été mise en œuvre pour étudier le comportement dans des conditions opératoires de nanoparticules de Co_3O_4 en tant qu'électrode pour l'électrocatalyse. Troisièmement, cette technique *in situ* a été utilisée pour les étapes de pré-nucléation des nanoparticules d'oxyde de fer ont été dévoilées ainsi que l'impact de la quantité d'énergie sur la croissance. De même, les processus de biominéralisation de phosphate et carbonate de calcium ont été suivis afin d'évaluer les processus de cristallisation. Enfin, l'électrodéposition de pyrocatechol a été étudié par localisation identique.

Mots-clés : microscopie électronique à transmission en phase liquide, électrocatalyse *in situ* et *operando*, nucléation et croissance nanoparticules, électrodéposition.

Abstract

The liquid phase Transmission Electron Microscope provides a unique opportunity for exploring the dynamical behavior of synthetic and biological materials at nanometric scale within *in situ* and *operando* conditions. Thus, in first instance, we established the most suited set of observation parameters, considering the nature of the reaction and/or the material analyzed; the electron beam effect; the sample deposition procedure as well as the observation mode. Then, the developed methodology was implemented to study the behavior in *operando* conditions of Co_3O_4 nanoparticles as an electrode material for the electrocatalysis of the oxygen evolution reaction. Third, the *in situ* set up was used to study the nucleation and growth of inorganic and biological nanoparticles. The pre-nucleation stages of the iron oxide nanoparticles were unveiled and the impact of the amount of energy in the growth. Similarly, mineralization processes of calcium phosphate and calcium carbonate were tracked in to evaluate the crystallization pathways. Finally, the observation by identical location the electrodeposition of pyrocatechol was explored.

Keywords: Liquid phase transmission electron microscopy, electrocatalysis *in situ* and *operando*, nanoparticle nucleation and growth, electrodeposition.

